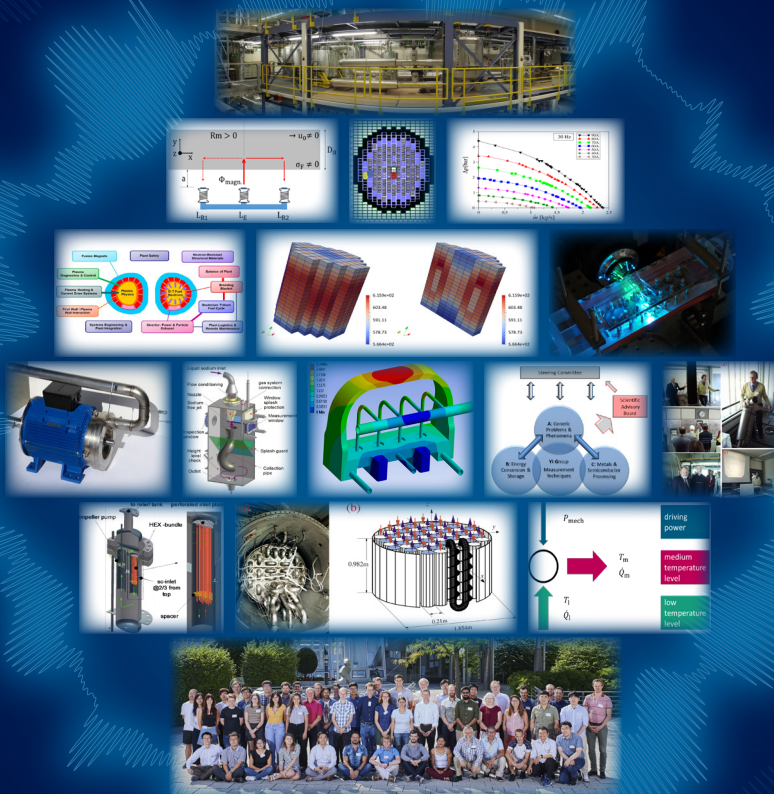


Thomas Wetzel · Walter Tromm · Joachim Knebel

# Everlasting Energy



In Memoriam  
**Prof. Dr.-Ing. Robert Stieglitz**



Thomas Wetzel, Walter Tromm, Joachim Knebel

Everlasting Energy

In Memoriam Prof. Dr.-Ing. Robert Stieglitz





# Everlasting Energy

In Memoriam Prof. Dr.-Ing. Robert Stieglitz

by

Thomas Wetzel, Walter Tromm, Joachim Knebel

## Impressum



Karlsruher Institut für Technologie (KIT)  
KIT Scientific Publishing  
Straße am Forum 2  
D-76131 Karlsruhe

KIT Scientific Publishing is a registered trademark  
of Karlsruhe Institute of Technology.  
Reprint using the book cover is not allowed.

[www.bibliothek.kit.edu/ksp.php](http://www.bibliothek.kit.edu/ksp.php) | E-Mail: [info@ksp.kit.edu](mailto:info@ksp.kit.edu) | Shop: [www.ksp.kit.edu](http://www.ksp.kit.edu)



*This document – excluding parts marked otherwise, the cover, pictures and graphs –  
is licensed under a Creative Commons Attribution-Share Alike 4.0 International License  
(CC BY-SA 4.0): <https://creativecommons.org/licenses/by-sa/4.0/deed.en>*



*The cover page is licensed under a Creative Commons  
Attribution-No Derivatives 4.0 International License (CC BY-ND 4.0):  
<https://creativecommons.org/licenses/by-nd/4.0/deed.en>*

Print on Demand 2025 – Gedruckt auf FSC-zertifiziertem Papier

ISBN 978-3-7315-1417-6

DOI 10.5445/KSP/1000179233





# Preface

A lasting gift of death to the living is an expanded view of life itself. We have understood this common statement as a mandate – to look back on the life of our colleague and friend Prof. Dr.-Ing. Robert Stieglitz, who died suddenly and unexpectedly on December 6, 2023, at the age of 58.

"Prof. Stieglitz was a great person and an internationally recognized scientist whose profound expertise and critical opinion were valued worldwide due to his broad knowledge in the field of fusion research, nuclear technology and renewable energies. He encouraged and motivated his colleagues, collaborators and partners with his kindness, openness and above all his wealth of inspiration. Prof. Stieglitz was an enthusiastic researcher and university teacher who enriched research-oriented teaching both nationally and internationally".

This is what the members of the Institute of Neutron Physics and Reactor Technology (INR) at the Karlsruhe Institute of Technology (KIT), which he headed since 2009, wrote on the condolence page of the institute after his death. And this is how we, the editors of this volume, feel. With this in mind, we asked colleagues who worked with Robert, if they would like to contribute to this memorial volume. You will see the impressive response on the following pages.

We hope that this volume will help those who miss Robert most, his family and friends, to look back on an important part of his life in the spirit of the phrase mentioned at the beginning. We would like to thank all the contributors for their great cooperation in putting this volume together. Special thanks go to Mrs. Birgit Zagolla, INR, for her tireless, motivating, and inspiring support at all stages of the editorial process.

Most of all, we thank and bow to Robert. Goodbye, dear friend!

*Joachim Knebel, Walter Tromm und Thomas Wetzel*



# Table of Contents

<b>Preface .....</b>	<b>i</b>
Joachim Knebel, Walter Tromm und Thomas Wetzel	
<b>Dynamo Karlsruhe vs Dynamo Riga: The match and its aftermath .....</b>	<b>1</b>
Frank Stefani, Gunter Gerbeth and Thomas Gundrum	
<b>Robert Stieglitz’ traces in the history of Karlsruhe Liquid Metal Laboratory (KALLA) ...</b>	<b>23</b>
Markus Daubner, Joachim Knebel and Thomas Wetzel	
<b>Historical overview of the HELMHOLTZ Alliance LIMTECH: Advancing liquid metal research and innovation .....</b>	<b>57</b>
Thomas Wetzel, Sven Eckert and Gunter Gerbeth	
<b>Prof. Dr.-Ing. Robert Stieglitz’ role in and contribution to the success of the FJOHSS ..</b>	<b>69</b>
Victor Hugo Sanchez-Espinoza, Fabrizio Gabrielli, Walter Tromm, Ingeborg Schwartz and Petra Klug	
<b>ITER and DEMO – Technology challenges on the way to fusion power .....</b>	<b>73</b>
Klaus Hesch and Robert Stieglitz†	
<b>International Fusion Materials Irradiation Facility - Demo Oriented NEutron Source (IFMIF-DONES) .....</b>	<b>89</b>
Christoph Kirchlechner, Dirk Radloff, Hans-Christian Schneider, Frederik Arbeiter, Dieter Leichtle, Sebastian Ruck, Klaus Hesch and Anton Möslang	
<b>Creep-fatigue assessment of breeding blanket components .....</b>	<b>97</b>
Roshan Rajakrishnan, Mathias Jetter, Guangming Zhou and Jarir Aktaa	
<b>Experimental test of a helical induction pump with rotating core .....</b>	<b>119</b>
Leo Bühler and Robert Stieglitz†	
<b>Scale separation in thermal turbulent flows – a specific Péclet number scaling analysis .....</b>	<b>127</b>
Sebastian Ruck	

**Technical approach and realization of a contactless, inductive flowmeter - the Phase-Sensitive Flowmeter ..... 137**

Dominique Buchenau

**Applying solar energy for cooling – a basic thermodynamic analysis ..... 159**

Hans-Martin Henning

**Modeling the calendering of lithium-ion battery electrodes and the impact on transport properties ..... 171**

Alexandra Wahn and Marc Kamlah

**Simulation of single control rod withdrawal transients in an LBE cooled reactor ..... 189**

Xue-Nong Chen, Yoshiharu Tobita and Andrei Rineiski

**Does Partitioning & Transmutation have a future as a nuclear waste management strategy?..... 197**

Bruno Merk, Lakshay Jain, Omid Noori-kalkhoran, Elfriede Derrer-Merk, Gregory Cartland-Glover, Lewis Powell, Andrew Jones, Anna Detkina, Dzianis Litskevich and Maulik Patel

**Thermal-hydraulic analysis of spallation target for accelerator-driven systems ..... 223**

Xu Cheng, Abdalla Batta and Joachim Knebel

**Analysis of the Steam Line Break (SLB) accident for the SMART Small Modular Reactor (SMR)..... 253**

Kanglong Zhang and Victor Hugo Sanchez-Espinoza



# Dynamo Karlsruhe vs Dynamo Riga: The match and its aftermath

Frank Stefani<sup>1</sup>, Gunter Gerbeth<sup>1</sup> and Thomas Gundrum<sup>1</sup>

<sup>1</sup> Helmholtz-Center Dresden-Rossendorf, Bautzner Landstr. 400, 01328 Dresden, Germany

## Abstract

In late 1999, after decades of preparatory work, two large-scale liquid-sodium dynamo experiments became operative and successfully showed self-excitation of a magnetic field. The single-scale, Ponomarenko-type dynamo in Salaspils, close to Riga (Latvia), was conceived and designed by Agris Gailitis. The two-scale,  $\alpha^2$ -type dynamo in Karlsruhe had been constructed by Robert Stieglitz. We recall the history of the race to the first liquid-metal dynamo, discuss the differences and commonalities, and sketch the lasting influence of these pioneering experiments.

**Schlagworte:** Geodynamo, Solar dynamo, Dynamo experiments, Liquid sodium

## 1 Introduction

On September 26, 1996, Robert Stieglitz gave a seminar at Forschungszentrum Rossendorf, titled “Wie entsteht das Magnetfeld der Erde” („How is the Earth’s magnetic field generated”). The lecture started with recalling the seminal experiment by Busse and Carrigan [1] on the generation of flow rolls in a rotating spherical shell (now known as “Busse rolls”) by the interaction of centrifugal and Coriolis forces and Ekman pumping. It went on by summarizing typical features of the geodynamo, and introduced the two main types of mean-field dynamos, namely the  $\alpha^2$  and the  $\alpha$ – $\Omega$  dynamo [2]. Robert then sketched the two concepts of experimental dynamos, based on ideas of Ponomarenko [3] on one hand, and of G.O. Roberts [4] and Busse [5] on the other hand. He continued with describing the Karlsruhe dynamo concept in much depth. For one of us (F.S.), who was new in magnetohydrodynamics at this time, the talk was a revelation: it combined a deep understanding of dynamo theory with an extraordinary mastery of the enormous technical challenges connected with such a large-scale liquid-sodium experiment.



Figure 1.1: Impressions from the *International Workshop on Homogeneous Dynamos*, organized by Robert Stieglitz and Ulrich Müller at Forschungszentrum Karlsruhe, March 20-22, 2000. (a) Agris Gaillitis and Robert Stieglitz during the visit of the dynamo experiment. (b) Robert Stieglitz, explaining the control panel to Andreas Tilgner, Cary Forest, Gunter Gerbeth, Ernests Platacis, and Philippe Cardin (from left to right). (c) Karl-Heinz Rädler and Willi Deinzer besides the central dynamo module. (d) Robert Stieglitz explaining a part of the piping system. (e) Robert Stieglitz during his talk on March 21. Photographs by Thomas Gundrum.

Three and a half years later, Robert Stieglitz and Ulrich Müller organized a workshop on homogeneous dynamos at Forschungszentrum Karlsruhe [6]. In the meantime, in late

1999, the two experiments in Riga and Karlsruhe had been successfully conducted, leading to a public controversy regarding priority. It was in this somewhat heated situation that Robert took the initiative (by picking up the phone to call one of us, G.G.) to objectify the entire discussion. The Karlsruhe organizers were kind enough to let the workshop start with various contributions from the Riga-Rosendorf team, to be followed by talks of the Karlsruhe-Bayreuth-Potsdam team, and a visit to the dynamo experiment (see Figure 1.1) on the next day. The workshop minutes summarized the main results in the following way: “Special emphasis was given to the Riga and Karlsruhe dynamo experiments, which achieved conditions of self-excitation in November and December 1999, respectively. For both cases clear evidence was presented that dynamo action was achieved. In the Riga dynamo experiment self-excitation was identified by the frequency of the dynamo state. In the Karlsruhe experiment dynamo action was demonstrated by the intensity of the generated mean magnetic field” [6]. With this Solomon-like judgement, a somewhat overstrained priority discussion gave way to the joint celebration of the concurrent successes of these two experiments, which were indeed realizations of two complementary dynamo concepts.

## 2 The match

In this section, we will delineate the theoretical background, the technical implementation, and the key results of the Riga and Karlsruhe dynamo experiment. Before that, however, we give a short overview about the history of our comprehension of the magnetic fields of the Earth, and other cosmic bodies.

### 2.1 Prelude

Magnetism has been known for millennia. Thales of Miletus was already aware of the attracting forces of lodestone, and the compass had been invented and used both by the old Chinese and the Olmecs. As early as 1269, Petrus Peregrinus published a systematic study [7] of the attracting and repelling forces of lodestone, in which he introduced the concept of polarity into science by distinguishing the north and south poles of the magnet. Inspired by this pioneering work, William Gilbert performed further experiments with small spheres of lodestone (“terrellae”), leading him to the plausible (but wrong) conclusion “...that the terrestrial globe is magnetic and is a loadstone” [8]. While this lodestone theory soon ran into trouble with the observation of the westward drift of the Earth’s magnetic field by Gellibrand in 1635 [9], it was still broadly accepted at

the times of Gauß. Only the detection of abrupt polarity reversals by David and Brunhes in 1904/05 [10] made it ripe for being replaced by something different.

Remarkably, then, the birth of modern dynamo theory was not initiated by that fundamental failure of the lodestone theory of the Earth's magnetic field, but by Hale's detection of Zeeman splitting in the spectrum of light measured over sunspots [11]. This observation led Larmor to speculate [12] that it could be "...possible for the internal cyclic motion to act after the manner of the cycle of a self-exciting dynamo, and maintain a permanent magnetic field from insignificant beginnings, at the expense of some of the energy of the internal circulation." With this explanation of a natural process in terms of the functioning principle of technical devices invented half a century earlier by Jedlik [13], Hjort [14], Siemens [15], and Wheatstone [16], the theory was put on the right track. Nowadays, dynamo science is well established, and successfully describes many aspects of planetary, stellar and galactic magnetic fields.

In contrast to this enormous progress in theory, hydromagnetic dynamo experiments seemed to be at the edge of technical feasibility for a long time. The key problem to achieve magnetic field self-excitation is that the critical magnetic Reynolds number  $R_m$  (defined as  $R_m = \mu \sigma L V$ , with magnetic permeability  $\mu$ , conductivity  $\sigma$ , characteristic length  $L$  and velocity  $V$ ) is typically of the order of 100, depending on the specific flow geometry. For the best liquid-metal conductor, sodium, the product  $\mu \sigma$  is approximately  $10 \text{ s/m}^2$ . Hence, to get an  $R_m$  of around 100, the product  $LV$  of length and velocity has to be as large as  $10 \text{ m}^2/\text{s}$ . To reach those values, it typically requires around one ton of liquid sodium, and 100 kW of mechanical power to move it (smaller devices would require even larger power, due to the power scaling  $P \sim R_m^3/L$  that applies in the turbulent regime). Another option to increase  $R_m$  is by using materials with a high magnetic permeability  $\mu$ . That "trick" was indeed realized in a series of rotating soft-iron cylinder experiments by Lowes and Wilkinson [17-19]. The history of these quasi-homogeneous, though not liquid, dynamo experiments is quite inspiring, not only for their step-by-step improvements, but also for the continuing comparison of the resulting field features with those of the geodynamo. Setting-out from a simple geometry of the rotating cylinders, which produced steady and oscillating magnetic fields, an improved design later allowed for the observation of field reversals. Of course, the experiments were compromised by the use of magnetic materials and the nonlinear field behavior, which is inevitably connected with the use of these materials. One attempt to get self-excitation with rotating non-magnetic copper cylinders failed. Moreover, although more or less homogeneous, these dynamos were not suited to study the back-reaction of the magnetic field on the fluid motion.

## 2.2 Dynamo Riga

The main idea of the Riga dynamo traces back to Ponomarenko's finding that a helically moving, electrically conducting cylinder embedded in an infinite stationary conductor is prone to self-excitation of a magnetic field [3]. This simple configuration, which can indeed be considered as the paradigm of a homogeneous dynamo, was analysed in more detail by Gailitis and Freibergs [20,21]. After transforming the convective instability of the original Ponomarenko dynamo into an absolute one (by adding an appropriate concentric back-flow region), a relatively low critical magnetic Reynolds number of approximately 20 was identified. With this promising number in mind, a first large-scale experiment was carried out in Leningrad in 1986 [22]. After having shown substantial field amplification, though no self-excitation, this experiment was stopped owing to a spilling out of sodium. Based on that experience, an improved experiment was designed and constructed in Salaspils, a town close to Riga (Figure 2.1a), with much effort spent on optimizing the geometry of the whole facility [23] and on fine-tuning the flow structure to obtain maximum helicity [24].

Starting in November 1999, more than ten experimental campaigns have been carried out with this device. During the cooling down of the sodium from the initial temperature of 300 °C (needed for assuring a good electrical wetting between sodium and the steel walls), some pre-experiments were conducted, showing again large amplifications of an externally applied field (similar in shape to the expected eigenfield, shown in Figure 2.1b). However, in the evening of 11<sup>th</sup> November 1999, at the highest rotation rate of the propeller, a self-excited field was observed on top of the amplified one, although only for a short period of 15 s [25]. For a slightly lowered rotation rate, a very slow field decay was recorded, after the excitation field had been switched off. As shown in Figure 2.1d, the frequencies of these two slowly growing and decaying signals recorded on 11<sup>th</sup> November 1999 (green squares) fit perfectly into the large pool of frequencies measured in later campaigns, a fact that strongly reassures the claim for dynamo action as made in [25].

Yet, due to some outbreak of a relatively minor amount (around 100 grams) of sodium from the sealing, the experiment had to be stopped, so that the saturated regime could not be reached in this November 1999 campaign. This had to be postponed to the July 2000 experiment [26], after the sealing problem had been fixed [26]. In later experiments, the measurement techniques were refined, finally allowing for a detailed investigation of the radial and axial structure of the magnetic field, some turbulence properties, and the saturation mechanism. More details regarding these experimental results, and their comparison with the numerical ones, can be found in [27-31], as well as in the

comprehensive summary [32]. Figure 2.1c illustrates a representative run from the June 2002 campaign, showing the propeller's rotation rate and the resulting magnetic field.

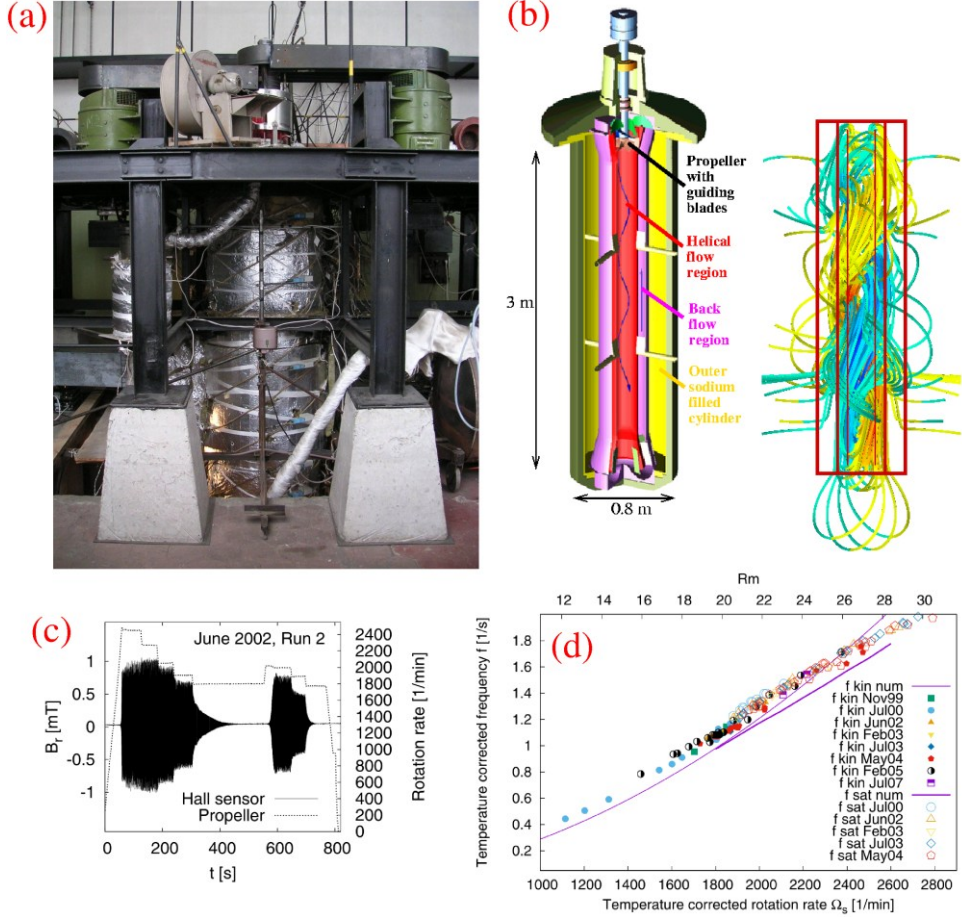


Figure 2.1: Riga dynamo experiment: (a) Photograph showing the main frame, the central module with thermal insulation, and the two motors. (b) Sketch of the central module with three concentric cylinders and the propeller region, and the simulated magnetic eigenfield. (c) One representative dynamo run from the June 2002 campaign, showing the propeller's rotation rate and the field measured at one external Hall sensor outside the cylinder. Note the threshold character of the self-excitation process, and the dependence of the saturation field strength on the rotation rate. (d) Compilation of (temperature corrected) eigenfrequencies of the field, measured during different campaigns between November 1999 and May 2004, jointly with the simulated data. Note the perfect fitting of the two early results from November 1999 (green squares) into the general scheme. (c) and (d) are adapted from [32].

After some necessary repairs of the machine, some late campaigns were carried out more recently [33-35], mainly intended to validate the working of the machine before eventually switching to a new design of the propeller region. With the latter modification, it was planned to implement a sort of “de-optimized” velocity profile, characterized by a too high azimuthal component, which is supposed to lead to a more complicated saturated state. According to numerical predictions [3], the latter should vacillate between a low and a high energy state [36]. It remains to be seen if that modification can still be realized.

## 2.3 Dynamo Karlsruhe

While the eigenfield of the Riga dynamo experiment has the same spatial scale as the underlying flow structure, the Karlsruhe dynamo (Figure 2.2a,b) is a two-scale experiment whose mean magnetic field is excited on a much larger scale than the small-scale flow that generates it. Interestingly, the main idea of the later Karlsruhe experiment can already be found in a 1967 paper by Gailitis [37], proposing to substitute the real helical turbulence of the outer core of the Earth by a sort of “pseudo-turbulence”. It was, however, the independent corroboration of this concept by Busse [5] that put the development of the Karlsruhe dynamo on track.

Another theoretical root of this experiment is the Roberts flow [4], a velocity pattern periodic in the horizontal coordinates  $x$  and  $y$  that comprises both a rotational and an axial flow. The collective induction of this flow configuration can be described in terms of the  $\alpha$ -effect of mean-field MHD [2], a quantity with the physical unit  $\text{m s}^{-1}$  that represents the non-mirrorsymmetric, or helical, part of the turbulent flow. For the Roberts flow, this  $\alpha$ -effect turns out to be highly anisotropic; it produces an electromotive force exclusively in horizontal directions but not in the axial one [38]. In the specific realization of the Karlsruhe experiment, a modified Roberts flow structure in each cell is realized by a flow through two concentric channels (Fig. 2.2b). In the central channel, the flow is straight, whereas in the outer “spiral staircase” channel it is forced on a helical path. The optimization to achieve a maximum  $\alpha$ -effect at a given pump power led to a number of 52 spin generators, a radius of 0.85 m and a height of 0.7 m for the central dynamo module.

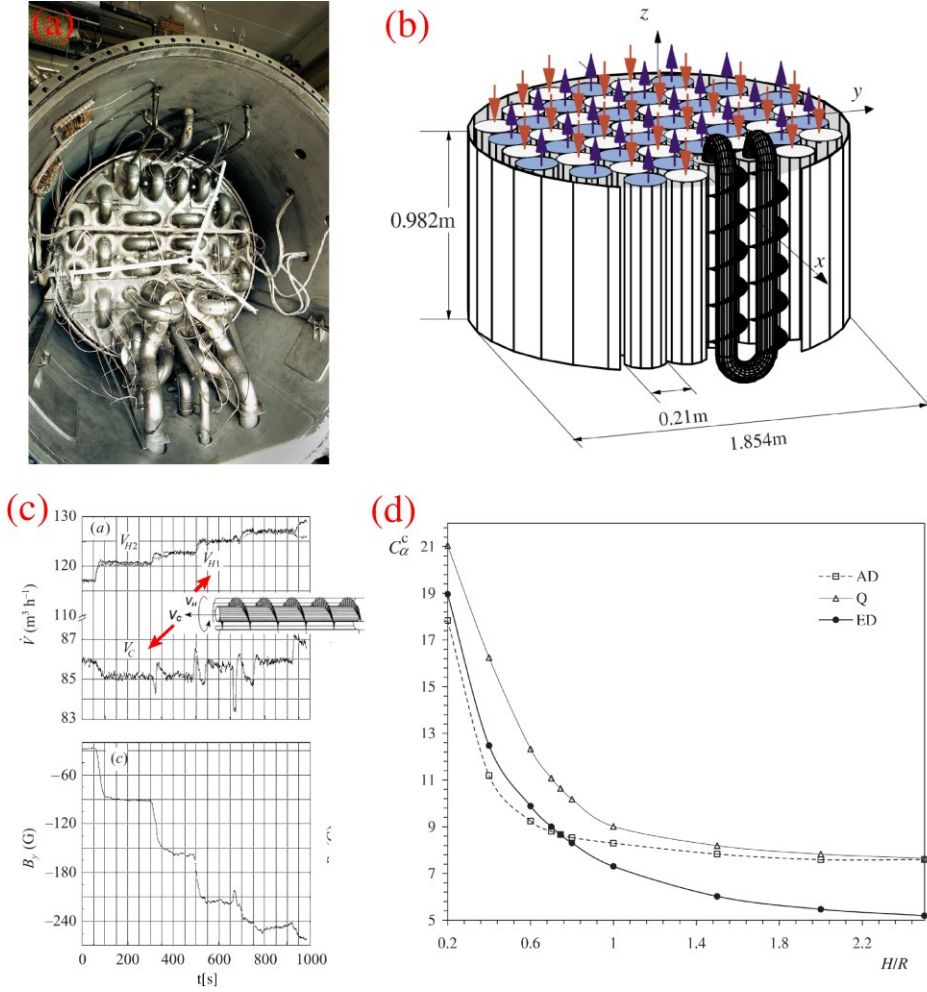


Figure 2.2: The Karlsruhe dynamo experiment. (a) Photograph of the central module with 52 spin generators. (b) Schematic of the inner part. (c) Data from one run, showing the increasing amplitude of the eigenfield with growing flow rate in the helical channel, with the flowrate in the straight central channel being mainly fixed. (d) Critical magnetic Reynolds number of the axial dipole (AD), the equatorial dipole (ED), and the quadrupole field (Q), in dependence on the ratio of height to radius of a Karlsruhe-type dynamo. At the actual value  $H/R=0.85$  of the Karlsruhe experiment, the equatorial dipole is dominant (i.e. has the lowest critical magnetic Reynolds number). However, even for slightly lower values of  $H/R$ , one could have expected the transition to an (geodynamo-like) axial dipole. (a) adapted from [41]. (b) adapted from [44]. (c) adapted from [42]. (d) adapted from [49].



In its relatively short lifetime, starting on 2<sup>nd</sup> December 1999 [39,40], the Karlsruhe experiment has produced many intriguing results related to imperfect dynamo bifurcation (Figure 2.2c), MHD turbulence [41-43], and the effect of periodic flow forcings [44]. The experimentally determined neutral line, separating dynamo and non-dynamo regions, was shown to be in very good agreement with numerical predictions resulting both from mean-field dynamo theory [45] and a direct simulation of the spin-generator system [46,47]. Later, data from the Karlsruhe experiment were used to distinguish between two different scaling laws for power consumption of the geodynamo [48].

After all those great successes, the Karlsruhe experiment was disassembled a bit in a rush, also to the chagrin of Robert. Unfortunately, in 2007, we were too late with our numerical prediction [49] that just a slight modification of the aspect ratio of the central module could have changed the dominant dipole direction from equatorial to axial (see Figure 2.2d), with interesting prospects for field-reversal studies. One of the lessons to learn from that is: do not scrap a well-running machine too early, when it might still be fit for more than a knacker's yard.

## 3 The aftermath

The pioneering experiments in Riga and Karlsruhe were followed by a number of further liquid metal experiments. Among them, we will highlight the “von Kármán sodium” (VKS) experiment as it indeed has shown dynamo action, while delineating other experiments only shortly. At the end of this section, we will sketch the DRESDYN precession experiment at HZDR.

### 3.1 Cadarache

The name of the “von Kármán sodium” (VKS) dynamo experiment (Figure 3.1) in Cadarache (France) refers to the correspondent flow that emerges between two rotating disks. This flow geometry is a realization of the so-called  $s_2+t_2$  flow (consisting of two poloidal vortices ( $s_2$ ) that are inward directed in the equatorial plane (+) and two counter-rotating toroidal vortices ( $t_2$ )) which had been shown to yield self-excitation at comparably low values of the critical  $Rm$ , both in spheres [50] and in cylinders [51].

The cylindrical vessel of the VKS experiment contained 150 l of liquid sodium, which was stirred by two motors with a total power of 300 kW. Only after the stainless steel of the impeller disks and blades had been replaced by soft iron, self-excitation was achieved in

2006 [52]. In some parameter regions, characterized by asymmetric forcings of the two impellers, most interesting dynamical regimes were recorded, including impressive magnetic field reversals [53-57]. Displaying characteristic features of low-dimensional dynamical systems, these surprising results encouraged theoretical efforts to understand the very essence of field reversals by using simple ordinary differential equation [58] or 1D partial differential equation models [59].

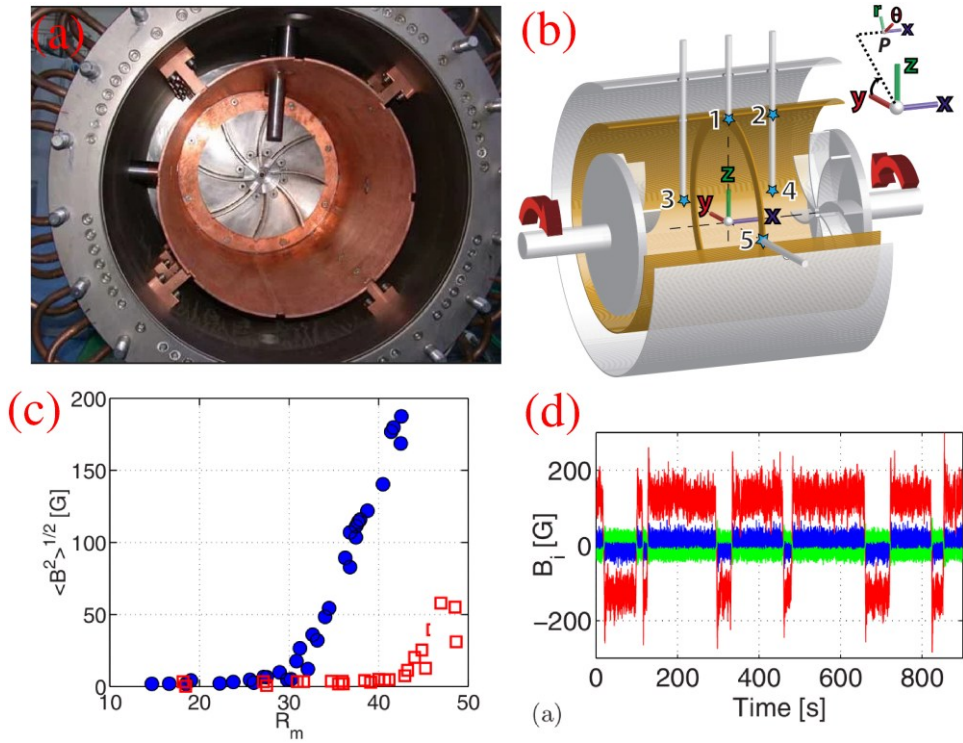


Figure 3.1: The von-Kármán-sodium (VKS) experiment in Cadarache. (a) Photograph of the inner part with copper hull and soft-iron impeller. (b) Schematic, indicating the counter-rotation of the two impellers. (c) Amplitude of the measured field in dependence on the magnetic Reynolds number  $R_m$ , at equal rotation rates of the impellers, both for “unscooping” rotation (blue) and “scooping” rotation (red). (d) One run showing reversals of the magnetic field. (b-d) adapted from [55].

Surprisingly, the self-excited eigenfield turned out to be basically an axisymmetric one, in contradiction to the non-axisymmetric equatorial dipole that was consistently predicted by all preparatory numerical simulations [60,61]. More recent simulations pointed to an essential role of the high magnetic permeability of the iron impellers, in addition to the local helicity in the propeller region [62-65]. Even today, a complete explanation of the working principle of the VKS dynamo and the detailed role of the soft-iron disks and blades is still elusive.

### **3.2 Further dynamo (related) experiments**

In terms of the underlying  $s^2t^2$  flow topology, the Madison dynamo experiment (MDX) was quite similar to the VKS dynamo. The differences to VKS are that MDX worked not in a cylinder but in a 1-m-diameter sphere, and that the flow was driven by nozzles instead of disks with blades. While, despite careful optimization, MDX has not yet shown unambiguous proof of self-excitation, many interesting results were obtained. First, the flow-induced magnetic field turned out to be dominated by an axial dipole component [66], despite the fact that an axial dipole cannot be induced by a large-scale axisymmetric flow. Further results were related to intermittent bursts of dynamo action [67], the detailed measurements of the magnetic field structure [68], its interpretation in terms of turbulent diamagnetism [69], and the estimation of the turbulence-enhanced resistivity (also called  $\beta$ -effect in mean-field MHD) on the order of 30 per cent for the highest  $R_m$  [70]. For the more recent plasma-dynamo activities in Madison, see [71].

The giant rotating sphere experiment in Maryland with a diameter of 3 m has provided a surge of most interesting results. With its water-filled variant, it led to the observation of a bistable torque regime [72], of various inertial waves [73], and of a precessional state in a supposedly solid-body rotation [74]. Recent liquid-sodium experiments with a smooth inner sphere [75] have provided first results concerning field induction. The occurrence of transient exponential field increases as observed in a recent experiment with a “roughened” surface of the inner sphere [76] is still under scrutiny.

The efforts of the Perm group to reduce the driving power for a Ponomarenko-type dynamo rely on the idea that an appropriate flow can be produced when the rotation of a torus is abruptly stopped and a fixed diverter guides the inertially continuing flow on a helical path [77]. In some preliminary experiments, important results on mean-field turbulence parameters have been obtained: first sodium experiment with  $R_m \sim 30$  quantified the turbulent  $\beta$ -effect to be in the range of 50 per cent [78], which is in

reasonable agreement not only with the above-mentioned results from the Madison experiment [70], but also (when scaled to the respective magnetic Reynolds number) with the estimated  $\beta$ -effect of the geodynamo in the range of 200-300 per cent [79].

The New Mexico Taylor-Couette experiment in Socorro [80] provided a substantial  $\Omega$ -effect that was planned to be later complemented by a corresponding  $\alpha$ -effect, to be realized by some pulsed jet-driven “plumes”. Motivated by galactic dynamo models, this experiment has successfully demonstrated, at  $R_m$  close to 120, the winding up of the toroidal field to an amplitude eight times the radial component of an applied poloidal magnetic field [81].

While not (yet) successful in reaching dynamo action, those experiments have made valuable contributions to the understanding of MHD flows at high  $R_m$ . The measured mean-field coefficients, in particular, may become instrumental for calibrating numerical models of various cosmic dynamos. Mean-field ideas were also successfully applied to the two recent disk-dynamos using copper disks with spirally formed gaps [82,83] to provide the induced current with an azimuthal component. Interpreted as an anisotropic mean-field conductivity [84], this provision makes these machines a sort of intermediate between homogeneous and inhomogeneous dynamos.

### 3.3 The DRESDYN precession experiment

Recent years have seen a surge in works devoted to the effects of astronomical, or harmonic forcings, such as libration, precession, or tides. In a small-scale experiment, using GaInSn [85], a tide-like electromagnetic force was used to study the synchronization of the helicity oscillation that is intrinsically connected with the sloshing of the large-scale circulation in Rayleigh–Bénard convection. The astrophysical background for this experiment was the quest for a sensitive, energy-efficient mechanism that is potentially capable of synchronizing the solar dynamo by planetary tidal forces (see [86] for a summary of the corresponding efforts).

As for precession, motivated by previous experiments [87-90] and encouraged by a successful dynamo simulation for the sphere [91], a large-scale dynamo experiment has been constructed over the last decade in frame of the DRESDYN-project at Helmholtz-Zentrum Dresden-Rossendorf [92-93]. A rotation vessel with a central cylindrical volume of 2 m height and 2 m diameter is supposed to rotate at rates of up to 10 Hz and to precess at up to 1 Hz (Figure 3.2a,b). Of the resulting magnetic Reynolds number of the global rotation,  $R_m \approx 700$ , approximately one-third is going into the first Kelvin mode with azimuthal mode  $m = 1$ . In a narrow, but finite, window of the precession ratio (or

Poincaré number) close to 0.1, an axisymmetric Taylor-vortex-like flow structure occurs (Figure 3.2c) whose favourable dynamo capabilities have been numerically evidenced (Figure 3.2d) and optimized [94-97]. The commissioning of the machine, including the first water experiments, is presently ongoing, first liquid-sodium experiments are planned for late 2025 or 2026.

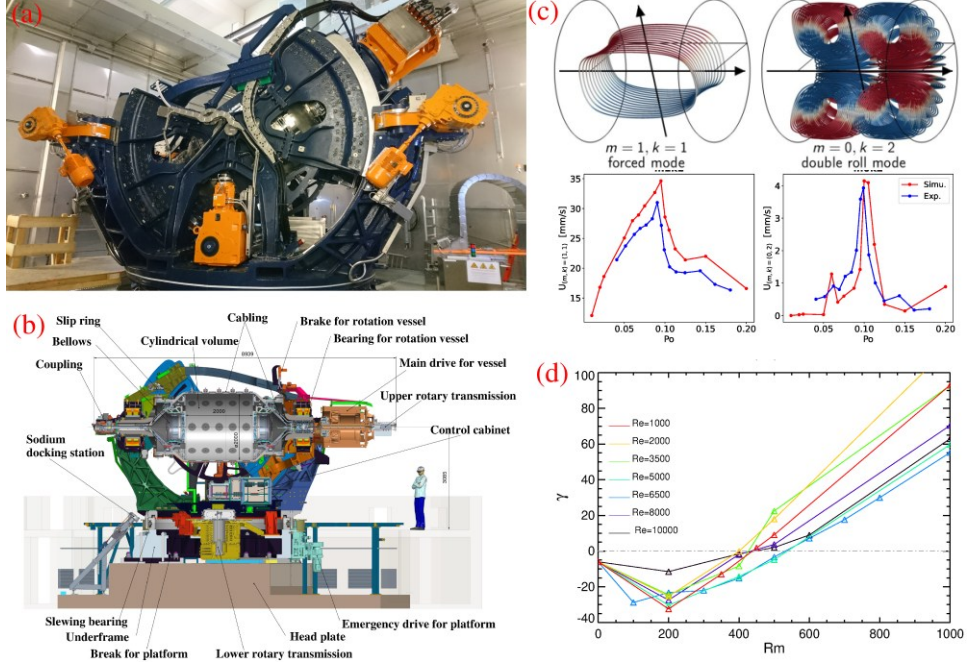


Figure 3.2: The DRESHDYN precession dynamo experiments: (a) Photograph of the full machine, taken on 17<sup>th</sup> October 2024. (b) Side-view drawing of the machine, with main parts indicated. (c) Illustration of the two main flow structures arising under precession that are most relevant for dynamo action: the directly forced mode with azimuthal wave number  $m=1$  and axial wave number  $k=1$ , and the double-torus like structure with  $m=0$  and  $k=2$ . The lower panel shows the measured and simulated amplitudes of both flow structures in dependence on the precession ratio (Poincaré number). (d) Growth rate of the magnetic eigenfield in dependence on the magnetic Reynolds number  $Rm$  (at the optimum Poincaré number), simulated for different Reynolds numbers. The critical value  $Rm=430$  is significantly below the technically achievable value of 700. (c, d) are adapted from [97].

## 4 Summary

In hindsight, one could get the impression that the sequence of liquid-metal dynamo experiments has followed a “hidden” logic dictated by the imperatives of geo- and astrophysical research. The Riga dynamo generates an oscillatory field, with a ratio of field period to (differential) rotation that is not dissimilar to that of the solar dynamo (although its eigenmode has an  $m=1$  azimuthal dependence, in contrast to the dominant  $m=0$  dipole of the Sun). The Karlsruhe- $\alpha^2$ -type dynamo, in turn, generated a steady magnetic field, just as the geodynamo does. As shown in Figure 2.2d, a minor geometry change would have allowed to excite an axial dipole, with the thrilling prospect to trigger reversals between up- and downward directed dipole fields (presumably mediated by an intervening equatorial dipole). However, the realization of such field reversals had to be left to the VKS experiment, which started to work as a dynamo when utilizing magnetic materials for the disks and blades. Meanwhile, the dynamo-synchronizing effect of tide-like forcings, which was originally investigated with view on the VKS experiment [98-99], is thought to play a decisive role in understanding the cycles of the solar dynamo, jointly with the precession-type forcing resulting from ellipticity changes of the solar orbit around the barycenter. Now it is left to the DRESDYN experiment to investigate the dynamo capabilities of those harmonic forcings. With this enterprise bringing the liquid-metal dynamo business to the edge of technical feasibility, it remains to be seen whether plasma experiments might once be able to take up the trail.

At any rate, the pioneering role of Robert Stieglitz and Agris Gailitis<sup>1</sup> in this decades-long scientific journey will always be remembered with admiration and gratitude.

---

<sup>1</sup> In the process of drafting this paper, we sadly learned about the passing away of Agris Gailitis on 6<sup>th</sup> October 2024, a few weeks after having given a lecture on “The Riga dynamo as an electrical machine” at the 13<sup>th</sup> pamir conference in Carry-le-Rouet.

## References

- [1] Busse, F.H. & Carrigan, C.R. (1976). Laboratory simulation of thermal convection in rotating planets and stars. *Science* 191, 81-83.
- [2] Krause, F. & Rädler, K.H. (1980). Mean-field magnetohydrodynamics and dynamo theory. Akademie-Verlag, Berlin.
- [3] Ponomarenko, Y. B. (1973). On the theory of hydromagnetic dynamos. *Zh. Prikl. Mekh. Tekh. Fiz. (USSR)* 6, 47–51.
- [4] Roberts, G. O. (1972). Dynamo action of fluid motions with two-dimensional periodicity. *Philos. Trans. R. Soc. Lond.* A271.
- [5] Busse, F. H. (1975). A model of the geodynamo. *Geophys. J. R. Astr. Soc.* 42, 437–459.
- [6] Stieglitz, R. & Müller, U. (2000). Edited Presentations of the International Workshop on Homogeneous Dynamos. Forschungszentrum Karlsruhe, March 20-22, 2000. IKET-Nr. 10/00.
- [7] Petrus Peregrinus de Maricourt (1995), *Opera*. Scuola normale superiore, Pisa.
- [8] Gilbert, W. (1958). *De Magnete*. Translated by P.F. Mottelay. Dover, New York.
- [9] Gellibrand, H. (1887). A discourse mathematical on the variation of the magneticall needle. Reprint edited by G. Hellmann, Berlin.
- [10] Brunhes, B. (1906). Recherches sur la direction de l'aimantation des roches volcaniques. *J. Phys.* 5, 705-724.
- [11] Hale, G.E. (1908). On the probable existence of a magnetic field in sun-spots. *Astrophys. J.* 28, 315-345.
- [12] Larmor, J. (1919). How could a rotating body such as the Sun become a magnet? *Rep. Brit. Assoc. Adv. Sci.*, 159–160.
- [13] [https://hu.wikipedia.org/wiki/Jedlik\\_Ányos](https://hu.wikipedia.org/wiki/Jedlik_Ányos)
- [14] Hjort, S. (1854). An improved magneto-electric battery. Patent GB 2198.
- [15] Siemens, C. W. (1867). On the conversion of dynamical into electrical force without the aid of permanent magnetism. *Proc. R. Soc. Lond.* 15, 367–369.
- [16] Wheatstone, C. (1867). On the augmentation of the power of a magnet by the reaction thereon of currents induced by the magnet itself. *Proc. R. Soc. Lond.* 15, 369–372.

- [17] Lowes, F. J. & Wilkinson, I. (1963). Geomagnetic dynamo - a laboratory model. *Nature* 198, 1158–1160.
- [18] Lowes, F. J. & Wilkinson, I. (1968). Geomagnetic dynamo - an improved laboratory model. *Nature* 219, 717–718.
- [19] Wilkinson, I. (1984). The contribution of laboratory dynamo experiments to our understanding of the mechanism of generation of planetary magnetic fields. *Geophys. Surv.* 7, 107–122.
- [20] Gailitis, A. & Freibergs, Y. A. (1976). Theory of a helical MHD dynamo. *Magnetohydrodynamics* 12, 127–129.
- [21] Gailitis, A. & Freibergs, Y. A. (1980). Nonuniform model of a helical dynamo. *Magnetohydrodynamics* 16, 116–121.
- [22] Gailitis, A. et al. (1987). Experiment with a liquid-metal model of an MHD dynamo. *Magnetohydrodynamics* 23, 349–353.
- [23] Gailitis, A. (1996). Design of a liquid sodium MHD dynamo experiment. *Magnetohydrodynamics* 32, 68–62.
- [24] Stefani, F., Gerbeth, G. & Gailitis, A. (1999). Velocity profile optimization for the Riga dynamo experiment. In *Transfer Phenomena in Magnetohydrodynamic and Electroconducting Flows* (eds Alemany, A. et al.) 31–44, Springer.
- [25] Gailitis, A. et al. (2000). Detection of a flow induced magnetic field eigenmode in the Riga dynamo facility. *Phys. Rev. Lett.* 84, 4365–4368.
- [26] Gailitis, A. et al. (2001). Magnetic field saturation in the Riga dynamo experiment. *Phys. Rev. Lett.* 86, 3024–3027 (2001).
- [27] Gailitis, A., Lielausis, O., Platadis, E., Gerbeth, G. & Stefani, F. (2002). Laboratory experiments on hydromagnetic dynamos. *Rev. Mod. Phys.* 74, 973–990.
- [28] Gailitis, A., Lielausis, O., Platadis, E., Gerbeth, G. & Stefani, F. (2003). The Riga dynamo experiment. *Surv. Geophys.* 24, 247–267.
- [29] Gailitis, A., Lielausis, O., Platadis, E., Gerbeth, G. & Stefani, F. (2004). Riga dynamo experiment and its theoretical background. *Phys. Plasmas* 11, 2838–2843.
- [30] Stefani, F., Gailitis, A. & Gerbeth, G. (2008). Magnetohydrodynamic experiments on cosmic magnetic fields. *Zeitschr. Angew. Math. Mech.* 88, 930–954.
- [31] Stefani, F., Giesecke, A. & Gerbeth, G. Numerical simulations of liquid metal experiments on cosmic magnetic fields. *Theor. Comp. Fluid Dyn.* 23, 405–429 (2009).



- [32] Gailitis, A. et al. (2018). Self-excitation in a helical liquid metal flow: the Riga dynamo experiments. *J. Plasma Phys.* 84, 73584030.
- [33] Gailitis, A. & Lipsbergs, G. (2017). 2016 year experiments at Riga dynamo facility. *Magnetohydrodynamics* 53, 349–356.
- [34] Lipsbergs, G. & Gailitis, A. (2022). 2022 year experiments at the Riga dynamo facility. *Magnetohydrodynamics* 58, 417–424.
- [35] Gailitis, A. (2024). Riga dynamo as an electrical machine. *Proceedings of the 13<sup>th</sup> pamir International Conference on Fundamental and Applied MHD*, September 16-19, 2024, Carry le Rouet, France, Paper 82.
- [36] Stefani, F., Gailitis, A. & Gerbeth, G. (2011). Energy oscillations and a possible route to chaos in a modified Riga dynamo. *Astron. Nachr.* 332, 4-10.
- [37] Gailitis, A. (1967). Self-excitation conditions for a laboratory model of a geomagnetic dynamo. *Magnetohydrodynamics* 3, 23–29.
- [38] Rädler, K.-H., Rheinhardt, M., Apstein, E. & Fuchs, H. (1998). The Karlsruhe dynamo experiment: A mean field approach. *Stud. Geophys. Geod.* 42, 224-231.
- [39] Müller, U. & Stieglitz, R. (2000). Can the Earth's magnetic field be simulated in the laboratory? *Naturwissenschaften* 87, 381-390.
- [40] Stieglitz, R. & Müller, U. (2001). Experimental demonstration of a homogeneous two-scale dynamo. *Phys. Fluids* 13, 561-564.
- [41] Müller, U. & Stieglitz, R. (2002). The Karlsruhe dynamo experiment. *Nonl. Proc. Geophys.* 9, 165–170.
- [42] Müller, U., Stieglitz, R. & Horanyi, S. (2004). A two-scale hydromagnetic dynamo experiment. *J. Fluid Mech.* 498, 31–71.
- [43] Müller, U., Stieglitz, R. & Horanyi, S. (2006). Experiments at a two-scale dynamo test facility. *J. Fluid Mech.* 552, 419–440.
- [44] Müller, U. & Stieglitz, R. The response of a two-scale kinematic dynamo to periodic flow forcing. *Phys. Fluids* 21, 034108 (2009).
- [45] Rädler, K.-H., Rheinhardt, M., Apstein, E. & Fuchs, H. (2002). On the mean-field theory of the Karlsruhe dynamo experiment. *Nonlin. Proc. Geophys.* 9, 171–187.
- [46] Tilgner, A. (1997). Predictions on the behaviour of the Karlsruhe dynamo. *Acta Astron. Geophys. Univ. Comen.* 19, 51–62.
- [47] Tilgner, A. (2002). Numerical simulation of the onset of dynamo action in an experimental two-scale dynamo. *Phys. Fluids* 14, 4092–4094.

- [48] Christensen, U. R. & Tilgner, A. (2004). Power requirement of the geodynamo from ohmic losses in numerical and laboratory dynamos. *Nature* 429, 169–171.
- [49] Avalos-Zuñiga, R., Xu, M., Stefani, F., Gerbeth, G. & Plunian, F. (2007). Cylindrical anisotropic  $\alpha^2$  dynamos. *Geophys. Astrophys. Fluid Dyn.* 101, 389–404.
- [50] Dudley, M. L. & James, R. W. (1989). Time-dependent kinematic dynamos with stationary flows. *Proc. R. Soc. A* 425, 407–429.
- [51] Xu, M., Stefani, F. & Gerbeth, G. (2008). The integral equation approach to kinematic dynamo theory and its application to dynamo experiments in cylindrical geometry. *J. Comp. Phys.* 227, 8130–8144.
- [52] Monchaux, R. et al. (2007). Generation of a magnetic field by dynamo action in a turbulent flow of liquid sodium. *Phys. Rev. Lett.* 98, 044502.
- [53] Berhanu, M. et al. (2007). Magnetic field reversals in an experimental turbulent dynamo. *Europhys. Lett.* 77, 59001.
- [54] Ravelet, F. et al. (2008). Chaotic dynamos generated by a turbulent flow of liquid sodium. *Phys. Rev. Lett.* 101, 074502.
- [55] Monchaux, R. et al. (2009). The von Kármán sodium experiment: turbulent dynamical dynamos. *Phys. Fluids* 21, 035108 (2009).
- [56] Gallet, B. et al. (2012). Experimental observation of spatially localized dynamo magnetic fields. *Phys. Rev. Lett.* 108, 144501.
- [57] Miralles, S. et al. (2014). Dynamo efficiency controlled by hydrodynamic bistability. *Phys. Rev. E* 89, 063023.
- [58] Pétrélis, F., Fauve, S., Dormy, E. & Valet, J.-P. (2009). Simple mechanism for reversals of Earth’s magnetic field. *Phys. Rev. Lett.* 102, 144503.
- [59] Stefani, F., Gerbeth, G., Günther, U. & Xu, M. (2006). Why dynamos are prone to reversals. *Earth Planet. Sci. Lett.* 243, 828–840.
- [60] Ravelet, F., Chiffaudel, A., Daviaud, F. & Léorat, J. (2005). Toward an experimental von Kármán dynamo: numerical studies for an optimized design. *Phys. Fluids* 17, 117104.
- [61] Stefani, F. et al. (2005). Ambivalent effects of added layers on steady kinematic dynamos in cylindrical geometry: application to the VKS experiment. *Eur. J. Mech. B/Fluids* 25, 894–908 (2006).
- [62] Verhille, G. et al. (2010). Induction in a von Kármán flow driven by ferromagnetic impellers. *New J. Phys.* 12, 033006.

- [63] Giesecke, A., Stefani, F. & Gerbeth, G. (2012). Influence of high-permeability discs in an axisymmetric model of the Cadarache dynamo experiment. *New J. Phys.* 14, 053005.
- [64] Nore, C., Léorat, J., Guermond, J.-L. & Giesecke, A. (2015). Mean-field model of the von Kármán sodium dynamo experiment using soft iron impellers. *Phys. Rev. E* 91, 013008.
- [65] Kreuzahler, S., Ponty, Y., Plihon, N., Homann, H. & Grauer, R. (2017). Dynamo enhancement and mode selection triggered by high magnetic permeability. *Phys. Rev. Lett.* 119, 234501.
- [66] Spence, E.J. et al. (2006). Observation of a turbulence-induced large scale magnetic field. *Phys. Rev. Lett.* 96, 055002.
- [67] Nornberg, M. D. et al. (2006). Intermittent magnetic field excitation by a turbulent flow of liquid sodium. *Phys. Rev. Lett.* 97, 044503.
- [68] Nornberg, M.D., Spence, E.J., Kendrick, R.D., Jacobson, C.M. & Forest, C.B. (2006). Measurements of the magnetic field induced by a turbulent flow of liquid metal. *Phys. Plasmas* 13, 055901.
- [69] Spence, E.J. et al. (2007). Turbulent diamagnetism in flowing liquid sodium. *Phys. Rev. Lett.* 98, 164503.
- [70] Rahbarnia, K. et al. (2012). Direct observation of the turbulent emf and transport of magnetic field in a liquid sodium experiment. *Astrophys. J.* 759, 80.
- [71] Forest, C.B. (2015). The Wisconsin plasma astrophysics laboratory. *J. Plasma Phys.* 81, 345810501.
- [72] Zimmerman, D.S., Triana, S.A. & Lathrop, D.P. (2011). Bi-stability in turbulent, rotating spherical Couette flow. *Phys. Fluids* 23, 065104.
- [73] Rieutord, M., Triana, S. A., Zimmerman, D. S. & Lathrop, D. P. (2012). Excitation of inertial modes in an experimental spherical Couette flow. *Phys. Rev. E* 86, 026304.
- [74] Triana, S.A., Zimmerman, D.S. & Lathrop, D.P. (2012). Precessional states in a laboratory model of the Earth's core. *J. Geophys. Res.* 117, B04103.
- [75] Adams, M.M., Stone, D.R., Zimmerman, D.S. & Lathrop, D.P. (2015). Liquid sodium models of the Earth's core. *Prog. Earth Planet. Sci.* 2, 29.
- [76] Rojas, R. E., Perevalov, A., Zürner, T. & Lathrop, D.P. (2021). Experimental study of rough spherical Couette flows: increasing helicity toward a dynamo state. *Phys. Rev. Fluids* 6, 033801.

- [77] Frick, P. et al. (2002). Non-stationary screw flow in a toroidal channel: way to a laboratory dynamo experiment. *Magnetohydrodynamics* 38, 143–161.
- [78] Frick, P. et al. (2010) Direct measurement of effective magnetic diffusivity in turbulent flow of liquid sodium. *Phys. Rev. Lett.* 105, 184502.
- [79] Fischer, M. et al. (2009). Inferring basic parameters of the geodynamo from sequences of polarity reversals. *Inverse Probl.* 25, 065011.
- [80] Colgate, S.A. et al. (2002). The New Mexico  $\alpha - \omega$  dynamo experiment: modelling astrophysical dynamos. *Magnetohydrodynamics* 38, 129–142.
- [81] Colgate, S.A. et al. (2011). High magnetic shear gain in a liquid sodium stable Couette flow experiment: a prelude to an  $\alpha - \Omega$  dynamo. *Phys. Rev. Lett.* 106, 175003.
- [82] Alboussière, T., Plunian, F. & Moulin, M. (2022). Fury: an experimental dynamo with anisotropic electrical conductivity. *Proc. R. Soc. A* 478, 20220374.
- [83] Avalos-Zuñiga, R. & Priede, J. (2022). Realization of Bullard’s disk dynamo. *Proc. R. Soc. A* 479, 20220740.
- [84] Plunian, F. & Alboussière, T. (2020). Axisymmetric dynamo action is possible with anisotropic conductivity, *Phys. Rev. Res.* 2, 013321.
- [85] Jüstel, P. et al. (2022). Synchronizing the helicity of Rayleigh-Bénard convection by a tide-like electromagnetic forcing. *Phys. Fluids* 34, 104115.
- [86] Stefani, F. et al. (2024). Rieger, Schwabe, Suess-de Vries: the sunny beats of resonance. *Solar Phys.* 299, 51.
- [87] Gans, R. F. (1970). On hydromagnetic precession in a cylinder. *J. Fluid Mech.* 45, 111–130.
- [88] Léorat, J. et al. (2003). Dissipation in a flow driven by precession and application to the design of a MHD wind tunnel. *Magnetohydrodynamics* 39, 321–326.
- [89] Léorat, J. (2006). Large scales features of a flow driven by precession. *Magnetohydrodynamics* 42, 143–151.
- [90] Mouhali, W. et al. (2012). Evidence for a cyclonic regime in a precessing cylindrical container. *Exp. Fluids* 53, 1693–1700.
- [91] Tilgner, A. (2005). Precession driven dynamos. *Phys. Fluids* 17, 034104.
- [92] Stefani, F. et al. (2012). DRES-DYN — a new facility for MHD experiments with liquid sodium. *Magnetohydrodynamics* 48, 103–114.

- [93] Stefani, F. et al. (2019). The DRES-DYN project: liquid metal experiments on dynamo action and magnetorotational instability. *Geophys. Astrophys. Fluid Dyn.* 113, 51–70.
- [94] Giesecke, A. et al. (2018). Nonlinear large scale flow in a precessing cylinder and its ability to drive dynamo action. *Phys. Rev. Lett.* 120, 024502.
- [95] Giesecke, A. et al. (2019). Kinematic dynamo action of a precession-driven flow based on the results of water experiments and hydrodynamic simulations. *Geophys. Astrophys. Fluid Dyn.* 113, 235–255.
- [96] Pizzi, F. et al. (2021). Prograde and retrograde precession of a fluid-filled cylinder. *New J. Phys.* 23, 123016.
- [97] Kumar, V. et al. (2023). The effect of nutation angle on the flow inside a precessing cylinder and its dynamo action. *Phys. Fluids* 35, 014114.
- [98] Giesecke, A., Stefani, F. & Burguete, J. (2012). Impact of time-dependent nonaxisymmetric velocity perturbations on dynamo action of von Kármán-like flows. *Phys. Rev. E* 86, 066303.
- [99] Giesecke, A., Stefani, F. & Herault, J. (2017). Parametric instability in periodically perturbed dynamos. *Phys. Rev. Fluids* 2, 053701.



# Robert Stieglitz' traces in the history of Karlsruhe Liquid Metal Laboratory (KALLA)

Markus Daubner<sup>1</sup>, Joachim Knebel<sup>1</sup> and Thomas Wetzel<sup>1</sup>

<sup>1</sup> Karlsruhe Institute of Technology, Karlsruhe, Germany

## Abstract

Robert Stieglitz has left many and deep scientific traces in an impressive range of disciplines. The lasting impact of his work is the result of a unique strategic quality based on his ability to fully comprehend even the most complex mechanisms with greatest scientific clarity. A fine example for this is the way he shaped the interface between basic research and the technical implementation of heavy liquid metal cooled technological systems during his time at the Karlsruhe liquid metal laboratory KALLA from 2002 to 2009. He formulated methodological lines and initiated technical implementations that are still visible in the laboratory and his work today. The following article will tell about these lines, their precursors and what has emerged from them to date. However, none of this would have had the same impact, had it not been for Robert's equally distinctive ability to bring together people and lead them to extraordinary achievements. His inspiring personality, always pointing at opportunities, possibilities and great perspectives, being demanding, yet always characterized by great humanity, shaped KALLA just as much as his scientific legacy. We miss him.

## 1 Prologue

On the following pages, we would like to tell the part of the history of the Karlsruhe Liquid Metal Laboratory (KALLA) that Robert Stieglitz particularly shaped. As far as possible, we will organize the information chronologically along the construction of experimental facilities and the setup and execution of experiments.

The history of the KALLA began a few years before Robert joined, namely at the end of the 1990s, after the old facilities of the Laboratory for Aerosol and Filter Technology (LAF) in Building 415 had been dismantled, freeing up a large pilot plant hall in the

immediate vicinity of the main building of the Institute of Nuclear and Energy Technology (IKET), now the Institute of Thermal Energy Technology and Safety (ITES).

For some time, a place had been sought for the urgent task of contributing to the solution of one of the most important problems of nuclear energy, namely the long-lasting toxicity of radioactive waste. The concepts presented by Carlo Rubbia (Energy Amplifier) [1] and Charles D. Bowman (ADS) [2] in the early 1990s showed that in a new type of reactor, the Accelerator Driven System, ADS, the half-lives of minor actinides, for example, can be dramatically reduced by transmutation, resulting in a significant reduction in the long-term hazard potential while at the same time increasing the energy yield. However, this requires a reactor vessel filled with liquid lead or eutectic lead-bismuth mixture (LBE), which simultaneously serves as a target for protons and as a cooling medium. Due to the scarce information on the handling, corrosion control and thermal-hydraulic behavior of these liquid metals, it was absolutely necessary to build suitable experimental facilities, which was finally made possible by the Helmholtz Associations Strategy Fund Project 99/16 "Thermohydraulic and material-specific investigations for the realization of an accelerator-driven system (ADS)" [3].

When the team led by the then group leader at KALLA, Joachim Knebel, had the large, empty technical center hall at their disposal in 1999, work began on building the supporting structure and the platforms (steel construction), the control rooms, the power supplies and the first three loops, which were to be filled with LBE. More background information on the concept at the time can be found in [4].

In order to be able to clarify some important technological questions first, the construction of a technology loop, later called THESYS, was started. For larger thermo-hydraulic experiments, construction of what is still the largest circuit at KALLA, THEADES, began shortly afterwards. At about the same time, work also began on a circuit for long-term corrosion studies, CORRIDA.



Figure 1: Part of THEADES loop at KALLA's test hall



At the end of 2002, Robert Stieglitz took over as group leader at KALLA and contributed his many years of experience with liquid metals, including from setting up the Geo-Dynamo experiment (see the article by Stefani et al. in this volume). Under his leadership, KALLA, which had originally only been set up for ADS experiments with LBE, also began to tackle new tasks with other liquid metals. In particular, sodium, with its excellent heat transport properties, and gallistan, an eutectic alloy of gallium, indium and tin, which is already liquid at room temperature and therefore particularly suitable as an experimental fluid in many cases, should be mentioned here.

In addition to his keen interest in the technological aspects, Robert's approach was characterized above all by focussing on the specific thermophysical properties of liquid metals, in particular the pronounced differences in scale between thermal and fluid dynamic boundary layers with all their consequences for the thermofluid dynamic behavior, for its modeling and for the engineering design of liquid metal-based heat transfer systems for ADS and other applications. On this basis, he formulated a whole canon of experiments that has shaped our work and the international state of knowledge about the thermofluid dynamics of liquid metals for ADS far beyond his time at KALLA and continues to be influential today.

A second formative and lasting foundation of Robert's work at KALLA was the combination of thermal fluid dynamics with materials science topics and bringing together the relevant researchers from different, wide-ranging disciplines. This was already planned before Robert joined KALLA. However, it was brought to life in a unique way by his inspiring personality, which showed opportunities, possibilities and great perspectives, challenging for all involved, yet always complemented by his deep humanity. The resulting close and reliable cooperation between various working groups, in particular around Georg Müller and Alfons Weisenburger from the Institute for High Power Pulse and Microwave Technology (IHM) and Jürgen Konys and Carsten Schroer from the Institute for Applied Materials Science (IAM) with the KALLA team at ITES is still a unique feature in the international research landscape for liquid metal technology. We will come back later to talk about particular technical successes that would not have been possible without this collaboration.

## 2 Development

### Oxygen Control System and KOCOS

Even before the first loop was put into operation, the first experiments were carried out in the new laboratory in 1999. These were preliminary tests to solve the corrosion problem. It was known from research work by V. Markov [5] that the expected corrosion of the stainless steel pipe walls would depend heavily on the oxygen concentration ( $O_2$ ) in the liquid mixture of 45 % lead and 55 % bismuth (Lead Bismuth Eutectic, LBE).

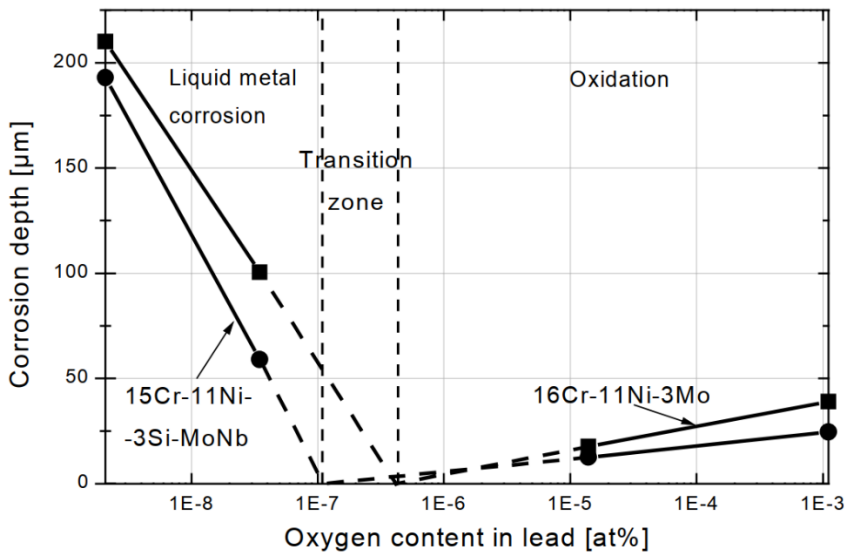


Figure 2.1: Corrosion behavior of two steels in liquid lead as a function of oxygen concentration after 3000h at 550 °C [5].

Figure 2.1 shows that the lower the  $O_2$  content, the greater the liquid metal corrosion in steels. If the  $O_2$  concentration is too high, on the other hand, an oxide layer slowly builds up on the pipe wall. It would therefore be ideal to keep the  $O_2$  concentration in the transition zone at all times. An oxygen control system (OCS) was therefore proposed [6], which was initially tested in KALLA in an experimental set-up called KOCOS (Kinetics of Oxygen Control System) [7] with stagnant LBE.

The principle of the system is based on the fact that a free, hot LBE surface is flooded with a gas mixture so that oxygen exchange can take place on the surface. In the actual

application, argon is used as the carrier gas, to which an argon-hydrogen mixture (5 %  $H_2$ ) is added in order to extract  $O_2$  from the LBE. To increase the  $O_2$  content in the LBE, an argon stream enriched with water vapor is added to the carrier gas instead.

Following promising tests in KOCOS, an OCS was provided for each of the first three LBE loops. An OCS is particularly important on the KALLA-CORRIDA loop, where materials can be tested for their long-term corrosion behavior against 550 °C hot LBE since its commissioning. Otherwise it would not be possible to compare different samples.

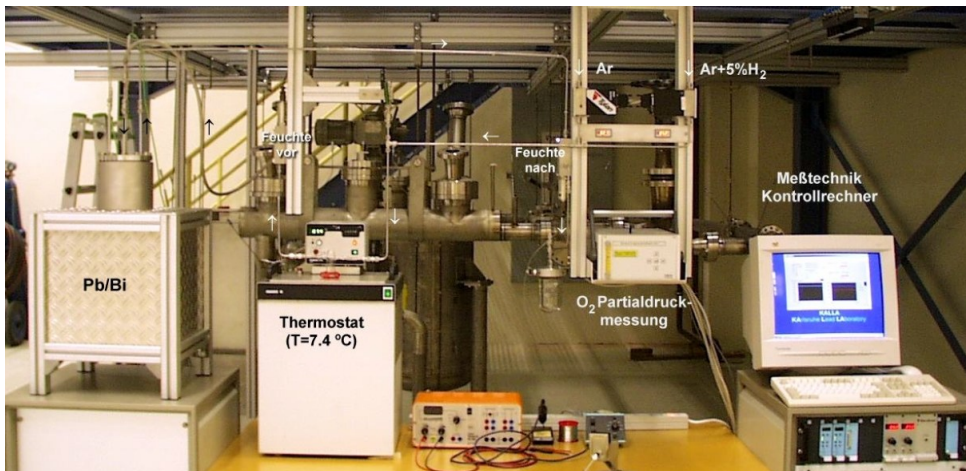


Figure 2.2: Photograph of KOKOS, 1999: Pb/Bi = LBE, Feuchte = Humidity, Partialdruckmessung = partial pressure measurement, Messtechnik-Kontrollrechner = instrumentation control PC

## Heat transfer on a single rod in the THESYS loop

The first loop completed at KALLA was the THESYS (Technologies for HEavy Liquid Metal SYStems), in its first version as a small, horizontal loop. As the name suggests, it was intended to test the practicality of technologies for the operation of LBE loops. In addition to oxygen control, various types of flow meters were installed and tested and verified by calorimetry. Some of them proved to be unsuitable, such as an impeller flow meter, whose needle bearing corroded after a short time, so that the impeller could no longer rotate correctly.

From the very beginning, KALLA aimed to carry out experiments on fuel rod simulators (high-performance electric heating rods) in order to investigate the heat transfer on

bundles, but also on individual rods. To this end, a miniature permanent magnet potential probe (MPP) was used to simultaneously measure the temperature and velocity profile in the inflow and in several planes along the heating element. Even the first heating rods, developed in-house at the institute, were designed to be movable with the help of a bellows system. However, unlike its use in sodium circuits, the MPP probe did not deliver a signal, which is due to the less favorable electromagnetic properties of the LBE. At the suggestion of Robert Stieglitz, a pitot probe was designed specifically for this purpose at the beginning of 2003 and the first differential pressure gauge with a diaphragm seal system was successfully used on the horizontal THESYS. However, in order to achieve greater heating, cooling capacities and volume flows, as well as to achieve a better conditioned, vertical flow of the rod, the first, horizontally arranged THESYS loop was dismantled and a new, vertically designed loop was completed in 2005 (see Fig. 2.3).

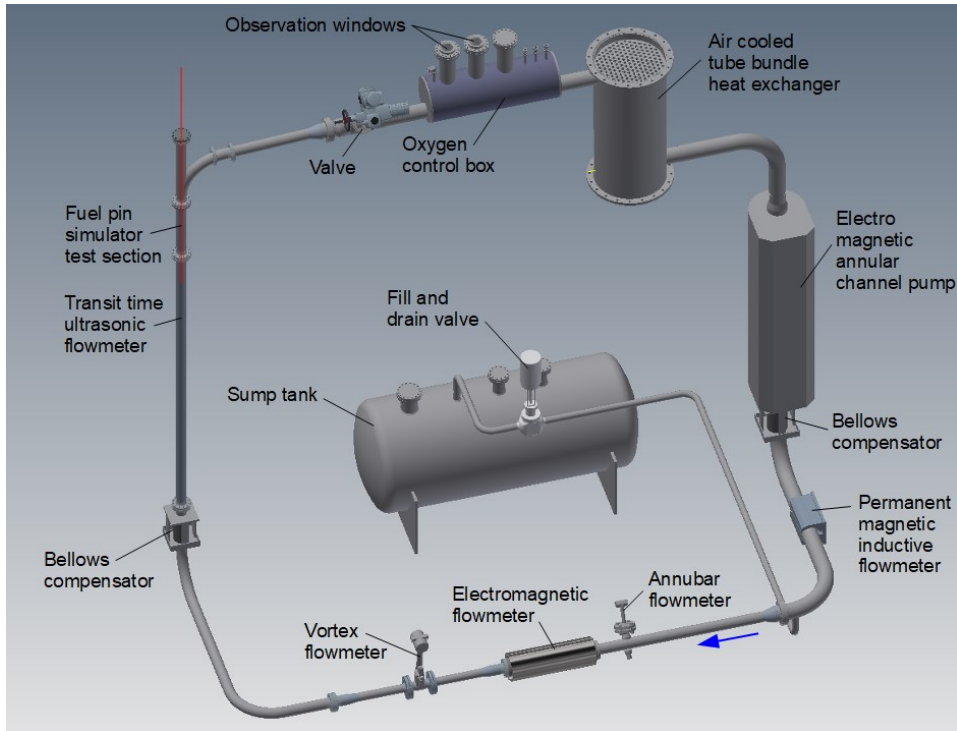


Figure 2.3: 3D view of the second THESYS loop with vertical test section

The more powerful, electromagnetic ring channel pump, a large shell-and-tube heat exchanger and high-performance heated rod from Thermocoax (THX) now allowed a much wider range of experiments. By optimising the pump frequency to 20 Hz, the ring channel pump was able to generate LBE volume flows of up to 16 m<sup>3</sup>/h and the THX rod delivered a total output of 22.4 kW over a length of 870 mm with a maximum heat flux of 1 MW/m<sup>2</sup>. The experimental investigations of the heat transfer along the single heated rod were carried out as part of J. Zeininger's doctoral thesis [8], completed in 2009, under the supervision of Robert Stieglitz. The flow and heating power, as well as the measuring levels on the heated rod, were varied by moving the rod. Due to the large movable length, no bellows could be used. Instead, a special lid design with O-ring, LBE scraper and gas barrier system was used. With a movable pitot probe, in which two thermocouples were integrated, temperatures and velocities, as well as their fluctuations, were recorded simultaneously with high frequency along a radial axis perpendicular to the rod's length axis. Two years later, a further, more intensive evaluation by L. Marocco et al. [9] provided further insights into and confirmed the high quality of the measurement data.

## **MEGAPIE Heated-Jet-Experiment in the THEADES loop**

As mentioned earlier, the facilities of KALLA were initially built for the investigation of components for an accelerator-driven, subcritical transmutation arrangement according to the concept of C. Rubbia [1]. This provides for three main components: a proton accelerator, a target fluid in which the protons generate fast neutrons in a spallation reaction (external neutron source) and a subcritical blanket in which fission reactions generate neutrons (internal neutron source) and release heat. In this process, the protons are introduced into the target fluid through an evacuated beam tube via a thin wall area, the so-called beam window. The target fluid is liquid lead or a eutectic lead-bismuth mixture (LBE) and is also used to cool the beam window and the blanket. An interruption of the proton beam leads to an interruption of the fission in the blanket, which results in advantages in terms of safety behaviour.

The MEGAPIE initiative [10] was launched in 1999 by Bauer (PSI), Salvatores (CEA) and Heusener (FZK) to demonstrate the functionality of such a spallation target system. In a joint effort by CEA, CRNS and SUBATECH France, ENEA Italy, FZK Germany, JAERI Japan, PSI Switzerland and SCK-CEN Belgium, the Megawatt Pilot Experiment (MEGAPIE) was planned, designed, built and operated with the proton accelerator SINQ at the Paul Scherrer Institute (PSI) in Switzerland as the first of its kind. Basic experiments on the cooling capability of the beam window were carried out at KALLA and are briefly de-

scribed below. More detailed summaries of the activities and lessons learned were written by Brian Smith 2006 [11] and Concetta Fazio 2008 [12], for example.

To ensure sufficient cooling of the MEGAPIE target, which is subject to high thermal loads, the flow had to be conditioned appropriately. The main flow was pumped downwards in an annular gap and deflected by 180 ° into a riser pipe at a deflector located near the hemispherical target. To prevent unacceptably high temperatures from occurring at the lowest point of the beam window, a jet flow was directed laterally to this region (calotte) through a rectangular nozzle. This flow geometry was reproduced on a 1:1 scale in the KALLA laboratory (see Fig. 2.4) and equipped with a large number of thermocouples. To demonstrate the cooling capability of the spherical calotte, the first step was to investigate the effect of the flow ratio in the main and jet channels without external beam window heating. In the heated jet experiment [13], the jet flow was heated before it was injected into the cold main flow via the bypass tube. The liquid metal experiment was accompanied by a water experiment in almost the same geometry to investigate the momentum field and a three-dimensional turbulent numerical flow simulation (CFD) [14].

In addition to a detailed investigation of the intended nominal operation of the MEGAPIE target with  $Q_{\text{main}}/Q_{\text{jet}} = 15$ , deviations from this were also investigated. It was shown that only very specific flow ratios are suitable for reliable cooling of the MEGAPIE design, as the jet is only able to capture most of the hemispherical lower part of the target in a few constellations.

The KALLA-MEGAPIE test module was embedded in the THEADS loop. This extends over an area of 15 x 8 meters and three floors in the KALLA hall. The mechanical centrifugal pump can generate up to 47m<sup>3</sup>/h volume flow and a maximum pressure of 6 bar. The liquid metal stream is first fed into the basement, from where it can be fed to the experiments via three ports. While the KALLA-MEGAPIE test module was still installed in the central of these ports and experiments still running, the KALLA team under guidance of Robert Stieglitz already started planning and eventually constructing the first experiments on cooling rod bundles at THEADES (see corresponding subchapter in this article). These experiments made it necessary to integrate a 500 kW heat exchanger in the THEADES loop. Likewise, an extension of the loop in height to accommodate an experiment with a free-falling-jet target was planned (see also the corresponding subchapter). Over the years, several changes and extensions of THEADES took place, while its basic concept proved to be a stable and versatile foundation. Figure 2.5 shows THEADES in 2024.

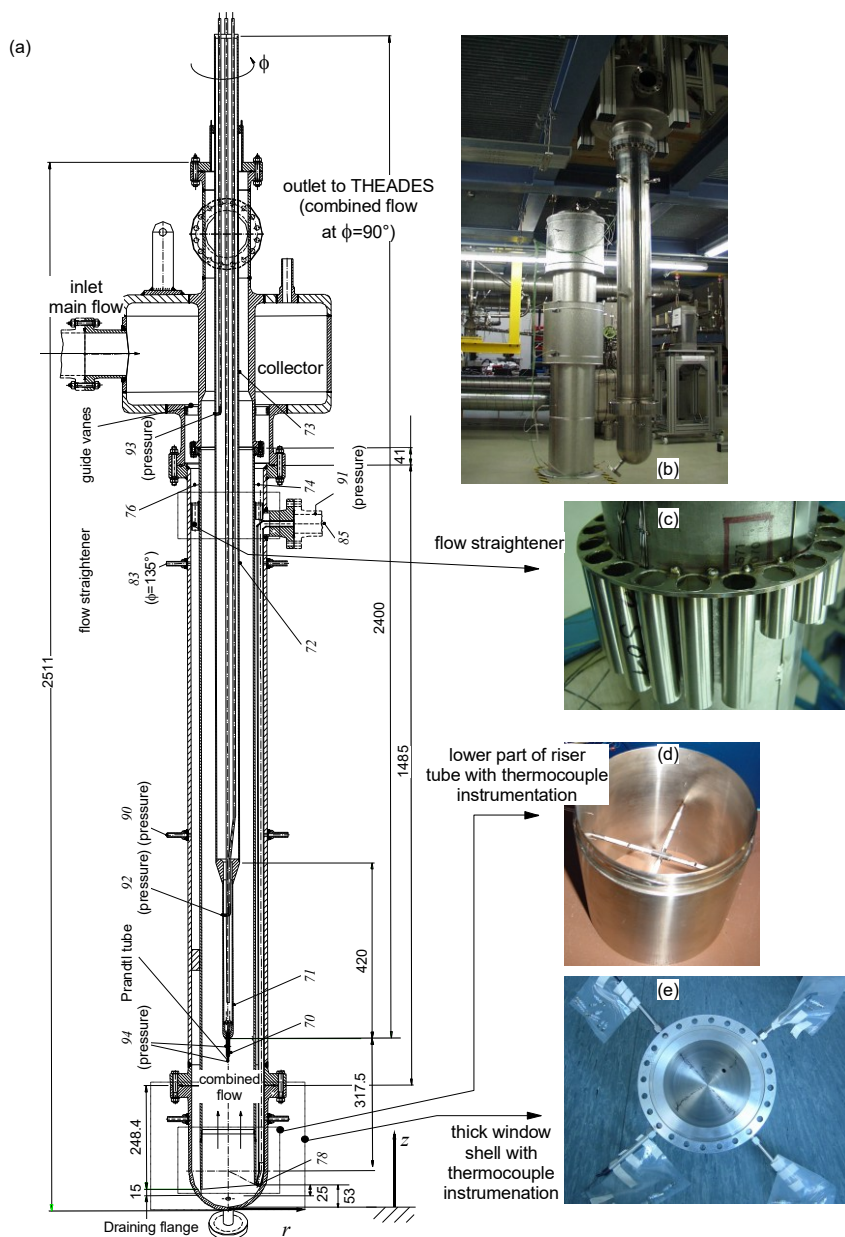


Figure 2.4: (a) Geometrical set-up of the heated jet experiment module and introduction of the coordinate system. The dimensions are in mm and the italic numbers indicate measurement positions. (b) Photograph of the module. (c) Flow straightener. (d) Lower part of the riser tube. (e) Instrumented lower shell.

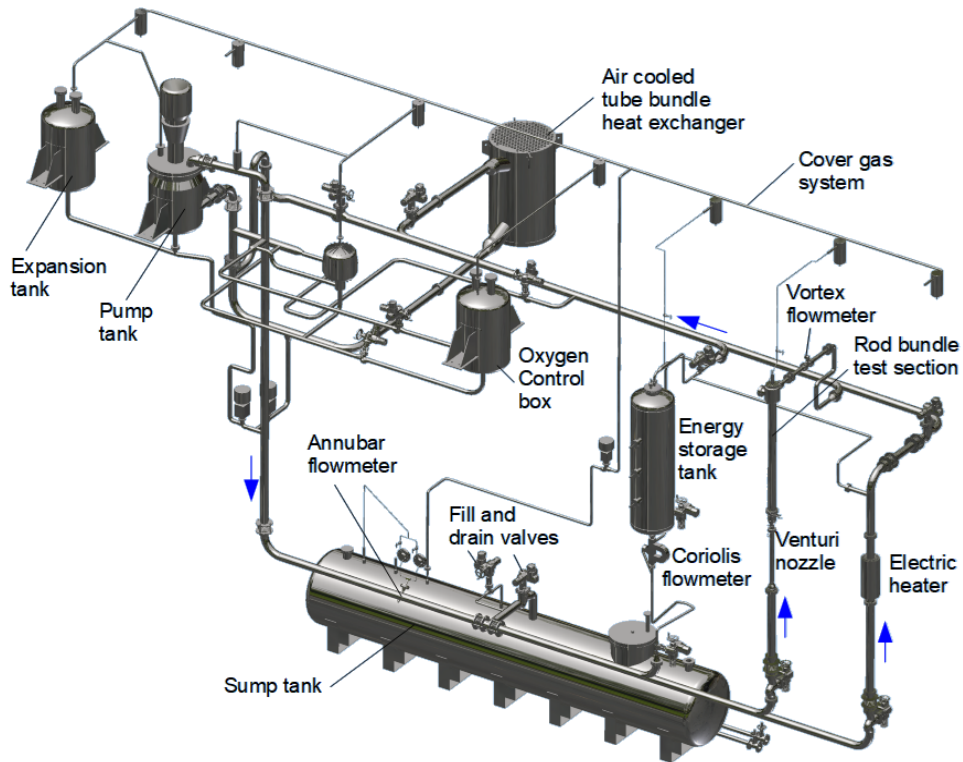


Figure 2.5: 3D view on THEADES in 2024

## KILOPIE HETSS-Experiment

In order to prove the coolability of the hemispherical beam window, it was also planned from the outset to investigate the heat transfer via an external beam window heating. For this purpose, a removable spherical base was already provided during the design of the KALLA-MEGAPIE test module, which has now been replaced by a new test unit. Since an output of 1 kW was intended for these experiments, the mockup at KALLA, like its counterpart at PSI, was named KILOPIE (Kilowatt Pilot Experiment), in reference to the MEGAPIE target. In the LBE test cycle of the Paul Scherrer Institute, the basic functionality of the setup and the measurement technology was demonstrated with small power and throughput, and the large series of tests with full flow rate etc. took place at KALLA.

The KILOPIE mockup had the same internal geometry as the lower part before, yet it was now possible to attach a heated beam window in the form of a 0.5 mm thin dome with a pressure flange to its bottom (see Fig. 2.6). The aim here was to determine the



heat transfer coefficient under real heat flux conditions ( $140 \text{ W/cm}^2$ ) and to investigate the positive effect of mixed convection (forced and buoyancy driven) on cooling [15]. With the help of the Low Pressure Plasma Spraying – Thin Film (LPPS-TF) technology of the Sulzer Metco Company, the idea of a high-heat flux sensor dish could finally be realized.

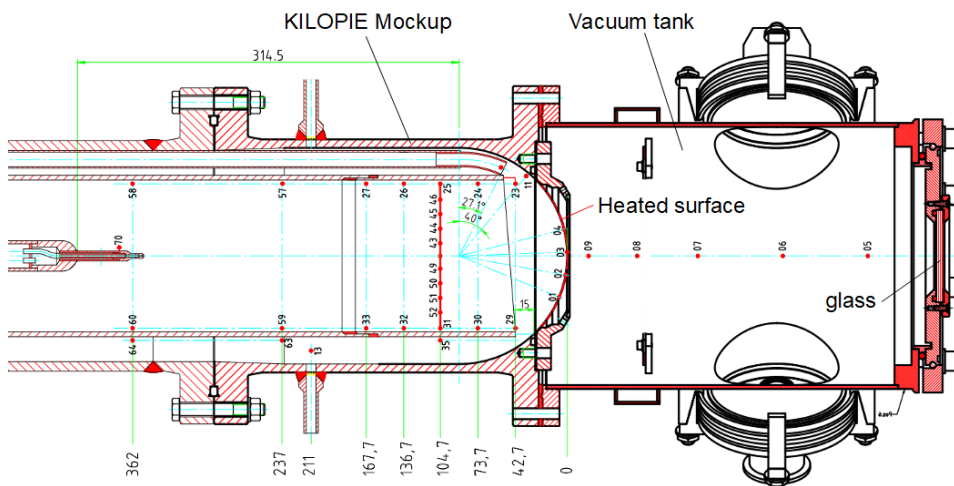


Figure 2.6: KILOPIE mockup with heated dome

A thin ceramic insulating layer was sprayed onto the spherical surface and thin meandering nickel tracks were located on top of it, which conducted the electric current and released the heat. For reasons of measurement accuracy and safety, a vacuum container was attached underneath, which allowed the infrared camera optical access via a glass window on the lower flange. In the event that a crack had occurred in the thin calotte, the vacuum container would have prevented liquid metal from spilling out directly. At the same time, sensors installed in the container would have detected the leakage and an emergency drain would have been initiated by the control system. For safety reasons, the infrared camera was attached to the side of the shaft below and only had a view of the heated calotte via a mirror. In conjunction with an emergency release, this mirror would have been folded down and the shaft closed. Any LBE remaining or flowing into the module would then have been fed into a collection container via this shaft if the glass broke. However, the spherical caps always remained intact during all campaigns. This provided prove that the beam window could be cooled and the MEGA-PIE target could be put into operation at PSI.

## MYRRHA Free Surface Target-Experiment

The most consistent development path towards an accelerator-driven system for the transmutation of long-lived nuclear fission products has been pursued since the early 2000s at the Belgian Nuclear Research Centre SCK-CEN in Mol. The goal of this work is to realize MYRRHA (Multi-purpose hYbrid Research Reactor for High-tech Applications) as a pilot project of an ADS at the Mol site, with strategic importance for and corresponding support from the entire European Union.

The primary coolant and simultaneously the target fluid for the spallation neutron source of MYRRHA will be LBE (lead-bismuth eutectic). Consequently, since 2002, KALLA has been consistently participating in the MYRRHA-related European research programs. One of the options for the spallation target system in MYRRHA was a design that dispensed with the previously mentioned beam window in the form of a calotte and instead allowed the proton beam to enter the target fluid directly via a hollow jet of liquid metal, as shown in Figure 2.7.

A near full-scale prototype with a nozzle diameter of 88 mm was developed and investigated within the EURATOM-THINS (Thermal Hydraulics in Innovative Nuclear Systems) project, which had been secured by Robert Stieglitz before his promotion from heading KALLA to leading the Institute for Neutron Physics and Reactor Technology. The nozzle produces a ring-like liquid metal curtain that converges into a liquid metal jet due to surface tension effects, forming both an inner and an outer free surface. The inner surface is exposed to the proton beam, while the curtain ensures the separation between the beamline and the reactor pool.

Particular attention must be paid to accurately detecting the surface shape, as the high-intensity proton beam, with a power of 2.4 MW, must not impact at the recirculation zone of the jet. While the outer free surface is easily detectable, the inner free surface is not directly accessible for optical investigation. Constraints from the target design mean that the inner free surface must be characterized through the proton beam tube.

A solution was found by using a digital camera to detect the inner free surface and reconstructing its shape based on depth-of-field information from the images. Comparisons with numerical pre-calculations showed very good agreement between experimental and numerical data. The experimental campaign was completed in 2014, and detailed results were published, e.g. in [16] and [17]. Figure 2.7 shows some photographs of the outer and inner free surfaces flow during the experiments, the latter being the foundations for the sophisticated postprocessing and evaluations described in [17].

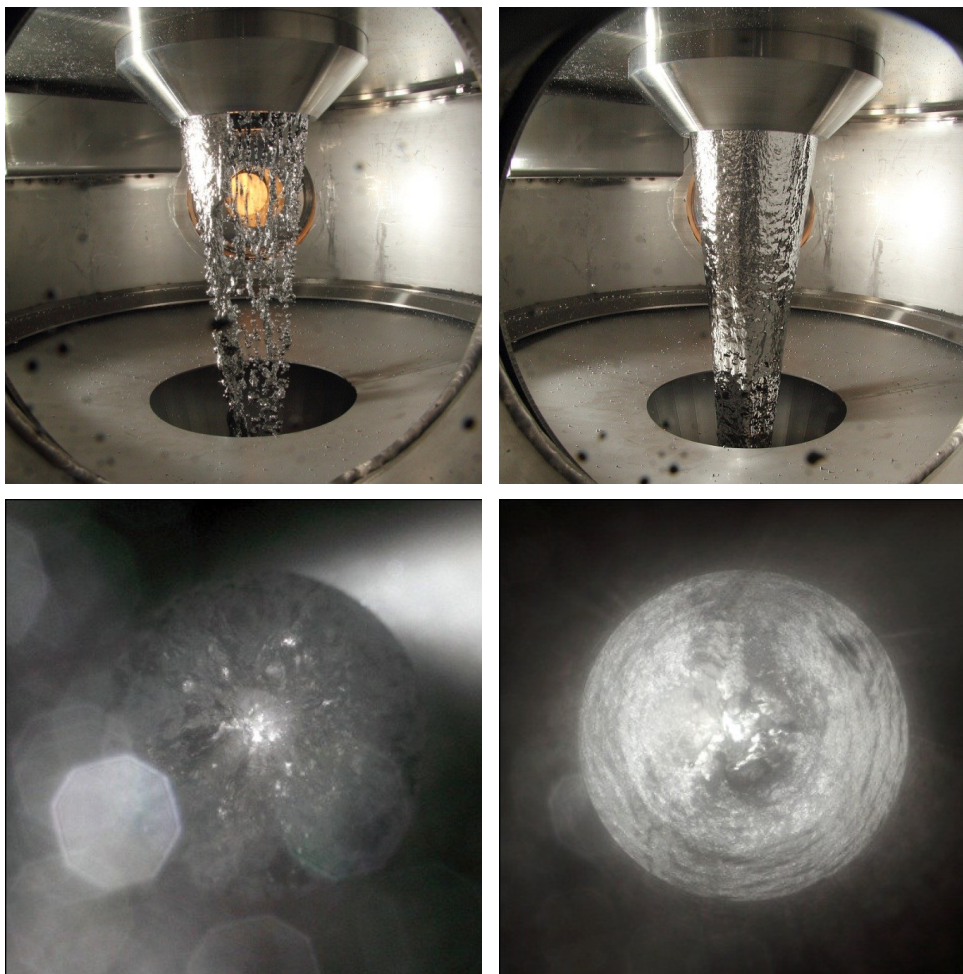


Figure 2.7: Free surface target experiment. Top left droplet flow at very low flow rate. Top right: stable outer surface at 4.6 l/s. Bottom left: inner surface at 4.6 l/s. Bottom right: inner surface with a stable horizontal section of about 1/3 of the total diameter in the center at 7 l/s.

## Steam Generator Tube Rupture (SGTR)-Experiment

A key safety concern in heavy liquid metal-cooled reactors like ADS is the interaction between the primary coolant (liquid metal) and secondary coolant (water/steam) during a steam generator tube rupture (SGTR). This occurs if a tube in the internal heat ex-

changer (IHX) ruptures, allowing high-pressure steam to flow into the liquid lead-bismuth eutectic (LBE) pool. This could lead to uncontrolled reactor core behavior, damage from pressure waves, or even a hazardous steam explosion.

The thermal fluid dynamics during an SGTR event are complex and their understanding is of utmost relevance for the safe design of an ADS. However, according experimental data is scarce due to the exceptional conditions to be realized. Consequently, at KALLA, under the guidance of Robert Stieglitz and in cooperation with the EU Joint Research Center, Institute of Energy in Petten, NL, a dedicated SGTR experimental facility was conceptualized in 2008 and built in 2010. The setup included three vessels: Reactor, Reservoir, and Relief tanks, connected by pipes and housed within a 21.5 m<sup>3</sup> safety bunker vessel designed to withstand 40 bar. The reactor tank featured a lead pool, a mock-up heat exchanger module with hexagonal rod bundles, and a pump (see Figure 2.8). The pump tank inner diameter was 300 mm, lead mass flow rate reached up to 72 kg/s, lead temperatures up to 400 °C and steam pressure up to 240 bar.

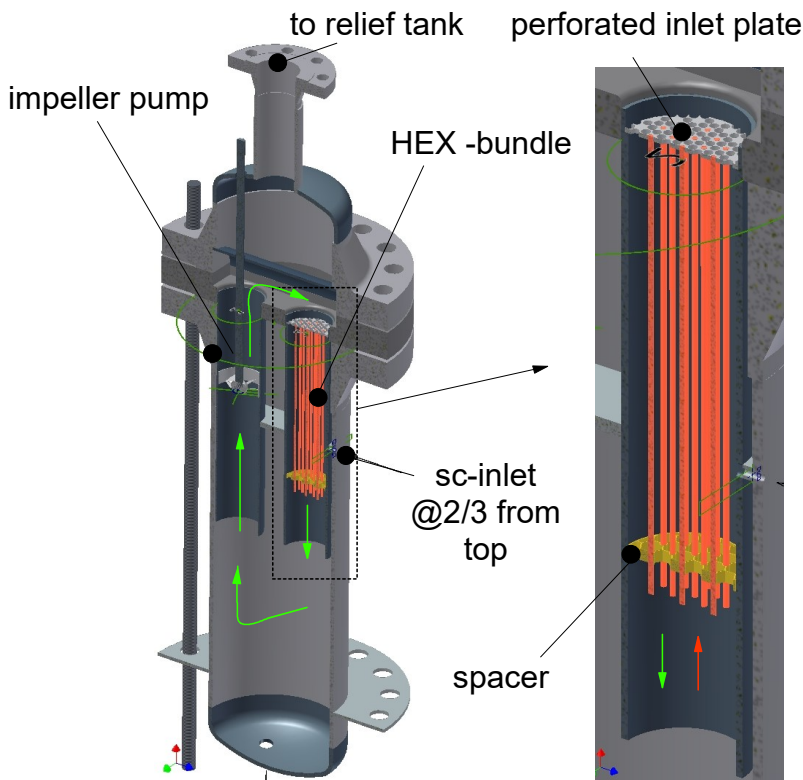


Figure 2.8: SGTR Experiment, pump and IHX vessel and IHX enlarged

Instrumentation included pitot tubes for velocity, thermocouples for temperature and bubble detection, and pressure sensors. To prevent lead freezing, 16 heating circuits (totaling over 34 kW) maintained temperatures, while unheated components were air-cooled. Pre-tests using nitrogen and water helped refine the setup before experiments with superheated steam and liquid lead.

The selection of relevant parameter ranges had been carefully done by Robert according to pre-test-simulations using the SIMMER code, performed by Michael Flad from the IKET Severe Accidents Group headed by Werner Maschek. The safety bunker vessel was and still is part of the ITES hydrogen safety test center at KIT, headed by Thomas Jordan and the setup therein was supported by the highly skilled team around Gerold Stern. All this is a fine example of Robert's ability to connect people and capabilities to achieve unique results even with limited budgets. Figure 2.9 shows the complete experimental setup inside the bunker vessel.

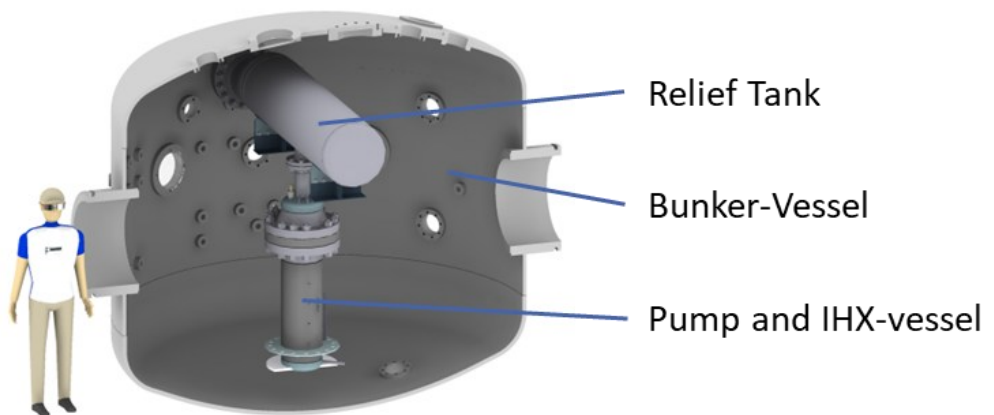


Figure 2.9: SGTR experiment, complete mockup inside the bunker vessel

The SGTR experiments investigated various configurations, flow directions, and injected steam volumes. Despite huge challenges faced during then experiments in view of reliable data collection, the comprehensive findings substantially contributed to further SGTR research and guidelines for Lead-cooled Fast Reactors (LFRs).

## **NUSTAR – Sodium Free Jet Experiment in the ALINA Cycle**

The aforementioned work on the beam window of the MEGAPIE target and the free-surface experiments on MYRRHA drew the attention of the Gesellschaft für Schwerionenforschung (GSI) in Darmstadt to KALLA in its plans for a target for the new Facility for Antiproton and Ion Research (FAIR) [18]. In the FAIR accelerator facility, particle beams of all kinds, from protons to uranium, are to be generated with unprecedented intensity, i.e. very high energy densities. By firing these beams at so-called targets, secondary beams are also created, with particles that do not occur naturally on Earth. A liquid metal free jet was seen as a promising target concept for this purpose, which is why Robert Stieglitz was asked by GSI to carry out a design study with an alkali metal free jet experiment as part of the NUSTAR collaboration (NUclear STructure, Astrophysics and Reactions). To generate the free jet under vacuum, the ALINA facility (Karlsruhe Lithium and Sodium Free Jet Experiments) had to be built and a test section with a contraction nozzle had to be developed to generate the free jet.

In order to be able to make accurate predictions regarding the shape of the free jet generated in the velocity range of interest for the nuclear target, an additional water free jet test section was built, which made it possible to carry out a combined experimental and numerical study of the turbulent flow in the contraction nozzle [19]. This allowed different nozzle shapes to be exchanged very easily and velocity measurements to be carried out using laser Doppler anemometry (LDA). Using a two-component LDA system with special optics, which allowed very small measurement volumes to be measured within the viscous boundary layer, velocity distributions in the direction of flow and transverse to it were precisely measured.

The aim was to achieve a free jet as stable as possible for the beam impact area with as little constriction and as rectangular a contour as possible. In the configuration for FAIR (GSI) sketched in Figure 2.10 (left), it can already be seen that the rectangular shape of the nozzle outlet cannot be maintained under any circumstances due to the surface tension of the medium. In order to ensure a stationary jet shape downstream, a uniform and stable velocity distribution should be achieved in the cross-section of the nozzle outlet and secondary flows, which naturally occur with rectangular geometries, should be minimized.

The nozzle design optimized and tested with the help of the water tests was then implemented in the construction of the contraction nozzle in the sodium test section in the ALINA loop, as can be seen in Figure 2.10 (right). In order to reduce the turbulence caused by the deflection and transition from round to rectangular cross-section, a

perforated basket with baffle plate was provided for flow conditioning in the flange area and a flow straightener downstream in the rectangular channel. Due to the high velocity of the free jet of around 4 m/s, the impact of the free jet in the tank sump would have caused a heavy splashing of sodium. To prevent this as far as possible, a coiled collecting pipe was installed in the test section, which ensures that the jet is gently deflected. The rectangular outer container has two round sight glasses and two rectangular measuring windows, which were additionally protected from any splashing sodium by bellows slides with stainless steel plates. These measurement windows simultaneously served as projection planes for measuring the silver reflecting surface contour of the free jet using the so-called "Double Layer Projection (DLP)" measurement method [20]. In this method, laser beams of different colors are beamed from different positions through a pane onto the free beam surface and reflected there. Due to the thickness of the disk, four laser points are visible on its inner and outer surface for each laser beam, two at the entrance and two at the exit. Precise knowledge of the geometric conditions, optical detection with a high-speed camera and a specially developed evaluation method can then be used to determine the 3D contour of the reflective object being examined.

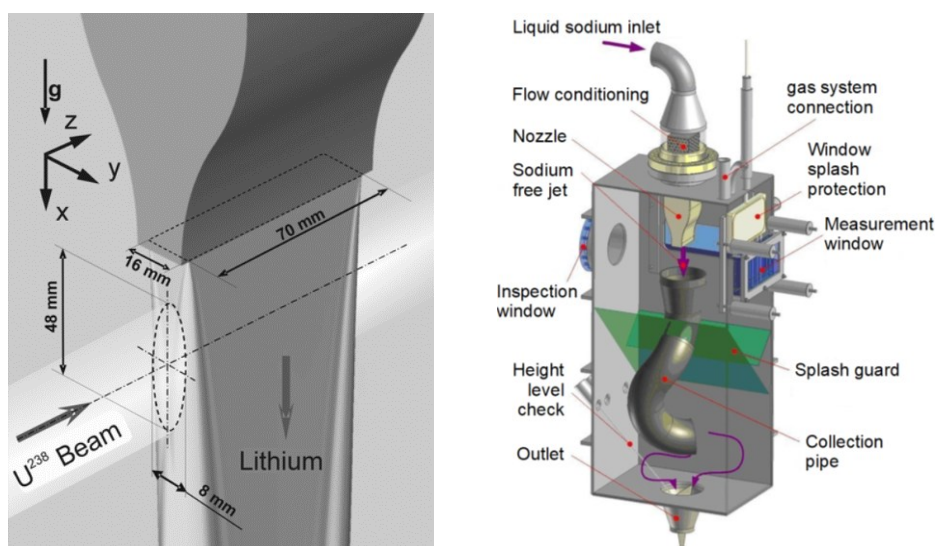


Figure 2.10: Liquid lithium free jet, nozzle and uranium-beam configuration (left) and view of the free jet test section (right)

This test section was embedded in the ALINA liquid metal loop, as described in [21]. Figure 2.11 shows the 3D arrangement of the components. The parts of the main sodium loop are colored red in the figure, the oil cooling loop green and finally the parts belonging to the gas system blue. The main loop shows the typical structure for liquid



metal systems with a sump tank for emergency drainage in the event of leakage and a secondary loop typical for liquid alkali metals with a cold trap for cleaning the liquid of oxides, both shown in orange. During operation, the linear flat channel induction pump can generate a flow rate of up to  $12 \text{ m}^3/\text{h}$  at a pressure of around 1 bar. As the experiments were to be carried out under the same conditions as later at GSI, a vacuum was generated in the test section. A heater enabled rapid heating to various temperature levels and testing of the prototype compact heat exchanger. For safety reasons, a special diphyll oil was used as a secondary medium instead of water to cool the sodium. This in turn was cooled outside the laboratory in another tube bundle heat exchanger with ambient air.

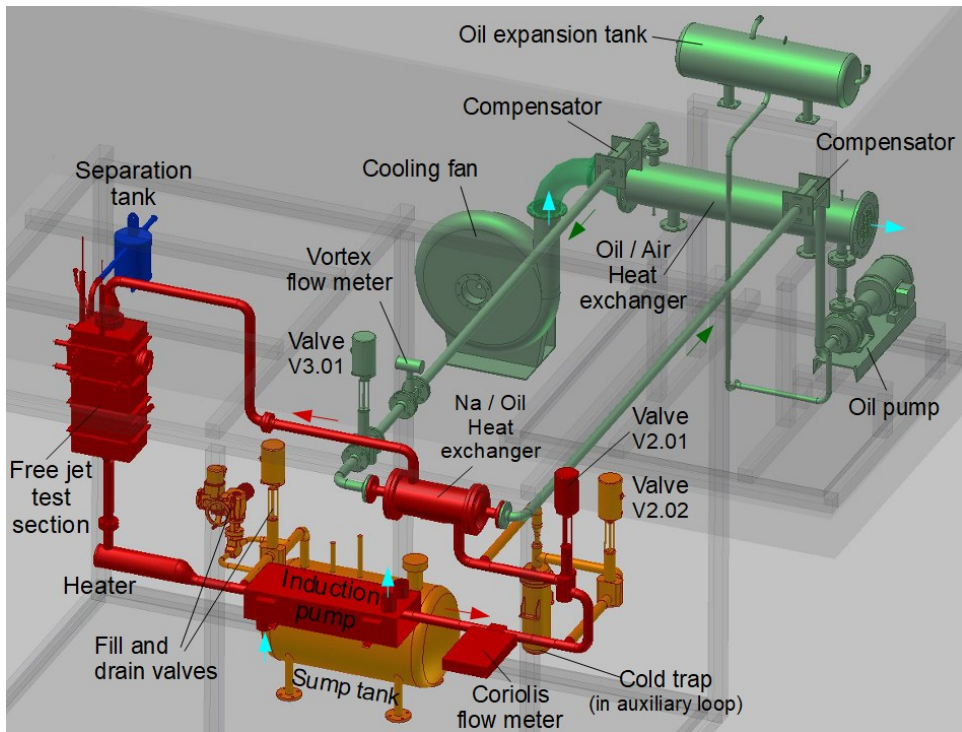


Figure 2.11: ALINA 3D total view

## LBE Heat Transfer in Hexagonal Rod Bundles

As mentioned above at the beginning of the section on the free surface target experiment in the framework of research and development for the MYRRHA ADS pilot project at SCK-CEN, Mol, Belgium, KALLA consistently did and still does contribute to EURATOM



research projects over almost two decades now. As a core part of that research Robert Stieglitz envisioned the investigation of LBE heat transfer at the surface of heated, vertically oriented rods, with the single rod experiment in the THESYS loop as the starting point and followed by consecutive experiments in hexagonal 19-rod-bundles in the THEADES loop at KALLA. Such hexagonal rod bundles are the preferred geometry for the fuel pin arrangement in ADS and MYRRHA in particular. As mentioned, the low Prandtl number of liquid metals, although reflecting their favorable heat transfer capabilities, prevents the application of classical thermal hydraulic models for turbulent heat transfer in core-representative geometries. Furthermore, experimental information for according flows in prototypical dimensions was very limited at the time, when the according research activities started at KALLA.

Robert was well aware of thermal hydraulic scaling laws, yet was also aware of the special requirements on design rules for nuclear systems and – most importantly – was an undaunted engineer, not afraid of undertaking a large scale experiment. Consequently, he envisaged a combination of scientifically derived research questions, a systematic approach with increasing complexity from experiment to experiment and maximum relevance by realizing prototypical dimensions for the MYRRHA core. That concept has grown into a consistent row of consecutive experiments, that has advanced the knowledge in the field substantially and is still being continued at KALLA.

At the time of Robert's departure from KALLA in 2009, a first experimental campaign in the frame of the European project EUROTRANS DEMETRA had been conceptualized, with a 19-pin-bundle with grid spacers (see Figure 2.12). This first campaign had been preceded by comprehensive isothermal hydraulic tests in a Reynolds-scaled bundle with water as transparent test fluid, allowing for laser-based local velocity measurements and an LBE test at THEADES with three of the 19 rods heated.

In the following years, in the frame of the EURATOM project THINS, a bundle with 19 electrically heated rods, producing ADS-prototypical surface heat flux in also fully prototypical geometry (heated length, p/d-ratio, spacer distance and geometry etc.) has been realized, marking a first-of-its-kind experiment, that received widespread acknowledgement in the scientific community. Just one example of the fidelity of this experiment: Detailed temperature profiles were obtained by means of thermocouples (24 positioned at the rod walls, 14 within the fluid) with 0.25 mm diameter, guided within the 0,5 mm thick "walls" of the spacers, to prevent any disturbance of the flow (see Fig. 2.12). Test parameters included typical ADS conditions in terms of operating temperature (200 °C - 450 °C), power density (up to 1.0 MW m<sup>-2</sup>) and velocity (up to 2 m s<sup>-1</sup>) of the LBE. The comprehensive results of this experiment have been published in Nuclear Engineering and Design in 2014 [22].

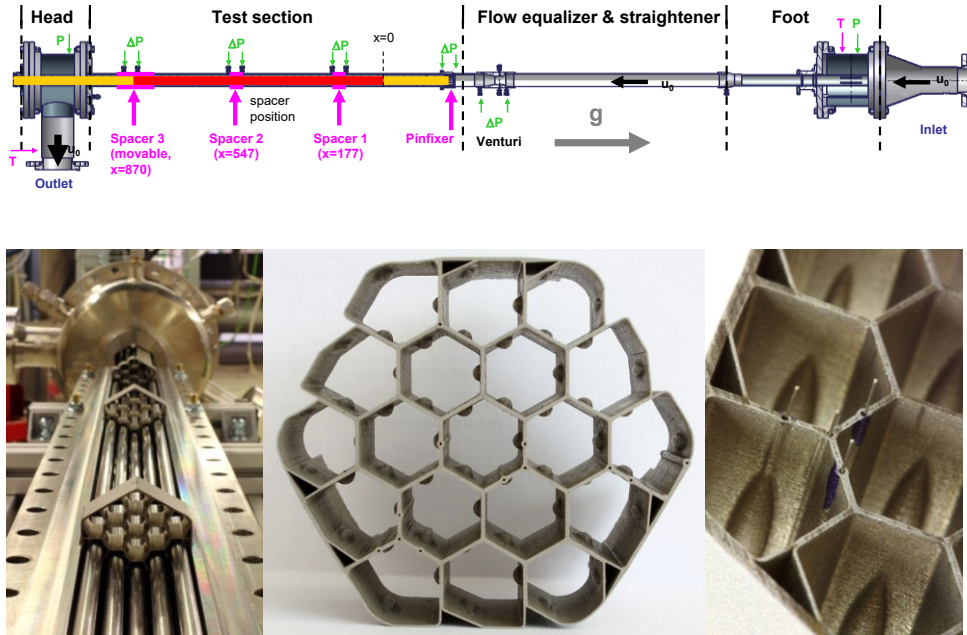


Figure 2.12: Sketch and several views of the test section in the rod-bundle experiment, details of the grid spacers with 0,25 mm diameter thermocouples

Within the subsequent FP7 EURATOM project SEARCH, a fully heated 19-rod bundle with wire spacers instead of the grid spacers was tested in the THEADES loop. Again, the measured quantities showed a high degree of reliability and reproducibility, and valuable lessons for the design and safety analysis of HLM-cooled systems could be derived from the results. The wire spacers, representing a preferred design alternative to the grid spacers, produce a swirl flow that leads to colder regions in the edges and hotter spots in the center of the bundle.

Figure 2.13 shows the heavy TC-instrumentation (that has become possible without disturbing the flow by minimizing TC-dimensions based on the experience gained with the previous experiments and “hiding” them in the spandrels between rods and wires) and some exemplary results in terms of Nu-numbers, as compared to existing correlations. The complete set of results has been published in Nuclear Engineering and Design in 2016 [23].

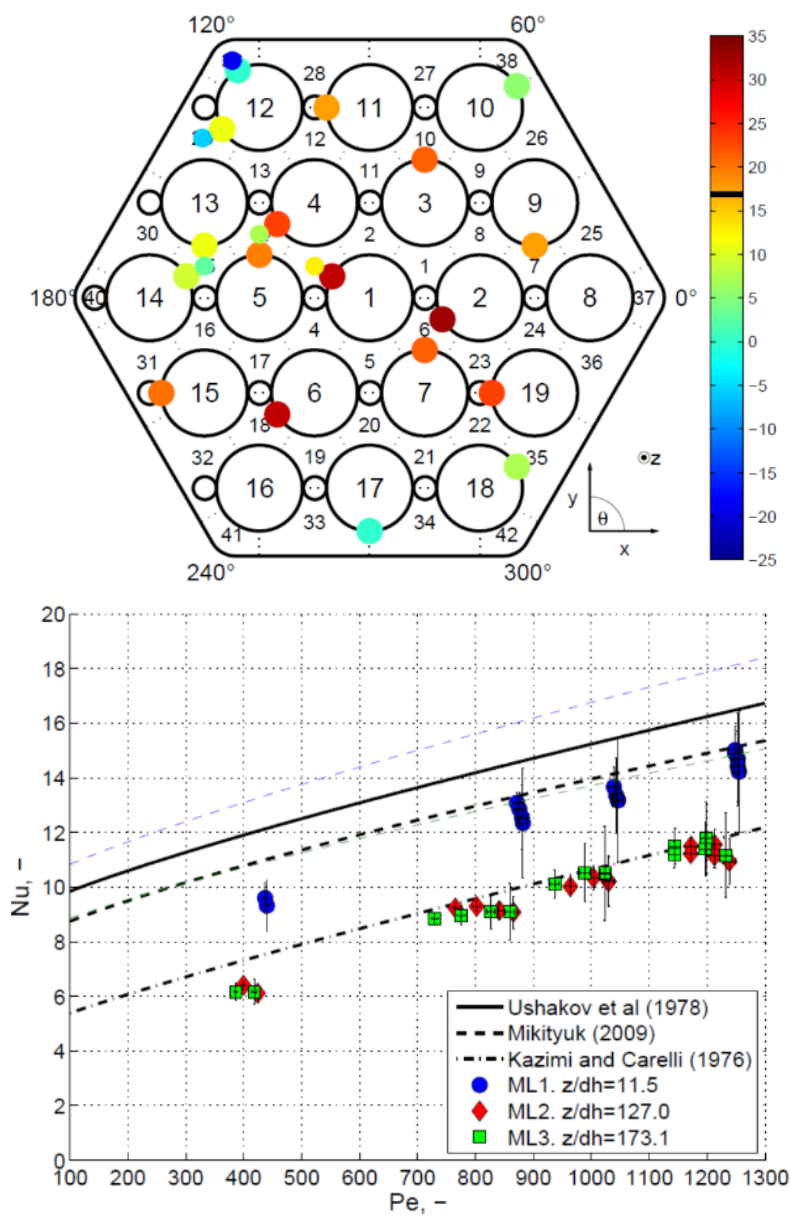


Figure 2.13: Experimental results on the heated 19-rod bundle with wire spacers. Top: temperature profiles (above bulk value) for the reference case. Bottom: measured and predicted Nusselt numbers [23, reproduced with permission].

One major safety concern in LBE cooled rod bundles with wire spacers are local blockages. Their effect of local overheating of rods may not be detectable by temperature measurements outside the ADS-core due to the high thermal diffusivity of the LBE. Hence, to investigate the effect of such local blockages, the test section from the SEARCH project has been modified for further studies within the EURATOM project MAXSIMA. Small blockage elements covering one sub-channel each have been placed at selected locations (one in the center and one in the edge). Additional thermo-couples were installed for detecting the local influence of the flow blockages. The SEARCH data as mentioned above served as reliable reference data, which provides an obvious and illustrative example for the unique conceptual quality of this subsequent series of experiments, far beyond the direct involvement of Robert Stieglitz. The results of this first set of blockage experiments has been published again in Nuclear Engineering and Design in 2018 [24].

Another series of experiments with relevance for ADS, this time looking at the influence of the so-called inter-wrapper-flow, occurring between the outer shells of fuel bundles in the reactor core of an ADS, has been conceptualized, designed and performed at KALLA within the EURATOM project SESAME. The inter-wrapper flow is important for fuel assemblies during decay heat removal operation and has been installed in the THESYS loop. For this campaign, the facility was upgraded with four parallel flow channels and three independent heating sub-systems, yet still based on the loop design realized during Robert's time at KALLA. Results of this experimental campaign from 2019 can be found in [25].

Prior to designing the blockages itself, experiments in the water facilities, built during Robert's time at KALLA for the above mentioned EUROTRANS DEMETRA experiments, had been performed within the EURATOM project MYRTE. They delivered valuable insights in the deposition processes of particles within the flow, leading to the local blockages and defining their shape and other characteristics. One such characteristic is a certain porosity, that might influence the local cooling of the rods next to the blockage. Another important effect is a potential deformation of single rods within the bundle due to e.g. fuel swelling, changing the flow distribution and with it the local cooling capability of the LBE. Experiments looking at these aspects are currently being prepared at KALLA in the frame of the EURATOM project PATRICIA and will be realized in THESYS and THEADES.

Parallel to these projects with a combination of well-defined specific application aspects and fundamental components, we also continue to perform pure fundamental research experiments. One example is the consistent work on heat transfer in plain tubes, cooled inside by liquid metals and exposed to complex heating conditions from outside. In a

recent project funded by the German Research Foundation (DFG), the influence of azimuthally inhomogeneous thermal boundary conditions on the heat transfer in a turbulent liquid metal tube flow has been investigated. Right now, in another DFG-funded project, the influence of mixed (forced and buoyancy driven) convection, that is particularly relevant in liquid metal flows with heat transfer, is in focus. The complex test section and the complete experimental setup of the first project phase is explained more in detail and results including a new Nu-correlation are being presented in [26]. A remarkable detail here is, that the liquid metal loop GALINKA, that hosts the test section in these experiments, has its origin in works of Robert Stieglitz during his time at KALLA. It has been the first loop using Gallium as working fluid and remains – through several transformations – a reliable workhorse in fundamental research at KALLA.

### 3 Epilogue

Since around 2012/2013, innovative applications of liquid metal technology have more and more been developed at KALLA, alongside the scientific foundations necessary for their implementation. The common point of these development lines is – in addition to advancing liquid metal technology and its scientific foundations, of course – our aim to contribute to sustainable energy solutions and industrial innovation against the backdrop of climate change and the resulting necessary transition to a CO<sub>2</sub>-free energy system. The following provides a brief overview of these development lines, along with references to further literature available on all our work.

#### **Methane Cracking for CO<sub>2</sub>-Free Hydrogen Production**

Thermochemical methane cracking aims to produce hydrogen and solid carbon without CO<sub>2</sub> emissions. At KALLA, we put strong research effort in utilizing liquid metal bubble column reactors that provide high-temperature capability and chemical stability for continuous operation. During the early development phase from 2012 to 2015, the HELiS (Hydrogen production Experiment in Liquid tin(Sn)) facility was established, featuring a vertical quartz glass reactor with liquid tin as the heat transfer medium. This work had been initiated by Nobel Prize laureate Prof. Carlo Rubbia and Prof. Klaus Töpfer as founding directors of the Potsdam based Institute for Advanced Sustainability Studies (IASS). Figure 3.1 shows Prof. Rubbia at KIT liquid metal material labs in 2013.

Initial experiments demonstrated high hydrogen yields at temperatures up to 1175 °C, with carbon collecting as a loose powder on the liquid metal surface, avoiding reactor

clogging. Between 2016 and 2018, simulations and thermo-chemical models were developed to optimize bubble dynamics and gas residence times and improving reaction conditions. In 2018 we received the Innovation Award of the German Gas Industry for our work on liquid metal based methane cracking.

From 2019 onwards, the technology was scaled for industrial applications in industrial collaborations, and with studies exploring reaction conditions for biogas and natural gas. We also considered options for the use of solar thermal energy for process heating, beginning in 2021. In 2023 and 2024 we were able to publish extensive experimental results on studies focused on cracking of gas mixtures and varying operating conditions, extending the process' applicability to natural gas and renewable feedstocks [27], [28], [29], [30]. The method continues to achieve high methane conversion rates and efficient carbon separation, demonstrating its potential for industrial implementation and thus enjoys strong attention within the scientific community.



Figure 3.1: Nobel Physics Prize laureate Prof. Carlo Rubbia (right) at KIT's liquid metal material lab in 2013 and first Carbon powder produced in the HELiS plant, featuring a liquid metal bubble column.

## NECOC Project: Negative Emissions through Carbon Synthesis

The NECOC project successfully developed a process chain for capturing CO<sub>2</sub> from the atmosphere and converting it into solid carbon. This innovative approach combines direct air capture (DAC), methanation, and liquid metal based methane pyrolysis. CO<sub>2</sub> is extracted from ambient air, converted into methane, and then decomposed into hydro-

gen and solid carbon in the KALLA liquid metal bubble column reactor technology. Demonstration campaigns proved the technical feasibility of this process, with the produced carbon showing promise for use in energy storage and construction materials. The project received widespread recognition, culminating in the 2023 Gips-Schüle Prize for its groundbreaking contributions to sustainable carbon management. NECOC highlights the potential for liquid metal technology to address global challenges by enabling carbon-negative industrial processes. At present the technology is advanced towards application for hard-to-abate industrial emissions, e.g. in cast iron production, cement production and waste incineration. Recent publications from 2024 on the topic can be found in ChemSusChem [31,32].

## **Liquid Metal-Based Concentrated Solar Power (CSP)**

Research at KALLA on exploring the use of liquid metals, such as lead-bismuth eutectic (LBE), as innovative heat transfer fluids for CSP plants can directly be traced back to Robert's influence and support of that technology.

A first experimental substantiation of this research was enabled by KITs participation in the LIMTECH Alliance, co-initiated by Robert and funded with more than 12 Mio. € by the HELMHOLTZ-Association of German National Research Centers from 2013 through 2017, see the according contribution on this alliance in the present publication. The SOMMER project, which stands for SOLar furnace arrangement with Molten-METal-cooled Receiver, made significant progress during this period and beyond. A 10-kW test system was developed, featuring a spiral-wound thermal receiver cooled by LBE. This design allowed for the precise measurement of heat flux densities that reached up to 4 MW/m<sup>2</sup>, demonstrating the efficiency and robustness of liquid metal-cooled systems under extreme concentrated sunlight conditions. Key results of this work have been published e.g. in Solar Energy in 2021 [33].

Fig. 3.2 shows the SOMMER facility at KALLA and a group photo taken around 2018 with the KIT liquid metal research community including Robert Stieglitz.

In addition to the experimental work, high temperature thermal energy storage solutions based on liquid metals as heat transport media were investigated numerically. These efforts highlighted the potential of liquid metals not only for CSP applications but also for broader high-temperature industrial processes. This development entered into a new series of experimental research projects at KALLA, that will be introduced in the following paragraph.





Figure 3.2: SOMMER facility at KALLA (top) and the KIT liquid metal researcher community in front of SOMMER's concentrator mirror, Robert Stieglitz stands second from right.



## Liquid Metal based Thermal Energy Storage and Process Technology

As mentioned above, starting in the CSP context, theoretical investigations had been launched on exploring the suitability of liquid metals as heat transport and storage fluids in high temperature heat storages. Several challenges like high density, low specific heat capacity and high cost lead to the necessity of a hybrid approach in form of e.g. a packed bed storage. Numerical simulations from KALLA were able to show for the first time, that such a packed bed storage could even be realized within a cost-efficient one-tank design and have been published in [34]. With these promising results, the VESPA project has been started and demonstrated the feasibility of a lab-scale packed-bed thermal storage system using liquid lead-bismuth and ceramic fillers experimentally [35]. These findings in turn provided the foundation for the development of a 100-kWh demonstrator, called DUOLIM. This first-of-its-kind experiment has recently been mocked up in the THEADES loop at KALLA, see figure 3.3.



Figure 3.3: DUOLIM heat storage demonstrator during mock-up at KALLA, © by Karlsruher Institut für Technologie Campus Services – Medienproduktion (left)

Structural materials compatibility with the liquid metal is a key in all these topics, aiming at temperatures far beyond 600 °C. One recent example of the continuing cooperation between KALLA and KIT materials scientists is a publication on potential filler materials for the storage concepts mentioned above [36]. The same consortium is involved in the LIMELISA project, focused on qualification of system components like valves and pumps for the envisaged high temperature storage systems based on liquid metal. LIMELISA is a cooperation between industrial partner KSB, Frankenthal, Germany, the German Aerospace Center, Cologne and KIT. Information on the LIMELIGHT test loop, that has been realized at KALLA recently for testing such equipment with flowing lead at up to 700 °C, can be found in [37].

Yet another example for the innovation potential of liquid metals is the NAMOSYN project, a large consortium of German companies and research institutions aiming at novel, efficient pathways to produce synthetic fuels, in particular oxymethylene ethers (OME). KALLA contributed to this in a joint effort with the Institute of Catalysis Technology at KIT and BASF, aiming at utilizing sodium vapor as catalyst in formaldehyde dehydrogenation. This process requires mastering a complex chain of evaporating, mixing of the metal vapor with other gases within a reactive flow and finally recondensing and separating of the reaction products. The MEDENA-mini-plant has been designed, built and operated for this purpose at KALLA and [38] contains key results of the experiments.

## 4 Conclusion

The history and present of KALLA cannot be thought of without Robert Stieglitz. We owe a deep debt of gratitude to Robert. He shaped fundamental principles of the laboratory's scientific work during his tenure as its head. As demonstrated by numerous examples in this contribution, his influence continues to resonate to this day. His scientific vision and the facilities established under his leadership form the foundation for KALLA's outstanding international position in liquid metal thermo-fluid dynamics research until today. The innovative development paths subsequently pursued at KALLA, such as heat storage and concentrated solar thermal energy, were also significantly supported by him long after his time in the laboratory.

One aspect that Robert was always very interested in, is measurement techniques for liquid metals. This complex, interdisciplinary field was just right to trigger his curiosity and ambition. We did not report on this aspect of his work here, as we had – looking at the sheer length – to limit ourselves to describing the (large) experiments, that have

been realized or envisaged by Robert or have built upon his conceptual influence. Nevertheless, if you are interested in this field and Robert's view on it, you may find the according chapters "Instrumentation" from the OECD NEA's "Handbook on Lead-bismuth Eutectic Alloy and Lead Properties, Materials Compatibility, Thermal-hydraulics and Technologies" helpful [39,40]. The 2007 edition had been written by Robert and the 2015 edition was essentially an update based upon the original chapter and again with strong support of Robert. He had provided us (the authors of this contribution who are also authors of the 2015 edition of the instrumentation chapter in the handbook) not only with the original 2007 manuscript and all the sources mentioned therein, but with his complete literature data base, permanently updated.

This generosity in sharing was a constituent part of Robert's personality and a foundation of his work in the scientific community. At KALLA, we will always honor his scientific legacy, his deep humanity, and his critical sense of humor. It will be easy for us, as we see his influence in our work and surroundings every day. Nevertheless: We miss him!

## References

- [1] C. Rubbia et al. Conceptual design of a Fast Neutron operated High Power Energy Amplifier, CERN/AT/95-44-ET. 1995  
<https://cds.cern.ch/record/289551/files/cer-0210391>
- [2] C.D. Bowman, E.D. Arthur, P.W. Lisowski, G.P. Lawrence, R.J. Jensen, J.L. Anderson, B. Blind, M. Cappiello, J.W. Davidson, T.R. England, L.N. Engel, R.C. Haight, H.G. Hughes, J.R. Ireland, R.A. Krakowski, R.J. LaBauve, B.C. Letellier, R.T. Perry, G.J. Russell, K.P. Staudhammer, G. Versamis, W.B. Wilson. Nuclear energy generation and waste transmutation using an accelerator-driven intense thermal neutron source. Nuclear Instruments and Methods in Physics Research Section A: Accelerators, Spectrometers, Detectors and Associated Equipment, Volume 320, Issues 1–2, 1992, [https://doi.org/10.1016/0168-9002\(92\)90795-6](https://doi.org/10.1016/0168-9002(92)90795-6)
- [3] J.U. Knebel, X. Cheng, G. Müller, G. Schumacher, J. Konys, O. Wedemeyer, G. Grötzbach, L. Carteciano. Thermalhydraulic and Material Specific Investigations into the Realization of an Accelerator Driven System (ADS) to Transmute Minor Actinides, 2000 Status Report, FZKA 6618, Forschungszentrum Karlsruhe, 2001, <https://doi.org/10.5445/ir/270050532>

- [4] J.U Knebel, X Cheng, C.H Lefhalm, G Müller, G Schumacher, J Konys, H Glasbrenner, Design and corrosion study of a closed spallation target module of an accelerator-driven system (ADS), Nuclear Engineering and Design, Volume 202, Issues 2–3, 2000, [https://doi.org/10.1016/S0029-5493\(00\)00367-8](https://doi.org/10.1016/S0029-5493(00)00367-8)
- [5] V. Markov. Lecture „Corrosion of structural materials in Pb-Bi and Pb“, Seminar on the concept of Lead-cooled Fast Reactors, Cadarache, 1997.
- [6] J.U. Knebel, G. Müller & G. Schumacher. Gas-Phase Oxygen Control Processes for Lead/Bismuth Loops and Accelerator Driven Systems, Jahrestagung Kerntechnik Karlsruhe, 1999.
- [7] C.H. Lefhalm, J.U. Knebel, K.J. Mack, Kinetics of gas phase oxygen control system (OCS) for stagnant and flowing Pb–Bi Systems, Journal of Nuclear Materials, Volume 296, Issues 1–3, 2001, [https://doi.org/10.1016/S0022-3115\(01\)00567-0](https://doi.org/10.1016/S0022-3115(01)00567-0).
- [8] J. Zeininger, Dissertation: Turbulenter Wärmetransport in flüssigem BleiWismut an einem vertikalen Heizstab im Ringspalt, KITopen-ID: 1000016315, 2009, <https://doi.org/10.5445/ir/1000016315>
- [9] L. Marocco, A. Loges, Th. Wetzel, R. Stieglitz. Experimental investigation of the turbulent heavy liquid metal heat transfer in the thermal entry region of a vertical annulus with constant heat flux on the inner surface. International Journal of Heat and Mass Transfer, Volume 55, Issues 23–24, 2012, <https://doi.org/10.1016/j.ijheatmasstransfer.2012.06.037>
- [10] G.S. Bauer, M. Salvatores, G. Heusener, MEGAPIE, a 1 MW pilot experiment for a liquid metal spallation target, Journal of Nuclear Materials, Volume 296, Issues 1–3, 2001, [https://doi.org/10.1016/S0022-3115\(01\)00561-X](https://doi.org/10.1016/S0022-3115(01)00561-X).
- [11] B. Smith (2006). Summary Report for MEGAPIE R&D Task Group X4: Fluid Dynamics and Structure Mechanics, PSI Bericht Nr. 06-01, March 2006, <https://www.osti.gov/etdeweb/servlets/purl/20896031>
- [12] C. Fazio, F. Gröschel, W. Wagner, K. Thomsen, B.L. Smith, R. Stieglitz, L. Zanini, A. Guertin, A. Cadiou, J. Henry, P. Agostini, Y. Dai, H. Heyck, S. Dementjev, S. Panebianco, A. Almazouzi, J. Eikenberg, A. Letourneau, J.C. Toussaint, A. Janett, Ch. Perret, S. Joray, J. Patorski, W. Leung, P. Meloni, P. Turroni, A. Zucchini, G. Benamati, J. Konys, T. Auger, A. Gessi, D. Gorse, I. Serre, A. Terlain, J.-B. Vogt, A. Batta, A. Class, X. Cheng, F. Fellmoser, M. Daubner, S. Gnieser, G. Grötzbach, R. Milenkovic, C. Latgé, J.U. Knebel. The MEGAPIE-TEST project: Supporting research and lessons learned in first-of-a-kind spallation target technology. Nuclear Engineering and Design, Volume 238, Issue 6, 2008, <https://doi.org/10.1016/j.nucengdes.2007.11.006>

- [13] R. Stieglitz, M. Daubner, A. Batta, C.-H. Lefhalm. Turbulent heat mixing of a heavy liquid metal flow in the MEGAPIE target geometry—The heated jet experiment. *Nuclear Engineering and Design*, Volume 237, Issues 15–17, 2007, <https://doi.org/10.1016/j.nucengdes.2007.02.016>
- [14] A. Batta, M. Daubner, X. Cheng. Investigation on turbulent mixing process in MEGAPIE target configuration, *Jahrestagung Kerntechnik Düsseldorf*, 2004, paper 203
- [15] J. Patorski, F. Gröschel (2008). Measurement of the Heat Transfer Coefficient for the Proton Beam Entry Window of the Liquid Metal Target, Volume 39, Issue 7, 2008, <https://doi.org/10.1615/HeatTransRes.v39.i7.20>
- [16] K. Litfin, J.R. Fetzer, A. Batta, et al. High-power spallation target using a heavy liquid metal free surface flow. *J Radioanal Nucl Chem* 305, 795–802 (2015). <https://doi.org/10.1007/s10967-015-4002-z>
- [17] A. Batta, A.G. Class, K. Litfin, Th. Wetzel, V. Moreau, L. Massidda, S. Thomas, D. Lakehal, D. Angeli, G. Losi, K.G. Mooney, K. Van Tichelen. Experimental and numerical investigation of liquid-metal free-surface flows in spallation targets. *Nuclear Engineering and Design*, Volume 290, 2015, <https://doi.org/10.1016/j.nucengdes.2014.11.009>
- [18] M. Durante, P. Indelicato, B. Jonson, V. Koch, K. Langanke, Ulf-G. Meißner, E. Nappi, T. Nilsson, Th. Stöhlker, E. Widmann and M. Wiescher. All the fun of the FAIR: fundamental physics at the facility for antiproton and ion research, *Phys. Scr.* 94 033001, 2019, <https://doi.org/10.1088/1402-4896/aaf93f>
- [19] S. Gordeev, L. Stoppel & R. Stieglitz. (2009). Turbulent liquid metal flow in rectangular shaped contraction nozzles for target applications. *International Journal of Computational Fluid Dynamics*, 23(6), 477–493. <https://doi.org/10.1080/10618560903048995>
- [20] M.P. Hillenbrand, R. Stieglitz & G.P. Neitzel. Detection of liquid–metal, free-surface flow using the DLP measurement technique. *Exp Fluids* 52, 179–192 (2012). <https://doi.org/10.1007/s00348-011-1214-z>
- [21] M. Daubner, F. Fellmoser and L. Stoppel. Technische Beschreibung der Versuchsanlage ALINA zur Untersuchung eines Natrium-Freistrahls. Vol. 7570. KIT Scientific Publishing, 2011. <https://doi.org/10.5445/ksp/1000021682>

- [22] J. Pacio, M. Daubner, F. Fellmoser, K. Litfin, L. Marocco, R. Stieglitz, S. Taufall, Th. Wetzel. Heavy-liquid metal heat transfer experiment in a 19-rod bundle with grid spacers. *Nuclear Engineering and Design*, Volume 273, 2014, <https://doi.org/10.1016/j.nucengdes.2014.02.020>
- [23] J. Pacio, M. Daubner, F. Fellmoser, K. Litfin, Th. Wetzel. Experimental study of heavy-liquid metal (LBE) flow and heat transfer along a hexagonal 19-rod bundle with wire spacers. *Nuclear Engineering and Design*, Volume 301, 2016, <https://doi.org/10.1016/j.nucengdes.2016.03.003>
- [24] J. Pacio, M. Daubner, F. Fellmoser, K. Litfin, T. Wetzel. Heat transfer experiment in a partially (internally) blocked 19-rod bundle with wire spacers cooled by LBE. *Nuclear Engineering and Design*, Volume 330, 2018, <https://doi.org/10.1016/j.nucengdes.2018.01.034>
- [25] J. Pacio, M. Daubner, F. Fellmoser, T. Wetzel. Experimental study of the influence of inter-wrapper flow on liquid-metal cooled fuel assemblies. *Nuclear Engineering and Design*, Volume 352, 2019, <https://doi.org/10.1016/j.nucengdes.2019.06.007>
- [26] T. Laube, B. Dietrich, L. Marocco, Th. Wetzel. Conjugate heat transfer of a turbulent tube flow of water and GaInSn with azimuthally inhomogeneous heat flux. *International Journal of Heat and Mass Transfer*, Volume 221, 2024, <https://doi.org/10.1016/j.ijheatmasstransfer.2023.125027>
- [27] C.M. Hofberger, B. Dietrich, I.V. Durán, R. Krumholz, L. Stoppel, N. Uhlenbruck, Th. Wetzel, Natural Gas Pyrolysis in a Liquid Metal Bubble Column Reaction System—Part I: Experimental Setup and Methods. *Hydrogen* 2023, 4, 295-306. <https://doi.org/10.3390/hydrogen4020021>
- [28] C.M. Hofberger, B. Dietrich, I.V. Durán, R. Krumholz, L. Stoppel, N. Uhlenbruck, Th. Wetzel, Natural Gas Pyrolysis in a Liquid Metal Bubble Column Reaction System—Part II: Pyrolysis Experiments and Discussion. *Hydrogen* 2023, 4, 357-372. <https://doi.org/10.3390/hydrogen4020025>
- [29] C. Hofberger, B. Dietrich, R. Krumholz, A.P. Noglik, M. Olbricht, S. Schatzmann, L. Stoppel, M. Richter, N. Uhlenbruck and Th. Wetzel, Technical Aspects of Natural Gas Pyrolysis in Liquid Metal Bubble Column Reactors. *Energy Technol.* (2024), 12: 2400183. <https://doi.org/10.1002/ente.202400183>
- [30] I. Durán, B. Dietrich, C. Hofberger, L. Stoppel, N. Uhlenbruck, Th. Wetzel, CO<sub>2</sub> Impact on Methane Pyrolysis as a Key Issue of Using Biogas as an Educt: A Theoretical Study, *International Journal of Energy Research*, 2023, 3684046, 23 pages, 2023. <https://doi.org/10.1155/2023/3684046>

- [31] N. Uhlenbruck, P. Pfeifer, B. Dietrich, C. M. Hofberger, R. Krumholz, A. Saxler, L. Schulz, L. Stoppel, T. Wetzel, *ChemSusChem* 2024, e202401779. <https://doi.org/10.1002/cssc.202401779>
- [32] N. Uhlenbruck, B. Dietrich, S. Heißler, C. M. Hofberger, R. Krumholz, L. Stoppel, V. Trouillet, P. G. Weidler, T. Wetzel, *ChemSusChem* 2024, e202401780. <https://doi.org/10.1002/cssc.202401780>
- [33] F. Müller-Trefzer, K. Niedermeier, F. Fellmoser, J. Flesch, J. Pacio, T. Wetzel. Experimental results from a high heat flux solar furnace with a molten metal-cooled receiver SOMMER. *Solar Energy*, Volume 221, 2021, <https://doi.org/10.1016/j.solener.2021.03.066>.
- [34] K. Niedermeier, L. Marocco, J. Flesch, G. Mohan, J. Coventry, Th. Wetzel, Performance of molten sodium vs. molten salts in a packed bed thermal energy storage. *Applied Thermal Engineering*, Volume 141, 2018, <https://doi.org/10.1016/j.applthermaleng.2018.05.080>
- [35] F. Müller-Trefzer, K. Niedermeier, M. Daubner, Th. Wetzel, Experimental investigations on the design of a dual-media thermal energy storage with liquid metal. *Applied Thermal Engineering*, Volume 213, 2022, <https://doi.org/10.1016/j.applthermaleng.2022.118619>
- [36] F. Müller-Trefzer, A. Heinzl, R. Hesse, A. Weisenburger, Th. Wetzel and K. Niedermeier, Screening of Filler Material for a Packed-Bed Thermocline Energy Storage Test Facility with Lead–Bismuth Eutectic as the Heat Transfer Fluid. *Energy Technol.* (2024), 12: 2300781. <https://doi.org/10.1002/ente.202300781>
- [37] K. Niedermeier, M. Lux, A. Purwitasari, A. Weisenburger, M. Daubner, F. Müller-Trefzer, Th. Wetzel, Design of the LIMELIGHT Test Rig for Component Testing for High-Temperature Thermal Energy Storage with Liquid Metals. *Processes* 2023, 11, 2975. <https://doi.org/10.3390/pr11102975>
- [38] M. Kamienowska, M.P. Deutschmann, M. Bender, L. Stoppel, M. Daubner, Th. Wetzel and K. Niedermeier, Experimental Demonstration of the Production of Hydrogen and Water-Free Formaldehyde Using Sodium Vapor. *Chemie Ingenieur Technik* (2024). <https://doi.org/10.1002/cite.202400007>
- [39] Handbook on Lead-bismuth Eutectic Alloy and Lead Properties, Materials Compatibility, Thermal-hydraulics and Technologies. 2007 Edition, NEA No. 6195 NUCLEAR ENERGY AGENCY, ORGANISATION FOR ECONOMIC CO-OPERATION AND DEVELOPMENT, ISBN 978-92-64-99002-9

- [40] Handbook on Lead-bismuth Eutectic Alloy and Lead Properties, Materials Compatibility, Thermal-hydraulics and Technologies. 2015 Edition, NEA No. 7268 NUCLEAR ENERGY AGENCY, ORGANISATION FOR ECONOMIC CO-OPERATION AND DEVELOPMENT, [https://www.oecd-neo.org/jcms/pl\\_14972/handbook-on-lead-bismuth-eutectic-alloy-and-lead-properties-materials-compatibility-thermal-hydraulics-and-technologies-2015-edition?details=true](https://www.oecd-neo.org/jcms/pl_14972/handbook-on-lead-bismuth-eutectic-alloy-and-lead-properties-materials-compatibility-thermal-hydraulics-and-technologies-2015-edition?details=true)



# Historical overview of the HELMHOLTZ Alliance LIMTECH: Advancing liquid metal research and innovation

*Thomas Wetzel<sup>1</sup>, Sven Eckert<sup>2</sup> and Gunter Gerbeth<sup>2</sup>*

<sup>1</sup> *Karlsruhe Institute of Technology, Karlsruhe, Germany*

<sup>2</sup> *Helmholtz-Center Dresden-Rossendorf, Germany*

## 1 Introduction

How can one find deeper meaning in a tragic loss like that of Robert Stieglitz, who unexpectedly passed much too early in December 2023? The authors, all being close colleagues and friends of Robert for many years and sometimes decades, try to find one possible answer with this contribution, by looking back at the HELMHOLTZ-Alliance LIMTECH, a 5-year joint research undertaking of Helmholtz-Zentrum Dresden-Rossendorf (HZDR), Karlsruhe Institute of Technology (KIT) and many more partners from science and industry. Robert has been the co-speaker of that alliance and had deep and decisive impact on its scientific vision, organizational structure and successful operation.

Strategic scientific development lines established by Robert long before the start of LIMTECH, along with fruitful scientific cooperation, built on trust between him and all core partners, have formed important parts of LIMTECH's foundations. LIMTECH has catalyzed groundbreaking research activities that extend far beyond its actual duration. Looking back today, we can trace the origins of much of our current work to LIMTECH – and with it a part of Robert's profound impact and enduring legacy on all of us.

We hope that the reader may find inspiration in the following retrospective, which we might not have created were it not for the loss of Robert. That would bring at least a certain measure of meaning to the incomprehensible.

However, before we go into the main text, one important remark needs to be made: The following retrospective has been created in large parts by using ChatGPT along with the final report of LIMTECH. We did not have the chance to discuss this technology and its use with Robert. So we do not know his view on it. He has been an extremely productive and fast writer, creative and illustrative and with the rare ability, to rise and speak imaginatively in front of the reader of his text. Yet, in doing so he also relied on re-reading,

re-working, re-thinking and re-combining contents that he had created and collected over his complete scientific life. In that sense, we hope, that he would have appreciated working with and challenging large language models, as we did here with our (including the author Robert Stieglitz) Final Report on LIMTECH from 2017. The version used was ChatGPT (GPT-3.5) for Mac as of January 4, 2025. Non-ChatGPT assisted parts of the text are *set in italics*.

## 2 Formation and Vision of the LIMTECH Alliance

The Helmholtz Alliance “Liquid Metal Technologies” (LIMTECH) was established in 2012 as a strategic initiative to unify and advance Germany’s global leadership in liquid metal research. By creating a comprehensive national competence center, LIMTECH aimed to consolidate academic, industrial, and institutional expertise in this critical field. *It lasted until 2017, after a successful mid-term evaluation in 2015.*

Liquid metals possess unique properties, such as high thermal conductivity and fluidity, making them invaluable in applications ranging from energy systems to materials processing and diagnostic technologies. However, harnessing their full potential required not only cutting-edge research but also systematic interdisciplinary collaboration. LIMTECH set out to address these challenges by fostering synergies among research institutions, universities, and industry partners.

The alliance’s vision extended beyond immediate technological advancements. It sought to establish sustainable networks and infrastructure that could serve as a foundation for long-term innovation. The inclusion of 14 institutional partners, including Helmholtz Centers (HZDR, KIT, FZJ, DLR)<sup>1</sup>, universities (TU Dresden, TU Bergakademie Freiberg, TU Ilmenau, LUH Hannover, Potsdam university, Göttingen university, RWTH Aachen), and international collaborators (e.g. Coventry University, UK; Institute of Physics, Latvia; RGS Development, Netherlands), underscored the breadth of its scope. LIMTECH also actively engaged industrial stakeholders, ensuring that its research was aligned with market needs and positioned for real-world impact.

*The Helmholtz Alliance LIMTECH consisted of 14 scientific projects grouped in three topics and a Young Investigator Group on Liquid Metal Measurement Techniques, as shown in Fig. 1. Topic A addressed basic problems and phenomena, whereas Topic B was devoted to new energy conversion and energy storage systems. Part C dealt with applications in metals and semiconductor processing with strong focus on energy savings.*

---

<sup>1</sup> For a list of abbreviations please refer to Appendix 2 at the end of this contribution

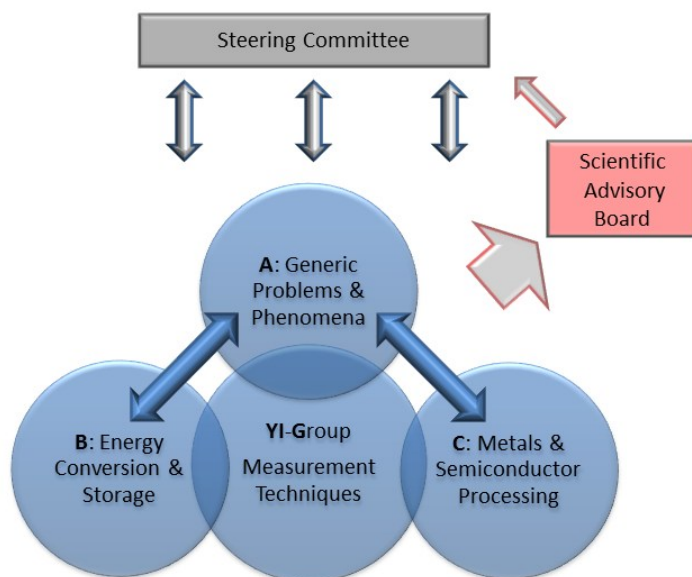


Fig. 1: Structure of the LIMTECH Alliance.

*As measurement techniques for liquid metal flows play a central role within LIMTECH, they were particularly developed in a cross-cutting way as a Young Investigator Group (YIG). The Alliance was complemented with a PhD programme to intensively support early stage careers.*

With a €10 million funding from the HELMHOLTZ Association and the active participation of over 120 researchers and students, LIMTECH became a hub of innovation and collaboration. The transition of many of its activities into ongoing Helmholtz research programs following the conclusion of its funding period in 2017 demonstrated the alliance's ability to create a lasting legacy in liquid metal research and applications.

### 3 Collaboration Across Institutions and Talent Development

At the heart of LIMTECH's success was its collaborative structure, which bridged gaps between institutions, disciplines, and sectors. Helmholtz Centers contributed state-of-the-art infrastructure and large-scale experimental capabilities, universities provided theoretical expertise and innovative research approaches, and industrial partners

ensured that the research outcomes were relevant and applicable to real-world challenges.

*During the course of the LIMTECH alliance, several international workshops or conferences were organized or co-organized, underlining the leading role LIMTECH has achieved in the research field of liquid metal technologies. Among these conferences and workshops were such in well established series like the 549. Heraeus-Seminar in 2013 in Bad Honnef, the 3rd International Workshop on Measuring Techniques for Liquid Metal Flows in 2025 in Dresden, the 10th PAMIR International Conference on Fundamental and Applied MHD in Cagliari, Italy in 2016 and new formats like the International Workshop on Safety in Heavy Liquid Metal (HLM) Cooled Fast Reactors at KIT in 2014 and the International Workshop on Liquid Metal Battery Fluid Dynamics, LMBFD 2017 in Dresden.*

The alliance placed a strong emphasis on human resource development, recognizing that the advancement of science relies not only on equipment and facilities but also on the skills and creativity of individuals. LIMTECH directly supported 10 postdoctoral researchers and 29 PhD students, while an additional 72 scientists and 12 PhD candidates contributed through external funding. This diverse group brought together expertise in physics, engineering, materials science, and energy systems, fostering a multidisciplinary approach to problem-solving.

A significant achievement in this area was the establishment of the LIMTECH Young Investigator Group (YIG), which focused on developing advanced measurement techniques for liquid metal flows. The YIG not only contributed to the alliance's scientific objectives but also served as a training ground for the next generation of researchers, equipping them with the skills and experience needed to lead future projects.

*Regular annual alliance meetings were held at different partner locations. The meetings often were complemented with interesting lab-tours on site, see Fig. 2. In addition, annual PhD workshops were organized to closely monitor the progress of the PhD students. During these meetings, also invited lectures from neighboring fields of science and soft-skill seminars took place.*

*So called seed grants have formed an essential part of this: In order to trigger the development of new research ideas and related projects, the steering committee decided to use a flexible part of the budget for making annual calls for seed projects beginning from 2014 and running successfully through till the end of the alliance. In total 14 such seed grants were funded in frame of the alliance. Topics included, e.g. the development of a small scale directional solidification setup for solidification of metallic alloys under combined AC and DC electromagnetic fields, contactless bubble detection with mutual*

*inductance tomography and electrical capacitance tomography as well as neutron radiography of Ga crystallization in electromagnetic fields.*



Fig. 2: Lab visit to the DRESHDYN facility, with Robert Stieglitz in the center (blue pullover)

The personal and professional growth of LIMTECH participants was evident in their career trajectories. Several PhD students and postdoctoral researchers advanced to professorships or leadership roles in academia and industry, reflecting the alliance's success in nurturing talent. Collaborative projects also exposed participants to international research environments, further enhancing their expertise and broadening their professional networks.

## 4 Pioneering Scientific Achievements

LIMTECH's research agenda was ambitious, spanning several domains of liquid metal science and technology. Its achievements significantly advanced understanding and applications in measurement techniques, energy systems, and materials processing.

## **4.1 Innovations in Measurement and Diagnostics**

One of the alliance's most notable contributions was the development of advanced diagnostic techniques for studying liquid metal flows. These methods included non-invasive technologies such as ultrasound Doppler velocimetry and magnetic field-based flow measurements. By enabling precise and real-time analysis of complex fluid dynamics, these tools expanded the capabilities of both fundamental research and industrial applications. For instance, these diagnostic techniques were instrumental in optimizing processes in energy systems and materials manufacturing.

## **4.2 Energy Applications: Liquid Metals in Energy Systems**

LIMTECH made significant strides in demonstrating the potential of liquid metals in sustainable energy systems. The SOMMER project (SOLar furnace arrangement with Molten-METal-cooled Receiver) investigated the use of liquid metals as heat transfer fluids in concentrating solar power (CSP) systems. These studies highlighted the superior thermal transport capabilities and high-temperature stability of liquid metals, making them ideal candidates for CSP applications.

Another major focus was liquid metal batteries, which have emerged as a promising solution for large-scale energy storage. LIMTECH addressed key challenges in this area, such as mitigating magnetohydrodynamic instabilities, which can affect battery performance. By improving the stability and efficiency of these systems, LIMTECH contributed to the development of energy storage solutions that could facilitate the integration of renewable energy sources.

## **4.3 Materials Processing and Manufacturing**

In the realm of materials processing, LIMTECH explored the use of liquid metals to enhance industrial techniques. Studies on electromagnetic flow control during metal solidification provided insights into improving casting processes, resulting in higher quality and more efficient production methods. Collaborative projects extended these findings to other areas, such as particle segregation and advanced recycling techniques, showcasing the versatility of liquid metal research and technology in addressing industrial challenges.

*The relevance and quality of the research done in LIMTECH is reflected in more than 15 prizes and awards won by the LIMTECH researchers, among them such prestigious ones as the da Vinci Medal of ERCOFTAC and the Werner-von-Siemens Excellence Award.*

## 5 Expanding the Horizons of Liquid Metal Research

While LIMTECH's primary focus was on advancing liquid metal technologies, its research often intersected with broader scientific and technological questions.

For example, the DRESDYN project, which studies magnetic field generation and planetary processes, linked liquid metal research to astrophysics. This work provided valuable insights into geodynamo processes and the behavior of magnetic fields in celestial bodies, demonstrating the fundamental relevance of liquid metals beyond industrial and energy applications.

Similarly, LIMTECH played a key role in the European SESAME project, which focused on the safety and efficiency of heavy liquid metal-cooled nuclear reactors. By contributing critical data and insights, the alliance supported advancements in nuclear technology, addressing global energy needs while emphasizing safety and sustainability.

*The development of the liquid metal bubble column technology for thermal decomposition or pyrolysis of methane within LIMTECH and in close collaboration with the Institut of Advanced Sustainability Studies in Potsdam is another example for expanding liquid metal applications. This process to produce clean hydrogen from natural or biogas is nowadays seen as one key technology for climate friendly and affordable energy supply.*

These examples illustrate LIMTECH's ability to bridge disciplinary boundaries, leveraging liquid metal research to address both practical and fundamental challenges.

## 6 Broader Impact and Legacy

The influence of LIMTECH extended far beyond its direct outputs. *Many of the scientific collaborations between universities and Helmholtz-Centers last until today, many of the LIMTECH doctoral students are now actively shaping the research landscape in the fields once addressed within the alliance, and the personal trust once grown within the LIMTECH community continues to form the basis for exchanging and advancing new ideas and developments.*

By fostering collaborations with industrial partners such as Siemens, ThyssenKrupp, and Nippon Steel, the alliance ensured that its research had practical applications and commercial potential. These partnerships accelerated the transfer of innovations from

the lab to the marketplace, reinforcing the relevance of liquid metal technologies in addressing real-world problems.



Fig. 3: Group photo from the 2013 Annual Meeting of the Alliance at Karlsruhe

LIMTECH's contributions were documented in 224 peer-reviewed publications, and 419 conference presentations, covering topics ranging from fluid dynamics to energy systems. These works enriched the global knowledge base and positioned the alliance as a leader in liquid metal research. Initiatives such as the International LIMTECH Young Scientist Award further enhanced its reputation, attracting talent and fostering global engagement.

*A large part and representative overview on the scientific results of LIMTECH has been published with open access in "IOP Conference Series: Materials Science and Engineering, Vol. 228, 2017" <https://iopscience.iop.org/issue/1757-899X/228/1>. This volume, made available at the Final LIMTECH Colloquium in September 2017, contains 26 separate contributions.*

The alliance's legacy is also evident in the continuation of its projects through Helmholtz research programs. *Prominent examples are liquid metal batteries, high temperature heat storage and materials recycling processes for rare metals.* By integrating its activities into these programs, LIMTECH ensured that its work would remain relevant and impactful, even after the formal conclusion of the alliance.



## 7 Conclusion: A Lasting Legacy

The LIMTECH Alliance succeeded in unifying a somewhat fragmented research landscape, delivering pioneering scientific achievements, and setting new standards for interdisciplinary collaboration. Its impact extended beyond liquid metal technologies, influencing fields as diverse as astrophysics, nuclear safety, and renewable energy systems.

Through its emphasis on collaboration, talent development, and practical application, LIMTECH demonstrated the transformative potential of interdisciplinary research. By fostering innovation and addressing critical global challenges, the alliance not only achieved its original goals but also laid the groundwork for future breakthroughs in science and technology.

## Acknowledgment

*The authors would like to take this opportunity to thank the Helmholtz Association of German Research Centers for funding LIMTECH. The funding instrument of Helmholtz Alliances was a very effective tool for supporting fruitful research cooperation between Helmholtz Centers and national and international universities. We would also like to thank the members of the Scientific Advisory Board Jaqueline Etay, Koulis Pericleous and Wilfried von Ammon, for their excellent scientific advice and continuous endorsement in the scientific and structural development of LIMTECH during the funding period. Finally, we are deeply indebted to all the partners and project leaders in LIMTECH for their extremely committed, constructive and trusting cooperation during the work in the Alliance and beyond.*

## Appendix 1: List of LIMTECH projects

- Project A1: Thermo-hydraulic Flow in a Sudden Expansion**  
**PI:** Prof. Robert Stieglitz (KIT)  
**Partners:** KIT, TUD
- Project A2: Magnetic Field Dynamos and Magnetorotational Instability**  
**PI:** Dr. Frank Stefani (HZDR)  
**Partners:** HZDR, KIT, UG, UP, IPUL, CU
- Project A3: Magnetically Induced Instabilities in Duct Flows**  
**PI:** Prof. Leo Bühler (KIT)  
**Partners:** KIT, TUI, CU
- Project A4: Magnetic Flow Control in Solidification**  
**PI:** Dr. Sven Eckert (HZDR)  
**Partners:** HZDR, RWTH, TUD
- Project A5: Liquid Metal Two-phase Flows and Magnetic Particle Separation**  
**PI:** Dr. Gunter Gerbeth (HZDR)  
**Partners:** HZDR, TUD, FZJ, TUBAF
- Project B1: Transition between Free, Mixed and Forced Convection**  
**PI:** Prof. Robert Stieglitz (KIT)  
**Partners:** KIT, TUD
- Project B2: Liquid Metals for Solar Power Systems**  
**PI:** Prof. Thomas Wetzel (KIT)  
**Partners:** KIT, HZDR, LUH, DLR
- Project B3: Liquid Metal Batteries**  
**PI:** Dr. Tom Weier (HZDR)  
**Partners:** HZDR, CU, TUI
- Project B4: Phase Changes in Liquid Metals for Direct Energy Conversion**  
**PI:** Dr. Wolfgang Hering (KIT)  
**Partners:** KIT
- Project B5: Carbon Dioxide free Production of Hydrogen**  
**PI:** Prof. Thomas Wetzel (KIT)  
**Partners:** KIT, LUH
- Project C1: Magnetic Flow Control in Growth and Casting of Photovoltaic Silicon**  
**PI:** Dr. Gunter Gerbeth (HZDR)  
**Partners:** HZDR, TUBAF
- Project C2: Magnetic Control in Ribbon Growth on Substrate of Silicon Wafers**  
**PI:** Dr. Vladimir Galindo  
**Partners:** HZDR, RGS Development

**Project C3: LIMMCAST: Modelling of Steel Casting**

**PI:** Dr. Sven Eckert (HZDR)

**Partners:** HZDR, TUBAF

**Project C4: Casting Technology for Oxide Dispersion Strengthened (ODS) Steels**

**PI:** Dr. Gunter Gerbeth (HZDR)

**Partners:** HZDR, IPUL, KIT

**Young Investigator Group (YIG):**

**Measurement Techniques for Liquid Metal Flows**

**PI:** Dr. Thomas Wondrak (HZDR)

**Partners:** HZDR, KIT, TUD, TUI, CU

## **Appendix 2: List of Abbreviations**

<b>ACCESS</b>	Aachen Center for Computational Engineering Science
<b>CU</b>	Coventry University (UK)
<b>DLR</b>	Deutsches Zentrum für Luft- und Raumfahrt (German Aerospace Center)
<b>FZJ</b>	Forschungszentrum Jülich
<b>HZDR</b>	Helmholtz-Zentrum Dresden-Rossendorf
<b>IPUL</b>	Institute of Physics Riga (Latvia)
<b>KIT</b>	Karlsruher Institut für Technologie
<b>LUH</b>	Leibniz Universität Hannover
<b>RWTH</b>	Rheinisch-Westfälische Technische Hochschule Aachen
<b>TUBAF</b>	Technische Universität Bergakademie Freiberg
<b>TUD</b>	Technische Universität Dresden
<b>TUI</b>	Technische Universität Ilmenau
<b>UG</b>	Universität Göttingen
<b>UP</b>	Universität Potsdam



# Prof. Dr.-Ing. Robert Stieglitz' role in and contribution to the success of the FJOHSS

## Frédéric Joliot / Otto Hahn Summer School

*Victor Hugo Sanchez-Espinoza, Fabrizio Gabrielli, Walter Tromm, Ingeborg Schwartz and Petra Klug*

*Karlsruhe Institute of Technology, Karlsruhe, Germany*

The Frédéric Joliot / Otto Hahn Summer School course represents the continuation of the Frédéric Joliot Summer Schools on “Modern Reactor Physics and the Modelling of Complex Systems”, which was created by CEA in 1995 to promote knowledge in the field of reactor physics, in a broad sense, and the international exchange of teachers, scientists, engineers and researchers. In 2001, Prof. Dr. Dan G. Cacuci joined as co-director and since then the School was renamed as Frederic Joliot / Otto Hahn Summer School and KIT has been the co-organizer. Beginning in 2004 the scope of the School was extended to include scientific issues related to nuclear fuels. The School, then led by Prof. Massimo Salvatores, became one of the unique summer Schools on Reactor Physics, lasting now for 30 years. In total more than 1500 participants of many countries of all continents visited the 10 days of classes, including technical visits and topical seminar lectures. The program has always been accompanied by social events and fascinating excursions, fostering a joint spirit during the School and far beyond.



25<sup>th</sup> Anniversary of the FJOHSS, August 2019, Karlsruhe © KIT, Amadeus Bramsiepe

According to the main philosophy of the School, recognized experts of different age, gender and nationality working in different sectors of the nuclear field (universities, research centers, TSOs, industry, regulators, international organisations like OECD, IAEA, WANO, start-ups) were won as lecturers for the 10-day classes. To foster the interaction and discussions of the participants with the lecturers, they were present the entire 10 days with the School resulting in very intensive and fruitful exchange of ideas, opinions, and perspectives. During all the courses, the objective was to enhance nuclear energy in civil applications and to foster its safety level and make it more economic. A second goal was to strive for excellence in the every-day work of the nuclear engineering experts in their workplaces. The dissemination of knowledge, networking of experts worldwide working in similar topics, and the increase of the safety culture, fostering at the same time innovations in the nuclear fields, were important drivers of the FJOHSS directors and scientific secretary as well as the International Advisory Board of the School.

It is worth mentioning that during the first eight years, each session of the FJOHSS was devoted to a mix of various topics identified by the Scientific Board with the support of the International Advisory Board. In 1995 for example, the topics were core physics, chaos, thermal hydraulics, 3D transport methods and tools for Monte Carlo calculations and spallation facilities. Starting with the extension of the scope in 2004, each year's School was devoted to a specific topic and it was agreed on alternating locations between France and Germany (France: Cadarache or Aix-en-Provence, Germany: Karlsruhe). Consequently, the FJOHSS was organized by CEA in the following years:

- 2004 (Generation IV reactors, Fuel and Fuel cycles)
- 2006 (Challenges and Innovations in LWR)
- 2008 (The role of experiments in nuclear reactor simulations and analysis)
- 2010 (Goals and Challenges for the Gen2 to Gen3 Transition)
- 2012 (Innovative Modular Nuclear Reactors: Concepts, Physics, and State-of-the-art Analysis Methods)
- 2014 (Nuclear Reactors: Bridging the Gap between Science and Industry)
- 2016 (Tomorrow's Liquid Metal Fast Reactors: Towards Improved Safety and Performance)
- 2018 (Maximizing the Benefits of Experiments for the Simulation, Design, and Analysis of Reactors)
- 2020 (High-fidelity Modelling and Simulation of Nuclear Reactors: Turning a Promise into Reality)
- 2022 (Nuclear Power in the Energy Transition)

- 2024 (Innovative approaches for streamlining the design, Deployment and operation of near-term and emerging reactors).

The following topics were the focus of the Schools held in Karlsruhe in the years:

- 2005 (Irradiated Fuel Management, Waste Treatment, Recycle and Decommissioning)
- 2007 (Sustainability of Nuclear Energy: GEN-IV, Partitioning & Transmutation, Waste Management)
- 2009 (Towards Implementation of Fast Reactor Technology: The Challenges)
- 2011 (High-fidelity Modelling for Nuclear Reactors: Challenges and Prospects)
- 2013 (Physics of advanced nuclear systems fuelled with transuranic fuels)
- 2015 (Enhanced Reactor Safety: Design and Simulation of LWR Evolutionary Cores)
- 2017 (Uncertainties in Nuclear Reactor Systems Analysis: Improving Understanding, Confidence and Quantification)
- 2019 (Innovative Reactors: Matching the Design to Future Deployment and Energy Needs)
- 2021 due to the COVID pandemic no School could be held
- 2023 (Digital Twins: New Horizons in Nuclear Reactor Design and Optimization)
- 2025 (The Technological Development Path from Proven Designs to Advanced Modular Reactors).

Prof. Dr.-Ing. Robert Stieglitz was the third Director of the Institute of Neutron Physics and Reactor Technology (INR), and thus the successor of Prof. Dr. Volker Heinzl as School Director for KIT in the year 2009. Since that time, a collegial, intensive, respectful and even friendly cooperation between Dr. Robert Jacqmin (Director representing CEA) and Prof. Dr.-Ing. Robert Stieglitz (Director representing KIT) started and lasted until December 2023, when Prof. Dr.-Ing. Robert Stieglitz unexpectedly and all of a sudden passed away, leaving behind a big vacuum in the School as well as in the nuclear and fusion community.

Prof. Dr.-Ing. Robert Stieglitz' expertise in fission, fusion, accelerator applications and renewable energy as well as his close relations with the German and European industry and his participation as expert in international committees and international organisations (IAEA, OECD) were extremely beneficial in selecting the proper topics of nuclear engineering and safety for the special courses. The courses always had the highest relevance for attendees with different backgrounds coming from industries, safety organisations, authorities and other stakeholders. With his expertise it was guaranteed

that sufficient novelty and innovative character was included in the courses, but also the appropriate lecturer experts for the selected issues could be found.

Moreover, Prof. Dr.-Ing. Robert Stieglitz was very passionate in moderating and promoting the discussions during the School so that the audience was very impressed and took home excellent knowledge not only from the lectures but as well from these discussions. Last but not least, he paved the way for interesting technical visits at KIT and overall Germany due to his very good connections with the nuclear industry, the regulators and utilities, being a highly valued member of the German Nuclear Safety Commission and actively participating in the German Nuclear Society.

We are very fortunate and proud to have worked countless hours with Prof. Dr.-Ing. Robert Stieglitz for the success of the FJOHSS. We will always remember his critical but warm-hearted and friendly personality and this memory of him will be an incentive, inspiration and encouragement for us to continue to lead the School into a successful future.



# ITER and DEMO – Technology challenges on the way to fusion power

*Klaus Hesch<sup>1</sup> and Robert Stieglitz<sup>2†</sup>*

<sup>1</sup> *Karlsruhe Institute of Technology, Fusion Programme Management, Karlsruhe, Germany*

<sup>2</sup> *Karlsruhe Institute of Technology, Institute for Neutron Physics and Reactor Technology, Karlsruhe, Germany*

## Preface

This is a reprint of an article Robert Stieglitz and Klaus Hesch produced together during the summer of 2023, few months before Robert's unexpected passing away in December of the same year. It was first published in *atw – Journal for Nuclear Power*, Vol. 68 No. 5 (September 2023).

## Abstract

Nuclear fusion as a virtually unlimited source of energy supply has attracted considerable attention recently, because of both the remarkable progress achieved at the US Lawrence Livermore National Laboratory with a laser-driven, inertial fusion approach, and a number of start-up enterprises attracting funds by pursuing game-changing solutions. The fusion development in Europe mainly focuses on magnetic confinement fusion, where a solid plasma physics basis beyond the actual implementation of the fusion reaction itself has been established. The international experimental fusion reactor ITER, currently under construction at Cadarache in the South of France, and the design of a Demonstration reactor (DEMO) within the EUROfusion project are the cornerstones of the European development. On the way to a fusion power plant, still a number of technology and related challenges have to be addressed. A brief overview is provided here.

**Keywords:** ITER, DEMO, European Fusion Roadmap, Fusion Technologies

# 1 Introduction

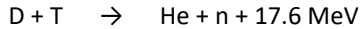
Nuclear fusion promises virtually unlimited energy production in a sustainable manner with a reduced radiological risk due to the absence of a nuclear power escalation. However, the technology is complex and still in the stage of step-wise maturation. While recently, remarkable progress has been achieved at the US Lawrence Livermore National Laboratory with a laser-driven, inertial fusion approach, the fusion development in Europe mainly focuses on magnetic confinement fusion, where a solid plasma physics basis beyond the actual implementation of the fusion reaction itself has been established. The international experimental fusion reactor ITER, currently under construction at Cadarache in the South of France, as illustrated in Figures 1 - 2, and the design of a Demonstration reactor (DEMO) within the EUROfusion project are the cornerstones of the European development. Nuclear fusion requires challenging solutions in quite a number of technological and technology-related areas. Game-changing solutions are being targeted by start-up companies aiming at early deployment of fusion; still, even if successful, these will not resolve all the challenges / requirements at once, and will not make obsolete the need for integration of the remaining subsystems and for licensing. This article provides a brief overview on the technology and related challenges on the way to magnetic fusion energy.



Figure 1: ITER construction at Cadarache, France: Aerial view of construction site.  
(Credit © ITER Organization, <http://www.iter.org/> )

## 2 ITER

ITER shall, for first time, demonstrate a magnetically confined, self-heating (i.e., “burning”) plasma on the basis of the D-T fusion reaction:



According to momentum conversation, 80 % of the reaction energy (i.e., 14.1 MeV) is carried by the neutron leaving the plasma chamber domain, while the remaining 20 % carried by the He ion is “captured” within the magnetic confinement of the plasma domain and provides heating of the plasma fuel through collisions, thus allowing to maintain the fusion reaction. The goal of ITER is to reach a Q factor of 10, i.e., to produce 10 times more fusion power than power injected into the plasma by the heating systems. This simple consideration, however, does not take into account the efficiency of the heating systems, so that the power effectively injected into the plasma is lower than the power supplied to the heating systems. E.g., for the Electron Cyclotron Resonance Heating (ECRH), an efficiency (or conversion factor) of 50 % appears to be in reach. Similar arguments for the efficiency hold for a set of electrically driven technical systems required to operate a fusion reactor, such as magnet system, cryoplant, fuel cycle. Furthermore, the thermodynamic efficiency providing the electric power by extracting heat from the blanket for conversion, i.e., in a turbine, is well below unity.

ITER will be the central facility to demonstrate a self-sustaining “burning” plasma through  $\alpha$ -particle (He ion) heating. So far, Q factors of  $\sim 0.7$  have been achieved with D-T reactions in the Joint European Torus (JET), a facility in operation since almost 40 years now. JET however, is constrained to a low magnetic field produced by normal conducting magnets, and its fusion power is by its small size. The point in time when the “burning plasma” will be reached in ITER is currently subject to a re-baselining caused essentially by non-conformities of delivered components. According to the previous schedule, fusion plasma operation has been foreseen in the early 2030ies. While ITER remains crucial for the European Roadmap to fusion power, the behaviour of the “burning plasma” can to a large extent be anticipated by more and more sophisticated modelling approaches used to define the successor of ITER, DEMO, as discussed below. So, while no surprises are expected, validation and eventually correction of the models is indispensable before the design of DEMO can be finalized.

ITER is based on a tokamak, i.e., the fusion plasma is confined by strong magnetic fields forming a torus shape. It will rely on a number of technological systems, part of which

have been validated on JET and other plasma physics experiments worldwide; nevertheless, due to the challenges of the large scale of ITER, most of these will be “first of a kind”. To be mentioned here are the magnets confining the plasma, the plasma heating systems also providing current drive necessary to maintain the plasma, systems for plasma diagnostics and control as well as for power and particle exhaust. Given the radiotoxicity of tritium, a closed deuterium-tritium fuel cycle is required. ITER will also be used to determine Beginning-of-Life effects in modules, called blankets, for testing the self-production of tritium. As the D-T reaction will produce neutrons and hence activation, remote handling systems will be required. An overarching challenge of course is safety demonstration and licensing.

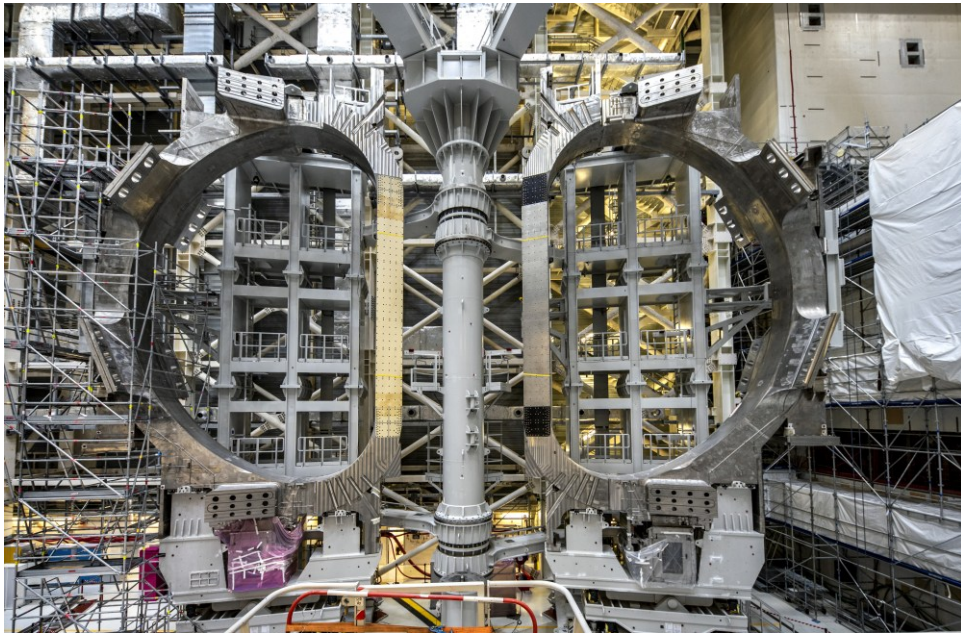


Figure 2: Assembly preparation of toroidal field coils  
(Credit © ITER Organization, <http://www.iter.org/> )

### 3 DEMO and the European Roadmap

Different from ITER, DEMO shall demonstrate electricity generation out of fusion power – in a way that commercial attractiveness comes into reach and industrial actors will take over. It is thus the central element of the European Roadmap to Fusion Energy (Figure 3).

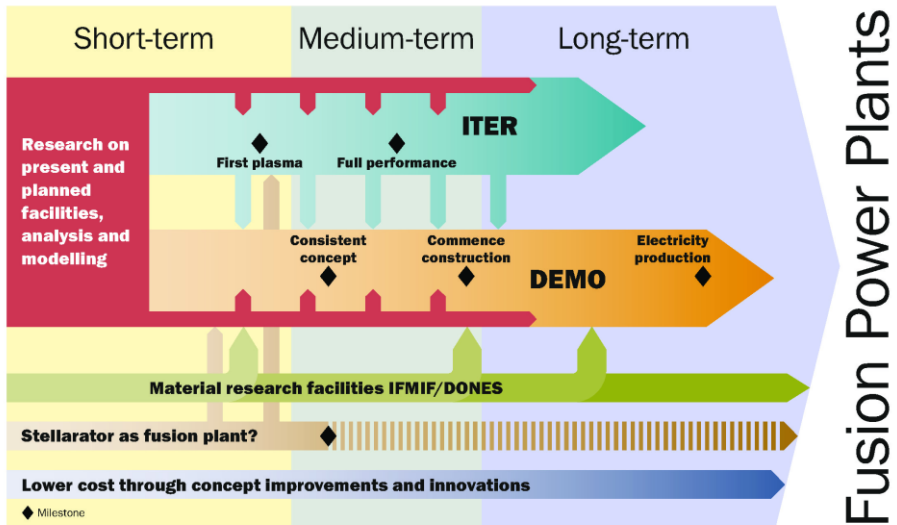


Figure 3: Schematic representation of the European Roadmap to Fusion Energy (Figure taken from: A.J.H. Donné et al., “European Research Roadmap to the realisation of fusion energy”, ISBN 978-3-00-061152-0, with kind permission of A.J.H. Donné)

As much as possible, DEMO will rely on technologies already developed for, and validated with, ITER. Nevertheless, a number of new technological challenges has to be mastered. First and above all, DEMO will accumulate substantial doses of neutron exposure and damage in the components located within the vacuum vessel surrounding the plasma. Thus, DEMO requires neutron-resistant materials in order to achieve a reasonably high duty cycle and overall time of operation, which is one to two orders of magnitudes above the overall neutron wall loads calculated for ITER. While for ITER, the expected damage and activation level in the structure does not require specific precautions and allows using materials certified in nuclear power reactors, DEMO has to anticipate commercial power plant operation requirements, specifically with respect to materials and component lifetime simultaneously at a low activation level, which requires dedicated low activation neutron-resistant materials, being different from those of nuclear fission reactors. The qualification of these materials in a fusion reactor typical neutron spectrum is indicated by the line “Material research facilities IFMIF-DONES” in the Roadmap sketch, as shown in Figure 3.

While the tritium for the operation of ITER will be supplied externally, DEMO will have to produce its own tritium after the initial filling – also in line with the requirements for a fusion power plant. This entails the deployment of a new fuel cycle technology and the related systems, i.e., the tritium breeding blanket inside the vacuum vessel. While test blanket modules will be inserted in ITER without direct impact on ITER operation, a reliable operation of the tritium breeding blanket will be a pre-requisite for operating DEMO as a whole. Furthermore, suitable remote-maintenance technologies have to be developed for the regular exchange of this component, capable to operate reliably at high shut-down dose rates. The closed DT fuel cycle of ITER cannot be extrapolated to DEMO, as the tritium throughput will be by orders of magnitude larger, which is a consequence of the higher duty cycle and the higher overall thermal power (1-2 GW of DEMO vs. 500 MW of ITER). Since the tritium release to the ambient is restricted to quite low quantities and also the tritium amount in components is limited for licensing reasons, the DT-fuel cycle is targeting to minimize of the overall tritium inventory thus requiring new solutions to be developed.

Electricity generation in a DEMO-reactor cannot be directly copied from existing nuclear fission power plants due to the inevitably pulsed operation of a tokamak reactor. Here, advanced energy conversion technologies based upon helium at high temperatures and the use of thermal storage technologies are under development to decouple thermal power generation from power conversion as addressed in the section Balance of Plant. Last but not least, the ongoing experience of ITER licensing has shown that it may not be the best solution to apply the existing standards and procedures developed for nuclear power plants. A new approach for fusion power plant licensing will have to be developed which is based on the hazard potential of the systems and components and is currently under discussion within the IAEA.

As mentioned above, the operation of a fusion reactor based upon the tokamak concept is intrinsically pulsed, i.e., in intervals with interruptions. This results from the need for inducing a toroidally flowing electric current in the plasma chamber, in order to generate a magnetic field complementing the fields of the toroidal and poloidal field coils for confining the plasma. This is realized by ramping the current in the central solenoid coil located on the torus centreline axis. Thus, in principle a tokamak represents an electric transformer where the secondary side is depicted by a single current turn, i.e., the plasma. An alternative magnetic plasma confinement approach is the so-called stellarator concept. Here, no induced circular current is required; instead, a particular arrangement of twisted coils around the plasma ring provides the magnetic confinement. In contrast to a tokamak, a stellarator has no circumferential symmetry thus posing new engineering challenges; however, this concept does not suffer from plasma current

driven instabilities. The most recent stellarator facility, Wendelstein 7-X at Greifswald, has successfully been set into operation with very promising results. While the stellarator development is lagging behind that of the tokamak by approximately one generation of facilities, a switch to this concept could be envisaged after DEMO depending on a further scientifically successful exploitation of Wendelstein 7-X. Similar to this parallel development on an alternative confinement concept, technological solutions for the major technological subsystems alternative to those pursued in main line of the DEMO conceptual design activity are being explored with a view to commercial attractiveness (energy efficiency of the plant, lifetime of components) and as fall-back solutions.

Currently, with the growing need of making new, sustainable energy solutions viable as early as possible, the European Roadmap is under revision. Both the possibility of accelerating DEMO via a stronger parallelization of developments, and of enhancing DEMO performance via an additional DT fusion test facility are being discussed.

## 4 Technical Systems and Challenges

There are numerous systems to be developed, and challenges to be tackled, around the central element of the burning plasma. An overview is indicated in Figure 4, and the different aspects are discussed in more detail below.

### 4.1 Fusion Magnets

The fusion plasma is confined by strong magnetic fields. In the tokamak concept, it takes the shape of a torus, while the stellarator plasma has a more complex geometry. For ITER, three types of superconducting coils are being realized: the toroidal field coils which directly surround the plasma chamber, the central solenoid in the middle of the torus, and the poloidal field coils surrounding the torus horizontally on the outside. The superconductor materials used are NbTi and Nb<sub>3</sub>Sn, with the latter posing a particular challenge, as the superconducting state is reached only after a heat treatment of the alloy, prohibiting the prior application of the Kapton® insulation. After the heat treatment, the material however is brittle and cannot be shaped, i.e., the shaping has to be done before heat treatment, and the Kapton® insulation afterwards. Still, a process has been developed and successfully implemented for the ITER toroidal field coils using this material. In the view of DEMO, however, it is not yet clear whether this technology can be extrapolated to the even larger dimensions and higher fields under consideration. Alternatively, high-temperature superconductor (HTS) solutions, so far neglected be-

cause of the price gap, could come into the play, and may even be the sole solution for larger, higher field stellarator magnets as compared to those of Wendelstein 7-X. Remarkable progress has been made in this field recently, e.g., the “uninsulated” HTS magnet coils presented by MIT. Nonetheless, although HTS offer unique opportunities, the knowledge on their neutron resistance is still in its infancies.

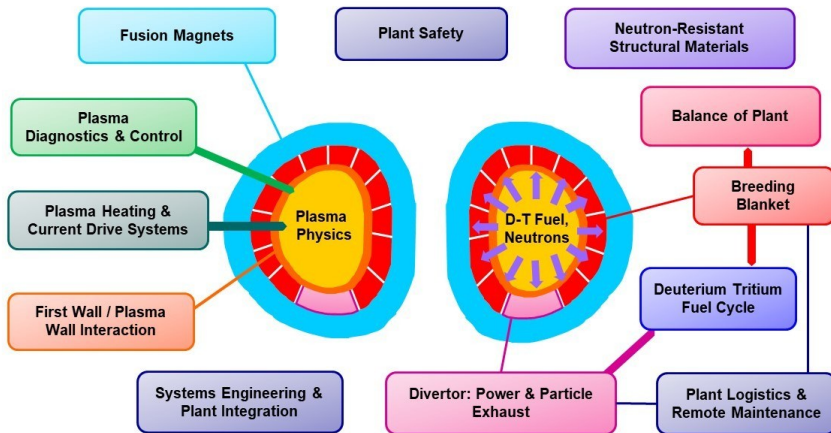


Figure 4: Overview on the technical systems and challenges of magnetic confinement fusion power  
(Credit © Karlsruhe Institute of Technology, [www.kit.edu](http://www.kit.edu) )

## 4.2 Plasma Heating Systems

Plasma heating systems are required to bring the plasma to the temperatures of 100–150 million Kelvin necessary for the DT fusion reaction to take place, and, even during the “burning” phase with self-heating, to stabilize the plasma by localized deposition of energy. For ITER, three heating systems are foreseen in order to optimize the plasma scenario: Ion cyclotron resonance heating (ICRH), electron cyclotron resonance heating (ECRH) and negative ion based neutral beam injection (NNBI). While ICRH and ECRH use electromagnetic radiation to deposit energy in the ions and electrons of the plasma at the respective resonance frequencies determined by the magnetic field, NNBI injects high-energetic neutral fuel atoms, which are generated by first producing negative ions in a Caesium atmosphere, which then are accelerated and neutralized before getting injected into the plasma. The reason for this multi-step approach is that the penetration depth of injected ions is very limited due to the magnetic field confining the plasma.



This can be overcome by using neutral atoms, which make their way deeper into the plasma before getting ionized. All the three heating systems for ITER now are in an advanced state of preparation. The goal for DEMO, in order to reduce complexity, is working with one heating system only. Given the drawbacks of NNBI (huge wall openings required vs. tritium confinement) and ICRH (trade-off between size of the antenna structures and sputtering effects), ECRH today seems to be the most promising heating system for DEMO.

### **4.3 First Wall and Plasma-Wall Interaction**

The plasma particles, ions and electrons, move along the magnetic field lines inside the confinement. Nevertheless, a certain fraction crosses the confinement border, still following a spiral trajectory and moving towards the intended exit point, the divertor. Even in normal operation, a small fraction of the plasma exhaust particles though hit the wall of the vacuum vessel, and this fraction can become large locally in the case of off-normal events, entailing sputtering and degradation of the wall facing the plasma, the so called “First Wall”. In former plasma-physics experiments, carbon as a low-Z element that will be fully ionized in the plasma, and thus will not emit electromagnetic radiation from electronic state transitions, had been the material of choice for the First Wall. The presence of tritium in real fusion reactors, however, prohibits the use of carbon due to the possibility of forming tritiated hydrocarbons. For ITER, a different low-Z element, beryllium, thus had been selected and tested in JET. As Beryllium unfortunately is toxic for a part of the population, there are now considerations to immediately move to the First Wall material that will have to be used for DEMO and fusion power plants anyway, tungsten – a choice that is dictated by the sputtering and heat resistance of the material.

### **4.4 Power & Particle Exhaust – the Divertor**

A fraction of the plasma particles will regularly leave the confinement and move, still affected by the magnetic fields, parallel to the walls of the toroidal vessel to the intended exit point, the divertor. This depletion (and replacement with new fuel) is necessary to remove impurities as well as the helium “ash” of the fusion reaction. The divertor is a ring-shaped component at the bottom of the torus-shaped plasma vessel, consisting of the inner and outer target plates, the dome which inhibits back-diffusion of the neutralized particles into the core plasma before they can be pumped away, and a supporting structure. The highly energetic plasma particles will hit the target plates, releasing their

kinetic energy. Thereby these plates will have to sustain heat loads of up to 20MW/m<sup>2</sup>. For ITER, a solution has been developed using tungsten “monoblocks” enveloping a water-cooled copper-chrome-zirconium alloy tube, with the joining of the monoblocks and the tube being a particular challenge. To limit the heat load, and also the sputtering damage caused by highly-energetic plasma ions, divertor “detachment” is considered as a solution. By injecting suitable material (e.g., noble gases or nitrogen) into the plasma exhaust stream, neutralization and energy dissipation by electromagnetic radiation can be achieved spreading the heat load over a larger area. This is being intensely studied for DEMO, along with improved divertor geometries and materials combinations. A Divertor Test Tokamak (DTT) is currently under construction at Frascati, Italy.

## 4.5 Plasma Diagnostics & Control

For stable and reliable operation of the plasma and thus the entire plant, the status of the plasma has to be monitored and controlled through the different phases, i.e., the ramp-up, the flat-top and the ramp-down, referring to the plasma temperature and current, respectively. From previous plasma physics experiments, quite a number of diagnostic techniques have been developed to detect the position, density and temperature distribution of the plasma, the plasma current as well as impurities, magneto-hydrodynamic (MHD) effects and instabilities. Many of these detect electromagnetic radiation (IR spectroscopy, bolometry, reflectometry, polarometry, ...) and fields. Exhaust gas analysis complements the in-vessel sensors to evaluate the plasma gas composition and impurity content. For a neutron emitting fusion plasma, neutron and gamma detection and determination of the local reaction rate is important in addition.

The actors to react to the sensor signals, to maintain the plasma and steer it in the desired way, are the heating (and current drive) systems allowing the localized deposition of energy, as well as the fueling systems (gas or – frozen – pellet injection) as well as in-vessel magnet coils – besides the central solenoid and the poloidal field coils.

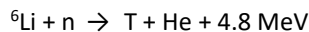
For ITER, there is an ongoing exercise to determine which sensor heads, mirrors, transmission lines etc. can withstand the neutron exposure at least for a reasonable time span, or how this can be extended. For DEMO, clearly the challenge is to develop control scenarios which can work with a severely reduced inventory of sensors suited for a harsh neutron environment – or can work in sufficient distance to it.

## 4.6 Deuterium-Tritium Fuel Cycle

ITER and DEMO rely on the D-T fusion reaction, which requires the operation of a closed tritium cycle because of the radiotoxicity of this hydrogen isotope. Tritium has a half-life of slightly more than 12 years and can easily substitute protium (usual hydrogen) in water. 1µg of tritium incorporation (as water or in aerosols) comes close to the occupational limit of 20mSv per year, and is well above the exposure limit of 1mSv per year for the general public. The technology for the ITER fuel cycle has been developed and is now being transferred to industrial scale; it relies on cryo-pumping, purification and isotope separation processes which have to be operated with a certain inventory each. As the tritium throughput for DEMO will have to be about two orders of magnitude higher than that of ITER (power and duty cycle scaling), extrapolation of the ITER processes is not possible. Assuming an (optimistic) tritium burn-up fraction of 2 %, the overall tritium inventory in the systems could easily pile up to ~15 kg, and even more, if the burn-up fraction is lower. This would present a serious obstacle to licensing. Thus, new processes have to be introduced, and are already under development. One major advance will be replacing the discontinuous cryopumping by continuous processes using mercury pumps. Another breakthrough is expected from the application of membrane processes for “Direct Internal Recycling”, i.e., re-directing ~80 % of the unburnt deuterium and tritium from the plasma exhaust directly back into the plasma, while the helium and other impurities to be removed stay in the remaining exhaust gas stream which will go to the purification and separation systems, thus reducing the tritium load and inventory there in proportion.

## 4.7 Tritium Breeding Blanket

ITER will receive external tritium supply, which can be provided from the tritium production in CANDU type reactors. For DEMO and subsequent fusion power plants, after having been equipped with a tritium start-up inventory of a few kg, tritium self-sufficiency is mandatory, also limiting the transportation risks for the hazardous nuclide. This can be achieved by so-called tritium breeding blankets around the plasma, but inside the vacuum vessel, making use of the reaction:



Theoretically, each neutron produced by a D-T fusion reaction thus can generate a new tritium atom. In reality, however not the entire area of the plasma facing wall can be occupied by blankets. Moreover, the blankets require structural materials. Thus, many

neutrons undergo nuclear reactions or are absorbed within matter not contributing to tritium breeding. Hence, neutron multiplication is necessary to compensate for this. As neutron multiplier materials, beryllium (or Be-rich compounds) or Pb are being considered. In the European fusion program, two combinations are being developed for DEMO, i.e., the so-called liquid breeder, an eutectic mixture of lithium and lead which will be pumped through the blanket structure, and the “solid breeder” variant consisting of lithium ceramics pebble beds surrounded by  $\text{TiBe}_{12}$  structures. For both approaches, test blanket modules are foreseen in ITER.

Beyond breeding tritium, the breeding blanket has the equally important function of transferring the heat generated by the neutron moderation and the nuclear reactions to a suitable primary coolant at a high temperature level for conversion into electricity. In the European program, two coolant options are being developed, i.e., water and helium. The water variant is deemed to be more mature because of the experience from the PWR plants. Nevertheless, radiation-induced chemistry will be different because of the different neutron energy spectrum with much higher energies in fusion. Moreover, the PWR range of 285 °C - 325 °C actually is not compatible with the operation temperature range of the structural material so far developed for fusion, EUROFER, which is between ~ 350 °C - 550 °C as discussed below. Helium can exploit the full range of this temperature window, giving access to higher efficiency due to the higher temperature level and the higher temperature rise - even though, as a compressible medium with less heat capacity than water, it will need higher pumping power -, and will avoid any coolant chemistry problems. However, components cannot be bought off the shelf but will have to be developed, while prototype facilities already exist.

Last but not least, another important function of the breeding blanket is shielding the superconducting magnets behind the vacuum vessel from the fusion neutrons.

## 4.8 Neutron-Resistant Structural Materials

The D-T fusion reaction intrinsically produces neutrons of 14.1 MeV energy. This is an order of magnitude higher than in “fast” fission reactors and much higher than the average neutron energy in water-moderated reactors. Hence, different damage rates and damage mechanisms in the exposed materials and components inside the plasma vessel (breeding blanket, divertor) have to be considered. Similar to fission neutrons, fusion neutrons cause displacement damage, i.e., displacement cascades propagating from the primary knock-on atom through the material, with the consequences being proportional to the deposited neutron energy. The exposure level is measured in “dis-

placements per atom" (dpa). A single neutron can cause, depending on the deposited energy, thousands to millions of displacements, with most of them relaxing to the original or an equivalent lattice position still within the propagation time of the cascade. Nevertheless, the remaining displacements accumulate. Furthermore, the neutrons can react with the nuclei of the structure, resulting in transmutation and activation. In transmutation reactions, light nuclei (H, He) are ejected; the resulting atoms can be trapped at grain boundaries and cause embrittlement. Activation reactions cause radioactivity, which has to be limited to the minimum possible level and should decay fast to definitely avoid the need for a long-term repository.

Given the fact that the activation of pure iron under fusion conditions will entail a decay time of ~100 years until recycling will be possible, the reduced-activation ferritic-martensitic steel EUROFER has been developed, avoiding / replacing alloy elements which could generate radioactive nuclides with long decay times like Ni. The material is well characterized with fission reactor neutrons, resulting in an operation temperature range from 350 °C to 550 °C under neutron irradiation. Below this range, irradiation embrittlement will move the brittle-to-ductile transition to values above room temperature, and yield strength and creep resistance will decrease significantly. Developments on alternative steels for a lower (water cooling) or a higher temperature range (helium cooling) are ongoing, yet neutron irradiation results so far are preliminary only. In general, the lack of the possibility of material irradiation with a fusion-relevant spectrum, i.e., 14 MeV neutrons, at substantial flux is an obstacle in the development and qualification of materials for the blanket and the divertor. To overcome this, construction of an accelerator-based neutron source, "DONES", has now been started at Granada, Spain. Still, it will take about 10 years until neutron exposures can start there and the necessary neutron dose rates can be accumulated.

As an estimate, the most exposed part of the breeding blanket will accumulate 20-30 dpa per year, depending on the layout of the power plant. The neutron resistance will determine the lifetime of the component in the reactor and hence the economic viability (see below).

## **4.9 Plant Logistics and Remote Maintenance**

Due to the neutrons produced in the fusion reaction, the components in the plasma vessel will become activated, and will require remote handling for maintenance and exchange. For ITER, this concerns the divertor elements at the bottom of the reactor vessel, as well as the First Wall panels covering it at the inside. These operations will be

provided by dedicated equipment that will access the inside of the vessel through ports, i.e., openings in the vessel usually closed by port plugs. Further port plugs serve as inserts for test modules for breeding blanket systems, and for the diagnostic equipment needed. As the port plugs “see” the fusion neutrons, their exchange has to be done by remote maintenance, too.

While the divertor and (few) port operations for DEMO could be very similar to those for ITER, the situation with the breeding blankets is completely different. Here, we have components of steel, filled with breeder and neutron multiplier materials, which, because of the stopping length of the neutrons, will be 1–1.5 m thick. Single sectoral, banana-shaped elements will weigh tens of tons. The current plan is to exchange them by lifting them through ports at the top of the vessel. Alternatively, there could be smaller compartments, reducing the payload for the remote handling system, however increasing substantially the number of pipe connections which have to be opened and re-welded. The development of a suitable, licensable remote maintenance system for DEMO, and the necessary tools, still represents a major challenge.

The duration and efficiency of these operations, in relation to the in-vessel lifetime of the components, will have a major impact on the availability of DEMO and any subsequent power plant. Thus, similarly to increasing blanket and divertor lifetime as much as possible, efficient, well-coordinated remote maintenance operations are key to the overall efficiency of the plant. To this end, an intelligent, integrated planning of the individual remote maintenance operations, taking into account the availability of tools, space requirements, pathways between the reactor vessels and the hot cell, storage space and operators, i.e., an integrated plant logistics model, has to be developed to allow rigorous optimization.

## **4.10 Energy Conversion - Balance of Plant**

As already mentioned, electricity generation from fusion is not just an extrapolation from fission. The pulsed operation (pulses of several hours with dwell times of 10-15 minutes are targeted for DEMO) will necessitate intermediate heat storage. Currently, molten-salt systems with different parameters for water or helium as the primary (blanket) coolant are being considered, with water, offering the lower temperature shift, requiring the larger storage. Complementary, and with the aim to reduce the intermediate storage requirement, steam turbines that would allow operation with changing load levels are under consideration. In any case, the dynamic behaviour of such combined conversion systems for the different load cases has to be understood. To

this end, pilot facilities for the two different primary coolants are under construction at Brasimone, Italy, and Karlsruhe, Germany. Furthermore, the blankets are not the only source of heat. Other sources are the divertor and the plasma heating systems (with the part of their energy consumption that is not sent to the plasma), of course at different temperature levels. It is a challenge to integrate these into the overall conversion cycle - as is the electricity supply for the different plant systems, e.g., the cryo-plant, the magnets and again the heating systems.

Once the stellarator concept will be mature enough to be developed into a power plant, the need for an intermediate heat storage may lose importance or may even disappear. Still, intermediate transfer to a secondary coolant will be necessary to avoid tritium diffusion and/or radiolysis products migration into the conversion systems.

#### **4.11 System Engineering and Plant Integration**

As shown so far, a fusion reactor / power plant will consist of quite a number of components / systems with different functions, each of them with a parameter range for operation with optimum and limiting values, in quite some cases depending on the material choice (breeding blanket, divertor, first wall, magnets, sensor and actuator systems). These components will not operate in isolation, but there are numerous interfaces between them, thus also relating the respective operation conditions and the performances. The system engineering task for DEMO and subsequent fusion power reactors first of all is to systematically understand the interfaces among the different components and their mutual impact, and to develop tentative, conceptually integral plant designs. At the appropriate level of maturity and characterization, this in the first place will lead to favourable technology choices.

Once the choices are made, the different components have to be integrated into a detailed, viable plant design. This will be supported by the development of a system code integrating the models of the components and their interactions into a single, powerful software tool for the optimization of the overall design and parameter choices. The development of such tool is already being addressed in the European program.

#### **4.12 Plant Safety & Licensing**

Licensing of ITER, DEMO and any subsequent fusion power plant will require an encompassing safety demonstration. Above all, the confinement of radionuclides, in particular tritium, has to be guaranteed for operation and maintenance as well as for management

and intermediate storage of radioactive waste. The most important first operational static confinement barrier is the vacuum vessel with its port extensions, but according to the defense-in-depth principle, further static and dynamic confinement barriers need to be implemented. An exhaustive set of accidental scenarios with lead cases enveloping minor accidents/incidents, and the corresponding protection measures, have to be defined. However, the latter are highly dependent on the design options chosen, so at present a design analysis is performed based only on the SSG guidelines formulated by the IAEA.

The licensing exercise for ITER so far has shown that transferring nuclear fission based regulations to a fusion plant might not be adequate due to differences in physics and hazard potential. Fission licensing regulations are adapted to risks that do not exist in fusion, in particular power escalations caused by reactivity events associated with potential consequences of the release of a high radionuclide inventory, which also is not given in the case of fusion. Using this framework for fusion would entail setting wrong priorities. Instead, an adapted licensing framework for fusion plants will have to be developed. This is already being actively addressed in the US and the UK; the IAEA has started a related initiative, and also in Europe and in Germany there are signals that the need for a specific fusion licensing framework has been understood at the political level.

## 5 Summary

There are many technical challenges on the way to fusion power. Among these, the interplay and integration of the different subsystems into one coherent plant design probably is the biggest one. All the areas where specific solutions are required are being addressed now within the European fusion program, of course, at different levels of maturity. At present, the finalization of the solutions required for ITER has priority. Nevertheless, in the sense of early deployment of fusion, other aspects like fusion-neutron-resistant materials or the tritium breeding blanket, must not be neglected. A specific licensing framework for fusion plants will be necessary.



# International Fusion Materials Irradiation Facility - Demo Oriented NEutron Source (IFMIF-DONES)

## A unique research infrastructure

*Christoph Kirchlechner, Dirk Radloff, Hans-Christian Schneider, Frederik Arbeiter, Dieter Leichtle, Sebastian Ruck, Klaus Hesch and Anton Möslang*

*Karlsruhe Institute of Technology, Karlsruhe, Germany*

### Abstract

IFMIF-DONES is a groundbreaking facility designed to test and qualify materials capable of withstanding the extreme conditions generated by deuterium-tritium (D-T) fusion, particularly the intense neutrons of the D-T reaction in future fusion power plants. Utilizing a deuteron beam and a liquid lithium target, the facility will produce a high flux of neutrons with an energy spectrum closely resembling the 14.1 MeV neutrons of D-T fusion. This will, for the first time, enable the irradiation of structural materials in fusion relevant damaging conditions for comprehensive testing and qualification. Since spring 2023, the construction of IFMIF-DONES has been underway in Granada, Spain, as part of the European Strategy Forum on Research Infrastructures (ESFRI) roadmap. This facility will serve the fusion research community, industry and regulatory bodies, enabling material irradiation and characterization and thus will be a backbone for the safe operation of fusion power plants. The ability to irradiate materials with fusion-relevant neutrons at IFMIF-DONES, coupled with subsequent characterization at KIT's Fusion Materials Laboratory, represents an indispensable step forward for Germany and Europe in the development of a safe and independent energy source based on fusion technology. This article briefly describes the importance of IFMIF-DONES for fusion research.

## Preface

Prof. Robert Stieglitz was an exceptional pioneer and a determined promoter of IFMIF-DONES. With remarkable vision and unwavering integrity, he played a pivotal role in advancing the planning, application, and realization of this groundbreaking facility. As a true bridge-builder between science and politics, he forged alliances and played a leading role in submitting the successful proposal for IFMIF-DONES to the Helmholtz Roadmap for Research Infrastructures. His mentorship and foresight profoundly shaped the careers of several scientists connected to the project, offering guidance and encouragement throughout its multifaceted preliminary phases. His premature passing leaves an irreplaceable void, but his legacy remains: the memory of a great person and visionary who lived for the future with honesty and passion.

With this article – which is based on a current proposal for funding Germany’s contribution to IFMIF-DONES – we commemorate the tireless dedication of Prof. Robert Stieglitz. He enabled numerous scientific projects through his visionary yet meticulously thought-out ideas, passed on his approach to science to the next generation through mentoring, and inspired as a person with his unique character. His example guides and inspires us.

## Introduction

Structural materials and functional materials, capable of withstanding unprecedented neutron radiation conditions and thermal power densities during plasma operation in a fusion reactor, have been the focus of worldwide research for decades. Understanding the degradation of materials and components caused by the 14.1 MeV neutrons of the fusion reaction is indispensable for design, licensing, operation, and safety of future fusion reactors. The International Fusion Materials Irradiation Facility - Demo Oriented NEutron Source (IFMIF-DONES) is a dedicated facility for the qualification and validation of materials for deuterium-tritium (D-T) fusion. IFMIF-DONES' primary mission is to produce fusion-like neutrons which are not available by any other irradiation facility, with the intensity necessary for materials qualification. IFMIF-DONES is being built since March 2023 in Granada, Spain, as a worldwide unique project on the European Strategy Forum on Research Infrastructures (ESFRI) Roadmap. It will produce high-energetic neutrons at sufficient intensity with a fusion specific spectrum in a reasonably large irradiation volume, in order to timely generate the most significant and critical elements of a materials database for characterization of materials for use in D-T fusion reactor in-vessel components. The intended German contribution to IFMIF-DONES aims at the

development, qualification and on-site delivery of critical components as in-kind contribution, as well as at the preparation of the German fusion community for exploiting the materials irradiated by IFMIF-DONES during its operation (see Fig. 1).

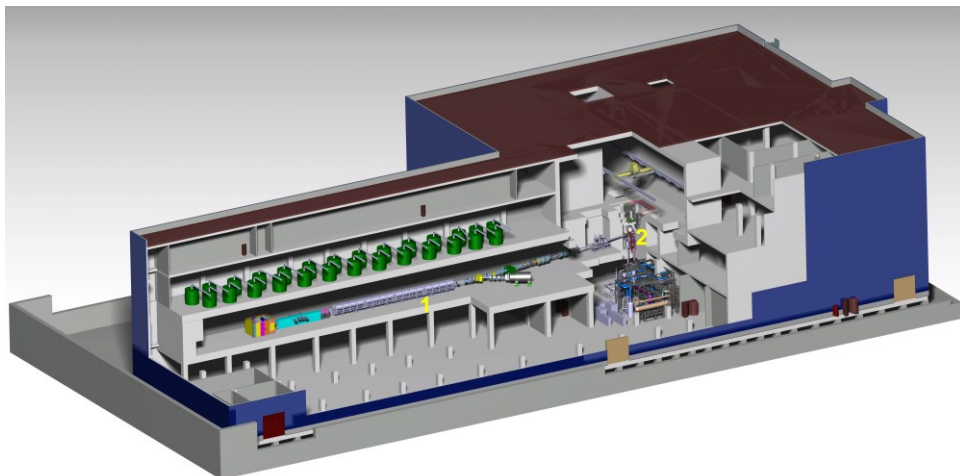


Fig. 1: Artist's view on the IFMIF-DONES main building with accelerator (1) and Test Cell (2), comprising the planned German contributions Lithium Target, High Flux Test Module (HFTM), and the Start-up and Monitoring Module (STUMM), [1]

## Why is IFMIF-DONES indispensable?

The success of future fusion power plants including ecological and economic criteria (such as availability, performance, and safety) strongly depends on the maturity and availability of the necessary fusion reactor materials. Large irradiation databases have been collected for several candidate materials from experiments in material test fission reactors (MTR) and accelerator-driven facilities. But the experiments performed until today have a major drawback specifically for structural materials: neither the achieved neutron fluence (total number of neutrons per unit area) nor the neutron energy spectra obtained are sufficiently representative to the expected conditions in a D-T fusion reactor. Material damage and property changes caused by different neutron spectra show both similarities and key differences. Neutron irradiation leads to two main effects: the formation of microstructural defects, such as dislocation loops, and the generation of transmutation products like He and H atoms. Transmutation is a complex function of the neutron spectrum and microstructural defects depend sensitively on the temperature history.

Elastic collisions result in displacement defects in the lattice (measured in dpa, displacements per atom), and subsequent obstacles to dislocation movement through the lattice. Fusion and fission neutron spectra exhibit very similar behaviour in terms of displacement effects, because the high energy primary knock-on atoms generated by fusion neutrons dissipate their energy in subcascades. Hence, neutron irradiation in fission MTR represents fusion conditions very well in terms of crystal defects like dislocation loops created in the lattice (see Fig. 2). Therefore, DEMO (Demonstration Fusion Power Plant) “baseline” materials have been and will continue to be irradiated worldwide in MTRs up to typical neutron fluences.

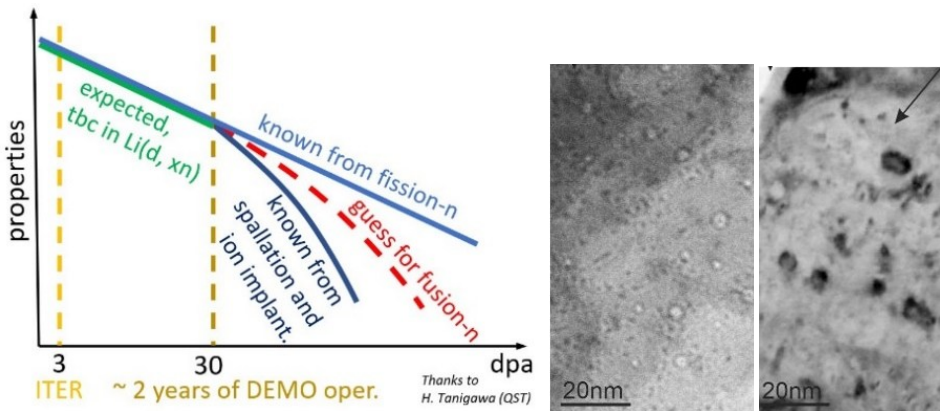


Fig. 2: Qualitative comparison of physical properties' degradation due to fission and fusion neutrons (redrawn after [2] and [3]). Note the logarithmic axes in this plot; voids (center) and dislocation loops (right) in irradiated W [4].

In inelastic collisions, transmutation products are generated. Particularly, the gaseous products He and H are of utmost importance for the degradation of fusion materials. Generation rates per dpa, i.e. He [appm/dpa] and H [appm/dpa], are widely used measures to distinguish and quantify the effects of different spectra. The high energy of 14.1 MeV D-T fusion neutrons compared to fission neutrons (typically < 3 MeV) leads to significantly higher gas production rates, as more absorption channels open up and the respective gas production cross sections increase with energy. Currently, there is no facility providing DEMO-relevant material data on inelastic collisions. Consequently, quantifying the effect of He/dpa and H/dpa ratios on material properties and material qualification is the main aim of IFMIF-DONES.

To be more specific: For Fe (and hence steels as the reference structural material), the He generation rate for a fusion first wall n-spectrum is around 10 appm/dpa, which is

approximately 40 times higher than for fission neutrons. This additional helium results in accelerated material embrittlement and enhanced material degradation by various mechanisms (e.g., bubble formation, and segregation to grain boundaries). Even more challenging is that the effect of transmutation helium on material properties strongly depends on the irradiation temperature, often exhibiting threshold limits as well as extremely steep gradients with respect to both irradiation temperature and He concentration. These changes in material property (e.g., severe embrittlement, dimensional changes, or reduced resistance to loads or load fluctuations) are well established through various experiments, including ion-irradiation in thin films, fission irradiation with doped materials to simulate He-effects, and spallation neutron irradiation. These findings are further supported by modelling and analyses. However, such results are “indicative”, as none of these experiments is fully representative or capable of generating reliable and validated data. The gaseous transmutation effects, in particular He formation in reduced activation ferritic-martensitic (RAFM) steels, and H formation as an additional threat for welds, drive the need for an intense fusion specific neutron source.

In summary, neutron damage in a MTR is not representative for the expected damage caused by 14.1 MeV neutrons of the D-T fusion reaction. Under a wide variety of typical operation conditions, data from fission irradiation are non-conservative in terms of material degradation and typically serve only as first estimates for conceptual design activities. However, nuclear license processes for fusion power plants must not be based on them. Consequently, there is unequivocal agreement in the fusion community that an intense, fusion-relevant neutron source for materials characterization is an essential pillar in fusion roadmaps<sup>1</sup> (see Fig. 3) and a historical gap to be overcome now.

## **The road to the accelerator-based facility IFMIF-DONES**

Before fusion plants can be operated, material properties and their potential degradation in service have to be understood as widely and deeply as possible, i.e. “qualified” and “validated”. Since the 1980s, several high-ranking international advisory boards evaluated a variety of neutron source proposals, including accelerator driven sources, beam plasma driven sources, and ion driven rotating target sources. They concluded that a dedicated accelerator driven Deuteron-Lithium source was the only reasonable option to meet the mission, taking into account criteria such as safety, technical maturi-

---

<sup>1</sup> See for instance <https://euro-fusion.org/eurofusion/roadmap/>

ty, (economic) viability, environmental acceptability, and last but not least, the quality of the neutron spectrum for generating material damage.

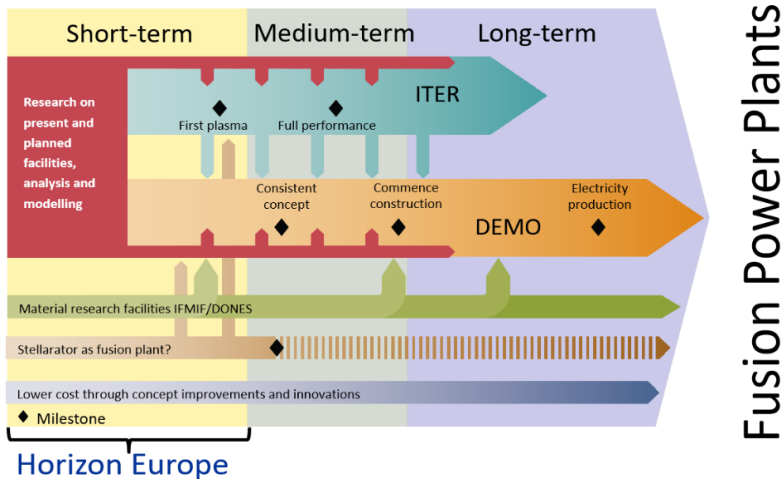


Fig. 3: Roadmap towards fusion electricity [5]

Since 1995, an International Fusion Materials Irradiation Facility (IFMIF) has been promoted and advanced under the umbrella of the International Energy Agency (IEA). The current IFMIF-DONES (Demo-Oriented NEutron Source) design is strongly based on the ideas and designs that have been developed since 2007 in the framework of the Engineering Validation and Engineering Design Activities (IFMIF/EVEDA) as part of the EU-Japan Broader Approach (BA) agreement. In each step, from pushing the idea of IFMIF through its detailed definition and its implementation within the IEA, the process and progress has been guided or led by KIT experts.

Only IFMIF-DONES will provide the calibration and final validation of material's response under 14.1 MeV neutrons, close gaps in current knowledge, reduce uncertainties and identify possibly new phenomena. The urgent need to construct and operate IFMIF-DONES is based on its impact on the design and construction of a fusion power plant, such as DEMO: Qualified data of fusion neutron tolerant materials are required in the final engineering phase and before licensing at the latest. I.e., IFMIF-DONES needs to come into operation ~ 15 years before any fusion power plant can start its operation.

## **The research fields and objectives of IFMIF-DONES**

IFMIF-DONES is designed to serve the fusion ecosystem by addressing the following research fields and objectives:

- Qualification of reference and candidate materials for fusion power plants;
- Generation of engineering data for design, licensing and safe operation of any fusion power plant, such as the EU-DEMO;
- Completion, calibration and validation of existing databases (mainly generated from MTR);
- Deepening of the fundamental understanding of radiation response of materials;
- Verification of material degradation models.

Besides, IFMIF-DONES will provide irradiation volumes and experimental areas which on the long term can be exploited for complementary scientific (e.g. nuclear physics) and nuclear medical (e.g. Mo-99 production that today is, to our knowledge, done in five fission reactors worldwide only) programs.

## **The objectives of the German contribution to IFMIF-DONES:**

The planned German contribution to IFMIF-DONES-D shall ensure two key aspects, and accordingly has two primary objectives:

- (i) Development and qualification of critical components for the accelerator-driven IFMIF-DONES neutron source as well as the provision of in-kind contributions for the IFMIF-DONES facility currently under construction in Granada, Spain;
- (ii) Build-up of high throughput scale bridging post-irradiation examination facilities for qualification of materials for fusion power reactors, irradiated by fusion-like neutrons. As the anticipated operational phase of IFMIF-DONES (with a foreseen start of operation in 2034) is at least 20 years, a significant participation in the continuous harvesting of the irradiation data of IFMIF-DONES will secure long-term international relevance, visibility and capabilities of the German fusion ecosystem and particularly research, qualification, validation and nuclear licensing of fusion materials.

## Outlook

At the time of writing, IFMIF-DONES is under construction in Granada, Spain, while the contributions of numerous European partners are increasingly taking shape. This also applies to the German contribution, which is currently being further specified at the technical level. Intensive efforts are also being made to secure financing for the German contribution to IFMIF-DONES.

## References

- [1] IFMIF-DONES 2024
- [2] H. Tanigawa et al., Journal of Nuclear Materials 417 (2011) 9-15
- [3] J. Knaster et al., Nuclear Fusion 57 (2017) 102016
- [4] M. Kimenkov et al., Journal of Nuclear Materials 592 (2022) 154950
- [5] <https://euro-fusion.org/wp-content/uploads/2022/10/Roadmap-illustrated.pdf>, 16.01.2025



# Creep-fatigue assessment of breeding blanket components

*Roshan Rajakrishnan<sup>1</sup>, Mathias Jetter<sup>1</sup>, Guangming Zhou<sup>2</sup> and Jarir Aktaa<sup>1</sup>*

<sup>1</sup> *Institute for Applied Materials, Karlsruhe Institute of Technology, Germany*

<sup>2</sup> *Institute for Neutron Physics and Reactor Technology, Karlsruhe Institute of Technology, Germany*

## Abstract

The breeding blanket components of future fusion reactors are expected to operate at extremely high temperatures due to the heat generated by the plasma. Under such conditions, creep-fatigue becomes a critical failure mode influencing the lifespan of these components, which are made of the structural material EUROFER97 and are subjected to irradiation and cyclic thermo-mechanical loading. To ensure the safe operation of fusion reactors, the design and evaluation of components must account for creep-fatigue damage.

The Creep Fatigue Assessment (CFA) tool developed at KIT facilitates this process by automating the application of various design standards, including those from the ASME BPVC, RCC-MRx, and DDC-IC. The CFA tool provides a fast and reliable method for evaluating finite element models of components within ANSYS. Through elastic and elastic-plastic thermo-mechanical analyses, creep-fatigue assessments are conducted on several first wall and other breeding blanket components, considering operating conditions and hold times.

By applying both elastic and inelastic design rules, critical regions in these components are identified. The creep-fatigue assessment is then used to estimate the maximum allowable cycles, according to each design standard.

**Keywords:** Creep-fatigue, design rules, breeding blanket, first wall

# 1 Introduction

The design of in-vessel components in future fusion reactors, made of the reduced activation ferritic-martensitic steel EUROFER97, need to be assessed regarding a range of failure modes. Due to significant thermo-mechanical loads throughout operation cycles, fatigue and creep might cause failure. The start-up and shut-down of a cycle cause fatigue damage, whereas loading during operation time leads to creep damage. A creep-fatigue interaction occurs when both types of damage occur together within a cycle. The assessment of creep-fatigue interaction is covered in two established design codes, RCC-MRx code [1] and ASME BPVC code [2], as well as in the EUROfusion document for Demo Design Criteria for In-vessel Components (DDC-IC) [3].

To automate the complicated and time consuming procedure for creep-fatigue assessment using the aforementioned criteria, a tool in form of a post-processing code for ANSYS [4] finite element (FE) models was developed. The idea and the use of CFA tool is already presented in multiple papers [5-7]. In this work, the CFA tool is applied to several designs of first wall (FW) components of a fusion reactor to evaluate and identify their susceptibility to creep-fatigue damage. Section 2 gives a brief overview of the CFA tool functionality. Section 3 presents and discusses the simulation results and CFA of components. Finally, conclusions are drawn in Section 4.

# 2 Creep-fatigue assessment

These codes prescribe two routes for carrying out creep-fatigue assessment. One is based on an *elastic* finite element simulation of a component model, the other is based on an *elastic-plastic/viscoplastic* (inelastic) simulation model. For the elastic route only one loading need to be simulated as shown in Figure 1, without any material data for plastic or creep behavior.

Primary loads (P) are mechanical in nature, while secondary loads (Q) are thermal. Analyses for primary (P) and for primary plus secondary (P+Q) loadings are performed separately, where static loadings are applied with a linear ramp (only one step). The current implementation of the CFA tool considers a cold cycle, where it is assumed that both the mechanical and thermal stresses occur anew each time. Loading per cycle is composed of changes in both the primary and secondary stresses.

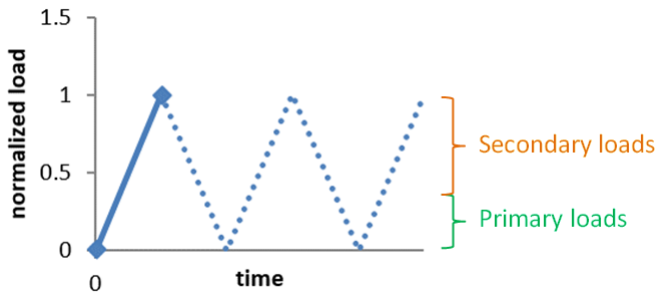


Figure 1: Schematic of cyclic loading for the elastic route

In the inelastic route the simulation model contains material models for cyclic plasticity and creep, which allows the calculation of stresses and strains and their evolutions during an entire cycle. Figure 2 illustrates a cycle as considered by the inelastic route. As the equivalent stress range reaches extremely high values in the first cycle, it is recommended to run several cycles and pick a more representative cycle which, particularly for the assessment according to the RCC-MRx rules, needs to be a stabilized one.

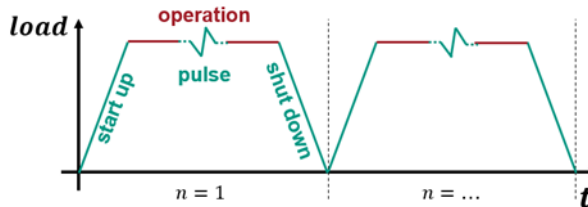


Figure 2: Schematic of cyclic loading for the inelastic route

## 2.1 Influence of ceramic breeder

Reduction of fatigue life time due to contact between EUROFER97 and ceramic pebbles at 550 °C was studied by Aktaa et al. [8], providing the means to calculate the number of cycles to fatigue failure based on aging duration and loading strain range, see Table 1. Currently, data is limited to an aging duration of 128 days. As no significant difference is seen between 64 and 128 days [8], the values for 64 days are used in this work.

Table 1: Parameter determined for the investigated strain ranges [8]

Strain range [%]	$N_{f,0}$	$b$ [1/d]
0.6	2833	0.02744
1.0	833	0.0206
1.6	310	0.0126

The following formula is used to calculate the reduced allowable number of cycles in the fatigue part of the creep-fatigue interaction:

$$N_j = N_{j,0} \exp(-bt) \quad (2-1)$$

with  $t$  and  $b$  denoting the aging time and the fitting parameter, respectively.

## 2.2 Requirements

Before the creep-fatigue assessment of the elastic route of RCC-MRx code can be used, some requirements against *Progressive deformation* (Level A criteria) must be checked. This is done with the following equations:

$$P_1 \leq 1.3 * S_m \quad (2-2)$$

$$P_2 \leq 1.3 * 1.5 * S_m \quad (2-3)$$

$$P_3 \leq 1.3 * 1.5 * S_m \quad (2-4)$$

These effective stresses are referred to as  $P_1$ ,  $P_2$  and  $P_3$  in the result tables. More details about the calculation are given in [9,10].  $S_m$  is the maximum allowable stress. As an alternative to the above equations, the so-called *3Sm rule* can be applied. It is defined as follows:

$$\text{Max}(\overline{P_L} + \overline{P_b}) + \overline{\Delta Q} \leq 3 * S_m \quad (2-5)$$

The check for requirements against *Progressive deformation* is implemented in the CFA tool. If a requirement is not met, the CFA tool normally does not start the creep-fatigue assessment at all but issues a corresponding error message. In the context of this work, the restrictions were relaxed somewhat in order to obtain more precise details about the level of effective stresses.

## 2.3 Material data

The structural material is primarily EUROFER97. The material's Young's modulus, density and thermal expansion necessary to describe the thermal and elastic material properties in FE simulations are taken from the RCC-MRx [1]. Material models describing inelastic deformation in ANSYS are prescribed by DDC-IC, which include a) plasticity laws of Chaboche kinematic hardening and Voce nonlinear-isotropic hardening law, and b) creep law of Modified Time Hardening (MTH), which describes primary creep deformation. Material data required for performing the CFA is sourced from RCC-MRx for its elastic and inelastic routes. For ASME and DDC-IC, the data from DDC-IC is used.

## 3 Creep-Fatigue assessment simulation models

In the following sub-sections, the simulation models in the framework programs FP8 and FP9, and the Prototypical Mock Up (PMU) of the First Wall are analyzed with the CFA tool. The models are so large (element number) that an analysis of entire areas was too time-consuming. Therefore, only cross-sections were examined, which can, however, be regarded as largely representative. The elastic route uses stress linearization to assess the compliance of component stresses with design rules. Stress linearization [11] is a technique used in FEA programs like ANSYS to convert complex, nonlinear stress distributions extracted along a user-defined path through the component thickness into simpler components (membrane, bending, and peak stresses) for assessment. For the chosen set of two geometric entities (nodes, edges, or surfaces) at either ends of component thickness, the CFA tool automates path creation using the algorithm described in [5]. In contrast, the inelastic route only analyses individual spots in the component.

The names of the columns in the following tables of the evaluation will be briefly explained. Path  $n^0$  indicates the numbers given to the path built for the assessment with the help of the elastic route of RCC-MRx code. The node numbers, node  $n^0$ , from the respective model are therefore used there.  $N_f$  indicates the number of cycles to failure considering the interaction of creep and fatigue damage. If the influence of ceramic pebbles from the breeder on EUROFER97 is taken into account, the notation is extended to  $N_{f,CerBre}$ .  $T_{max}$  denotes the highest temperature during the representative cycle either along the path (elastic route) or at the respective node (inelastic route).

### 3.1 Fuel-breeder pin

Creep-fatigue assessment was carried out on two subsequent versions of the cladding of the fuel-breeder pin [12], which are referred to according to the framework program (FP8 and FP9) in which they were created, see Figure 3.

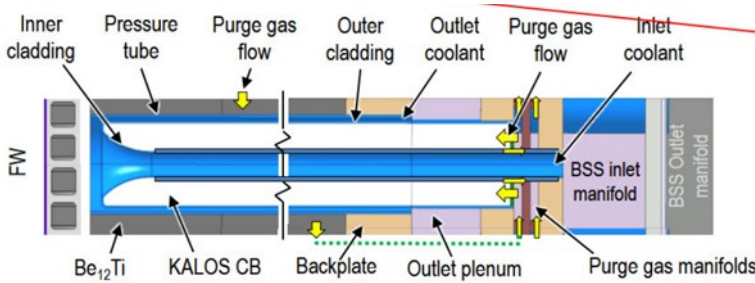


Figure 3: Fuel-breeder pin concept [12]

Thermo-mechanical loading of claddings comes from volumetric heating during operation and the associated thermal expansion, and gas pressure surrounding the pin. Purge gas flows inside the pin, between the inner and outer cladding. Outside the pin, the coolant helium gas flows between the outer cladding and the pressure tube with a pressure of 8 MPa. For the FP8 model two configurations for the purge gas pressure namely 0.2 MPa or 8 MPa were considered. For the FP9 model only a purge gas pressure of 8 MPa is considered. The region of interest for carrying out creep-fatigue assessment within the cladding of a pin is the curvature, which connects the inner and outer cladding. Especially in FP8 where the inner cladding is thicker than the outer cladding, the thickness transition within the curvature leads to stress concentrations there (see Figure 4). Though FP9 no longer has a difference in thickness between inner and outer cladding, stress concentrations still preferentially occur at the cladding. The straight sections of the claddings are inconspicuous in terms of stress concentrations in both versions (FP8, FP9). For the current assessment of a fuel-breeder pin, the elastic as well as the inelastic route were considered. In case of the elastic route, the conservative method of RCC-MRx code was used. In case of the inelastic route the assessment was performed based on the DDC-IC rules. For the anticipated service lifetime of two years and a load cycle spanning 2 hours and 15 minutes with 2 hours holding time (see Figure 5), the number of cycles  $N_d$  that the components must endure is calculated from the ratio of anticipated lifetime to the duration of one cycle to be 7787. Allowable cycle number of

each analyzed path or node is evaluated with the calculated design lifetime cycle number.

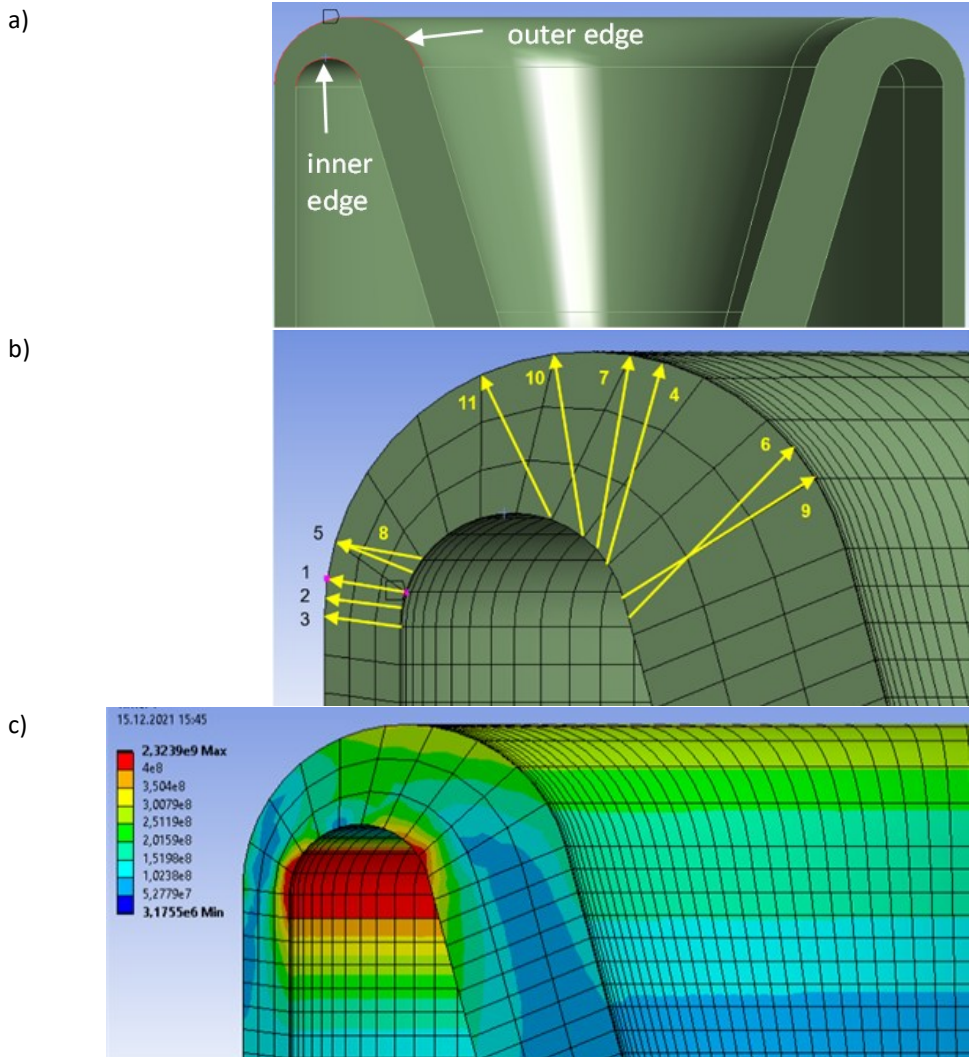


Figure 4: Assessment of the curvature connecting inner and outer cladding of FP8 model with pressure difference

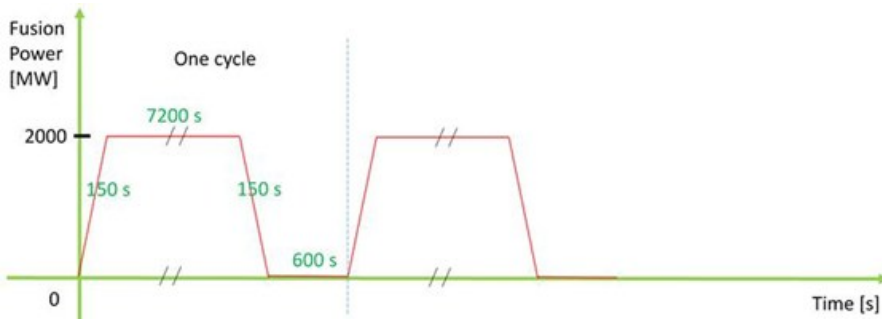


Figure 5: Cycle of heat power loading

### 3.1.1 CFA results for FP8 with pressure difference (8 MPa to 0.2 MPa)

In this chapter the FP8 model with pressure differences between helium coolant (8 MPa) and purge gas (0.2 MPa) is analyzed at the curvature area. Figure 4a shows the inner and outer edge where the nodes are placed to generate the paths through the part. Figure 4b shows the inner and outer node for the most critical part (pink points). Figure 4c shows the equivalent stress distribution at this area and significant high stresses are visible at the inner node of the critical path.

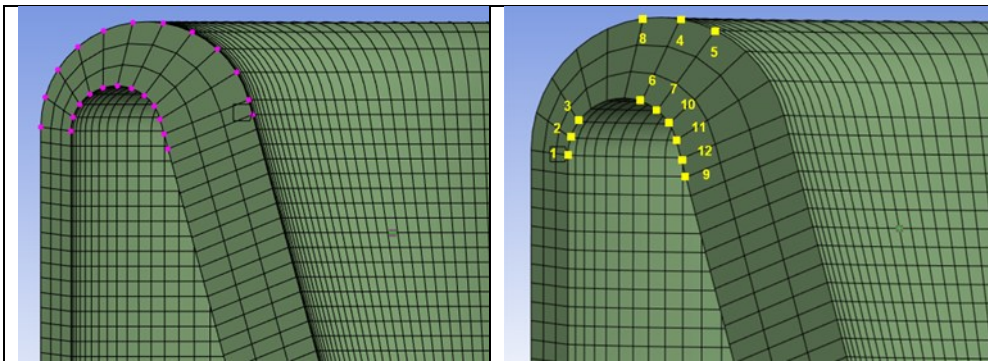


Figure 6: Assessment of curvature connecting inner and outer cladding of FP8 model with pressure difference

Table 2 shows the results of the ten paths with the lowest numbers of cycles to failure generated in the curvature area based on the elastic route of RCC-MRx code. The most critical path, number 1 in this case, can only endure 3628 cycles and an even lower number of 1510 cycles when influence of ceramic pebbles is considered. This is less than



the 7787 cycles defined as the required design lifetime. Under the influence of the ceramic pebbles there are four more critical paths found. Based on these findings the creep-fatigue assessment leads to the conclusion that the design cannot be used in this way.

Table 2 shows also the check of the requirements against *progressive deformation* in section 2.2, where nine paths (in red) do not fulfill these requirements. Because of this, technically the creep-fatigue assessment should not be carried out at all. For performing creep-fatigue assessment with the inelastic route, nodes are selected in place of paths as shown in Figure 6a. Ten nodes with the fewest numbers of cycles to failure are indicated in Figure 6b. The results of creep-fatigue assessment following the inelastic route of DDC-IC/ASME BPVC are shown in Table 3.

The most critical spot, with node number of 1, can only endure 1094 cycles and a little bit lower number of 1081 cycles when influence of ceramic pebbles is considered. This small difference can be explained by the fact that creep damage is very dominant at this node. In total five of the assessed nodes, numbers 1 to 5, do not reach the required number of cycles of 7787 cycles.

Table 2: Elastic route of creep-fatigue assessment for curvature of FP8 model with pressure difference

Path n°	$T_{max}$	$N_f$	$N_{f,CerBre}$	$P_1$	$P_2$	$P_3$	$S_m$	$3S_m$
1	445	3628	1510	194	300	280	149	583
2	446	5908	2474	193	281	264	148	539
3	447	7096	2984	192	279	262	148	536
4	453	8234	3802	243	254	251	148	544
5	445	17185	7183	174	284	264	149	575
6	455	26985	11314	212	229	224	148	521
7	452	27893	11708	241	253	250	148	524
8	444	57303	23888	164	269	249	149	553
9	457	72914	30199	147	175	168	147	432
10	450	90129	37231	238	246	244	149	481

Table 3: Inelastic route of creep-fatigue assessment for curvature of FP8 model with pressure difference

Node n <sup>o</sup>	$T_{max}$	$N_f$	$N_{f,CerBre}$
1	447	1094	1081
2	445	1250	1233
3	444	3979	3910
4	440	6235	5830
5	441	7109	6587
6	447	9255	8389
7	450	11719	10356
8	439	12363	10866
9	465	38397	26892
10	453	39900	26856

### 3.1.2 CFA results for FP8 without pressure difference (8 MPa to 8 MPa)

FP8 model with no pressure differences (helium and purge gas equal at 8 MPa) is analyzed at the curvature area, this is studied to check the impact of purge gas pressure on the result. The assessment is carried out in the same way as presented before. Considering the number of cycles, all paths reach the required number of cycles (see Table 4).

However, a few paths still do not meet all requirements against *progressive deformation*, even if their overruns are minimal compared to the FP8 model with pressure difference. The path numbered 1 has the lowest number of cycles to failure. After that, however, the sequence of the paths changes compared to the assessment of the FP8 model with pressure difference.

The results of creep-fatigue assessment following the inelastic route of DDC-IC/ASME BPVC are shown in Table 5. Apart from critical nodes 1 and 2, can only endure about 2200 cycles, all other assessed nodes can exceed the required 7787 cycles.

Table 4: Elastic route of creep-fatigue assessment for curvature of FP8 model without pressure difference

Path n°	$T_{max}$	$N_f$	$N_{f,CerBre}$	$P_1$	$P_2$	$P_3$	$S_m$	$3S_m$
1	445	17527	9880	151	246	227	149	436
4	453	27770	11847	203	217	213	148	462
2	446	28583	15643	153	235	218	148	409
3	447	31409	17606	154	237	220	148	410
6	455	92362	38692	179	198	193	148	440
7	452	99390	41525	202	216	212	148	448
5	445	175115	73231	138	233	214	149	431
10	450	188674	78244	202	210	208	149	421
9	457	216253	89922	132	157	150	147	370
11	449	414293	139099	197	202	201	149	397

Table 5: Inelastic route of creep-fatigue assessment for curvature of FP8 model with pressure difference

Node n°	$T_{max}$	$N_f$	$N_{f,CerBre}$
1	447	2145	2095
2	445	2203	2151
7	450	18523	15334
6	447	37569	26483
10	453	45107	29129
4	440	113204	50060
11	461	138220	58097
12	457	172776	72276
5	441	179422	74987
9	465	191624	79952

### 3.1.3 CFA results for FP9 without pressure difference (8 MPa to 8 MPa)

In this sub-section the FP9 model with no pressure differences between helium and purge gas is analyzed at the curvature area between the inner and outer cladding, shown in Figure 7.

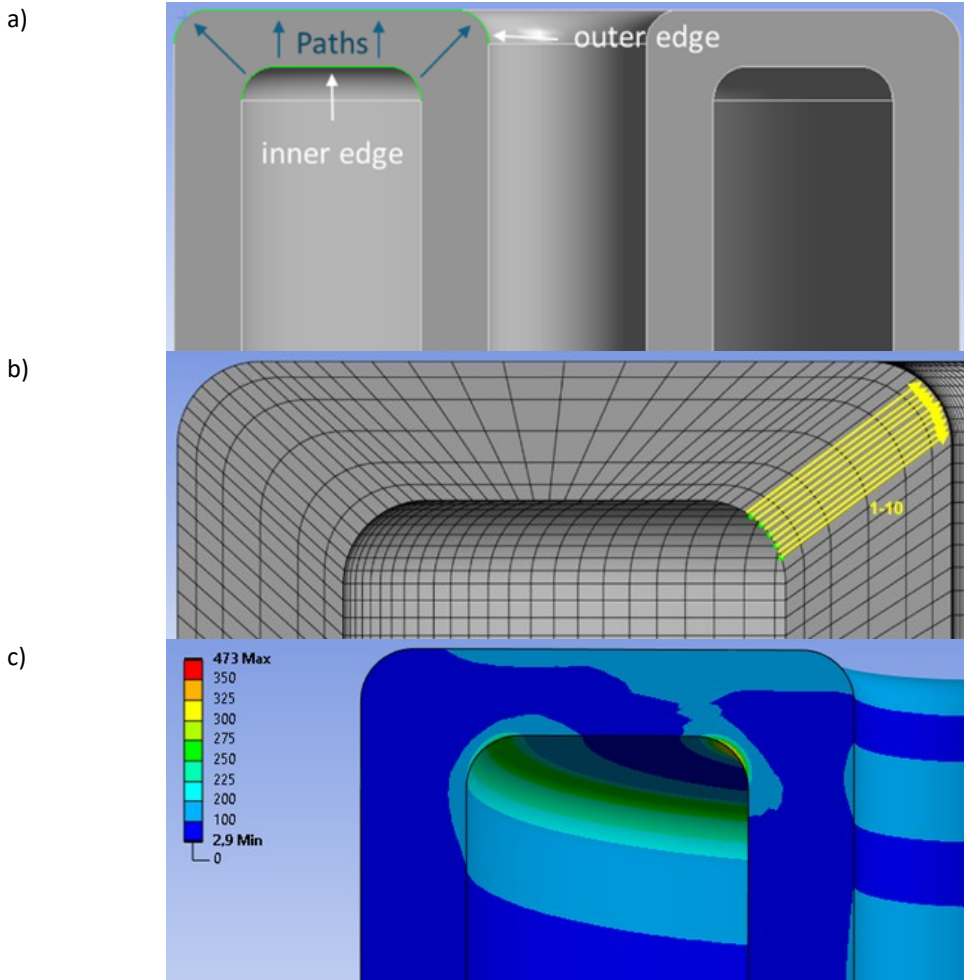


Figure 7: Assessment of curvature connecting inner and outer cladding of FP9 model without pressure difference

Figure 7a shows the edges with nodes (green), which are used for generating the assessment paths through the material volume. The ten most critical paths are visualized in Figure 7b. The distribution of the von Mises equivalent stress within the curvature already indicates a possible higher thermo-mechanical loading in this area. The stress distribution is shown in Figure 7c. The results of the creep-fatigue assessment based on the elastic route is given in Table 6. All the checked paths exceeded the required number of cycles many times over. Also, the requirements against *Progressive deformation* have been met by all paths.

Table 6: Elastic route of creep-fatigue assessment for curvature of FP9 model without pressure difference

Path n <sup>o</sup>	$T_{max}$	$N_f$	$N_{f,CerBre}$	$P_1$	$P_2$	$P_3$	$S_m$	$3S_m$
1	464	311353	125201	80	83	82	147	156
2	464	311885	125287	78	81	80	147	152
3	464	312507	125387	76	78	78	147	147
4	466	320785	126699	58	61	60	146	114
5	466	321868	126868	55	57	57	146	107
6	466	323134	127064	52	54	53	146	101
7	466	324311	127246	49	51	50	146	95
8	465	348716	130838	72	74	74	146	139
9	465	349562	130957	69	71	71	146	133
10	465	350597	131102	66	68	68	146	127

Most critical nodes are along the inside of the strongest bulge of the curvature. Results of creep-fatigue assessment following the inelastic route of DDC-IC/ASME BPVC are shown in Table 7. Applying this standard still one node will not reach the required number of cycles. Taking ceramic pebbles into account even four nodes are critical. All analyzed as well as the ten most critical nodes are highlighted in Figure 8 (a and b).

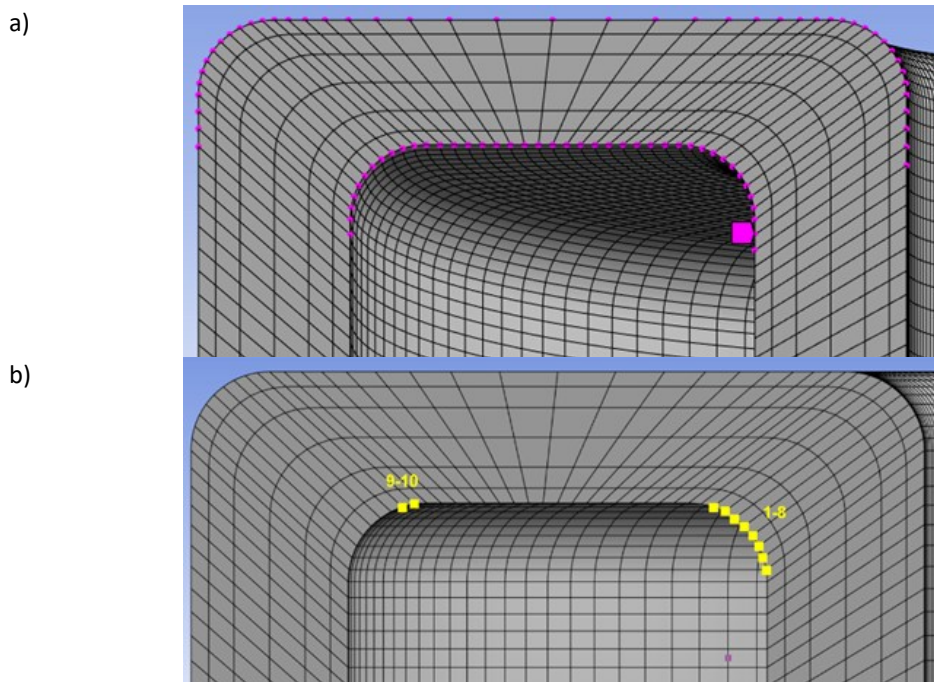


Figure 8: Assessment of curvature connecting inner and outer cladding of FP9 model without pressure difference

Table 7: Inelastic route of creep-fatigue assessment for curvature of FP9 model with pressure difference

Node n <sup>o</sup>	$T_{max}$	$N_f$	$N_{f,CerBre}$
1	464	4097	1704
2	469	13519	5627
3	462	14901	3646
4	466	18312	3724
5	449	44105	29572
6	461	48051	11036
7	474	58948	35579
8	448	60346	36083
9	449	62088	36699
10	471	82774	35349

### 3.2 FW-PMU of HCPB Breeding Blanket

Creep fatigue assessment was performed for the First Wall – Prototypical Mock Up (FW-PMU) [13]. The body of FW is split into several sections (a-d) for the assessment process. Steady-state thermal analysis considers heat flux of  $0.75 \text{ W/mm}^2$  applied on the section of FW termed FWd shown in Figure 9 and convection heat transfer through fluid lines to provide the temperature distribution, while fluid pressure of 8 MPa is considered in structural simulations.

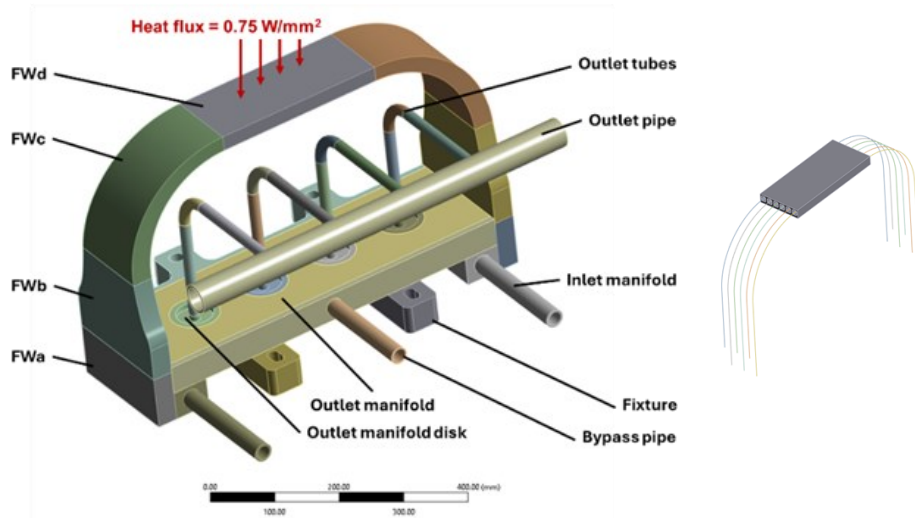


Figure 9: FE model of FW-PMU (left) and fluid lines in FW (right)

Figure 10 shows high temperature and deformation concentration at FWd, making it a candidate for creep-fatigue assessment. To reduce the computational cost, the sub-modeling of the FWd section is done using body temperature and cut displacements imported from the global model. In Figure 11, secondary stresses from the global and sub-model have good agreement demonstrating a successful sub-modelling. Paths for the application of elastic rules are defined between the flux-facing surface and the surface of the fluid line with the highest stress as shown in Figure 12. With requirements against *progressive deformation* (Level A criteria) under the *3Sm rule* found to be met, the elastic CFA was carried out.

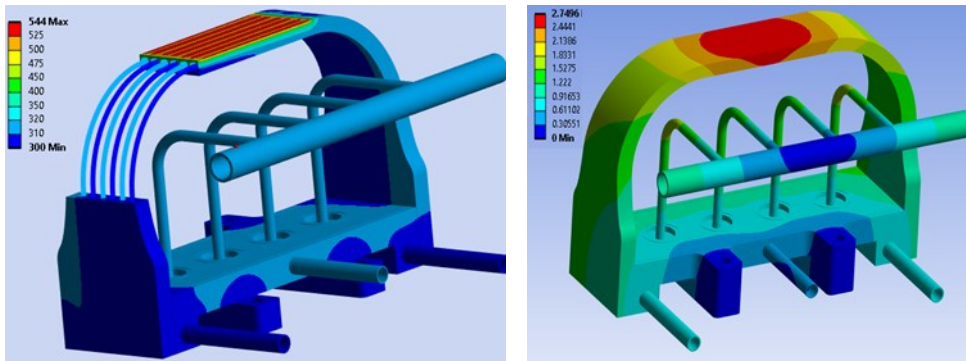


Figure 10: Contour plot of temperature ( $^{\circ}\text{C}$ ) in the FW-PMU and fluid lines (left) and deformation (P+Q) (right)

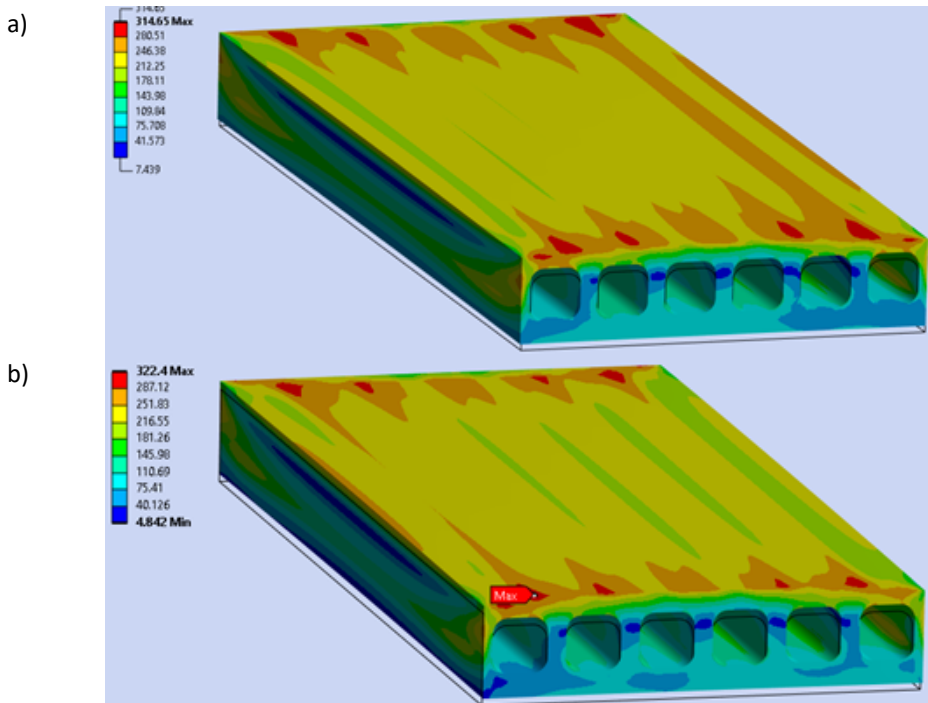


Figure 11: Contour plot of the simulated stress (MPa) in FWD from the (P+Q) step of a) global model and b) sub-model



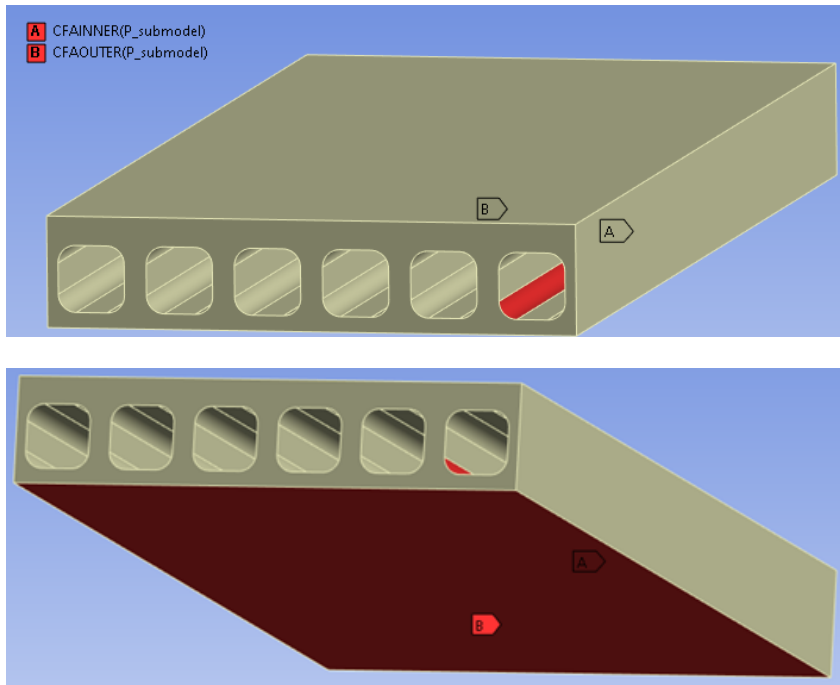


Figure 12: Assessment of region between the cooling channel and the flux facing surface of FWd

The inelastic analysis uses an elastic-plastic material model with time-hardening for EUROFER97. The initial step applies cooling channel pressure. In step 2, the imported temperature and displacement loads are activated. In step three, a hold time of one hour is applied with the creep effect activated, and the initial time increment is reduced to one second. The fourth step deactivates imported loads and creep effects to simulate unloading.

Steps 2-3-4 shown in Figure 13 constitute a cycle and are repeated for additional cycles. Hundred cycles are simulated with restricted frequency of output data recording for cycles 2-99 to reduce database size. Creep and total strains are highest on the hot side of FW. Thermal gradient acting along the cross-section induces a compression load on the hotter region, characterized by a large negative volumetric stress as seen in-Figure 14. During cool-down, this loading direction is reversed. Observed trends remain nearly unaltered in all cycles.

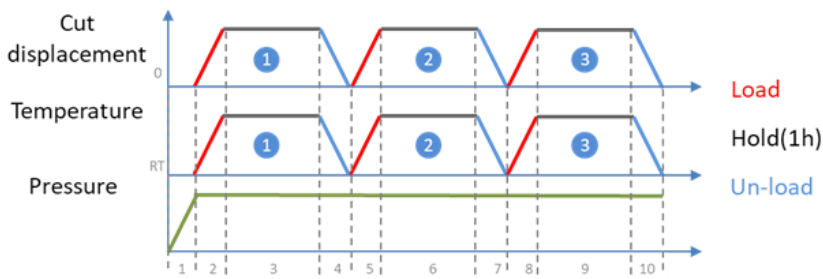


Figure 13: Schematic representation of boundary conditions used for cyclic loading

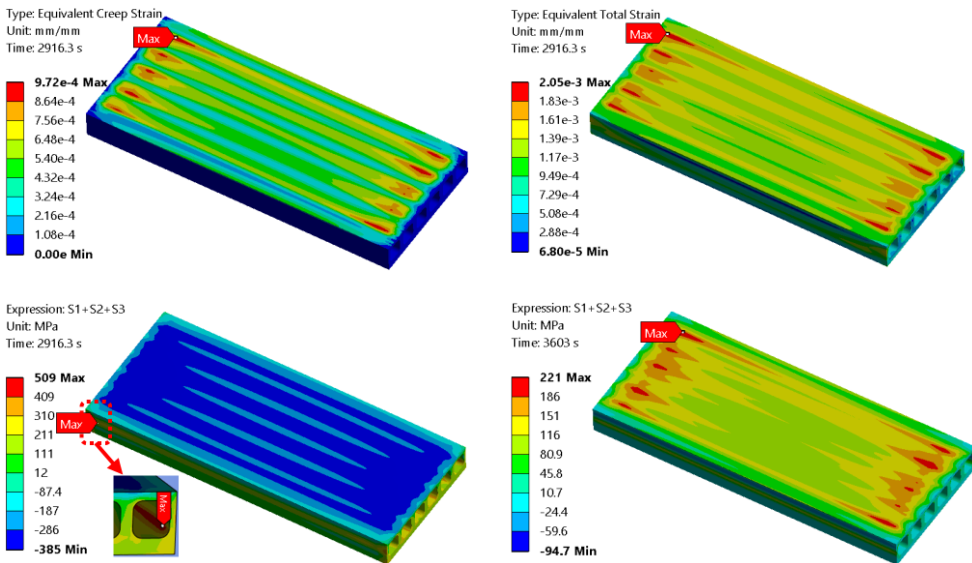


Figure 14: Contour plot of equivalent creep strain (top left), equivalent total strain (top right), and volumetric stress (MPa) at the end of hold time (lower left, with cut out of the region with maximum), and volumetric stress at the end of unloading (lower right).

A list of nodes with the largest inelastic strains, equivalent stress, and volumetric stress, as shown in Figure 15, is used to screen for critical regions where the search for critical nodes can be widened later. Using this approach, ASME-inelastic and DDC-IC identify the same critical node found on the flux-facing side. As DDC-IC accounts for cyclic softening, it makes a less conservative estimate of the allowed number of cycles.

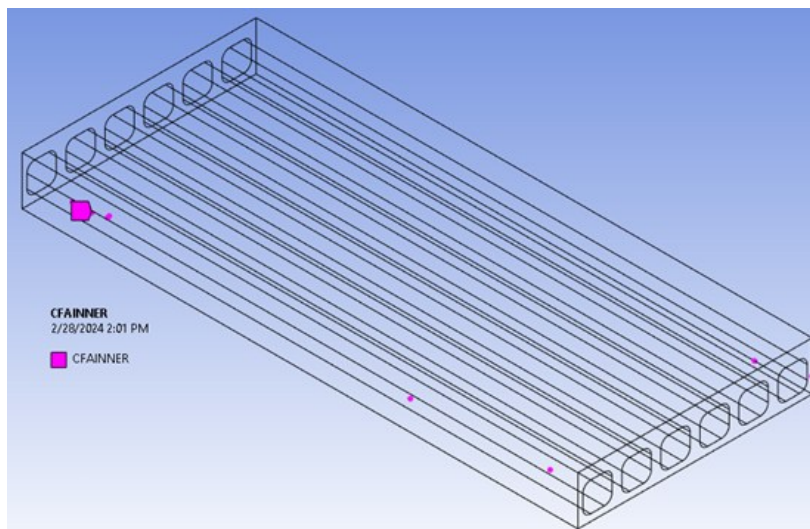


Figure 15: Selection of nodes for initial screening for critical region

The RCC-MRx inelastic code is applied at the hundredth cycle where the stress-strain hysteresis is reasonably stabilized. The results of creep-fatigue assessments are summarized in Table 8.

Table 8: Summary of CFA assessments using elastic and inelastic design codes

	ASME		DDC-IC	RCC-MRx	
	Elastic	Inelastic (Cycle 1)	Inelastic (Cycle 1)	Elastic	Inelastic (Cycle 100)
<b>Max. allowable cycles</b>	4	161	992	14480	743
<b>Creep damage</b>	0.9958	0.9423	0.9465	0.9092	0.9984
<b>Fatigue damage</b>	0.0004	0.0058	0.0229	0.0388	0.0006

Damage is consistently creep-driven with minor contribution from fatigue. While the ASME elastic rule is the most conservative, the RCC-MRx equivalent is the least conservative. The inelastic rule of ASME is less conservative than the elastic rule. On the contrary, the inelastic route of RCC-MRx is more conservative than its elastic rule. While RCC-MRx, in general, is seen to underestimate creep damage, the large difference

between its elastic and inelastic routes is attributed to the difference in the stress value at the assumed stabilized cycle. While the elastic rule refers to the stabilized curve at half-life, the inelastic rule considers the selected cycle from the simulation. For better agreement between the two rules, simulation needs to be continued till a stabilized cycle is reached.

As the model is considerably large, additional cycles could not be simulated. However, the inelastic rules of RCC-MRx and DDC-IC have better agreement between themselves than other rules. The location of the identified critical nodes on the component is illustrated in Figure 16 with z and x axes views of FWd, where the weak regions are seen to be located close to the farthest ends of FWd and present in the region between the heat flux facing surface and the cooling channels underneath. The DDC-IC identified two consequent nodes with similar results.

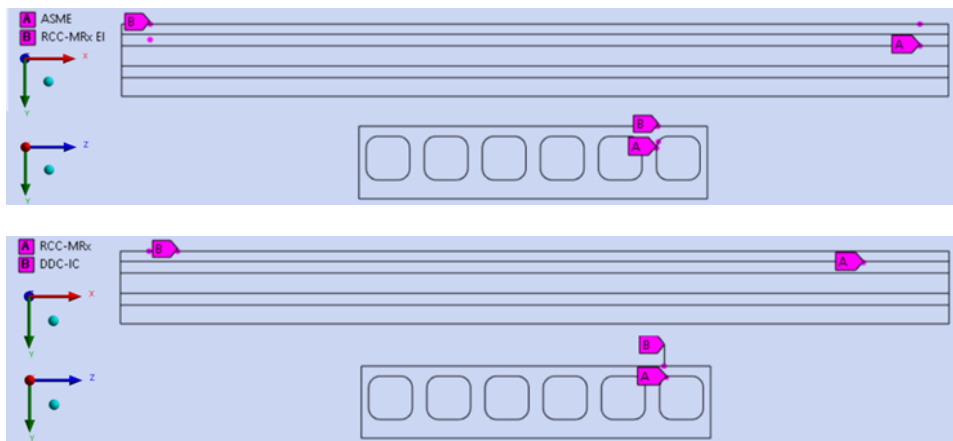


Figure 16: Critical nodes in FWd identified by elastic (top) and inelastic (bottom) design rules implemented in the CFA tool

## 4 Conclusion

Elastic and inelastic analyses of several designs of the first wall components were performed with the help of the FE program ANSYS. Using the CFA tool, the simulation data was used to perform a creep-fatigue assessment of the components. The tool proved instrumental in the detection of progressive deformation in certain components

which led to design changes. Creep-fatigue damage in the qualified designs was calculated and critical regions where damage may first occur were identified.

When multiple design rules were applied, the identified critical regions were not identical but regions under similar types of deformation. Among the design rules, the elastic route of ASME is very conservative in the estimation of an allowable number of cycles while RCC-MRx is much less conservative.

Good agreement was found in the results obtained from the application of inelastic routes of RCC-MRx and DDC-IC. While they are considerably conservative in comparison to the elastic route of RCC-MRx, they are much less conservative than ASME.

## References

- [1] Afcen - 2012- RCC-MRx Code, (2012).
- [2] ASME boiler & pressure vessel code. Section 3: Division 1, Subsection NH, 2004.
- [3] DEMO DESIGN CRITERIA FOR IN-VESSEL COMPONENTS (DDC-IC) PART-B: DESIGN CRITERIA AND ANALYSIS PROCEDURES, (2022).
- [4] Ansys® Academic Research Mechanical, Release 2023 R2, (2023).
- [5] M. Mahler, F. Özkan, J. Aktaa, ANSYS Creep-Fatigue Assessment tool for EUROFER97 components, Nucl. Mater. Energy 9 (2016) 535–538.  
<https://doi.org/10.1016/j.nme.2016.05.017>.
- [6] M. Mahler, J. Aktaa, Eurofer97 Creep-Fatigue assessment tool for ANSYS APDL and workbench, Nucl. Mater. Energy 15 (2018) 85–91.  
<https://doi.org/10.1016/j.nme.2018.03.001>.
- [7] M. Muscat, P. Mollicone, J.H. You, N. Mantel, M. Jetter, Creep fatigue analysis of DEMO divertor components following the RCC-MRx design code, Fusion Eng. Des. 188 (2023) 113426. <https://doi.org/10.1016/j.fusengdes.2023.113426>.
- [8] J. Aktaa, M. Walter, E. Gaisina, M.H.H. Kolb, R. Knitter, Assessment of the chemical compatibility between EUROFER and ceramic breeder with respect to fatigue lifetime, Fusion Eng. Des. 157 (2020) 111732.  
<https://doi.org/10.1016/j.fusengdes.2020.111732>.

- [9] P. Lamagnère, Y. Lejeail, C. Petesch, T. Lebarbé, P. Matheron, S. Taheri, A. Martin, Design Rules for Ratcheting Damage in AFCEN RCC-MRX 2012 Code, in: Vol. 1 Codes Stand., American Society of Mechanical Engineers, Anaheim, California, USA, 2014: p. V001T01A061. <https://doi.org/10.1115/PVP2014-28324>.
- [10] Y. Lejeail, P. Lamagnère, C. Petesch, T. Lebarbé, P. Matheron, A. Martin, Application Case of RCC-MRX 2012 Code in Significant Creep, in: Vol. 1 Codes Stand., American Society of Mechanical Engineers, Anaheim, California, USA, 2014: p. V001T01A042. <https://doi.org/10.1115/PVP2014-28492>.
- [11] J.L. Gordon, OUTCUR: An Automated Evaluation of Two-Dimensional Finite Element Stresses, in: ASME Pap. 760-WAPVP-16, ASME Winter Annual Meeting, New York, NY, 1976.
- [12] G. Zhou, F.A. Hernández, P. Pereslavitsev, B. Kiss, A. Retheesh, L. Maqueda, J.H. Park, The European DEMO Helium Cooled Pebble Bed Breeding Blanket: Design Status at the Conclusion of the Pre-Concept Design Phase, *Energies* 16 (2023) 5377. <https://doi.org/10.3390/en16145377>.
- [13] G. Zhou, Test of a HCPB First Wall PMU – Engineering Design and Manufacturing Activities in 2021, *EUROfusion*, 2021.

# Experimental test of a helical induction pump with rotating core

Leo Bühler<sup>1</sup> and Robert Stieglitz<sup>2†</sup>

<sup>1</sup> Karlsruhe Institute of Technology, Institute for Thermal Energy Technology and Safety

<sup>2</sup> Karlsruhe Institute of Technology, Institute for Neutron Physics and Reactor Technology

## Abstract

A design of a new type of liquid metal electromagnetic pump for medium flow rates and moderate pressure heads has been developed. The major difference compared to existing concepts is that the central iron core, which closes the magnetic flux lines, is fabricated from a single iron piece, which may freely rotate in order to avoid magnetization losses. The pump was designed and manufactured at KIT and tested in the liquid metal NaK loop of the MEKKA facility. Its performance curve (pressure head vs. flow rate) and efficiency have been determined for a variety of frequencies and magnitudes of applied 3-phase current.

**Keywords:** Liquid metal EM pumps, helical induction pump, rotating iron core

## Preface

The present work results from a collaboration of both authors. We had the idea to design, manufacture and test a medium-scale liquid metal pump at reasonable costs. Although the work had been completed already several years ago, the results were never fully published, neither at a conference nor in a journal, despite the intention of doing so. Unfortunately, in December 2023 the second author, our dear friend and colleague Robert Stieglitz, unexpectedly passed away. Upon this sad circumstance, I remembered our collaboration on EM pumps and thought that it could be a good idea to publish the results now, in order to recall to the magnetohydrodynamics community Robert's unforgettable achievements in MHD and in particular the Karlsruhe geodynamo experiment (Stieglitz & Müller, 2001; Müller, Stieglitz, & Horanyi, 2004). The present manuscript has been presented at the *13th pamir International Conference on Fundamental and Applied MHD* (Bühler & Stieglitz, 2024), and submitted to the journal *Magnetohydrodynamics*.

# 1 Introduction

Liquid metals, such as sodium (Na), sodium-potassium (NaK), Lithium (Li) and lead-lithium (PbLi), have been proposed as coolants in fast nuclear reactors or in blankets of future fusion reactors due to their high thermal conductance, their applicability at high temperature, and their favourable interaction with neutrons for fuel breeding purposes. For circulation of those electrically conducting fluids through circuits and heat exchangers on reactor scales, usually large annular linear induction pumps (ALIP) are the preferred choice at high flow rates (Nashine & Rao, 2014). Electromagnetic pumps have the advantage that they are hermetically tight with no penetration of a rotating axle. The latter could pose risks of potential leaking, which would represent a safety issue in case of alkali liquid metals or in nuclear applications. However, on medium scales ALIPs operate at quite poor efficiency, as shown for instance in (Polzin, Pearson & Webster, 2013), where the maximum efficiency was about only 5 % or smaller.

For applications on a laboratory scale, permanent magnet rotor pumps became an interesting option for moderate flow rates and pressure heads due to their relatively simple design (Brekis, et al., 2023; Bucenieks, Platadis, Mikanovskis, Zik, & Mehta, 2017). Higher pressure heads can be achieved by a helical design of the pump channels (Bucenieks, Platadis, Mikanovskis, Zik, & Mehta, 2017). Instead of a rotating magnetic shaft as used in the latter references, it is possible to apply rotating magnetic fields created externally by 3-phase currents as proposed, e.g. in (Avilova, Doktorova, Marin, Povsten, & Turchin, 1965) for pumping of liquid metals.

Based on the physical principles of helical induction pumps, we developed a design of a new type of liquid metal pump for medium flow rates and moderate pressure heads. The design is shown in Figure 1. The main components are the helical annular pump channel (1), which is placed in the stator (2) of a former 11 kW induction motor that became available at the institute. The flow is supplied to the annular channel through a DN40 pipe (12) followed by an axial-radial manifold (3). After passing the helical pumping channel (1), the liquid metal continues its path through a conical diffuser (5, 7). Finally, the fluid passes openings at the end of the diffuser body and it is collected in a larger annular compartment before it leaves the pump through the DN40 exit pipe (12). Magnetic flux lines are closed via a soft iron core (15). While in previous designs of helical induction pumps such as e.g. (Avilova, Doktorova, Marin, Povsten, & Turchin, 1965), the laminated core fabricated from thin transformer plates for reducing induction losses, was entirely submerged in the liquid metal flow, we have chosen here a different approach. In the present design, the iron core, which is fabricated from a single solid



piece, is fully accessible from one side (the left side in Figure 1). For minimization of magnetization losses, the core is mounted on two ball bearings (13) and (14) and permitted momentum-free rotation. During the start-up of the pump, the core accelerates quickly until the rotation rate reaches the frequency of the stator field for which induced currents and Ohmic losses in the iron core then vanish.

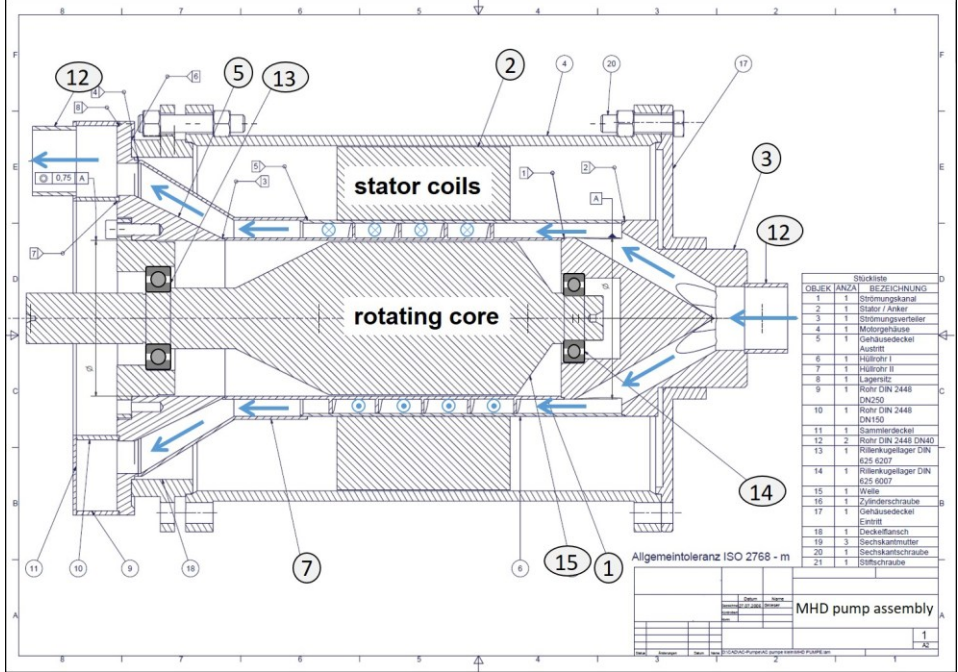


Figure 1: Design of the helical induction pump, MHD pump assembly.

In the following, we estimate some properties of the pump. As structural material for the spiral channel walls, stainless steel with a wall thickness of 2 mm was used with electrical conductivity  $\sigma_{\text{steel}} = 1.24 \times 10^6 \text{ 1}/\Omega\text{m}$  and magnetic permeability  $\mu_0$  of free space. A typical penetration depth  $\delta = \sqrt{2 / \mu_0 \sigma \omega}$  for magnetic inductive waves at a frequency of  $f = \omega / 2\pi = 30 \text{ Hz}$  is about  $\delta_{\text{steel}} = 83 \text{ mm}$  in stainless steel so that the shielding effect, i.e. the reduction of magnetic field in the fluid by eddy currents in the wall, remains small at about 2.5 %. For the liquid metal NaK ( $\sigma_{\text{NaK}} = 2.79 \times 10^6 \text{ 1}/\Omega\text{m}$ ) we may estimate at the same frequency  $\delta_{\text{NaK}} = 55 \text{ mm}$  which indicates that the traveling

magnetic field affects the fluid in the entire spiral gap which has a radial dimension of 10 mm. The field drops across the pump channel by roughly 17 %. If the fluid moved synchronously (no friction losses, no pressure drop) at the mean spiral radius  $r_s$ , i.e. with the mean rotation speed  $r_s \omega$  of the magnetic field, we could expect at 30 Hz a flow rate through the 10 mm  $\times$  30 mm cross section of the spiral channel (Figure 2) as  $\dot{V}_s = 3.45 \times 10^{-3} \text{ m}^3/\text{s}$ . This leads with fluid density ( $\rho_{\text{NaK}} = 863 \text{ kg/m}^3$ ) to an upper limit for mass flowrate of  $\dot{m}_s = 2.98 \text{ kg/s}$ . With viscous effects and Ohmic losses present, and when the pump has to deliver a certain pressure head, the flow rate will become smaller than these ideal values.

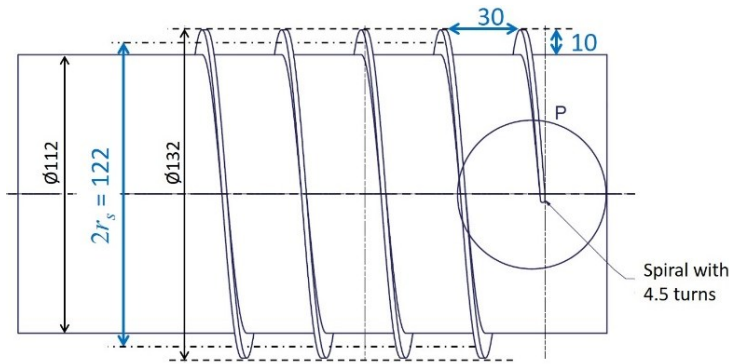


Figure 2: Details of the helical channel.

The pump was manufactured at the KIT workshop. Photographs displayed in Figure 3 show the finished pump and its components before assembly. After a pressure test and confirmed tightness, the pump was inserted for testing in the liquid metal NaK loop of the MEKKA facility (Barleon, Mack, & Stieglitz, 1996). In order to enable entire draining of the spiral channel by gravity after the tests are completed, the pump was installed with the rotation axis in vertical orientation and inflow from below.

A 3-phase power supply with adjustable frequency and current was used during the experiments. The temperature of the liquid metal was monitored by thermocouples in front and after the pump, primarily for determination of temperature-dependent fluid properties. The flowrate was measured by a Coriolis flow meter in the NaK loop and the pressure head developed by the pump was detected through a capacitive differential pressure transducer (Barleon, Mack, & Stieglitz, 1996). In addition, the rotation rate of the iron core was measured by an optical sensor.

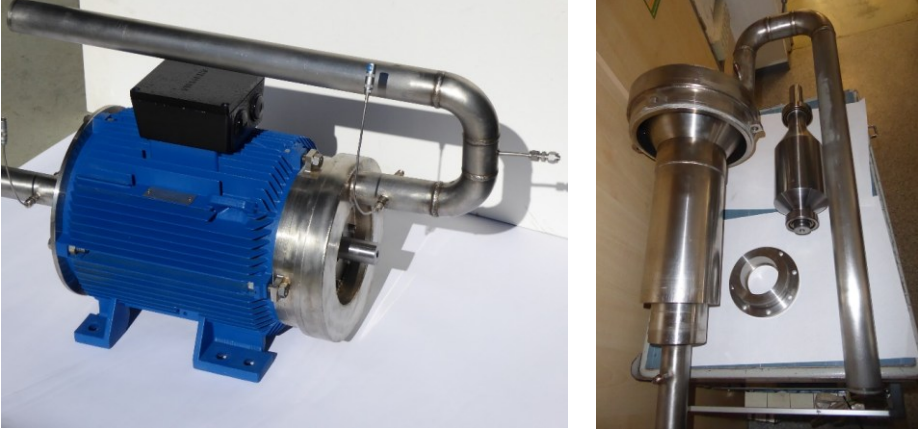


Figure 3: Photograph of the assembled pump (left) and its components (right).

## 2 Experimental results

Experiments have been performed by setting the frequency and magnitude of currents in the 3-phase stator coils to predefined values while the flow loop is initially closed by a valve. Then the control valve is opened in small increments leading to a stepwise increase of the flow rate. The pressure head developed by the pump and the flow rate are measured after steady state conditions established. In the following, the pump characteristics are shown with a focus on pressure head  $\Delta p(\dot{m})$  and efficiency  $\eta(\dot{m})$  for the specified frequency and current magnitude  $I$ . Here,  $I$  denotes the sum of currents over all three phases. The pump efficiency  $\eta$  is defined as the ratio of the delivered hydrodynamic power  $\Delta p \dot{V}$  in terms of pressure head  $\Delta p$  and volumetric flow rate  $\dot{V}$ , and the electric power  $P_{el}$  supplied to the engine, i.e.  $\eta = \Delta p \dot{V} / P_{el}$ .

In a first series of experiments the total current is fixed to  $I = 60\text{A}$  while the pump performance is tested for various frequencies in a range from 20 Hz to 60 Hz. Results displayed in Figure 4 reveal, as expected, that the pressure head  $\Delta p$  decreases with increasing mass flowrate  $\dot{m}$ . With increasing frequency, 20 Hz  $\rightarrow$  30 Hz  $\rightarrow$  40 Hz, the maximum mass flowrate increases further, due to a higher rotation rate of the magnetic field. However, beyond 40Hz the maximum mass flow does apparently not increase further and the maximum pressure heads become smaller. The maximum efficiency is achieved at a frequency close to 30 Hz.

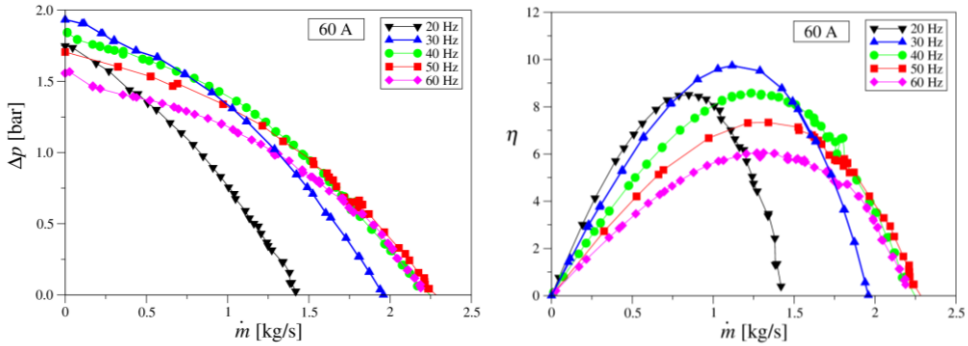


Figure 4: Pressure head  $\Delta p$  (left) and efficiency  $\eta$  (right) versus mass flowrate  $\dot{m}$  for a total current  $I=60\text{A}$  and various frequencies.

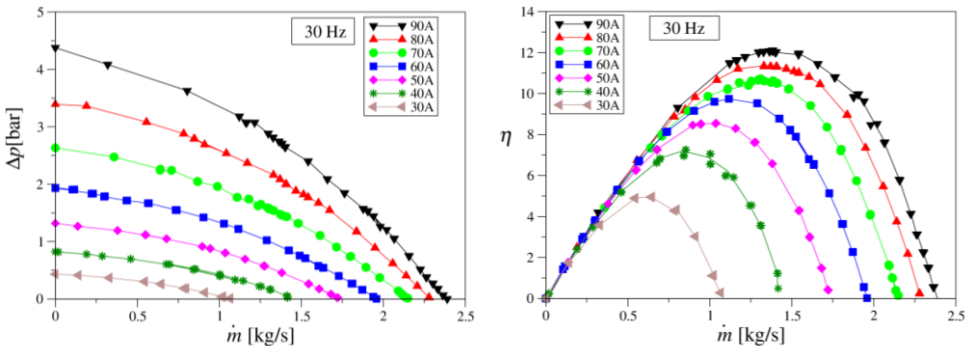


Figure 5: Pressure head  $\Delta p$  (left) and efficiency  $\eta$  (right) versus mass flowrate  $\dot{m}$  for a frequency of 30 Hz and various strengths of currents  $I$ .

In a next step, the frequency is fixed at 30 Hz, which is considered close to an optimum value with respect to pressure head and efficiency. In a series of experiments, it is then analyzed how the pump performs with different strengths of applied current. Results for pressure head  $\Delta p$  and efficiency  $\eta$  are displayed in Figure 5. It can be observed that the maximum pressure head  $\Delta p_{\max}$  as well as the efficiency  $\eta_{\max}$  increase monotonically with increasing currents. Results for  $\Delta p_{\max}$  and  $\eta_{\max}$  are summarized in Figure 6. At the highest investigated current  $I = 90\text{ A}$ , a maximum pressure head  $\Delta p = 4.4\text{ bar}$  and efficiency  $\eta = 12.1\text{ \%}$  are achieved. From the results it can be anticipated that with currents higher than  $I = 90\text{ A}$  even higher  $\Delta p$  and  $\eta$  values should be possible. Unfortunately, in the present experimental campaign, higher currents could not be applied in stationary

conditions due to a lack of active stator cooling and the upper bound on coil temperature.

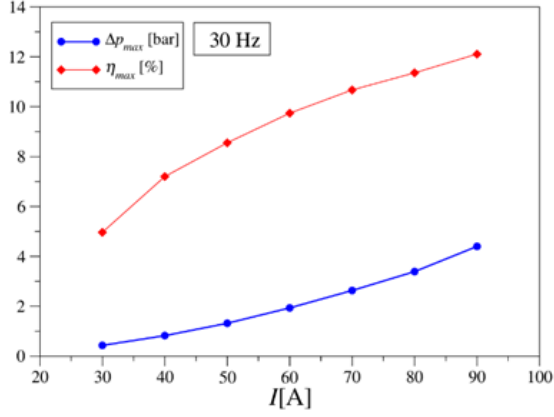


Figure 1: Maximum values  $\Delta p_{max}$  and  $\eta_{max}$  as function of  $I$  for a frequency of 30Hz.

### 3 Conclusions

A new type of helical induction pump has been designed, built, and tested using NaK as liquid metal. The pump works best close to 30 Hz and results are quite promising. The pump delivers a maximum pressure head  $\Delta p = 4.4$  bar and maximum flowrate of about  $10 \text{ m}^3/\text{h}$ . The highest efficiency of  $\eta = 12.1 \%$  at a slip  $s = (\dot{V}_s - \dot{V}) / \dot{V}_s = 0.53$  seems quite good, despite the fact that so far no optimization has been performed for the pump channel geometry. Moreover, with forced (internal) cooling of the stator, it should be possible to allow for larger currents with further increase in  $\Delta p$  and  $\eta$ . Since the central core is fully accessible from outside, it should be also possible to replace it by an active 3-phase-powered non-rotating one for future improvement.

## References

- Avilova, E. M., Doktorova, T. V., Marin, N. I., Povsten, V. A., & Turchin, N. M. (1965). Development and operation of helical-flow induction pumps. *Magnetohydrodynamics*, 1, 81-83.
- Barleon, L., Mack, K.-J., & Stieglitz, R. (1996). The MEKKA-facility a flexible tool to investigate MHD-flow phenomena. *Forschungszentrum Karlsruhe, FZKA 5821*.
- Brekis, A., Buligins, L., Buceniekis, I., Goldsteins, L., Kravalis, K., Lacis, A., . . . Jekabsons, N. (2023). Electromagnetic pump with rotating permanent magnets operation at low inlet pressures. *Fusion Engineering and Design*, 194, 113919.
- Buceniekis, I., Platacis, E., Mikanovskis, O., Zik, A., & Mehta, V. (2017). Helical type EM induction pump with permanently magnetized rotor for high pressure heads. *Magnetohydrodynamics*, 53, 423-428.
- Bühler, L., & Stieglitz, R. (2024). Experimental test of a helical induction pump with rotating core. 13th International PAMIR Conference - Fundamental and Applied MHD, September 15 – 19. Carry-le-Rouet, France.
- Müller, U., Stieglitz, R., & Horanyi, S. (2004). A two-scale hydromagnetic dynamo experiment. *Journal of Fluid Mechanics*, 498, 31-71.
- Nashine, B., & Rao, B. (2014). Design, in-sodium testing and performance evaluation of annular linear induction pump for a sodium cooled fast reactor. *Annals of Nuclear Energy*, 73, 527-536.
- Polzin, K., Pearson, J., & Webster, K. (2013). Testing of an annular linear induction pump for the fission surface power technology demonstration unit. *National Aeronautics and Space Administration. NASA/TP—2013–217487*.
- Stieglitz, R., & Müller, U. (2001). Experimental demonstration of a homogeneous two-scale dynamo. *Physics of Fluids*, 13(3), 561-564.

# Scale separation in thermal turbulent flows – a specific Péclet number scaling analysis

*Sebastian Ruck*

*Institute for Neutron Physics and Reactor Technology, Karlsruhe Institute of Technology, Karlsruhe, Germany*

## Abstract

The breakdown of the coupling between the momentum and heat transfer in a thermal turbulent field is crucial for turbulent transport processes and thermal turbulent mixing. It is the consequence of an irreversible decay of turbulence-induced fluctuations by thermal diffusion due to molecular diffusivity and by dissipation due to molecular viscosity with flow structures of different length scales, leading to a deviation of the smallest scales for turbulent heat transfer from the Kolmogorov scale with varying Prandtl numbers. On the basis of a phenomenological view, a specific Péclet number approach for a scale-dependent derivation of the smallest length scale of turbulence-induced heat transport in turbulent flow with non-unity Prandtl number from the specific advection-diffusion equation is reported.

**Keywords:** Scale Separation, Turbulent Transport, Turbulent Heat Transfer, Turbulent Scales

## 1 Introduction

Flow dynamics in turbulent flows are characterized by a wide range of length scales. The large scales of turbulent flow structures are determined by the boundaries of the flow situation and are close to the order of magnitude of the general characteristic flow scales. Turbulent flow structure smaller than the Kolmogorov length scale  $\eta$ , time scale  $t_\eta$ , and velocity  $u_\eta$ , are determined by the dissipation rate  $\varepsilon$  and fluid viscosity  $\nu$  (Kolmogorov (1941)). Depending on the Prandtl number, the coupling between momentum and heat transfer varies as a result of the so-called scale separation, leading to a deviation of the Kolmogorov scales from the smallest scales of turbulence-induced heat transport (also called ‘smallest temperature scales’ in the following) with the length scale  $\eta_T$ , time scale  $t_{\eta_T}$ , and velocity  $u_{\eta_T}$ . In general, scale separation denotes the

process that the smallest temperature length scale in turbulent heat transfer can differ significantly from the smallest length scale of turbulence-induced momentum transfer. The irreversible decay of turbulent fluctuations by thermal diffusion due to molecular diffusivity and dissipation due to molecular viscosity occurs with flow structures of different length scales leading to different cut-off wave numbers in the kinetic energy spectrum and temperature variance spectrum, respectively. The smallest temperature scales are larger than the Kolmogorov scales in low Prandtl number fluids (Obukhov (1949), Corrsin (1951)) and vice versa in high Prandtl number fluids (Batchelor (1959)). Turbulent transport process and thermal turbulent mixing of a passive scalar is dominated by advection with turbulent flow structures. The breakdown of large turbulent scales carrying the passive scalar into smaller scales determines the dynamics of these processes and is of significant importance. Therefore, the understanding of scale separation is crucial for modelling, predicting and analyzing heat transfer phenomena in turbulent flows where Prandtl numbers differs from unity.

Without intention of questioning existing concepts, a quite heuristic approach was made to analytically derive the smallest temperature length scale, i. e. the Obukhov-Corrsin-scale and Batchelor-scale. It was tried to illustrate the process of scale separation simplistically. On the basis of a phenomenological view, a specific Péclet number approach for a scale-analytical derivation of the smallest temperature scales in turbulent flow of non-unity Prandtl number is reported in the following. (The term ‘specific’ denotes the limitation of the observation space to a flow structure with a specific length scale referring to a specific wave number.)

## 2 Specific Péclet Number Approach

First of all, various assumptions for the underlying turbulent flow must be presumed to provide the environment for the elaboration of a heuristic specific Péclet number approach. Here, a fully developed, homogeneous turbulent flow at high Reynolds numbers (on basis of the characteristics of the mean velocity field) is assumed. The vortex decay in the framework of the Richardson energy cascade as well as the Kolmogorov (1941) similarity hypotheses for turbulent transport are valid within the corresponding length scale and wave number ranges, respectively. The considered turbulent flow consists of three-dimensional, multiscale structures which interact with each other and move in a chaotic manner in their self-influenced flow field. In this context, a flow structure is associated (in a Lagrangian frame) with a rotational lump of fluid of a specific velocity  $u(l)$  and time scale  $t(l) = l/u(l)$ , which is coherent over its spatial extent  $l$ .



Each length scale  $l$  refers to an inverse wave number  $\kappa$  in the spatial spectral range of the energy spectrum, i. e.  $l \sim \kappa^{-1}$ . The smallest length scale of the flow field is determined by the Kolmogorov scale  $\eta$  and the length scales of the large, energy-containing turbulent structures is denoted by  $l_t$ . A mean temperature gradient is imposed on the flow field leading to the development of a temperature field. The temperature is assumed to be a passive scalar, so that turbulent momentum transport is independent of heat transport in the turbulent flow field and the advection of heat is considered due to the motion of turbulent flow structures. Furthermore, high Péclet numbers (on basis of the characteristics of the mean temperature field) is assumed.

Although, the temperature field exhibits a wide range of scales due to motion of the flow structures, the temperature variations are not the exclusive by-products of turbulent momentum transport and its statistical parameters will depend not only on the dissipation rate  $\varepsilon$  and kinematic viscosity  $\nu$ . The heat transfer by advection and diffusion, and the irreversible decay due to the molecular diffusivity smoothing out local temperature gradients are the two different mechanisms significant for the behavior of the turbulent heat transfer in turbulent flow. Thus, the dynamics of the temperature field are governed by the advection-diffusion equation. The turbulence-induced heat transport with a turbulent flow structure of length scale  $l$  leads to the occurrence of a temperature variation  $\Delta T(l)$  across the turbulent flow structure. These temperature variations are small compared to the mean temperature differences of the flow field and vary randomly with the motion of turbulent flow structures. Temperature variations of different  $\Delta T(l)$  induced by motion of turbulent flow structures of different size  $l$  cause differently intense molecular heat fluxes: a turbulent flow structure with the length scale  $l$  and velocity  $u(l)$  generates a temperature gradient  $\Delta T(l)/l$  by turbulence-induced advection  $u(l) \cdot \Delta T(l)/l$  and, thus, causes the specific heat flux  $u(l) \cdot \Delta T(l)/l$  due to molecular conduction, with the temperature thermal diffusivity  $a$ . Since the cut-off wave number in the temperature variance spectrum indicating the onset of the irreversible decay of temperature fluctuations is associated with the increasing dominance of heat transfer by molecular conduction as pointed out by Corrsin (1951), the smallest length scales in the temperature field are given by a specific Péclet number  $Pe_l = u(l) \cdot l/a$ . A direct outcome from the advection-diffusion equation. For sufficiently large flow structures the specific Péclet number is  $Pe_l \gg 1$  due to the comparable high specific velocities and length scales of the associated turbulent flow structures. Thermal diffusion by molecular conduction plays a minor role compared to advection for the specific total heat transfer. Temperature gradients generated with turbulent motion depend on length scales and velocities of the flow structures. With decay and distortion of turbulent flow structures in the cascade, their length scales

reduce and so do the length scales of the temperature gradients. The smaller the turbulent flow structure, the smaller the length scale of the corresponding temperature gradient. For smaller flow structures, the influence of viscosity on the momentum transport increases. The advective heat transfer reduces and the contribution of molecular diffusion on the specific total heat transfer gains increasingly importance. The effect of the decreasing length scales leads to a quadratic increase in heat conduction and a linear decrease in advection. Following Obukhov's hypotheses (Obukhov (1949)), that the distances across fluctuating temperature potentials become such small, that the equalization of these temperature differences occur by molecular heat transfer only – thermal diffusion by molecular conduction largely determines the heat transfer for specific Péclet numbers of the order  $Pe_l \leq 1$ . The specific temperature gradients  $\Delta T(\eta_T)/\eta_T$  generated due to the motion of flow structures with the length scale  $\eta_T$  and the velocity  $u(\eta_T) = u_{\eta_T}$  are balanced by the molecular heat flux  $a \cdot \Delta T(\eta_T)/\eta_T^2$ , instead of being transported by even smaller flow structures. Under the assumption of neglectable internal energy generation by dissipation, the specific advective heat transport corresponds to the molecular heat conduction at the length scale  $\eta_T$ . The dimensionless advection-diffusion equation reduces to the specific Péclet number of

$$Pe_{\eta_T} = \frac{u_{\eta_T} \cdot \eta_T}{a} \sim 1 \quad . \quad (2.1)$$

While in the turbulent flow field dissipation due to molecular viscosity terminates the inertia-induced momentum transport for decreasing length scales, in the turbulent temperature field thermal diffusion due to molecular diffusivity leads to the cessation of the turbulence-induced heat transport by advection. The smallest scale of turbulence-induced heat transport in the temperature field is determined by the specific Péclet number  $Pe_l$ , i. e. the product of specific Reynolds number  $Re_l$  and Prandtl number  $Pr$ . Depending on the fluid properties, there is a more or less strong coupling between turbulent momentum and heat transfer, which is reflected in turbulent heat transport varying with the Prandtl number and demonstrated in numerous experimental and numerical studies. The coupling between the momentum transfer and heat transfer determines how fast or slow - with decreasing length scales of turbulent flow structures - the molecular heat flux compensates the temperature differences induced by advection. While for fluids with a Prandtl number  $Pr$  of the order of unity, the Kolmogorov scale  $\eta$  and the length scale  $\eta_T$  are of the same order of magnitude, both scales differ in fluids with Prandtl numbers far away from unity. On basis of the aforesaid established hypothetical environment for specific heat transfer in turbulent flow, scaling-relations for determining the smallest temperature length scale for fluids with Prandtl numbers  $Pr \ll 1$  and  $Pr \gg 1$  are deduced in the following.

## 2.1 Fluids with $Pr \ll 1$

Due to the high thermal conductivity of fluids with Prandtl numbers of  $Pr \ll 1$ , say liquid metals, heat conduction dominates the specific total heat transfer of turbulent structures with length scales larger than the Kolmogorov length scales, which can be inferred from the specific Reynolds number and Péclet number

$$Re_\eta = \frac{u_\eta \cdot \eta}{\nu} \sim 1, \quad \text{with } a \gg \nu \text{ for } Pr \ll 1 \rightarrow \frac{u_{\eta_T} \cdot \eta_T}{\nu} \gg 1. \quad (2.2)$$

$$Pe_{\eta_T} = \frac{u_{\eta_T} \cdot \eta_T}{a} \sim 1$$

The product of the smallest scale of the temperature  $\eta_T$  field and the corresponding specific velocity  $u_{\eta_T}$  is significantly larger than the equivalent of the Kolmogorov scales for  $a \gg \nu$ . Supposing a growth of the length scale with the velocity, it is obvious that the smallest temperature length scale  $\eta_T$  is larger than the Kolmogorov length scale  $\eta$ ,

$$\eta_T \gg \eta \quad \text{for } Pr \ll 1. \quad (2.3)$$

The inertia subrange of the kinetic energy spectrum covers the inertia-convective range and the inertial-diffusive range of the temperature variance spectrum (Tennekes and Lumley (1972)). Within the inertia-convective subrange advection dominates the heat transfer, while within the inertial-diffusive subrange advection and molecular conduction contribute to the heat transfer. Referring to  $l \sim \kappa^{-1}$ , length scale depending subranges for specific heat transfer in turbulent flow for fluids with Prandtl numbers of  $Pr \ll 1$  can be defined correspondingly, as shown schematically in Figure 2.1 a. According to Eq. (2.1) and Eq. (2.3), the turbulence-induced advection  $u(l) \cdot \Delta T(l)/l$  with turbulent flow structures of length scale  $l < \eta_T$  are diffused more quickly by molecular heat flux than transported by advection in the further course of the cascading vortex decay. I. e. thermal diffusion by molecular conduction leads to the irreversible termination of the turbulence-induced advective heat transport and the disappearance of turbulent temperature variations. Thus, turbulence-induced heat transport by advection for flow structures with length scales of  $l < \eta_T$  is negligible.

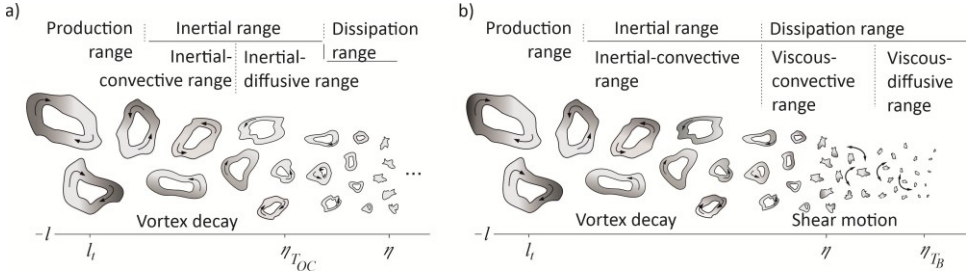


Figure 2.1: Flow structures of different scales in turbulent flow for a)  $Pr \ll 1$  and b)  $Pr \gg 1$ .

As long as in the cascade process the decreasing vortex structures of the length scale  $l$  are still so large that viscosity plays a negligible role, i. e.  $l \gg \eta$ , and their motion is determined only by inertia, i. e.  $l \ll l_t$ , the kinetic energy flux across the cascade equals the dissipation rate  $\varepsilon$  and, thus, the scaling-relation (Frisch (1995))

$$\varepsilon \sim \frac{u(l)^3}{l}; \quad \eta \ll l \ll l_t \quad (2.4)$$

is valid. According to Eq. (2.3), the length scale  $\eta_T$  is much larger than the Kolmogorov length scale  $\eta$ . Assuming additionally that the length scale  $\eta_T$  is much smaller than the length scale of the large, energy-containing turbulent structures  $l_t$ , according to Eq. (2.4), the product of the velocity  $u_{\eta_T}$  and the length scale  $\eta_T$  is given by

$$u_{\eta_T} \cdot \eta_T \sim \varepsilon^{1/3} \cdot \eta_T^{4/3}; \quad \eta \ll \eta_T \ll l_t. \quad (2.5)$$

The substitution of  $u_{\eta_T} \cdot \eta_T$  in Eq. (2.1) by Eq. (2.5) results in a scaling-relation for the smallest temperature length scale depending on the molecular diffusivity  $a$  and the dissipation rate  $\varepsilon$ . It is the basis for the definition of the Obukhov-Corrsin-scale (Obukhov (1949), Corrsin (1951))

$$\eta_{T_{OC}} \equiv \left( \frac{a^3}{\varepsilon} \right)^{1/4}; \quad Pr \ll 1; \quad \eta_T \gg \eta \quad (2.6)$$

for quantification of the smallest temperature length scale in turbulent flow for fluids with Prandtl numbers of  $Pr \ll 1$ .

## 2.2 Fluids with $Pr \gg 1$

For fluids with Prandtl numbers of  $Pr \gg 1$ , temperature fluctuations persist for length scales smaller than the Kolmogorov length scale. This is obvious from inferring the specific Reynolds number and Péclet number

$$\begin{aligned} Re_\eta &= \frac{u_\eta \cdot \eta}{\nu} \sim 1 \\ Pe_{\eta_T} &= \frac{u_{\eta_T} \cdot \eta_T}{a} \sim 1 \end{aligned} \quad , \quad \text{with } a \ll \nu \quad \text{for } Pr \gg 1 \quad \rightarrow \quad \frac{u_{\eta_T} \cdot \eta_T}{\nu} \ll 1. \quad (2.7)$$

With the assumption that length scales grow with velocities, the smallest temperature scale  $\eta_T$  is smaller than the Kolmogorov length scale  $\eta$ ,

$$\eta_T \ll \eta \quad \text{for } Pr \gg 1. \quad (2.8)$$

While the energy transport by inertia-induced vortex decay within the framework of the energy cascade ends due to dissipation, advective heat transport by shear motion of the flow field remains for smaller length scales, as described by Batchelor (1959). The process is schematically sketched in Figure 2.1 b with the length scale dependent subranges transferred from the corresponding spectral subranges of the temperature variance spectrum (Tennekes and Lumley (1972)). Within the viscous-convective subrange, flow movement is dominated by shear flow and heat is solely transferred by advection. Per definition, the viscous-convective subrange starts with the dissipation range, i. e. with a non-negligible increase of viscous friction effects on the decaying vortices in the cascade process. It ends when the length scales of the shear flow motion are so small that molecular conduction contributes substantially to the heat transfer indicating the start of the viscous-diffusion subrange. The advective heat transport by turbulent shear motion of flow structures with the length scale  $\eta_T$  and the velocity  $u_{\eta_T}$  is fully balanced by molecular heat flux  $a \cdot \Delta T / \eta_T^2$ . Thus, it is convenient to assume that there is no relevant contribution from turbulence-induced heat transport by advection from flow structures with length scales of  $l < \eta_T$ . Since shear flow motion of flow structures with length scales of  $l \leq \eta$  is dominated only by viscosity, the motion of flow structures limited to the scale range from  $\eta$  down to the length scale of their disappearance is attributed to Stokes flow. While the advective heat transfer is still determined by turbulence, the change of velocity gradients of the shear flow is uniform (Batchelor (1959)) and the Kolmogorov scales and the smallest temperature scales follow the linear relation

$$\frac{u_{\eta_T}}{\eta_T} \sim \frac{u_\eta}{\eta}; \quad l \leq \eta. \quad (2.9)$$

With Eq. (2.9), Eq. (2.1) results in

$$\eta_T^2 \sim \frac{\eta}{u_\eta} \cdot a ; \quad l \leq \eta . \quad (2.10)$$

The dissipation rate  $\varepsilon$  can be approximated by means of an order of magnitude estimation for the dissipation function of the internal energy with the Kolmogorov scales (Davidson (2015)),

$$\varepsilon \sim \nu \cdot \left( \frac{u_\eta}{\eta} \right)^2 . \quad (2.11)$$

The substitution of  $\eta/u_\eta$  in Eq. (2.10) by  $\sqrt{\nu/\varepsilon}$  according to Eq. (2.11) leads to a scaling-relation for the smallest scale of heat transfer in turbulent flow in dependence of the dissipation rate  $\varepsilon$  and molecular properties  $a$  and  $\nu$ . It defines the Batchelor-scale

$$\eta_{TB} \equiv \left( a^2 \cdot \frac{\nu}{\varepsilon} \right)^{1/4} ; \quad Pr \gg 1 , \quad \eta_T \ll \eta \quad (2.12)$$

for quantification of the smallest temperature length scale of turbulent flow for fluids with Prandtl numbers of  $Pr \gg 1$ .

### 3 Summary

A heuristic perspective on the scale separation was presented. Here, the turbulence-induced advection of a turbulent flow structure generates a corresponding temperature gradient and, thus, causes a heat flux due to molecular conduction. The specific advection-diffusion equation for a Péclet number of unity leads to the scale at which the advective heat transport by a turbulent flow structure is fully balanced by molecular heat conduction and defines the smallest temperature scales. By means of this simple scale-depended consideration for specific heat transfer of turbulent flow, the smallest temperature length scale for fluids with Prandtl numbers  $Pr \ll 1$  and  $Pr \gg 1$  can be derived.

## References

- Batchelor, G. K. (1959). Small-scale variation of convected quantities like temperature in turbulent fluid - Part 1. General discussion and the case of small conductivity. *Journal of Fluid Mechanics*, 5(1):113-133.
- Corrsin, S. (1951). On the Spectrum of Isotropic Temperature Fluctuations in an Isotropic Turbulence. *Journal of Applied Physics*, 22: 469-473.
- Davidson, P. A. (2015). *Turbulence - An Introduction for Scientists and Engineers*. Oxford University Press, Oxford, 80.
- Frisch, U. (1995). *Turbulence: The Legacy of A. N. Kolmogorov*. Cambridge University Press, Cambridge, 102.
- Kolmogorov, A. N. (1941). Local structure of turbulence in an incompressible viscous fluid at very large Reynolds numbers. *Dokl. Akad. Nauk SSSR*, 30: 299-303.
- Obukhov, A. M. (1949). Structure of temperature field in turbulent flow. *Izvestiya Seriya Geograficheskaya i Geofizicheskaya*, engl. Übersetzung FTD-HT-23-394-70, 13(1):58-69
- Tennekes, H. and Lumley, J. L. (1972). *A First Course in Turbulence*. MIT Press, Cambridge, Massachusetts, 286.





# Technical approach and realization of a contactless, inductive flowmeter - the Phase-Sensitive Flowmeter

*Dominique Buchenau*

*Ernst-Abbe-Hochschule Jena, Dept. SciTec, Jena*

## Abstract

The development of contactless operating measurement technique reveals as a complex but promising trend in the field of sensor technology. The clear advantage of contactless sensor systems is, that no physical contact or other connections are necessary on the object to be measured. The advantage of contactless, inductive velocity measurement techniques unfold his full potency in the field of sensors applied to fast rotated engine parts, for example, shaft drives in production facilities, converting plants, casting of liquid metals or cooling of GEN-IV Heavy Liquid Metal Fast Reactors (LMFR) and transmutation systems. The approach of the current paper is targeted on the well-investigated idea, that the movement of an electrically conducting body in presence of an external, alternating magnetic induction field alters the phase or amplitude distribution along the penetration depth. The penetration depth depends on the excitation frequency of the external field, the electrical conductivity of the measurement object and its magnetic permeability. Therefore, it is from a certain importance to distinguish electrically conductive materials from materials which combine conductive with ferromagnetic properties. The classification of contactless flowmeters and velocity sensors depends mainly on the generation of the external magnetic field, necessary for the interaction with an electrically conducting fluid flow. Known are flowmeters like *Shercliff's Magnetic Flywheel* or arrangements collected under the denomination *Lorentz-Force-Velocimetry*. Such principles are based on the interaction of permanent magnets, mounted in rotatable or displaceable bearings with an electrically conducting body or fluid. For flowmeters, like the so-called *Phase-Sensitive-Flowmeter* the magnetic field is generated by a transmitter coil, driven by a harmonically or pulsed electrical current. According to Faraday's law of induction, every change in the magnetic field strength over time results in a ring voltage. If the change in induction takes place in an electrically conductive material, the induced voltage gives rise to an electric current,

which is referred to as eddy current. This eddy current in turn generates a magnetic induction field, which is directed in such way, that it opposes the exciting induction field. The superposition of the applied external magnetic induction field and the induced magnetic field by the eddy currents within a conducting material follows a well-defined amplitude and phase distribution. That phase distribution is furthermore altered in dependence of the velocity of the electrically conducting material in interaction with the external excitation field. The velocity dependent phase shift can be applied to measure the averaged velocity of a solid body or a fluid. A common and useful advantage using contactless, electromagnetic flowmeters is the possibility to circumvent difficulties related to chemical abrasiveness, interfacial- and temperature dependent boundary effects. The avoidance of any locomotive parts as a typical feature of permanent magnet-based systems relieves the contactless, electromagnetic flowmeter from mechanical hysteresis effects, as thermally driven aging effects of the applied bearings and holdings as well as the inertia determined effects. In the present publication an electrotechnical description of a *Phase-Sensitive-Flowmeter* is presented. Basic dependencies, different embodiments and some selected test results from experimental campaigns are illustrated and discussed. The flow of liquid metal is approximated by a conducting layer of a certain dimension in the direction of the applied magnetic field.

**Keywords:** Electrical conductivity, magnetic permeability, magnetic Reynolds number, frequency, amplitude, magnetic flux, induction, phase-shift, temperature, drift, calibration, lock-in amplifier, Phase-Sensitive-Flowmeter

## 1 Introduction

The controlled transport of liquid metals is of critical importance for various applications, like the apportioning of the melt in foundry processes or for particularly cases in applied research, such as automatic control of highly complex, thermo-hydraulic transmutation systems or spallation sources [1-3]. All these applications have in common, that they require a safe process management and an efficient commitment of available resources. The peculiar treatment, which liquid metals require are constituted by their special physical and chemical properties. Beside the elevated melting temperatures of liquid metals, the complex wetting behavior, the corrosiveness and abrasiveness impose special challenges with respect to the conveying equipment and with respect to the applicable measurement technique to control and to automatize such facilities. A small number of different contactless measurement techniques for liquid metals are known.

In the early sixties of the last century, J. A. Shercliff suggested an electromagnetic flowmeter which comprises a rotatable soft iron plate carrying a plurality of magnetic poles equidistantly spaced and each facing a pole of opposite polarity on the other [4-7]. The idea and implementation of such a device was the first embodiment of a highly effective contactless flowmeter for liquid metal applications. During the past years a lot of effort has been spent, to optimize and apply Shercliff's ideas in laboratory use and industrial applications [8]. Beside the mentioned advantages of contactless flowmeters, *Shercliff's flywheel* constitutes its industrial applicability since from a manufacturing point of view it is easy to realize. The avoidance of electrically energized parts, like coils, avoids any isolation and cooling problems in a wide range. A similar type of flowmeter consists of a single cylindrical permanent magnet magnetized perpendicularly to its symmetrical axis, about which it can freely rotate in the close vicinity of a liquid metal flow [9]. The electromagnetic torque on the magnet caused by the liquid metal flow sets the magnet into rotation. The equilibrium rotation rate depends only on the flow rate and the geometrical properties of the magnet and the channel or pipe. A third contactless electromagnetic flowmeter based on permanent magnets has been recently published under the name *Lorentz force velocimetry* [10]. As the name suggests, the Lorentz force sensor measures the electromagnetic force exerted by the flow on a closely placed permanent magnet. The force behaves proportional to the electrical conductivity of the fluid and the square of the applied magnetic field strength  $F_L \sim \sigma_F u B^2$ . According to Newton's third law of motion the induced Lorentz force is counter balanced by a force  $F_M$  which acts on the magnet. Beside permanent magnet-based flowmeters, several embodiments of a transformer-based principle have been presented and compared with each other [1-3, 11-14]. The so-called *Phase-Sensitive-Flowmeter* applies an alternating induction field to an electrically conducting pipe-flow. Two, only magnetically coupled receiver coils act as sensing elements, which are equidistantly spaced to the emitter coil. The whole set-up is working as an intersected transformer with two secondary coils. The application of AC-signals enlarges the number of possible measuring quantities, like amplitude, phase- or frequency-shift. Especially the detection of the flow dependent phase-shift of induced signals between the receiver and emitter coil turned out to be very insensitive against electromagnetic noise in the vicinity of the sensor. A closely related functional principle has been developed by [2,3]. Here, the *Phase-Sensitive-Flowmeter* consists of two emitter coils which are supplied with AC currents in opposite directions. The arrangement of emitter coils is comparable to an Anti-Helmholtz coil pair which surrounds a pipe, completely filled with liquid metal. In the symmetry plane between the oppositely directed magnetic induction fields, a third coil is installed which acts as a receiver coil. In the frame of the present publication four contactless flowmeters are compared to each other concerning technical and experimental indications.

Therefore, the present paper is organized as follows. The introduction is followed by a detailed technical description of the measurement principle. Beside the technical approaches a detailed description of the embodiments [1-3,11-14] of laboratory models is provided, followed by different experimental test cases and measurements.

Based on theoretical predictions, we compare the applicative potential of flowmeter principles, which are usually applied in measurement techniques. Finally, the paper is concluded by a short discussion of theoretical predictions and test results.

## 2 The Phase-Sensitive-Flowmeter

### 2.1 The Sensor without conducting layer

The phase shift is obtained from the solution of the differential equation of a periodically energized, series coil-resistor circuit, which is connected in parallel by a parasitic capacitance  $C$  of one receiver coil each in  $S_1$  &  $S_2$ .

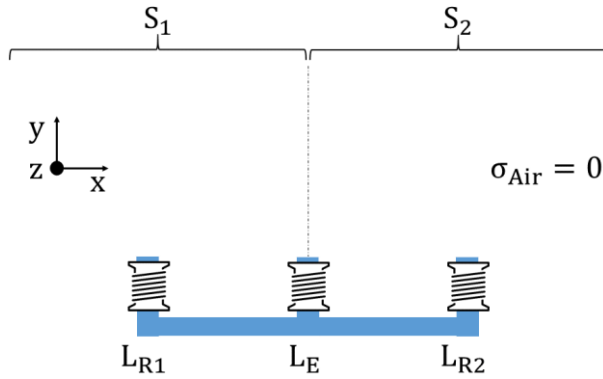


Figure 2.1: Combination of two magnetic circuits  $S_1$  &  $S_2$  to a phase-shift flowmeter. Magnetic flux guide in blue color,  $L_{R1}$  and  $L_{R2}$  are receiver coils,  $L_E$  depicts the emitter coil.

The phase shift between current and voltage in a single receiving coil  $L$  is given by:

$$\Delta\varphi = \arctan\left(-\omega_A C R^{-1}\left(R^2 + \omega_A^2 \cdot L^2 - \frac{L}{C}\right)\right) \quad (2.1)$$

For further considerations, it should be assumed, that the parasitic capacitance  $C$  is negligibly small and its influence becomes only effective at high excitation frequencies. This leaves the simplified expression for the phase calculation from Eq. (2.1):

$$\Delta\varphi = \arctan(\omega_A \cdot \tau) \quad (2.2)$$

in which  $\tau = L(\mu_r)R^{-1}$  denotes the time constant. The circular frequency is defined by  $\omega_A = 2\pi \cdot f_A$ . For the reduction of the magnetic stray field of the sensor and to enlarge the signal quality all coils are interspersed with laminated mild iron (blue structure in Fig. 2.1) providing a low magnetic resistance. The mentioned lamination of the flux iron reduces the eddy current-induced field displacement of the magnetic induction field at high frequencies (Skin-Effect). A phase shift  $\Delta\varphi_{ER}$  between the transmitter coil and one receiver coil (for same geometrical dimensions) appears as:

$$\Delta\varphi_{ER} = \arctan\left(\frac{\omega_A \tau_{ER}(\mu_{r(E)} - \mu_{r(R)})}{1 + (\omega_A \tau_{ER})^2 \mu_{r(E)} \mu_{r(R)}}\right) \quad (2.3)$$

According to Eq. (2.3) the following terms are agreed:

$$\omega_A L_0 R^{-1}(\mu_{r(E)} - \mu_{r(R)}) = \omega_A \tau_{ER}(\mu_{r(E)} - \mu_{r(R)}) = \omega_{0(E)} - \omega_{0(R)} \quad (2.4)$$

in which  $L_0$  denotes the inductance of the air-core coil as an emitter- or receiver coil (same dimensions and windings) and  $\omega_{0(E)}$  and  $\omega_{0(R)}$  dimensionless frequencies. For the phase-shift between emitter and one receiver coil we write:

$$\Delta\varphi_{ER} = \arctan\left(\frac{\omega_{0(E)} - \omega_{0(R)}}{1 + \omega_{0(E)} \cdot \omega_{0(R)}}\right) \quad (2.5)$$

The peak frequency  $\hat{\omega}_A$  of the transformer arrangement can be calculated from Eq. (2.3) applying  $\partial_{\omega_A} \Delta\varphi_{ER} = 0$  to:

$$\hat{\omega}_A = \frac{1}{\tau_{ER}} \cdot \sqrt{\frac{1}{\mu_{r(E)} \mu_{r(R)}}} = \frac{1}{\tilde{\tau}_{ER}} \quad (2.6)$$

## 2.2 The sensor with conducting layer

For the case, that an electrically conducting layer is inserted into the sensor (cf. Fig. 2.2), Eq. (2.3) must be extended by the characteristic diffusion time  $\tau_D = \mu_0 \mu_{r(F)}(f_A) \sigma_F D_0^2$  in which  $\mu_{r(F)}(f_A)$  describes the frequency dependent relative permeability  $\mu_{r(F)}(f_A)$  and the electrical conductivity of the layer, denoted by  $\sigma_F$ .

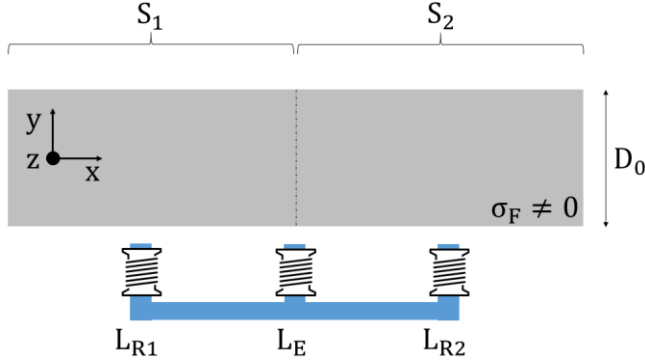


Figure 2.2: Combination of two magnetic circuits  $S_1$  &  $S_2$  to a phase-shift flowmeter with conductive layer (infinite in  $z$ -direction) of liquid medium ( $\sigma_F \neq 0$ ).

Therefore, we obtain:

$$\Delta\varphi_{ER} = \arctan\left(\frac{\omega_A \cdot ((\tilde{\epsilon}_E - \tilde{\epsilon}_R) + \tau_{D(0)})}{1 + (\omega_A \cdot (\tilde{\epsilon}_{ER} + \tau_{D(0)}))^2}\right) \quad (2.7)$$

If the electromagnetic properties of the conducting layer, such as electrical conductivity  $\sigma_F$  or magnetic permeability  $\mu_{r(F)}$  are varied for constant  $D_0$ , we receive:

$$\Delta\tau_D \approx \left(\frac{\Delta\sigma_F(T)}{\sigma_F} + \frac{\Delta\mu_{r(F)}}{\mu_{r(F)}}\right) \cdot \tau_{D(0)} \quad (2.8)$$

For isothermal conditions, with  $\Delta\sigma_F(T) = 0$ , we find:

$$\Delta\tau_D \approx \left(\frac{\Delta\mu_{r(F)}}{\mu_{r(F)}}\right) \cdot \tau_{D(0)} \quad (2.9)$$

According to the law of induction, every change in the magnetic field strength over time results in a ring voltage. If the change in induction takes place in an electrically conductive material, the induced voltage gives rise to an electric current, which is referred to as eddy current. This eddy current in turn generates a magnetic induction field, which is directed in such way, that it opposes the exciting induction field. At high frequencies, the resulting weakening of the exciting field means that almost no magnetic field can be detected inside the conductive material.

This shielding effect of the eddy currents is known as the Skin-Effect. Therefore, eddy currents will have a considerable influence on the relative magnetic permeability of electrically conductive materials. Since eddy currents are generated not only by a time-

dependent change in induction, but also by the movement of the material with the speed  $u$  in an induction field, the change in permeability of the material must also be a function of the speed  $u$  and thus of the magnetic Reynolds number  $Rm$ :

$$Rm = \mu_0 \mu_{r(F)} (f_A) \sigma_F u_0 D_0 = \frac{b_{ind.}}{B_0} = \frac{j_{ind.}}{j_0} \quad (2.10)$$

The magnetic Reynolds number appears as the ratio between the induced magnetic field  $b_{ind.}$  to the applied magnetic field  $B_0$ . The linear superposition between the induction field  $B_0$  and the induced magnetic induction field  $b_{ind.}$  can be expressed by:

$$\frac{B_0 \pm b_{ind.}}{B_0} = 1 \pm Rm = 1 \pm \frac{u_0}{D_0} \cdot \Delta\tau_D = 1 \pm \frac{\Delta\tau_D}{\tau_{D(0)}} \quad (2.11)$$

That means, the diffusion time of the magnetic field in the electrically conductive medium decreases by  $Rm$  in the sphere of influence of  $S_1$  and decreases by the order of magnitude of  $Rm$  in the sphere of  $S_2$  (cf. Fig. 2.3 and 2.4).

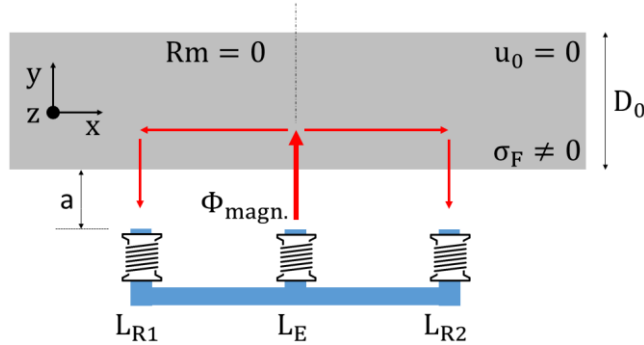


Figure 2.3: Equal distribution of magnetic flux  $\Phi_{magn.}$  within the electrically conductive layer.

According to that result, Eq. (2.7) turns to:

$$\Delta\varphi_{ER}(Rm) = \arctan \left( \frac{\omega_A \cdot ((\tilde{\tau}_E - \tilde{\tau}_R) + \tau_{D(0)} \cdot (1 \pm Rm))}{1 + (\omega_A \cdot (\tilde{\tau}_{ER} + \tau_{D(0)} \cdot (1 \pm Rm)))^2} \right) \quad (2.12)$$

The modulation of the phase-shift by  $Rm$  shifts the peak frequency. The peak frequency  $\hat{\omega}_{A(Rm)}$  can be calculated from Eq. (2.12) applying  $\partial_{\omega_A} \Delta\varphi_{ER}(Rm) = 0$  to:

$$\hat{\omega}_A(Rm) = \frac{1}{\tau_{ER} \cdot \sqrt{\mu_{r(E)} \mu_{r(R)} + \tau_{D(0)} \cdot (1 \pm Rm)}} \cong \frac{1}{\tilde{\tau}_{ER} + \tau_{D(0)} \cdot (1 \pm Rm)} \quad (2.13)$$

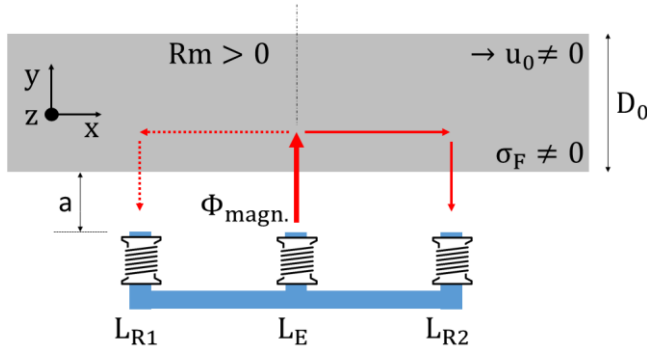


Figure 2.4:  $R_m$ -modulated distribution of magnetic flux  $\Phi_{\text{magn.}}$  within the conductive layer.

## 3 Design of a Phase-Sensitive-Flowmeter

### 3.1 Emitter- and receiver coils on opposite sides of the layer

The design of the contact less *Phase-Sensitive-Flowmeter* is based on a transformer principle (cf. Fig. 5.1 and 5.2) operating without any locomotive parts [1-3,11-14]. The detector head of the *Phase-Sensitive-Flowmeter* (cf. Fig. 3.1) consists of two receiving coils and one emitter coil, placed on opposite sides of the electrically conducting medium. The emitter coil  $L_E$  is fed by a temperature stabilized alternating current  $I_E$  of constant angular frequency  $\omega_A = 2\pi f_A$ . For the reduction of the magnetic stray field of the sensor and to enlarge the signal quality all coils are interspersed with laminated mild iron (blue in Fig. 3.1) providing a low magnetic resistance of the sensor arrangement. The alternating magnetic flux is perpendicularly orientated to the propagation direction of the electrically conducting material (cf. Fig. 3.1).

A symmetrical adjustment of the *Phase-Sensitive-Flowmeter* arrangement is achieved for the case that the emitter flux is distributed half-and-half over both receiver coils, when the conductive layer is at rest. The equal distribution of the alternating magnetic flux is disturbed by the movement of the conducting layer. The information about the averaged velocity  $u_0$  or flow rate  $Q$  is provided by a voltage difference  $U_D$  or phase-shift  $\Delta\varphi_{ER}(R_m)$  between the emitter and receiver coils according to Eq. (2.12). The induced phase-shift  $\Delta\varphi$  is proportional to the magnetic Reynolds number  $R_m$ . Contributing parameters beside the permeability are the electrical conductivity of the layer  $\sigma_F$ , the averaged velocity of the layer  $u_0$  and the dimension of the pipe or channel  $D_0$ . The



dimensionless frequency  $\omega_0$  of the *Phase-Sensitive-Flowmeter* contributes to the magnitude of a measurable phase-shift.

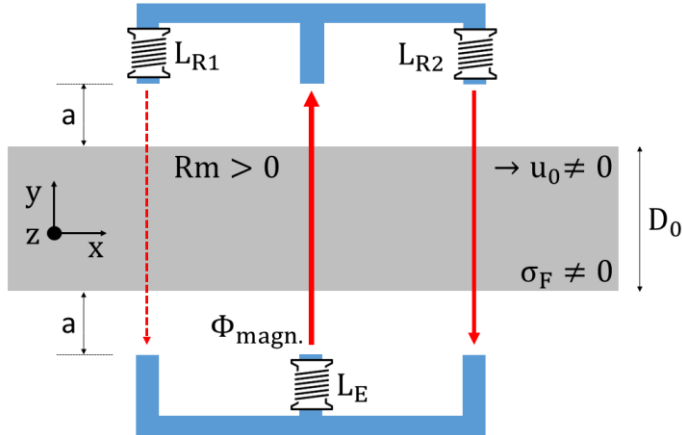


Figure 3.1: Equal distribution of magnetic flux  $\Phi_{\text{magn.}}$  within the electrically conductive layer.

The flow rate sensor must be calibrated concerning the distance “a” between the coils and the conducting layer and a stable temperature of the sensor. Some comparable measurements of the flow-induced phase-shift in dependence of the flow profile at an emitter frequency of  $f_A = 620 \text{ Hz}$  are shown in Fig. 3.2. For the case of an asymmetric flow profile the flow was directed, by means of a variation of the cross-section of a faucet  $A/A_0$ , close to the wall located in the vicinity of the emitter coil (cf. Fig. 3.2) and the receiver coils (cf. Fig. 3.2).

The distance between the faucet and the *Phase-Sensitive-Flowmeter* was chosen to  $l = 125 \text{ mm}$  which is smaller than the homogenization length defined by  $l_H \sim (10 - 20)D_0$ . A remarkable property of the transformer principles compared to the electromechanical principles is that the flow measurement is obviously not affected from an asymmetric flow profile for low velocities of the electrically conducting layer and within the plane in which emitter- and receiver coils are arranged (cf. Fig. 3.3).

The one-sided arrangement of transmitter and receiver coils is affected by an asymmetric flow profile.

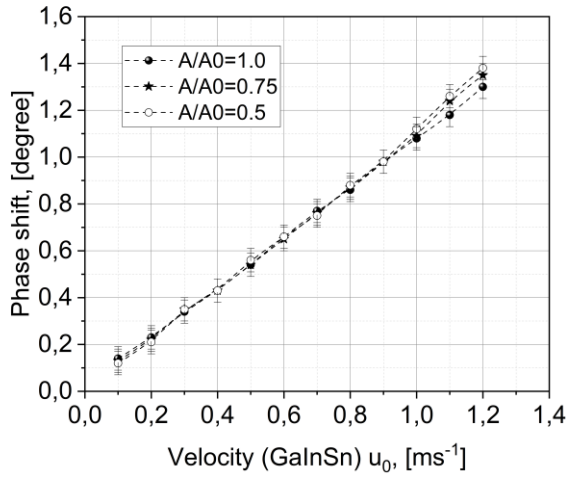


Figure 3.2: Measurement of the flow-induced phase-shift in dependence of the flow profile at an emitter frequency of  $f_A = 620$  Hz and  $R_m < 0.1$ . The flow is directed close to the wall located in the vicinity of the emitter coil (GalnSn-test facility at HZDR).

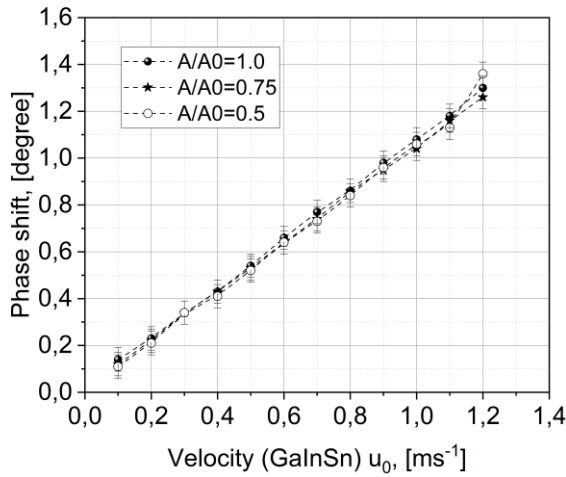


Figure 3.3: Measurement of the flow-induced phase-shift in dependence of the flow profile at an emitter frequency of  $f_A = 620$  Hz and  $R_m < 0.1$ . The flow is directed close to the wall located in the vicinity of the receiver coils (GalnSn-test facility at HZDR).

### 3.2 Phase-Sensitive-Flowmeter with coaxial coils

An alternative design of a *Phase-Sensitive-Flowmeter* has been suggested by [2,3]. Here, two active coils are energized by a harmonic electric current (cf. Fig. 5.3) generating a harmonically oscillating magnetic induction field. A receiver coil is placed in the symmetry plane between the emitter coils. For a perfect adjustment of the flowmeter the superposition of both induction fields vanishes for the case, that both emitter currents are phase-shifted by 180 degrees. The movement of an electrically conductive material asymmetrizes the distribution of the superpositioned induction field in the order of magnitude of the magnetic Reynolds number. In contradiction to the proposed design in [2,3], the *Phase-Sensitive-Flowmeter* is operated as shown in Fig. 3.4. The flowmeter consists of two receiver coils  $L_{R1}$  (200 windings) and  $L_{R2}$  (200 windings) and one emitter coil  $L_E$  (100 windings), which is supplied by an alternating electric current  $I_E$ . The averaged spacing between both receiver coils to the emitter coil is 15 mm.

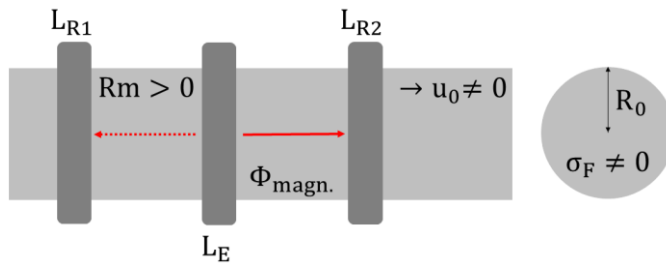


Figure 3.4:  $Rm$ -modulated distribution of magnetic flux  $\Phi_{\text{magn.}}$  within the conductive layer.

Figure 3.5 shows the linear transfer behaviour with increasing excitation frequency for different transmitter coil currents (RMS). As soon as the flow of electrically conducting fluid is turned on the magnetic field lines are dragged downstream, where a receiver coil  $L_{R1}$  is placed. The magnitude of the measurement effect is proportional to  $Rm$ . The flow direction can be detected by the sign of the measured RMS signal from the receiver coil or the phase shift between the emitter and receiver coils.

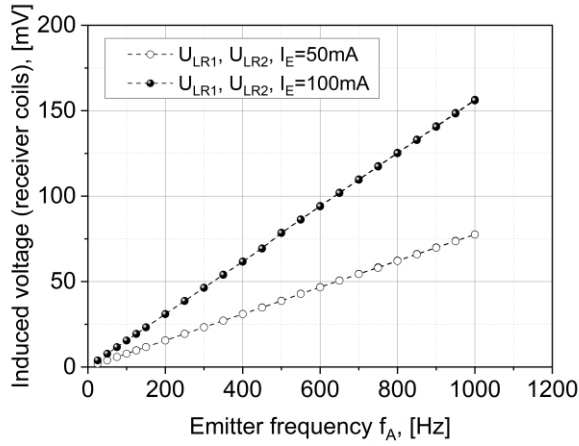


Figure 3.5: Induced receiver-coil voltages for the empty flowmeter at different frequencies and different emitter-coil current, according to Faraday's law of induction.

Referring to Fig. 3.6 the evaluable frequency range of the flow induced phase-shift exhibits an optimum, mainly determined by magnitudes which are contributing to the diffusion time  $\tau_{D(0)}$ . The evaluable frequency range was measured for an averaged velocity of  $u_0 = 1 \text{ ms}^{-1}$ .

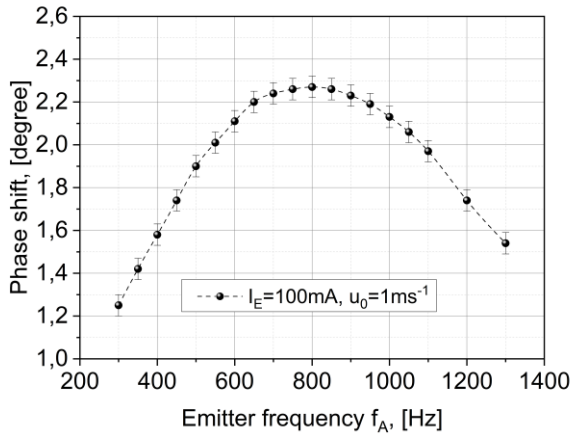


Figure 3.6: Frequency response for  $R_m < 0.1$  measured on an insulating pipe in dependence of the averaged GaInSn-flow for different emitter frequencies (GaInSn-test facility at HZDR).

The measurements of the flow induced phase-shift in dependence of the emitter frequency result in a linear dependence as shown in Fig. 3.7. Corresponding to Fig. 3.7 the steepest ascend of the phase-shift is obtained for the optimum frequency of about  $\hat{f}_A = 800$  Hz.

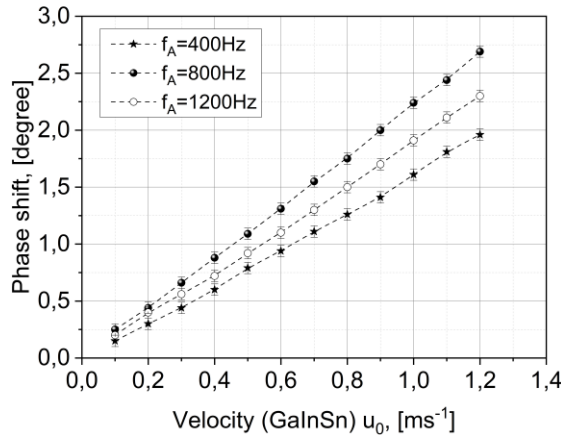


Figure 3.7: Flow induced phase-shift measured for  $R_m < 0.1$  on an insulating pipe in dependence of the averaged GalnSn-flow for different emitter frequencies (GalnSn-test facility at HZDR).

### 3.3 Phase-Sensitive-Flowmeter for local measurements

The *Phase-Sensitive-Flowmeter* (cf. 5.4) consists of an axial arrangement of two receiving coils  $L_{R1}$  and  $L_{R2}$  and an emitter coil  $L_E$ , whereas the emitter is placed in the center between both receiver coils [15-17]. Contrary to the descriptions from the sources mentioned, the sending coil is fed by a stabilized alternating current  $I_E$  of constant frequency.

All coils are encapsulated by a thin cylindrical shaped stainless-steel sheath (cf. 5.4). The alternating magnetic flux provided by the emitter coil enforces the volume around the stainless-steel sheath with a magnetic flux at an adjusted angular frequency (cf. Fig. 3.8). According to a symmetrical arrangement of the sending and receiving coils the equal distribution of the alternating magnetic flux over the receiver coils can be disturbed by the movement of the conducting flow around the sheath (cf. Fig. 3.9).

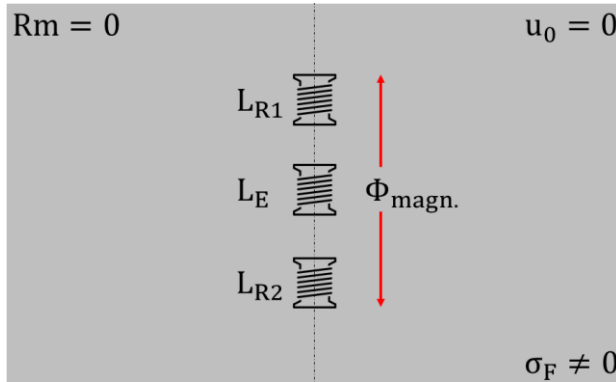


Figure 3.8: Local *Phase-Sensitive-Flowmeter* without flux guide immersed into a conductive layer of liquid medium. Equal distribution of magnetic flux for  $Rm = 0$  (sheath not shown for simplicity).

The information about the averaged velocity  $u_0$  is provided by a voltage difference or phase-shift between the receiver coils. The phase-shift of the flowmeter is proportional to the magnetic Reynolds number  $Rm$ . In contradiction to the flow dependent voltage difference the phase-shift turned out to be less sensitive against electromagnetic distortions. During experimental investigations Lock-in amplifiers were used to measure the averaged velocity dependent phase-shifts. These available Phase-sensitive-amplifiers offer an angle resolution of  $10^{-3}$  degrees combined with a high drift stability.

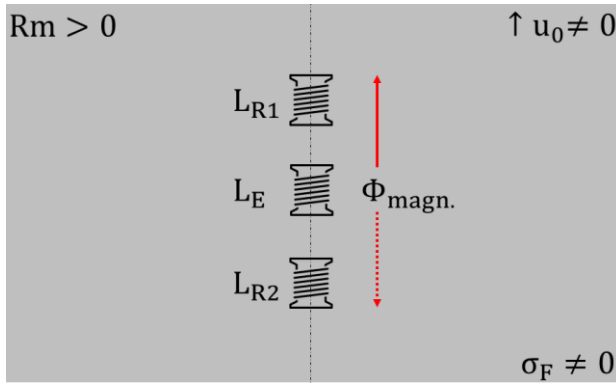


Figure 3.9: Local *Phase-Sensitive-Flowmeter* without flux guide immersed into a conductive layer of liquid medium. Unequal distribution of magnetic flux for  $Rm \neq 0$  (sheath not shown for simplicity).

### 3.3.1 Design of the Phase-Sensitive-Flowmeter

The coil holder in the selected shape is made from PVC (test version) but fully producible in stainless steel  $\mu_r \approx 1$  or ceramics for extended operational temperatures. The sensitive length of the sensor is 30 mm. The emitter coil holds 200 windings with a wire diameter of 0.24 mm. Both receiver coils hold 400 windings each with a wire diameter of 0.15 mm. The emitter coil provides an ohmic resistance of  $R_E=2.6$  Ohm the receiver coils provide a resistance of  $R_R=13.1$  Ohm each. The sheath is made from stainless steel, thickness of the wall: 0.3 mm. The whole diameter (outer diameter) of the local probe measures 12 mm. The flow direction is such, that the mean flow direction is parallelly aligned to the longitudinal axis of the sensor. The interaction between the magnetic induction field and the flow takes place mainly in the skin depth  $\delta_E$ .

### 3.3.2 Experimental procedures and results

Figure 3.10 unveils the flow induced voltage-difference measured between both receiver coils. As it can be seen, the dependence of the voltage-difference as a function of the GaInSn-velocity follows a linear function for magnetic Reynolds numbers smaller than  $Rm < 1$ .

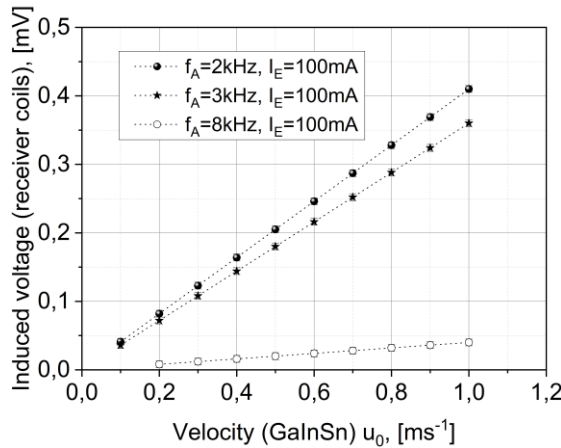


Figure 3.10: Flow induced voltage-difference in dependence of the averaged GaInSn-velocity measured with the local *Phase-Sensitive-Flowmeter* (GaInSn-test facility at HZDR).

The measured voltage-difference appears being strongly dependent on the selected emitter frequency, determining the interaction volume between the flow and the emitter field. The input-current of the emitter-coil was adjusted to  $I_E=100$  mA (RMS). Referring to Figure 3.11 the evaluable frequency range of the flow induced phase-shift exhibits an optimum determined by the electrical characteristics of the emitter and receiver coils.

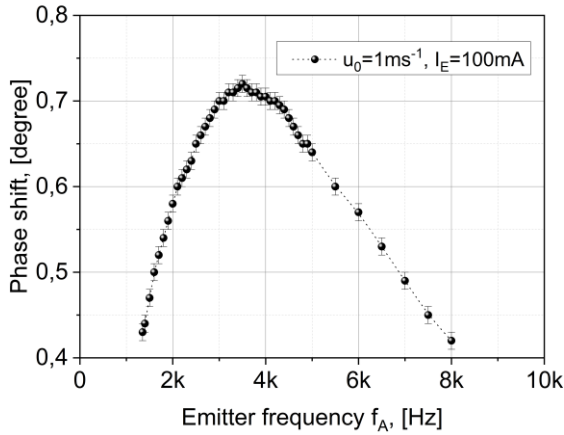


Figure 3.11: Phase response of the local *Phase-Sensitive-Flowmeter* (GaInSn-test facility at HZDR).

Distinctive is the appearance of an optimum close to  $\hat{f}_A = 3.5$  kHz. In contrast to the measurement of the flow-induced voltage-difference  $U_D$  between the receiver coils, the measurement of the phase-shift is stable for input currents of approximately 10 mA (RMS). The measurement of the flow induced phase-shift appears as expected in a linear dependence from the averaged GaInSn-velocity (cf. Fig. 3.12).

In contradiction to the voltage-difference measurements, the detection of velocities smaller than  $0.1 \text{ ms}^{-1}$  are possible because of the high sensitivity of the applied Lock-in principle. Based on the analysis of several measurements (10 periods of the induced signal) at  $\hat{f}_A = 3.5$  kHz, the temporal resolution of the principle was determined to 3 ms. The penetration depth of the applied magnetic field into the GaInSn-melt decreases with the adjusted emitter frequency.



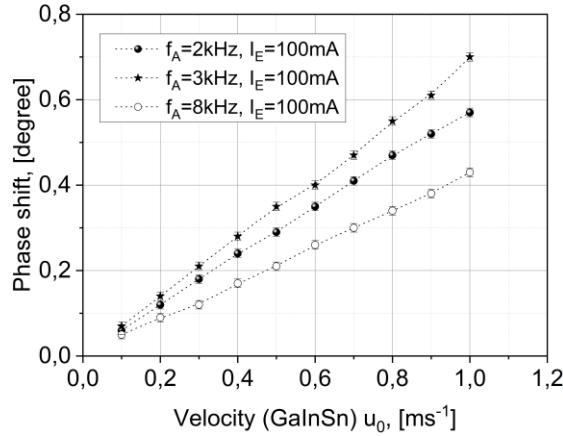


Figure 3.12: Linear dependence of the measured phase-shift from the adjusted GaInSn-velocity measured with the local *Phase-Sensitive-Flowmeter* (GaInSn-test facility at HZDR).

## 4 Summary

In the present contribution an electrotechnical description of a *Phase-Sensitive-Flowmeter* is presented, based on electrotechnical ( $L, R, C$ ), physical ( $\mu_{T(F)}(f_A), \sigma_F$ ), fluidodynamical ( $u_0, R_m$ ) and geometrical input quantities ( $D_0, a$ ) in different embodiments. Related test results from experimental campaigns are illustrated and discussed. Various embodiments of the functional principle have been proposed and realized. All proposed designs or embodiments are operated as *Phase-Sensitive-Flowmeters*. It has been found, that these types of flow sensors have a non-negligible dependence on the fluid temperature, which makes it necessary to calibrate the flowmeters for operational conditions. In future, the introduced electrotechnical model of the sensor will be further improved by temperature compensation methods.

In retrospect, the important and trend-setting suggestions and proposals of Robert Stieglitz should be emphasized once again.

## 5 Appendix



Figure 5.1: Phase-Sensitive-Flowmeter (one-sided, HZDR).

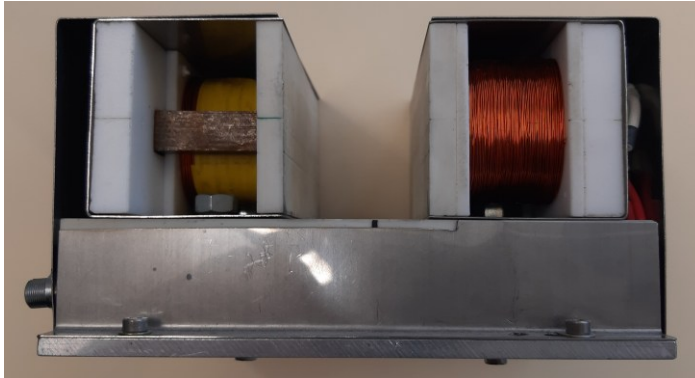


Figure 5.2: Phase-Sensitive-Flowmeter (two-sided, HZDR).

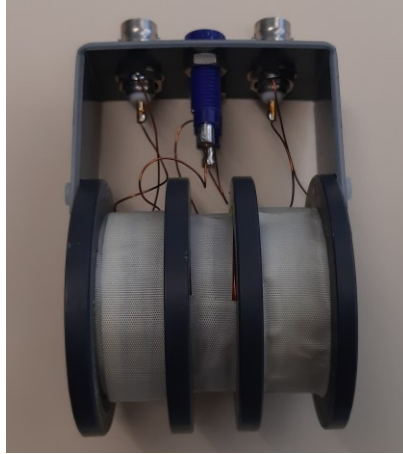


Figure 5.3: Phase-Sensitive-Flowmeter with coaxial coils (HZDR).

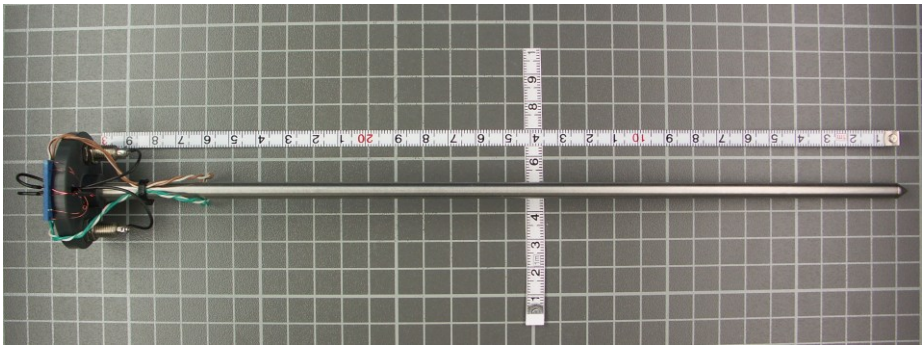


Figure 5.4: Phase-Sensitive-Flowmeter for local measurements (HZDR).

## References

- [1] Buchenau, D.; Eckert, S.; Gerbeth, G.; Stieglitz, R.; Dierckx, M. (2011) Measurement technique developments for LBE flows, *Journal of Nuclear Materials*, 415 (3), pp 396-403.
- [2] Schulenberg, T., Stieglitz, R., Müller, G., Konys, J. (2007), Liquid metal technology development in the Karlsruhe Liquid metal Laboratory (KALLA), *Jahrestagung Kerntechnik*, Karlsruhe, 22.-24. Mai 2007.
- [3] Schulenberg, T; Stieglitz, R. (2010) Flow measurement techniques in heavy liquid metals, *Nuclear Engineering and Design*, 240 (9), pp. 2077-2087
- [4] Shercliff, J. A. (1953) The theory of the D.C. electromagnetic flow meter for liquid metals, Atomic Energy Research Establishment: Report X/R 1052.
- [5] Shercliff, J. A. (1957) Improvements in or relating to Electromagnetic Flow-meters, Patent No. 13957/57.
- [6] Shercliff, J. A. (1962) The Theory of Electromagnetic Flow Measurement Cambridge University Press, Cambridge.
- [7] Shercliff, J.A. (1987), The Theory of Electromagnetic Flow Measurement – Induction Devices, Cambridge University Press, ISBN 9780521335546.
- [8] Buchenau, D.; Galindo, V.; Eckert, S. (2014) The magnetic flywheel flow meter: Theoretical and experimental contributions, *Applied Physics Letters*, 104 (22), 223504
- [9] Priede, J.; Buchenau, D.; Gerbeth, G. (2011) Single-magnet rotary flowmeter for liquid metals, *Journal of Applied Physics*, 110.
- [10] Thess, A.; Votyakov, E. V.; Kolesnikov, Y. (2006) *Phys. Rev. Let.* 96, 164501
- [11] Weissenfluh, Th. (1985), Probes for Local Velocity and Temperature Measurements in Liquid Metal Flow, *Int. J. Heat and Mass Transfer*, 28 (8), pp. 1563-1574.
- [12] Priede, J.; Buchenau, D.; Gerbeth, G. (2011) Contactless electromagnetic phase-shift flowmeter for liquid metals, *Measurement Science and Technology*, 22, 055402.
- [13] Ratajczak, M.; Hernández, D.; Richter, T.; Otte, D.; Buchenau, D.; Krauter, N. and Wondrak, T. (2017) Measurement techniques for liquid metals, *Materials Science and Engineering*, 228 (1).

- [14] Looney, R.; Priede, J. (2019) Concept of a next-generation electromagnetic phase-shift flowmeter for liquid metals, *Flow Measurement and Instrumentation* 65, pp 128-135.
- [15] Zirkunov, V. E.; Scheigur, B. D.; Schermons, G. J.; Kalnins, R. K. (1973) *Kontaktlose Kontrolle von Flüssigmetallströmungen*, Riga, Zinatne, pp 49-51.
- [16] Forbriger, J.; Stefani, F. (2015) Transient eddy current flow metering, *Measurement Science and Technology*, 26, 105303
- [17] Looney, R.; Priede, J. (2018) Alternative transient eddy-current flowmetering methods for liquid metals, *Flow Measurement and Instrumentation*, <https://doi.org/10.1016/j.flowmeasinst.2018.11.011>.



# Applying solar energy for cooling – a basic thermodynamic analysis

*Hans-Martin Henning*

*Fraunhofer Institute for Solar Energy Systems ISE, Freiburg, Germany and Institut für nachhaltige technische Systeme INATECH, Technische Fakultät, Albert-Ludwigs-Universität, Freiburg, Germany*

## Abstract

To use solar energy for driving a cooling process seems to be a promising application of heat transformation processes, in particular under conditions where cooling loads are – at least partly – caused by solar irradiation. For many years significant research and development efforts have been made to develop solar cooling systems that use solar thermal collectors to provide heat as main driving energy for this purpose [1,2]. Mainly heat driven cooling processes using absorption or adsorption refrigeration technology were applied and overall systems were studied and optimized in many pilot and demonstration projects. At the time of carrying out these projects, photovoltaic conversion of solar energy into useful cooling turned out to be less promising regarding economic competitiveness due to the comparatively high cost for the solar generated electricity. As this situation regarding cost aspects has changed significantly it seems worthwhile to compare the two concepts under a new focus. In this paper basic thermodynamic relations are applied for this purpose. In summary, the result of this analysis indicates that using photovoltaic systems for cooling has several significant advantages compared to the use of solar thermal collectors.

**Keywords:** Heat transformation process; solar cooling; heat driven cooling; photovoltaic system; solar thermal collector system.

## 1 Introduction

Heat transformation processes are processes in which a useful heat flow takes place from a lower to a higher temperature – in other words, exactly the opposite of the heat flow that automatically takes place in nature and is directed from a higher to a lower temperature. Such heat transformation processes, which play an important role in many

technical applications, require a thermodynamic cycle. There are basically two main processes that can be considered for this, namely processes in which mechanical energy – or electrical energy in conjunction with an electric engine that provides mechanical energy – is used as driving energy source (see Figure 1.1) or processes that use high-temperature heat as driving energy source (see Figure 1.2) (for the following equations and definitions in chapter 1 see for instance [3]).

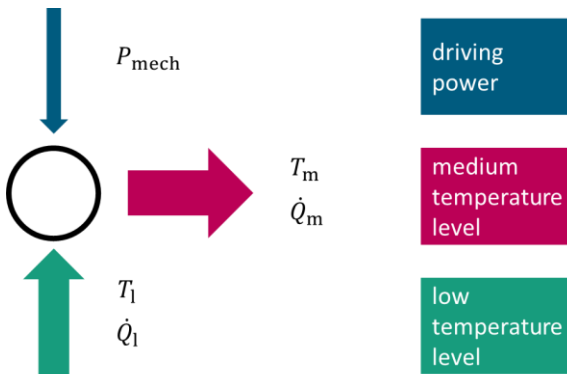


Figure 1.1: Mechanically driven heat transformation process.

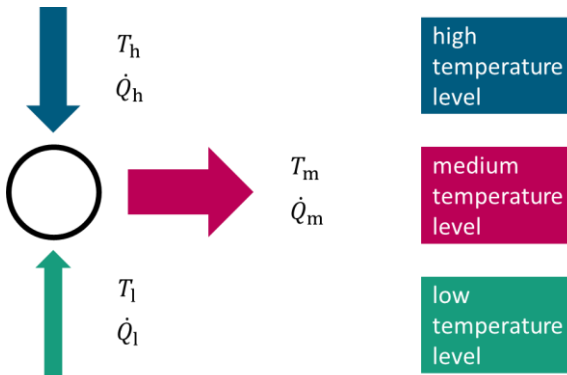


Figure 1.2: Heat driven heat transformation process.

For these processes, the maximum possible conversion efficiencies under the assumption of ideal, fully reversible conditions, i.e. without any irreversibilities, can be derived from the first and second laws of thermodynamics as a function of the respective temperatures. For a machine of the first type with mechanical (or electrical) driving



energy source, the coefficient of performance for cooling, defined as the fraction between useful heat flux and driving energy flux, is given by:

$$\varepsilon_{\text{cool,rev,mech}} = \frac{\dot{Q}_l}{P_{\text{mech}}} = \frac{T_l}{(T_m - T_l)}, \quad (1)$$

with

$\varepsilon_{\text{cool,rev,mech}}$  reversible coefficient of performance (COP) for cooling with mechanical driving energy source,

$\dot{Q}_l$  useful cooling capacity,

$P_{\text{mech}}$  mechanically driven energy flux,

$T_l$  low temperature (in K) at which cold is provided (heat is extracted) and

$T_m$  medium temperature (in K) at which (waste) heat is released.

The most widespread technical realization of mechanical heat transformation processes are vapor compression processes applying the Clausius-Rankine cycle and using refrigerants suitable for the particular temperature range, which is defined by the concrete application (e.g. building air-conditioning, refrigeration in industry of food sector, etc.). The basic process is composed of four phases: (1) the refrigerant evaporates in the evaporator which is heated by an external heat source; (2) the refrigerant in the gas phase is compressed in a mechanical compressor; (3) the refrigerant condenses at a higher temperature and pressure level in the condenser and releases heat to an external heat sink; (4) the refrigerant is fed back to the evaporator via an expansion valve (throttle). Based on this basic cycle, various improvements and optimizations are possible and used in the broad range of technical solutions using different types of compressors, heat exchangers, heat exchanger cascades, etc.

The corresponding equation of the reversible coefficient of performance for a chiller driven by high temperature heat is given by:

$$\varepsilon_{\text{cool,rev,therm}} = \frac{\dot{Q}_l}{\dot{Q}_h} = \frac{1 - \frac{T_m}{T_h}}{\frac{T_m}{T_l} - 1}, \quad (2)$$

with

$\varepsilon_{\text{cool,rev,therm}}$  reversible coefficient of performance (COP) for cooling with heat as driving energy source,

$\dot{Q}_h$  thermally driven energy flux and

$T_h$  high temperature (in K) at which the driving heat is provided.

The most widespread technical realization of such a thermally driven heat transformation is also based on the evaporation and condensation of refrigerants at different temperature and pressure levels, which, however, are undergoing a reversible bonding with a second substance (liquid or solid) after evaporation in order to be released at a higher temperature and pressure under the addition of the driving heat flux. In such machines using absorption (liquid sorbent) or adsorption (solid sorbent) processes, the mechanical compressor is therefore replaced by a "thermal compressor".

Real processes achieve only a fraction of the ideal coefficient of performance (COP) according to equations (1) and (2); this fraction is called the Carnot efficiency factor,  $\xi_{\text{Carnot}}$ , and is defined as:

$$\xi_{\text{Carnot}} = \frac{\varepsilon_{\text{real}}}{\varepsilon_{\text{rev}}} \quad (3)$$

with  $\varepsilon_{\text{rev}}$  denoting the reversible COP for the corresponding cycle and  $\varepsilon_{\text{real}}$  the COP of real technical systems. Independent of the type of cycle and its technical realization, the COP for the use as a heat pump,  $\varepsilon_{\text{hp}}$ , – i.e. the use of the heat flux at the medium temperature level as useful heat flux – is by 1 greater than the COP for cooling for same temperatures at all temperature levels:

$$\varepsilon_{\text{hp}} = 1 + \varepsilon_{\text{cool}}. \quad (4)$$

## 2 Comparison of solar electric and solar thermal cooling approaches

A promising application of heat transformation processes is to use solar energy for driving a cooling process. This is particularly valid under conditions, in which cooling loads are essentially induced by high solar radiation values, since under these conditions a high temporal correspondence between cooling load and the availability of solar energy for driving the cooling process can be expected. Such conditions are for instance given by cooling applications in buildings. In principle, the two previously described methods of cooling generation are suitable here: a mechanically driven vapour compression chiller in combination with the use of photovoltaic electricity generation for operating an electric engine can be applied on the one hand and a thermally driven chiller in combination with solar thermal collectors to provide the driving heat can be used on the other hand. These two concepts will be compared with each other based on

fundamental thermodynamic considerations under the general assumption that no optical concentration is applied.

## 2.1 Comparison under design conditions

For the comparison of solar cooling with solar thermal and solar electric processes, a typical application in the building sector is assumed: to operate a central cooling system, cold water is to be cooled from 12 °C to 6 °C, resulting in an average temperature of 9 °C on the cold side. A temperature of 35 °C is assumed as the medium temperature level at which heat is released to the environment in a cooling tower. For both processes, i.e. the mechanical cooling process as well as the heat driven cooling process, the simplifying assumption of a typical value of the Carnot efficiency factor of 0.5 is applied (see e.g. [4]).

Based on the conditions described before, equations 1 and 3 result in a coefficient of performance of 5.4 for mechanical cooling. For a photovoltaic system with commercially available solar cells, the efficiency  $\eta_{PV}$  under standard test conditions (solar irradiation perpendicular to the PV module  $G_{\perp} = 1000 \text{ W/m}^2$ ; ambient temperature 25 °C) can be assumed as 22 %. In addition, we assume a conversion efficiency  $\eta_{conv}$  of 95 % for the conversion of the direct current of the photovoltaic system into mechanical energy to drive the mechanical cooling process. Thus, for the conversion of solar radiation energy into cooling an overall coefficient of performance,  $\epsilon_{cool,PV}$ , results as:

$$\epsilon_{cool,PV} = \epsilon_{cool,mech} * \eta_{conv} * \eta_{PV} = 5.4 * 0.95 * 0.22 = 1.13. \quad (5)$$

For heat driven cooling processes, the coefficient of performance depends largely on the driving temperature level. At a driving temperature of 90 °C, as it is common for standard absorption chillers on the market, equation 2 results in a coefficient of performance of 0.8 (assuming a Carnot efficiency factor of 0.5 as said before), while a driving temperature of 200 °C, as it would be common for a triple-effect absorption chiller, results in a coefficient of performance of about 2. While the coefficient of performance increases with increasing driving temperature, the efficiency of a solar thermal collector behaves in exactly the opposite way: for a given level of irradiation, the efficiency decreases with increasing operating temperature – and this operating temperature is exactly the driving temperature of the heat driven cooling process. The efficiency of solar thermal collectors is usually represented according to the following equation [2]:

$$\eta_{st} = c_0 - c_1 \cdot \frac{(T_h - T_{amb})}{G_{\perp}} - c_2 \cdot \frac{(T_h - T_{amb})^2}{G_{\perp}}, \quad (6)$$

with

- $\eta_{st}$  efficiency of the solar thermal collector  
 $c_0, c_1, c_2$  loss coefficients of the solar thermal collector  
 $T_{amb}$  ambient temperature in K and  
 $G_{\perp}$  solar irradiation perpendicular to the collector plane in  $W/m^2$ .

The loss coefficients and thus the irradiation and temperature-dependent efficiency result from the specific design of the thermal solar collector, in particular the measures to reduce thermal losses and the optical properties of the glass cover and absorber. Typical values for a flat plate collector and an evacuated tube collector as the two most common designs for optically non-concentrating solar collectors are given in Table 2.1 (see e.g. [5]).

Table 2.1: Typical characteristic values for optically non-concentrating solar thermal collectors.

Collector type	$c_0$	$c_1$	$c_2$
Unit	-	$W/(m^2K)$	$W/(m^2K^2)$
Flat plate collector, FPC	0.85	3.0	0.004
Vacuum tube collector, ETC	0.83	1.5	0.002

The product of the coefficient of performance of the thermally driven cooling process and the solar thermal collector at a given ambient temperature  $T_{amb}$  is obtained as a function of the driving temperature – and thus the operating temperature of the collector –  $T_h$ :

$$\varepsilon_{cool,st}(T_h) = \varepsilon_{cool,therm}(T_h) \cdot \eta_{st}(T_h). \quad (7)$$

Figure 2.1 shows this overall coefficient of performance for the conversion of solar radiation into cooling based on a solar thermal process as a function of the driving temperature  $T_h$ . At the same time, the figure shows the coefficient of performance of the thermally driven cooling generation based on equation 2, assuming a Carnot efficiency of 0.5, as well as the efficiency of the solar thermal collectors using the loss coefficients according to Table 2.1 as function of the driving temperature  $T_h$ .

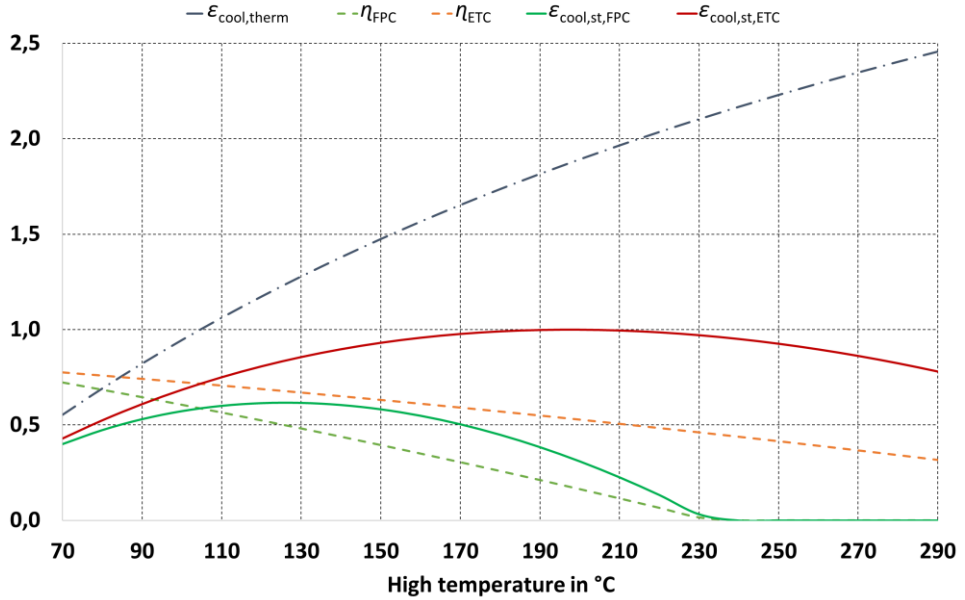


Figure 2.1: Curves of coefficient of performance of the thermally driven cooling process ( $\epsilon_{cool,therm}$ ), the efficiencies of the solar thermal collectors ( $\eta_{FPC}$ ,  $\eta_{ETC}$ ) and the coefficient of performance for solar thermal cooling ( $\epsilon_{cool,st,FPC}$ ,  $\epsilon_{cool,st,ETC}$ ); a value of 1000 W/m<sup>2</sup> was assumed for irradiation and 35 °C for the temperature on the medium temperature level.

For the specified boundary conditions, the use of a flat plate collector (FPC) results in a maximum overall conversion efficiency for solar thermal cooling  $\epsilon_{cool,st,FPC}$  of approximately 0.62 at a driving temperature of 126 °C. When using an evacuated tube collector (ETC), the maximum coefficient of performance  $\epsilon_{cool,st,ETC}$  is about 1.0 and this value is reached at around 198 °C.

Under design conditions, for a solar thermal process with vacuum tube collectors using a suitable thermal cooling process, such as a triple-effect absorption chiller, can therefore be expected that an almost similar conversion efficiency from solar radiation to cooling is achieved as with a corresponding system that uses photovoltaic modules in combination with mechanically driven cooling.

## 2.2 Consideration under partial load conditions

In real operation, design conditions for solar systems only occur at a few times, namely in particular when the solar converter is exposed to vertical irradiation of  $1000 \text{ W/m}^2$ , e.g. in the case of a system facing south and optimized for summer operation in summer at noon time. Most cooling processes are only slightly dependent on partial load over a wide range, which means that the cooling capacity provided is proportional to the driving power. Therefore, it is sufficient to consider the solar converters for partial load conditions. Photovoltaic modules show a low dependence of efficiency over wide radiation ranges. For a commercially available photovoltaic module based on silicon solar cells, the dependence of the efficiency can be well described by the following third-degree polynomial [6]:

$$\eta_{PV}(G_{\perp}) = a_3 \cdot G_{\perp}^3 + a_2 \cdot G_{\perp}^2 + a_1 \cdot G_{\perp} + a_0 \quad (8)$$

For the specific module, the values are given by  $a_3 = 9.72 \cdot 10^{-11} (\text{W/m}^2)^{-3}$ ,  $a_2 = 2.18 \cdot 10^{-7} (\text{W/m}^2)^{-2}$ ,  $a_1 = 1.59 \cdot 10^{-4} (\text{W/m}^2)^{-1}$  and  $a_0 = 0.182$ .

At a fixed operating temperature  $T_h$ , the efficiency for a solar thermal collector is given by equation 6, which can be expressed in the following form:

$$\eta_{st}(G_{\perp}) = b_0 - b_1 \cdot \frac{1}{G_{\perp}} \quad \text{with} \quad b_0 = c_0 \quad \text{and} \quad b_1 = c_1 \cdot (T_h - T_{amb}) + c_2 \cdot (T_h - T_{amb})^2 \quad (9)$$

Since most heat driven cooling machines require an almost fixed driving temperature for given temperatures on the low temperature (useful cooling) and medium temperature (heat rejection) side, the solar collector system is operated at almost fixed temperatures independent of the actual irradiation. Figure 2.2 shows the irradiation-dependence of the efficiency of a photovoltaic system and the corresponding efficiencies of the solar thermal collectors for different operation temperatures. For the flat-plate collector (indicated FPC), only the operation temperature of  $90 \text{ }^{\circ}\text{C}$  was considered, which is typical for a single-effect absorption chiller. For the vacuum tube collector (ETC), an operating temperature of  $140 \text{ }^{\circ}\text{C}$  (double-effect absorption chiller) and  $200 \text{ }^{\circ}\text{C}$  (triple-effect absorption chiller) was also considered.

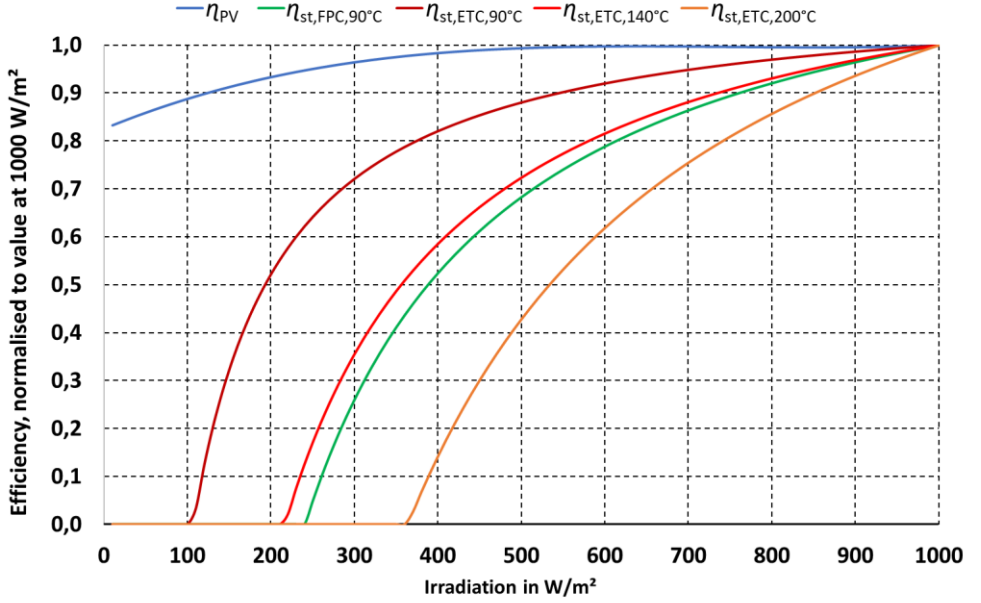


Figure 2.2: Efficiency normalized to the value at 1000 W/m<sup>2</sup> as a function of irradiation for a photovoltaic module and solar thermal collectors at different constant operation temperatures.

The figure clearly shows that the efficiency of photovoltaic systems is much less dependent on the perpendicular irradiation than the efficiency of solar thermal collectors, if they are operated at a fixed temperature, as is usual in the case of heat driven cooling. The reason for this is that the absorbed energy decreases in proportion to the irradiation, but the thermal losses remain the same regardless of the irradiation. This can be expressed more clearly by transforming equation 9, taking into account the definition of efficiency as the ratio of usable heat flux,  $\dot{Q}_{\text{use}}$ , and vertical irradiation multiplied by the area of the collector  $A$ :

$$\eta_{\text{st}} = \frac{\dot{Q}_{\text{use}}}{A \cdot G_{\perp}} = b_0 - b_1 \cdot \frac{1}{G_{\perp}} \quad ==> \quad \dot{Q}_{\text{use}} = A \cdot (b_0 \cdot G_{\perp} - b_1) \quad (10)$$

with

$\dot{Q}_{\text{use}}$       usable heat flow and

$A$           collector area.

The result shows that – even with almost the same conversion efficiency from solar irradiation to cooling at the design point – the behavior at partial load for photovoltaics

is clearly superior to that of solar thermal conversion. Since most of the operation takes place at incident radiation levels lower than at design conditions, this results in a clear advantage for photovoltaic driven cooling processes.

## 2.3 The importance of heat rejection

Another fundamental consideration results from the energy required for heat rejection. As the energy required for heat rejection plants (pumps, fans) is by no means negligible in real processes, the efficiency of the cooling process plays a significant role in the auxiliary energy required to operate the solar-powered cooling process. In general, the amount of heat flux to be dissipated via the heat rejection plant,  $\dot{Q}_{\text{reject}}$ , is calculated from the sum of the driving power,  $P_{\text{drive}}$ , and the usable cooling capacity,  $\dot{Q}_{\text{cool}}$ :

$$\dot{Q}_{\text{reject}} = P_{\text{drive}} + \dot{Q}_{\text{cool}} \quad (11)$$

Using the definition of the coefficient of performance of the cooling process,  $\varepsilon_{\text{cool}}$ , as the ratio of usable cooling capacity and driving power, the following applies:

$$\dot{Q}_{\text{reject}} = P_{\text{drive}} + \dot{Q}_{\text{cool}} = \dot{Q}_{\text{cool}} \cdot \left(1 + \frac{1}{\varepsilon_{\text{cool}}}\right) \quad (12)$$

The results for the previously considered examples are summarized in Table 2.2.

Table 2.2: Comparison of the necessary heat rejection heat flux per useful cooling for different (solar driven) cooling processes.

Variant; driving energy source	Coefficient of performance for cooling process	Specific heat flux for heat rejection
	-	Watts of heat flux for heat rejection per Watts of usable cooling capacity
(Photovoltaic) electric	5.4	1.19
(Solar) thermal at a driving temperature of 198 °C (see example above with vacuum tube collector)	1.9	1.53 (30 % higher than for photovoltaic case)
(Solar) thermal at a driving temperature of 90 °C (corresponding to single-effect absorption cooling system)	0.8	2.25 (90 % higher than for photovoltaic case)



Even for the previously considered design case at high temperature (198 °C), in which the overall efficiency for the conversion of solar radiation energy into useful cooling for the photovoltaic and solar thermal processes are of a similar order of magnitude, the lower conversion efficiency of driving energy into cooling results in an almost 30 % higher heat flux to be dissipated via the heat rejection plant. For a standard single-effect absorption cooling system (operation temperature 90 °C), the corresponding value results in an increase of 90 %.

### 3 Summary

The analysis of different options for the conversion of solar irradiation into useful cooling applying basic thermodynamic relationships reveals various reasons that photovoltaic driven processes are superior to using solar thermal conversion in combination with heat driven processes. A highly efficient solar collector combined with a suitable thermally driven cooling process still achieves almost the same overall efficiency as the combination of a photovoltaic system combined with a mechanically driven cooling process under design conditions. However, both the less favorable behavior under partial load conditions of solar thermal collectors compared to photovoltaic modules and the higher heat flux for heat rejection to be dissipated to the environment in the case of thermally driven cooling due to their lower COP compared to mechanically driven cooling clearly speak in favor of photovoltaics.

Nevertheless, research and development activities on solar thermal processes for cooling were carried out for many years [1,2]. Main background was the significantly lower cost for the provision of driving heat provided by solar thermal collectors compared to the cost for the provision of electrical energy with photovoltaic modules. However, this argument is no longer valid under today's cost conditions. The specific costs for a unit of useful power or heat flux, respectively, calculated using a life cycle cost calculation ("Levelized Cost of Electricity" or "Levelized Cost of Heat") are now in the same range for both solar conversion technologies – depending on system size and location between a minimum of about 2 €-Cents per kWh at places with high annual irradiation up to about 10 €-Cents per kWh under less favourable conditions.

The analysis was focused on applying solar energy for cooling and examples were corresponding to the application for air-conditioning of buildings. Of course, solar thermal collectors can also be used to provide domestic hot water and contribute to space heating in the heating season, which could be used as an argument in favour of

solar thermal energy conversion. However, the heat transformation cycles applied for cooling can – at least in principle – be also used for heating application by working as a heat pump. This means to use the heat at medium temperature level as useful heat source for space heating and hot water production. The evaporator then must be connected to an environmental heat source such as ambient air or the ground using a ground coupled heat exchanger.

It is important to note that the analysis given here applies to optically non-concentrating solar collectors. A separate consideration is necessary for solar collectors with optical concentration, which require tracking following the position of the sun and which can achieve significantly higher temperatures. However, this type of collectors is typically applied in much larger plants, which thus are less suitable for use in a building context.

Finally, it must be mentioned that many applications exist for the advantageous use of heat driven heat transformation processes, especially when usable waste heat fluxes are available, so that the thermal driving heat to operate the cooling process can rely on a cost-effective – or even cost-free – heat source.

## References

- [1] Henning, H.-M. (Editor) (2007). *Solar-assisted air-conditioning in buildings – A handbook for planners*. Springer-Verlag, 2007, ISBN 978-3-211-73095-9
- [2] Henning, H.-M., Motta, M., Mugnier, D. (Editors) (2013). *Solar Cooling Handbook: A Guide to Solar Assisted Cooling and Dehumidification Processes*. Ambra /V. ISBN 978-3-99043-438-3
- [3] Baehr, H. D., Kabelac, S. (2016). *Thermodynamik – Grundlagen und technische Anwendungen*. Springer Vieweg, 16. Auflage, ISBN 978-3-662-49567-4
- [4] Granryd, E. et al. (2005). *Refrigerating Engineering*. Department of Energy Technology. Division of Applied Thermodynamics and Refrigeration. Royal Institute of Technology, KTH Stockholm, 2005
- [5] SPF Institute for Solar Technology. *SPF Testing Reports – Collectors*. Website: <https://www.spftesting.info/data/1.collectors/> (accessed on 2024-11-13).
- [6] Henning, H.-M., Technische Energiesysteme für Gebäude 1: Verfahren, Komponenten. Vorlesung 11: Solarenergienutzung – Photovoltaik. Lecture KIT, Department of mechanical engineering, Winter Semester 2014/15.

# Modeling the calendering of lithium-ion battery electrodes and the impact on transport properties

## Accounting for the viscoelastic binder behavior

Alexandra Wahn <sup>1</sup> and Marc Kamlah <sup>1</sup>

<sup>1</sup> Karlsruhe Institute of Technology, Institute for Applied Materials, Karlsruhe, Germany

### Abstract

The active material particles of electrodes of lithium-ion batteries are held together by a binder, which in many cases is PVDF. When simulating the calendering process it is essential to account for a possible viscoelasticity of this binder material. In this work, we introduce and validate a core-shell model for the calculation of mechanical compaction of such electrodes by the discrete element method (DEM). In addition, the core-shell approach is employed to estimate, in the framework of the resistor network method, the dependence of the effective electronic conductivity of cathodes on the degree of compaction, and compared to an alternative modeling, as well as to an experiment. The core-shell concept proved to be a valid model for both, compaction and transport calculation.

**Keywords:** Lithium-ion batteries, cathodes, viscoelasticity of binder, calendering, effective electronic conductivity

## 1 Introduction

In electrochemical energy storage using lithium-ion technology, the electrodes consist of micro- or even nanoscale active material particles to shorten the solid-state diffusion paths and to increase the active surface area. The granular active material is held together and connected to the current collector by a binder. Since active materials on the

cathode side are often very poor electronic conductors, additives such as conductive carbon black are mixed into the binder. The composite electrode of lithium-ion technology therefore consists of 4 phases: (i) The active material for the lithium intercalation, in between the pore space filled with (ii) electrolyte for the transport of the lithium-ions, as well as the (iii) binder for the mechanical cohesion and the (iv) conductive carbon black for the electronic contact. Typically, binder and carbon black are present as a homogenous mixture.

This composite is compacted during production by calendaring in order to increase the energy and power density and to improve the mechanical and electronic contact. During calendaring in the manufacturing process, the electrolyte is not yet present, i.e. a dry binder material during compaction. During operation of the battery, the electrolyte is present and the interaction of electrolyte and binder plays a role. Nevertheless, since calendaring increases the tortuosity of the pore space of the electrode and thus the resistance of ionic transport, a degree of compaction has to be found that optimally balances electronic and ionic transport with regard to energy storage. Simulation can make an efficient contribution here instead of experimental trial-and-error.

It must be taken into account that binders such as polyvinylidene fluoride (PVDF) exhibit viscous mechanical behavior. Creep and relaxation processes can therefore occur that cannot be captured by linear-elastic modeling of the binder properties. However, this is important because these processes influence not only the geometric configuration of the granular electrode, but also its ionic and electronic transport properties.

The aim of this work is to develop a model that takes viscoelastic properties of the binder into account in the simulation of calendaring and to investigate their influence on the electronic transport properties. The appropriate method for simulating the collective mechanical behavior of granular materials is the discrete element method (DEM). In DEM, the equations of motion are solved for all particles in an assembly under the action of contact forces. This method has already been used in preliminary work [1-3], but viscoelastic properties have not yet been taken into account. The resistor network method (RN) for calculating effective transport properties of granular composites was also developed in preliminary studies in the group, whereby it was previously assumed that the electronically conductive binder/carbon black phase is homogeneously distributed in the pore space [4-7]. Since this modeling, unlike experiments, shows practically no influence of calendaring on the effective electronic conductivity of the electrode, an alternative model was to be developed for this.

In view of these considerations, this work is organized as follows: In Section 2, we will recall shortly basic assumptions and equations of the classical Hertz theory of elastic

contact [8,9]. Furthermore, we will summarize Radok's approach [10,11] of viscoelastic mechanical contact. In Section 3, we will introduce a modelling approach for the mechanical contact for spherical particles consisting of a stiff elastic core of active cathode material surrounded by a viscoelastic shell of binder/carbon black mixture. In Section 4, we will transfer the core-shell approach to the estimation of electronic transport in cathodes and compare it to the above mentioned previous modeling concept with a homogenously distributed binder/carbon black mixture. A special focus of this discussion is on the influence of calendering on effective electronic conductivity. Finally, some conclusions are drawn in Section 5.

## 2 Elastic and viscoelastic spherical contact

This section recalls basic relations of the established theories of Hertz [8,9] and Radok [10,11] for elastic and viscoelastic contact of spherical particles, respectively.

### 2.1 Classical Hertz theory of elastic mechanical contact

Hertz' classical theory [8,9] describes the mechanical normal contact of two elastic half spaces, which are of convex shape and possess a smooth and frictionless surface. In our work, we consider exclusively spherical shapes. The radius of the circular contact area of two spheres  $i$  and  $j$  in contact is given by

$$r_c = \sqrt{R_{eff} \delta_n^{ij}}, \quad (2.1)$$

where  $R_{eff}$  is the effective particle radius according to

$$\frac{1}{R_{eff}} = \frac{1}{R_i} + \frac{1}{R_j} \quad (2.2)$$

and  $\delta_n^{ij}$  is the overlap of the two spheres. The normal stress, i.e. of the contact pressure has the distribution

$$p_{Hertz}(x) = p_0 \sqrt{1 - (x/r_c)^2} \quad (2.3)$$

with  $x$  being the distance from the center of the contact area and

$$p_0 = 2E_{eff}r_c/(\pi R_{eff}), \quad (2.4)$$

while with the help of the respective Young's moduli and Poisson ratios the effective modulus is given by

$$\frac{1}{E_{eff}} = \frac{(1-\nu_i)^2}{E_i} + \frac{(1-\nu_j)^2}{E_j} . \quad (2.5)$$

Using the effective shear modulus

$$G_{eff} = \frac{1}{2} \frac{E_i E_j}{(1+\nu_i)(2-\nu_i)E_j + (1+\nu_j)(2-\nu_j)E_i} ,$$

the contact pressure can also be expressed as

$$p_{Hertz}(x) = \frac{4}{\pi R_{eff}} 2G_{eff} \sqrt{r_c^2 - x^2} . \quad (2.6)$$

From Eqs. (2.3) and (2.4), the resultant normal contact force

$$F_{Hertz} = 4/3 E_{eff} \sqrt{R_{eff} \delta_n^{ij} \delta_n^{ij}} \quad (2.7)$$

is obtained. Thus, the mechanical normal contact interaction can be interpreted as a rheological model consisting of a non-linear so-called Hertzian spring. For quasi-static numerical simulations, this spring is in parallel to a non-physical damper to remove kinetic energy from the system [12-14].

## 2.2 Radok's theory of mechanical contact of viscoelastic spheres

The basic idea of Radok's theory of viscoelastic contact consist of replacing the multiplication by elastic constants in the Hertz theory by a convolution integral with the relaxation function  $\Psi(t)$  of the viscoelastic material under consideration [10,11]. In this way, history dependence is introduced, with contact radius, contact pressure, and contact force, respectively, given in the form

$$r_c(t) = \sqrt{R_{eff} \delta_n^{ij}(t)} , \quad (2.8)$$

$$p_{Radok}(x, t) = \frac{4}{\pi R_{eff}} \int_0^t \Psi(t-t') \frac{d}{dt'} \sqrt{r_c(t')^2 - x^2} dt' , \quad (2.9)$$

$$F_{Radok}(t) = \frac{8}{3R_{eff}} \int_0^t \Psi(t-t') \frac{d}{dt'} r_c(t')^3 dt' . \quad (2.10)$$

In our work, we focus on the so-called Maxwell-Zener model of viscoelasticity, which as a rheological model consists of a parallel connection of an elastic spring (stiffness  $E_2$ ) with a series connection of an elastic spring (stiffness  $E_1$ ) and a linear dashpot (viscosity  $\eta$ , relaxation time  $\tau = \frac{\eta}{E_1}$ ) [15]. The related relaxation function is

$$\Psi(t) = E_1 e^{-\frac{t}{\tau}} + E_2. \quad (2.11)$$

To account for spherical contact, instead of linear springs we employ non-linear Hertzian springs. Then, the contact force is obtained as

$$F_{MZ}(t) = \frac{R_{eff}}{1-\nu^2} \int_0^t \sum_{i=1}^2 E_i e^{-\frac{(t-t')}{\tau_i}} \sqrt{\delta_n^{ij}(t')} \dot{\delta}_n^{ij}(t') dt', \quad (2.12)$$

where  $\frac{1}{\tau_2} = 0$ , since there is only one dashpot and, thus, only one relaxation time.

A detailed discussion of this theory, its implementation in the discrete element method [16], as well as its properties under monotonic loading, hold times and varying deformation rate can be found in [17].

### 3 A core-shell model for elastic particles surrounded by a viscoelastic shell

As mentioned in the introduction, binders such as PVDF show viscoelastic mechanical behavior [18]. The location of the binder/carbon black mixture in the composite electrode is not known to follow any clear trends. It can be equally distributed in the space around the active material particles, it may sit in bottlenecks between them, or it may surround them.

#### 3.1 Modifications of the original rheological models for core-shell contact

One option to model the presence of the binder/carbon black mixture during DEM simulation of compaction processes could be by separate viscoelastic particles in the space between elastic active material particles. However, in this case, they have to be at least one order of magnitude smaller than the active material particles, which would lead to a very large number of particles with the majority of them of computationally expensive history dependent viscoelastic behavior. Besides the computational cost, the

major issue with this is that in the context of the DEM, it is essential to comply with the assumption of small overlaps required by Hertz theory. This cannot be obeyed for small soft particles in contact with large stiff ones.

For this reason and in order to limit the number of particles to the number of active material particles, we follow here a different approach. In our work, the spherical active material particles are surrounded by a shell of constant thickness, which represents the mechanical viscoelastic properties of the binder/carbon black mixture. Thus, the composite core-shell particles are spherical, as well, and we can still exploit the simple kinematics of spherical contact. We take the elastic core to consist of lithium nickel manganese cobalt oxide (NMC), while the shell is to be of viscoelastic PVDF. The thickness of the shell is designated by  $\hat{R}_{Shell}$ , whereas the total radius of the spherical composite particle is denoted by  $R_{CS}$ .

For an in-depth understanding of the deformation processes during contact of such composite particles, extensive simulations with the finite element method (FEM) have been carried out. We consider the finite element solution as the exact solution of the related continuum mechanics problem and take this as reference solution for our DEM modeling. All details of the finite element model and the results can be found in [19]. Here, we summarize the main qualitative trends:

- 1.) The deformation behavior of the stiff elastic core and of the soft viscoelastic shell is very different. In particular, the viscoelastic shell is laterally squeezed outside of the contact zone of two composite particles by the stiff cores.
- 2.) With increasing compression, i.e. overlap, the contact force response gets dominated by the stiff elastic cores.

In view of these findings, the basic formulation of the contact force of such composite particles consist of a parallel connection of the previously introduced rheological models, namely an elastic Hertzian spring and a viscoelastic Maxwell-Zehner model:

$$F_{CoreShell} = F_{Shell}(q(\hat{R}_{Shell}/R_{CS}), t) + F_{Core}(\delta_n(\hat{R}_{Shell}/R_{CS}, \delta_n^{ij})) \quad (3.1)$$

Here,  $F_{Shell}$  represents the viscoelastic shell and  $F_{Core}$  describes the elastic core, while  $q$  and  $\delta_n$  are dimensionless functions introduced to adapt the basic model in Eqn. (3.1) to the quantitative behavior observed in the reference solutions obtained by FEM modeling.

Concerning the viscoelastic contribution  $F_{Shell}$ , the relation (2.8) for the contact radius is extended to



$$r_{c,FEM} = \sqrt{q \left( \frac{\hat{R}_{Shell}}{R_{CS}} \right) R_{eff} \delta_n^{ij}(t)} . \quad (3.2)$$

For quasi-static loadings, function  $q$  is denoted as  $q_0$ , which was fitted to FEM results yielding the expression

$$q_0 \left( \frac{\hat{R}_{Shell}}{R_{CS}} \right) = \begin{cases} 0.0, & \text{for } \frac{\hat{R}_{Shell}}{R_{CS}} \leq TOL \\ -0.22 \log_{10} \left( \frac{\hat{R}_{Shell}}{R_{CS}} \right) + 1.0 & , \text{ else.} \end{cases} \quad (3.3)$$

Here, the threshold value  $TOL$  defines the minimum of the ratio  $\frac{\hat{R}_{Shell}}{R_{CS}}$  of the thickness of the viscoelastic shell to the core-shell particle radius to have an impact on the overall force response. Fit function (3.3) satisfies the limit conditions  $q_0 \left( \frac{\hat{R}_{Shell}}{R_{CS}} = 0.0 \right) = 0.0$  and  $q_0 \left( \frac{\hat{R}_{Shell}}{R_{CS}} = 1.0 \right) = 1.0$ , meaning either pure elastic behavior without shell or pure viscoelastic behavior for vanishing core.

By investigating the difference  $F_{Core} = F_{CS,FEM} - F_{Shell}$ , where  $F_{CS,FEM}$  is the total force response of a composite particle in FEM simulations, i.e. the reference solution, the modification

$$F_{Core} = 4/3 E_{Core,eff} \sqrt{R_{CS,eff}} (\delta_n^{ij})^3 \delta_n^{ij} \quad (3.4)$$

of the Hertzian formulation (2.7) was identified for the contribution of the core. As a result of fitting to FEM results, the function

$$\delta_n^{ij} \left( \frac{\hat{R}_{Shell}}{R_{CS}}, \delta_n^{ij} \right) = m \left( \frac{\hat{R}_{Shell}}{R_{CS}} \right) \delta_n^{ij} + b \left( \hat{R}_{Shell}/R_{CS} \right) \quad (3.5)$$

was found with

$$m \left( \frac{\hat{R}_{Shell}}{R_{CS}} \right) = \begin{cases} 0.042 (\hat{R}_{Shell}/R_{CS})^{-1.17294}, & \text{for } \frac{\hat{R}_{Shell}}{R_{CS}} \geq TOL \\ 0.0 & , \text{ else} \end{cases} \quad (3.6)$$

and

$$b \left( \frac{\hat{R}_{Shell}}{R_{CS}} \right) = \begin{cases} 0.0 & , \text{ for } \frac{\hat{R}_{Shell}}{R_{CS}} > 0.5 \\ 0.0006 (\hat{R}_{Shell}/R_{CS})^{-1.60079}, & \text{for } 0.5 > \frac{\hat{R}_{Shell}}{R_{CS}} \geq TOL \\ 1.0 & , \text{ else} \end{cases} \quad (3.7)$$

These definitions satisfy the limiting conditions  $\hat{\delta}_n^{ij}(0.0, \delta_n^{ij}) = 1.0$  with  $m(0.0) = 0.0$ ,  $b(0.0) = 1.0$  and  $\hat{\delta}_n^{ij}(1.0, \delta_n^{ij}) = 0.0$  with  $m(1.0) = 0.0$ ,  $b\left(\frac{\hat{R}_{shell}}{R_{CS}} > 0.5\right) = 0.0$ , where the former accounts for the absence of a shell while the latter represents the vanishing of the core.

The detailed motivation and derivation of the above model equations can be found in [19]. As one outcome of the discussions there, the threshold value for  $TOL$  was chosen as

$$TOL = 0.002.$$

### 3.2 Final formulation for the contact force of two core-shell particles

As a result of the FEM simulations, it was found that two different cases have to be distinguished when formulating the contact force of two composite particles. In the first case, during the initial contact period defined by  $\delta_n^{ij} \leq \min(\hat{R}_{shell}^i, \hat{R}_{shell}^j)$ , the geometric overlap concerns only the viscoelastic shells. For the other case, i.e. for later loading states identified by  $\delta_n^{ij} > \min(\hat{R}_{shell}^i, \hat{R}_{shell}^j)$ , it turned out that the contact force is completely dominated by the elastic cores.

In the latter, the final state according to  $\delta_n^{ij} > \min(\hat{R}_{shell}^i, \hat{R}_{shell}^j)$ , the contact force simply reads as

$$F_{CS}(\delta_n^{ij}) = \frac{4}{3} E_{Core,eff} \sqrt{R_{Core,eff}} (\bar{\delta}_n^{ij})^3 \quad (3.8)$$

with

$$\bar{\delta}_n^{ij} = \delta_n^{ij} - \min(\hat{R}_{shell}^i, \hat{R}_{shell}^j)$$

while the effective radius  $R_{Core,eff}$  and the effective modulus  $E_{Core,eff}$  are defined in analogy to Eqs. (2.2) and (2.5), respectively. The contact radius is given by

$$r_c = \sqrt{R_{Core,eff} \bar{\delta}_n^{ij}} \quad (3.9)$$

The initial contact state defined by  $\delta_n^{ij} \leq \min(\hat{R}_{shell}^i, \hat{R}_{shell}^j)$ , where there is overlap of the viscoelastic shells only, is much more complex. Written down in time discrete form, departing from Eqs. (2.7) and (2.10), Eqs. (3.1) – (3.5) yield the expression for the total contact force of two composite particles in this case as

$$\begin{aligned}
 F_{CS}(t + \Delta t) = & \\
 & F_{1,shell}(t) e^{-\frac{\Delta t}{\tau}} + \Delta t E_{1,shell}(t) e^{-\frac{\Delta t}{2\tau}} \sqrt{R_{CS,eff} (\delta_n^{ij})^3 \delta_n^{ij} (q_1(\hat{R}_{shell}/R_{CS})_{eff})^{3/2}} \\
 & + F_{2,shell}(t) + \Delta t E_{2,shell}(t) \sqrt{R_{CS,eff} (\delta_n^{ij})^3 \delta_n^{ij} (q_0(\hat{R}_{shell}/R_{CS})_{eff})^{3/2}} \\
 & + \frac{4}{3} \kappa E_{Core,eff} \sqrt{R_{CS,eff} (\delta_n^{ij})^3} \delta_n^{ij} (\hat{R}_{shell}/R_{CS})_{eff} . \tag{3.10}
 \end{aligned}$$

Factor  $\kappa = \frac{E_2}{1365.9 \text{ MPa}}$  allows to account for a shell material different from PVDF. Now, instead of Eqn. (3.3), function  $q_0$  accounting for the quasi-static behavior of the viscoelastic shell in the second term of Eqn. (3.10) is expressed in terms of effective radii, which are defined in analogy to before:

$$q_0 \left( \left( \frac{\hat{R}_{shell}}{R_{CS}} \right)_{eff} \right) = \begin{cases} 0.0 & , \text{for } \left( \frac{\hat{R}_{shell}}{R_{CS}} \right)_{eff} \leq 0.002 \\ -0.22 \log_{10} \left( \frac{\hat{R}_{shell}}{R_{CS}} \right)_{eff} + 1.0 & , \text{else} \end{cases} \tag{3.11}$$

On the other hand, fit function  $q_1$  representing in the first term the spontaneous response was found to be

$$q_1 \left( \left( \frac{\hat{R}_{shell}}{R_{CS}} \right)_{eff} \right) = 1.1 + 3.4 (3.5 \cdot 10^{-13}) \left( \frac{\hat{R}_{shell}}{R_{CS}} \right)_{eff} . \tag{3.12}$$

Eqn. (3.5) is now expressed in terms of effective radii, as well. In addition, a fit factor  $\alpha = \sqrt{\frac{0.01 \text{ mm}}{R_{CS}}}$  is introduced to allow for composite particles of different radii  $R_{CS}$  yielding  $\hat{\delta}_n^{ij}$  in the form

$$\hat{\delta}_n^{ij} \left( \alpha, \left( \frac{\hat{R}_{shell}}{R_{CS}} \right)_{eff}, \delta_n^{ij} \right) = \alpha \cdot \left( m \left( \left( \frac{\hat{R}_{shell}}{R_{CS}} \right)_{eff} \right) \delta_n^{ij} + b \left( \left( \frac{\hat{R}_{shell}}{R_{CS}} \right)_{eff} \right) \right) . \tag{3.13}$$

Eqs. (3.6) and (3.7) are adopted in analogy. Finally, the contact radius in the initial contact situation is given by

$$r_c = \sqrt{q_0 R_{CS,eff} \delta_n^{ij}}. \quad (3.14)$$

Again, due to the limited space available here, we refer the reader for a detailed motivation and derivation of the model to the thesis [19].

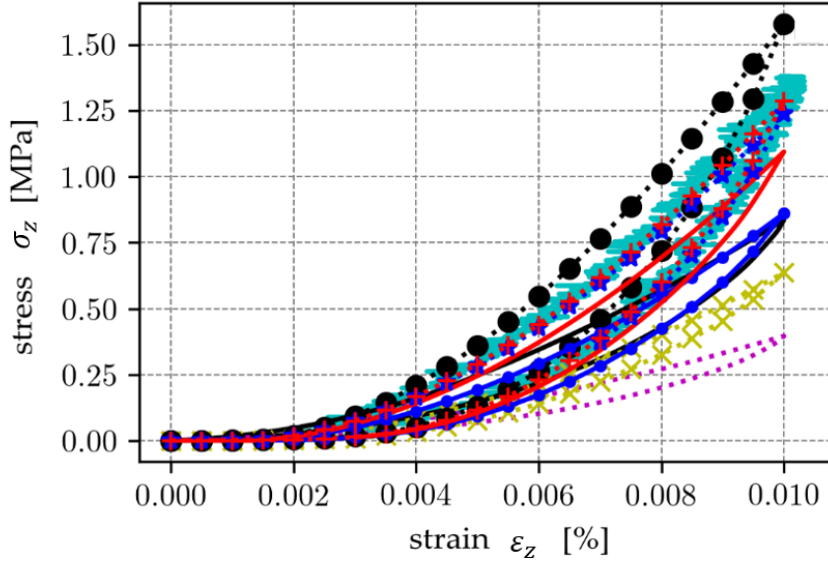
### 3.3 Simulation of quasi-static compaction processes and comparison to experiment

The above described core-shell contact model has been implemented in the in-house DEM-code *kitGran*. An integration procedure for the equations of motion has been developed to account for the time dependent behavior of viscoelasticity [17,19]. The material parameters for NMC and PVDF used here are listed in Tab. 3.1.

Table 3.1: Material parameters for NMC and PVDF

	NMC622 [21]	PVDF [18]
density	$\rho = 4.75 \text{ g/cm}^3$	$\rho = 1.8 \text{ g/cm}^3$
modulus	$E = 142 \text{ GPa}$	$E_1 = 404.6 \text{ MPa}$ $E_2 = 1365.9 \text{ MPa}$
Poisson ratio	$\nu = 0.25$	$\nu = 0.4314$
viscosity	-	$\eta = 728.28 \text{ MPa s}$

In addition, during simulation of quasi-static processes, a non-physical viscosity has to be assigned to NMC in order to remove kinetic energy from the system and density scaling has been applied for achieving stable solutions [17]. The initial configurations are created by the random close packing algorithm (RCP) which generates random particle structures with no overlaps [20].












	number of particles		$\frac{\hat{R}_{shell}}{R_{CS}}$	packing factor (CS)	packing factor (AM)
experiment	5.7 Mio.				
core-shell approach (CS)	250		0.04	0.632	0.564
			0.08		0.496
	500		0.02	0.621	0.595
			0.025		0.586
			0.02 and 0.04		0.578
			0.03		0.578
			0.04		0.560
			0.06		0.526

Figure 3.1: Experiment: Measurement of macroscopic stress and strain during loading and unloading of a PVDF layer [22]. Core-shell model: Simulation of quasi-static loading and unloading of various assemblies of core-shell particles.

Fig. 3.1 shows the simulation of quasi-static compaction for various parameters in comparison to an experiment [22] of uniaxial compression of a PVDF layer. It turns out that with the right choice of shell thickness ( $\hat{R}_{shell}/R_{CS} = 0.025$ ), number of composite particles ( $\geq 500$ ) and initial packing density (62.1 %), the experiment can be reproduced

very well. A particle mixture of  $\hat{R}_{shell}/R_{CS} = 0.02$  and  $\hat{R}_{shell}/R_{CS} = 0.04$  works equally well. Both, relocation of particles and the viscoelasticity of the shells are reasons for the occurrence of a loading-unloading hysteresis. In view of these findings, we conclude that the core-shell concept is appropriate for simulating the mechanical compaction of lithium-ion battery electrodes consisting of active material particles and binder/carbon black mixture.

## 4 Transfer of the core-shell approach to the estimation of electronic transport in cathodes

As mentioned before, there is no established knowledge on the location of the binder/carbon black mixture in the complementary space of the active material particles. Still, the previous section has shown that the developed core-shell approach is capable of modeling the mechanical compaction of lithium-ion battery electrodes in the presence of viscoelastic binder. On the other hand, the core-shell approach must not necessarily be a valid model for calculating the electronic and ionic transport. For example, if the binder would form a solid shell around active material particles, their surface would be isolated from lithium-ions in the electrolyte and no electrochemical reaction could occur.

In previous work [4-7], the resistor network method (RN) has been applied to calculate effective transport properties in electrodes. In RN, the system of particles and pores is converted into two separate networks of nodes consisting of particle or pore centers, respectively, as well as edges, i.e. the related bottleneck resistances due to contact areas or pore throats. When computing electronic transport in a cathode, it was assumed that the binder/carbon black mixture is homogenously smeared out according to its volume fraction in the complementary space of the active material particles, i.e. the pore space. This means that every location in the pore space is shared by electrolyte and binder/carbon black according to the volume ratio between them. During the DEM simulation of calendaring, the plausible assumption was made that only the volume available for the liquid electrolyte is reduced while the volume of the binder/carbon black mixture is not changed. The reduction of ionic transport properties by electrode compaction could be represented in this way. However, the approach of a smeared binder/carbon black phase shows nearly no influence of calendaring on the effective electronic conductivity of a cathode. This is counterintuitive and not in agreement with experiments.

In [23], RN was developed further for calculating the effective conductivity of a network of spherical shells. In our work, the effective electronic conductivity  $\kappa_{eff}$  of the binder/carbon black mixture has been calculated for increasing compaction by both RN methods, i.e. for a smeared binder/carbon black mixture and for a network of binder/carbon black shells. In this comparison, the active material particles were assumed to be perfect insulators in simulations, while the contribution of NMC622 in experiments might not be negligible. Besides two different initial packing factors and two different amounts of binder/carbon black mixture have been considered. For the smeared binder/carbon black mixture this means two different volume fractions in the pore space, while for the core-shell approach this means different shell thicknesses. For each parameter combination of initial packing factor and shell thickness, 10 realizations have been simulated. Note that for the structures with smeared binder/carbon black phase on the one hand and with core-shell particles on the other, the compaction processes lead to different configurations, even when starting from the same parameter set.

Fig. 4.1 shows the results of the experiment and the simulations for increasing compaction strain. For the dimensionless representation, the conductivity of 1000 S/m for carbon black according to [24] has been used. This value has been adopted for the electronic conductivity of the binder/carbon black mixture when comparing the two simulation methods. In the compaction range of 0.005 to 0.015, the experimental results [22] show a linear increase with compaction, while the increase appears to get weaker at higher degrees of compaction.

Concerning the simulation results, the average of 10 values is shown while the bars indicate the spread of the results. The first observation is that the two modeling approaches, namely smeared binder/carbon black mixture and core-shell model, enclose the experimental results from above and below, respectively. The second observation is that the results for the smeared binder/carbon black mixture are significantly above the experimental results. Third, it can be seen that the smeared binder/carbon black mixture model hardly shows any dependence on compaction strain. If at all, there is even a slight decrease with compaction in contrast to the experiment. This is due to the fact that with increasing compaction the tortuosity of the pore space, where the binder/carbon black mixture is assumed to be situated in the smeared approach, increases.

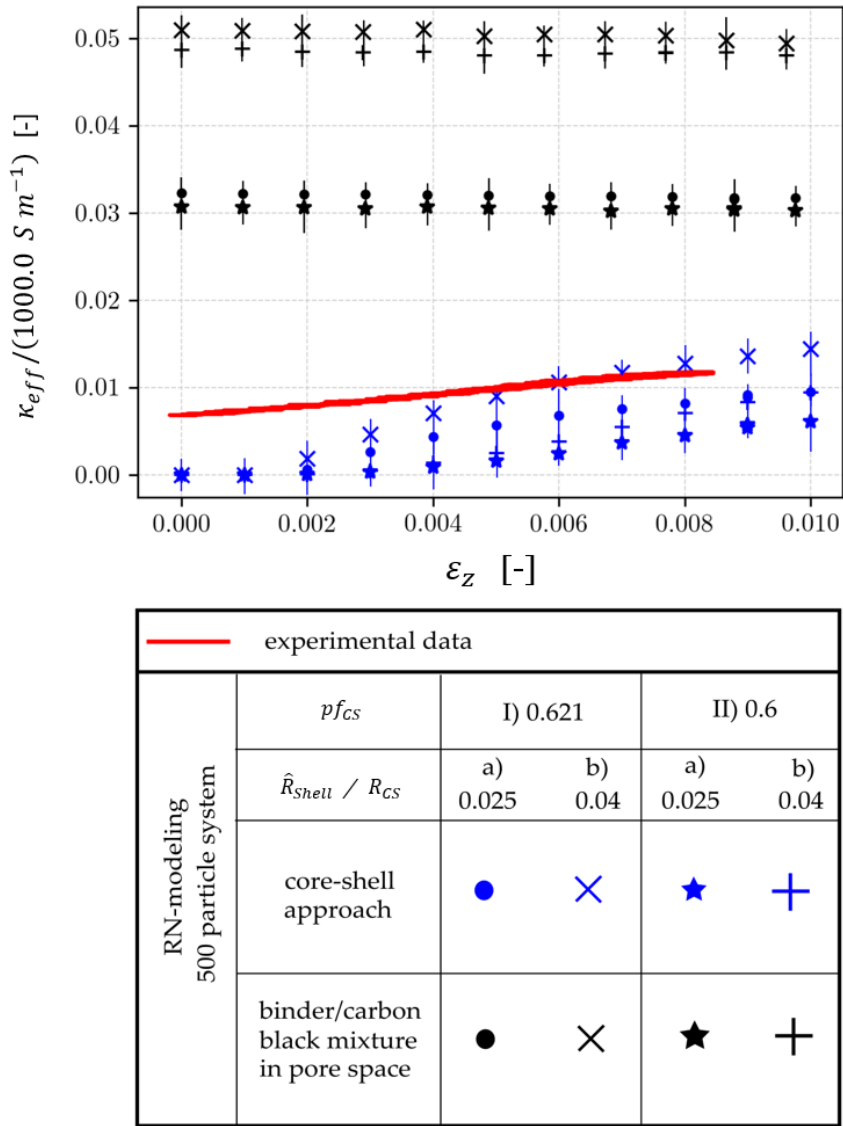


Figure 4.1: Experiment: Measurement of the effective electronic conductivity with increasing compaction [22]. RN modeling: Calculations of the effective electronic conductivity for smeared binder/carbon black mixture and core-shell approach.



In contrast, the core-shell approach shows a clear increase of the effective electronic conductivity with compaction. The results start from zero, as in the initial configurations generated by the RCP, there is yet no overlap between particles and, thus, no percolation at all. The trend with increasing compaction appears to be linear, while at higher compaction, the increase seems to get weaker. On the other hand, the slope of the increase is higher than in the experiment. A higher initial packing density, as well as a thicker shell lead to higher values of the effective electronic conductivity. For the former, a higher initial packing density leads to larger contact areas at equal compaction rates. Concerning the latter, thicker shells provide more volume of electronically conducting binder/carbon black mixture. The best approximation to the experimental results is obtained for the higher initial packing density and the thicker shell while, eventually, the values go even beyond the experimental results.

In this context, it is interesting to note that a shell thickness with a ratio of  $\hat{R}_{shell}/R_{CS} = 0.045$  was found to correspond to the mass of the binder in the electrode composition [19]. Furthermore, it must be taken into account that the experimental results are affected by a contribution of the contact resistance between electrode layer and the plates of the measurement setup, meaning that the measured electrode layer alone may have a higher conductivity than the one shown in Fig. 4.1. On the other hand, since DEM simulations of compaction have given the best agreement with the experiment for  $\hat{R}_{shell}/R_{CS} = 0.02$  &  $0.04$ , there is room for further improvement of the core-shell model for the effective electronic conductivity.

## 5 Conclusions

In this paper, a core-shell approach has been introduced to account for the presence of viscoelastic binder when simulating calendering by the discrete element method. A variation of shell thickness and initial packing density was compared to an experimental result. As an outcome, we found that the core-shell concept is appropriate for simulating the mechanical compaction of lithium-ion battery electrodes consisting of active material particles and viscoelastic binder/carbon black mixture.

As a further step, the core-shell concept was applied to the calculation of the effective electronic conductivity of electrode layers. It was compared to a previously introduced method with a smeared binder/carbon black mixture sharing the pore space with the electrolyte and to an experiment. We found that both the two RN methods for calculating the effective electronic conductivity can be considered yielding reasonable and

computationally efficient results with the additional property of providing estimates for the upper and lower limits.

## Acknowledgement

This work has been funded by the German Research Foundation (DFG) in the framework of the research training group “SiMET - Simulation of Mechano-Electro-Thermal Processes in Lithium-Ion Batteries” (No. GRK 2218/2, Project number 281041241).

## References

- [1] Gan, Y., Kamlah, M. (2010). Discrete element modelling of pebble beds: With application to uniaxial compression tests of ceramic breeder pebble beds. *J. Mech. Phys. Solids*, 58, 129-144.
- [2] Ott, J., Voelker, B., Gan, Y., McMeeking, R. M., Kamlah, M. (2013). A micromechanical model for effective conductivity in granular electrode structures. *Acta Mechanica Sinica*, 29, 682-698.
- [3] Becker, V., Kamlah, M. (2021). A theoretical model for the normal contact force of two elastoplastic ellipsoidal bodies. *J. Appl. Mech.* 88, 031006.
- [4] Birkholz, O., Gan, Y., Kamlah, M. (2019). Modeling the effective transport properties of the solid and the pore phase in granular materials using resistor networks. *Powder Technology* 351, 54-65.
- [5] Birkholz, O., Neumann, M., Schmidt, V., Kamlah, M. (2021). Statistical investigation of structural and transport properties of densely-packed assemblies of overlapping spheres using the resistor network method. *Powder Technology* 378, 659-666.
- [6] Birkholz, O., Kamlah, M. (2021). Electrochemical modeling of hierarchically structured Lithium-ion battery half-cells. *Energy Technology*, 9, 2000910.
- [7] Becker, V., Birkholz, O., Gan, Y., Kamlah, M. (2021). Modeling the influence of particle shape on mechanical compression and effective transport properties in granular Lithium-ion battery electrodes. *Energy Technology*, 9, 2000886.

- [8] Hertz, H. (1881). Über die Berührung fester elastischer Körper. *J. Reine Angew. Math.*, 92, 156–171.
- [9] Johnson, K. L. (1987). *Contact mechanics*. Cambridge University Press.
- [10] Radok, J. R. M. (1957). Visco-elastic stress analysis. *Quarterly of Applied Mathematics*, 15, 198–202.
- [11] Lee, E. H., Radok, J. R. M. (1960). The contact problem for viscoelastic bodies. *J. Appl. Mech.*, 27, 438–444.
- [12] Itasca Cosulting Group (1998). *PFC2D 2.00 Particle Flow Code in Two Dimensions*. Minneapolis
- [13] Kruggel-Emden, H., Wirtz, S., Sisek, E., Scherer, V. (2006). Modeling of granular flow and combined heat transfer in hoppers by the discrete element method (DEM). *J. Pressure Vessel Technol.*, 128, 439–444.
- [14] Limtrakul, S., Boonsrirat, A., Vatanatham, T. (2004). DEM modeling and simulation of a catalytic gas–solid fluidized bed reactor: a spouted bed as a case study. *Chemical Engineering Science*, 59, 5225–5231.
- [15] Haupt, P. (2000). *Continuum Mechanics and Theory of Materials*. Springer, Berlin et al.
- [16] O'Sullivan, C. (2011). *Particulate Discrete Element Modelling: a Geomechanics Perspective*. CRC Press, London.
- [17] Wahn, A., Gan, Y., Kamlah, M. (2022). Viscoelastic behavior in discrete element method realized by interparticle Maxwell-Zener model. *J. Micromech. Mol. Phys.*, 7, 197–212.
- [18] Narayan, S., Rao, C. L., Kumar, S. (2008). Modeling of the viscoelastic properties of PVDF through the fractional differential model. *International Journal of Comadem*, 11, 2–8.
- [19] Wahn, A. (2024). *Partikelbasierte Methoden für die Berechnung von effektiven Transporteigenschaften und Mechanik in granularen Mehrphasen-Elektroden*. Dissertation, Karlsruhe Institute of Technology.
- [20] Jodrey, W. S., Tory, E. M. (1979). Simulation of random packing of spheres. *Simulation*, 32, 1–12.
- [21] Sangrós Giménez, C., Finke, B., Schilde, C., Froböse, L., Kwade, A. (2019). Numerical Simulation of the Behavior of Lithium-Ion Battery Electrodes During the Calendaring Process Via the Discrete Element Method. *Powder. Technol.*, 349, 1–11.

- [22] Brendel, T. (2023). Personal communication. Karlsruhe Institute of Technology.
- [23] Birkholz, O. (2024). Modeling transport properties and electrochemical performance of hierarchically structured Lithium-ion battery cathodes using resistor networks and mathematical half-cell models. Dissertation, Karlsruhe Institute of Technology.
- [24] Guy, D., Lestriez, B., Bouchet, R., Guyomard, D. (2006). Critical role of polymeric binders on the electronic transport properties of composites electrode. J. Electrochem. Soc., 153, A679-A688.

# Simulation of single control rod withdrawal transients in an LBE cooled reactor

Xue-Nong Chen <sup>1</sup>, Yoshiharu Tobita <sup>1</sup> and Andrei Rineiski <sup>1</sup>

<sup>1</sup> Karlsruhe Institute of Technology, Institute for Neutron Physics and Reactor Technology, Karlsruhe, Germany

## Abstract

In the ANSELMUS EU-Project [1], models and computer codes for safety analyses of nuclear systems cooled by Lead-Bismuth Eutectic (LBE) and lead are assessed. In particular, spatial kinetics effects during Control Rod Withdraw (CRWD) are investigated. A new CRWD model for the SIMMER-IV code is developed at KIT so that CRWD with a constant speed can be simulated. The spatial kinetics effects on the power shape are evaluated by comparing relative variations in time of local power densities and of the total one. The dynamic reactivity values during CRWD have been confirmed to be close to those obtained by static calculations.

**Keywords:** SIMMER-IV code, Spatial kinetics, Control rod withdraw, LBE-cooled reactor, ANSELMUS project

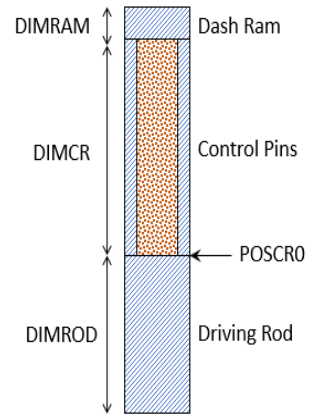
## 1 Introduction

Lead-Bismuth-Eutectic (LBE) is a eutectic alloy of lead and bismuth. It is used as coolant in some proposed designs of fast reactors and accelerator-driven systems (ADS). KALLA (Karlsruhe Lead Laboratory) is a pioneer laboratory in Europe for developing the LBE coolant technology, and Prof. Robert Stieglitz was the KALLA head in early 2000s. In memory of him, this paper deals with LBE cooled reactor safety. The paper summarizes results of studies for the ANSELMUS EU-Project [1], in which models and computer codes for safety analyses of nuclear systems cooled by Lead-Bismuth Eutectic (LBE) and lead are assessed.

A Control Rod Withdrawal (CRWD) transient is a possible accident initiator in a nuclear reactor and should be studied for reactor safety assessment. We simulated such transi-

ent with the SIMMER-IV code [2] for a LBE-cooled reactor design, MYRRHA, which was studied at KIT in the past, see Ref. [3]. A critical core configuration is considered. The assumption is that one of six control rods is withdrawn with a certain velocity. The purpose of this exercise is to investigate 3-D spatial effects with respect to power distribution evolution during the transient and to use these 3-D results to examine the applicability of simple point-kinetics (PK) models.

The SIMMER-IV code includes advanced fluid-dynamics and spatial neutron kinetics models. The code can be used to perform the analysis of spatial kinetics effects during CRWD. At KIT, a MYRRHA sub-critical core configuration was investigated with SIMMER-IV in the past. This investigation serves as a good basis for the study, described in the following.



## 2 SIMMER-IV CRWD model and simulation

### 2.1 CRWD model development

In general, with the SIMMER code one can simulate particle movement, which is treated as movement of fluid. In the new CRWD model developed for SIMMER-IV and applied in this study, the control rod includes absorber and structure materials, B4C and steel, which are in the particle form. The new model forces the control and steel particles to move uniformly at a certain user-defined velocity at a given Control Rod (CR) location. Figure 1 shows the geometry of the CRWD model. The new model is based on this geometry description. The volume fractions of absorber and steel particles are given in the conventional way as part of the SIMMER input file. Data for the CRWD model are provided as additional part of the input file, including the effective CR position and its velocity.

### 2.2 SIMMER-IV simulation

Figure 2 shows the MYRRHA core map, with the CR to be withdrawn, the neighboring fuel assembly (FA) near the CR and the peaking FA in the core center marked in yellow, blue and red, respectively. The core is loaded with MOX fuel with 33 % Pu, so that the reactor is critical. The effective delayed neutron fraction is 343 pcm and the CR to be

withdrawn, marked in yellow, has an integral reactivity worth of about 0.85 \$. The control rod is withdrawn downwards from a fully inserted position to a position outside the active core.

Figure 1: Geometry of the CRWD model.

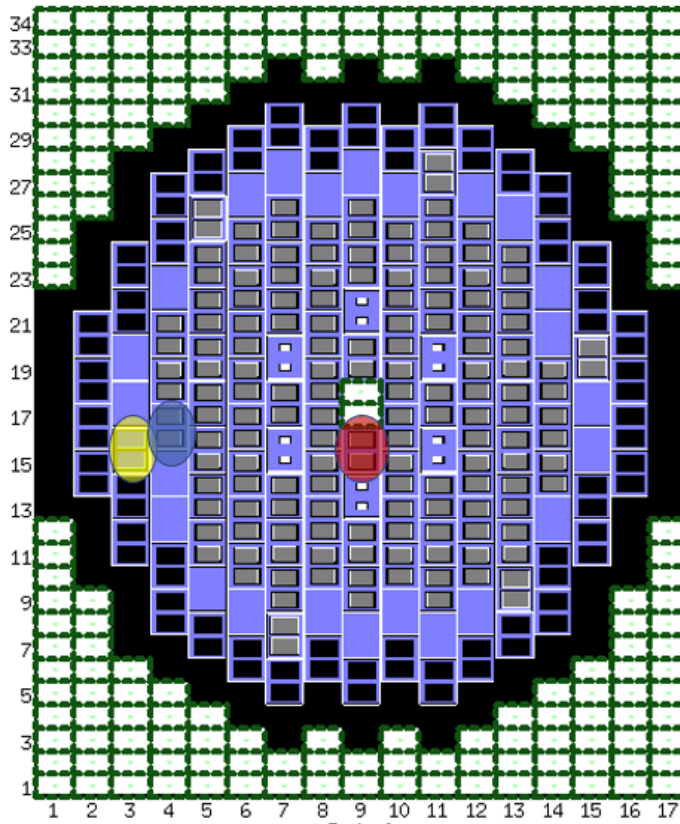


Figure 2: SIMMER-IV simulation model, with the CR to be withdrawn, the neighboring FA and the peaking FA in the core center marked in yellow, blue and red, respectively.

Figure 3 shows the reactivity vs. the B4C upper boundary location, i.e. the interface between absorber and dash ram.

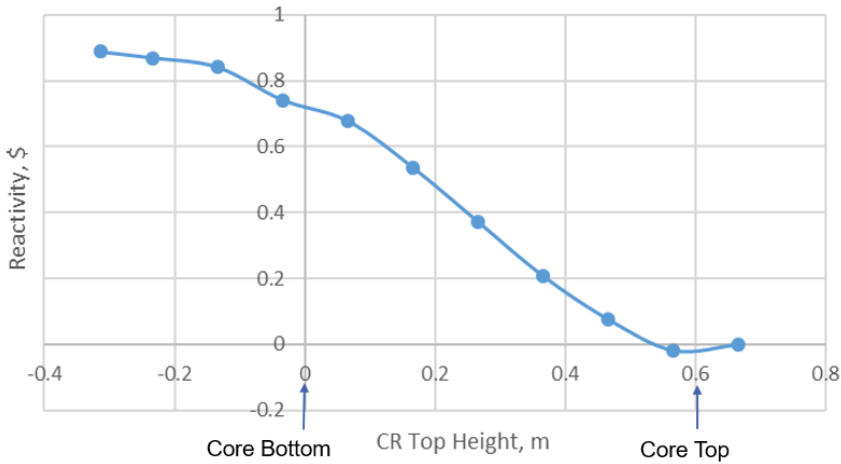


Figure 3: Static CR withdrawal reactivity as function of the axial position of B4C top location.

### 3 Simulation results and discussion

The results for a full control rod withdrawal starting at 20 s and lasting 3 s, corresponding to insertion of about 0.27 \$/s, are presented in Figure 4. It shows the power of the peak power (peaking) FA, the neighboring FA and the average FA. Because of the positive reactivity insertion during the CR withdrawal, the FA power increases and then, due to Doppler feedback, stabilizes at a higher power level. The FA power is normalized by its initial value at 0 s. The power of the peaking FA clearly behaves almost in the same way as the average one, while the one of the neighboring to CR location FA increases by 15 % more than the average one. This is the local 3-D CRWD effect on power distribution.

The total reactivity insertion is about 0.9 \$, which can result in a fuel melting in the fuel pellet center at the hottest FAs. The left plot of Figure 5 is the material distribution at 30 sec (10 sec after the CRWD start), where one can see the fuel melting at the radial meshes 8 and 9. The right plot of Figure 5 shows the fuel center temperature and the coolant temperature in Kelvin at the midplane of the hottest FA.



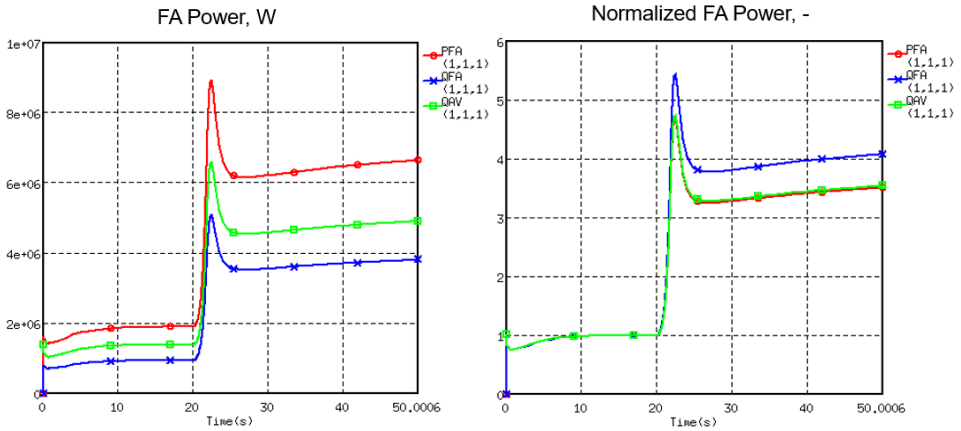


Figure 4: Transient results of FA power (left) and normalized FA power (right). The CR withdraw starts at 20 s and no scram occurs. PFA (red), QFA (blue) and QAV (green) stand for the peaking FA, the neighboring to CR location FA and the average FA, respectively.

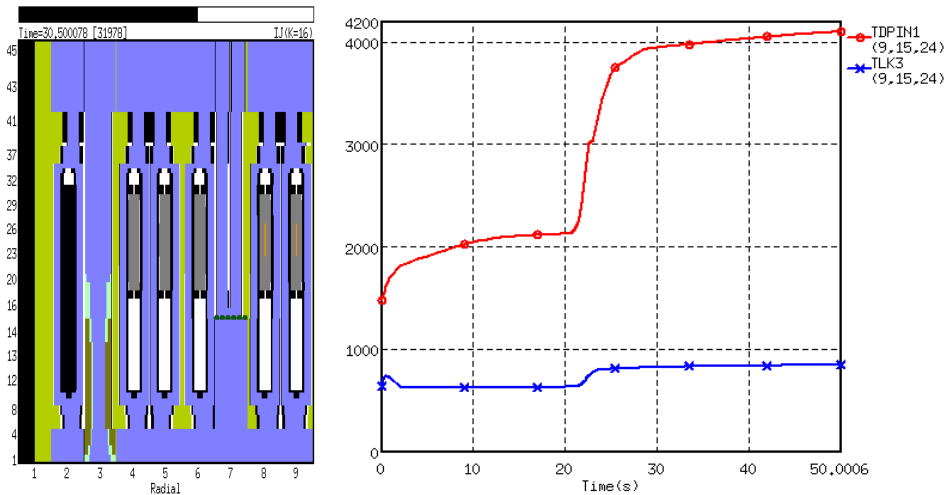


Figure 5: Material distribution (left) and temperature transient (right). The red and blue lines stand for the fuel central temperature and the coolant temperature at the midplane of the hottest FA.

In order to obtain the CRWD reactivity components, we performed calculations for a new case: with a very low fixed power of 10 kW, so that the temperatures of all materials remain almost unchanged. The calculated total reactivity is the dynamic reactivity due to CRWD, this reactivity curve is computed with the transient flux and presented in Figure 6 as the red line with dots. The static CRWD reactivity curve, computed with

static k-eff calculations and shown in Figure 3, is also presented in Figure 6 as the blue dots. The difference between these two curves is appreciable, because they are computed with different material and temperature distributions. Additional static reactivity calculations based on the transient temperature and material distribution have been carried out too. The result is shown in Figure 6 with square red points denoted as “Static Extra Calculation” in the legend.

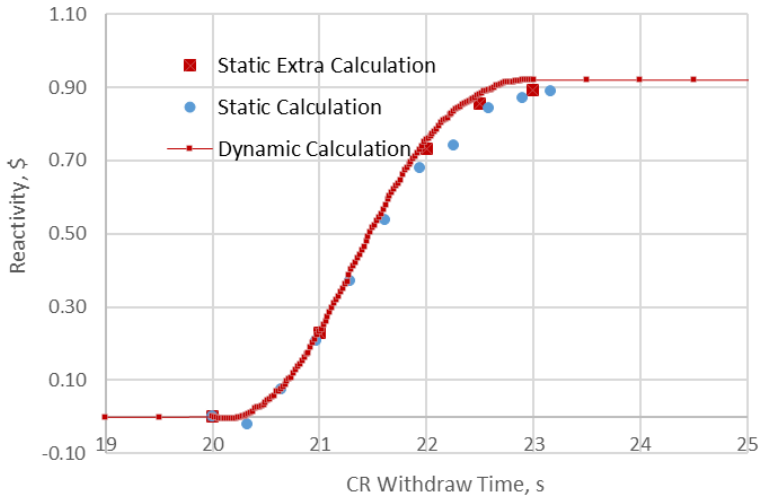


Figure 6: CRWD dynamic and static reactivities.

The difference between the static and the dynamic reactivity values is only a few cents, so the consistency of dynamic and static reactivity values is confirmed.

The transient flux differs from the steady-state one at the beginning of a power excursion because of

- $1/v$ -related term,  $v$  meaning neutron velocity, in the neutron transport equation, which influences the flux spectrum as an additional absorption term when the power increases, thus reducing the spectrum at lower energies, and
- delayed neutrons, which are in a relatively small amount when the power increases: as compared to a steady-state. As the delayed neutron spectra are softer than prompt fission ones, the transient flux spectrum is reduced in addition at lower energies during the power increase as compared to those obtained by static calculations.

Slower neutrons are in general more important in LWRs with uranium fuel because of a higher neutron fission cross-section to capture one ratio at lower energies. Thus, the dynamic reactivity can be lower in LWRs during the power increase as compared to the static one.

Faster neutrons are in general more important in fast reactors with MOX. Thus, the dynamic reactivity can be higher in FRs as compared to the static one during the power increase.

## 4 Conclusion

This study shows that the single CR withdraw may cause an average power increase by about 5 times and a local power overshooting at the neighboring FA by 15 %, but there is almost no effect on the peaking factor of the hottest fuel assembly.

## Acknowledgements



This study has received funding from the European Union's Horizon EURATOM 2021 Research and Training Programme under Grant Agreement No 101061185.

The content of this paper reflects only the authors' views and the European Commission cannot be held responsible for them.

The authors would like to express their gratitude to the JAEA for the provision of SIMMER under a JAEA-KIT/CEA agreement on the exchange of information and collaboration to develop the code.

## References

- [1] ANSELMUS Project (2024). <https://www.anselmus.eu>.
- [2] Yamano, H., Fujita, S., Tobita, Y., Sato, I., & Niwa, H. (2008). Development of a three-dimensional CDA analysis code: SIMMER-IV and its first application to reactor case. Nucl. Eng. Des. 238(1): 66-73.

- [3] Kriventsev, V., Rineiski, A., & Maschek, W. (2014). Application of safety analysis code SIMMER-IV to blockage accidents in FASTEF subcritical core. *Ann. Nucl. Energy*, 64: 114-121.

# Does Partitioning & Transmutation have a future as a nuclear waste management strategy?

*Bruno Merk<sup>1,2</sup>, Lakshay Jain<sup>1</sup>, Omid Noori-kalkhoran<sup>1</sup>, Elfriede Derrer-Merk<sup>1</sup>, Gregory Cartland-Glover<sup>3</sup>, Lewis Powell<sup>1</sup>, Andrew Jones<sup>1</sup>, Anna Detkina<sup>1</sup>, Dzianis Litskevich<sup>1</sup> and Maulik Patel<sup>1</sup>*

<sup>1</sup> School of Engineering, University of Liverpool, Liverpool, UK

<sup>2</sup> School of Physical Sciences, University of Liverpool, Liverpool, UK

<sup>3</sup> STFC Daresbury Laboratory, Warrington, UK

## Abstract

A solution for nuclear waste management is frequently highlighted as a critical prerequisite for the future success of nuclear technologies. Beyond the concept of deep geological disposal, the technological approach of reducing nuclear waste through transmutation was actively researched in the late 20th century. However, progress in this field has significantly slowed over the past decade, with critics raising concerns about the high cost and complexity of the proposed solutions, which have been perceived as offering limited impact on the overall disposal challenge.

In this context, we provide a baseline overview of the current status of partitioning and transmutation, focusing on key lessons learned and the inherent limitations of existing approaches. Building on this analysis, we propose ideas and approaches aimed at developing a visionary pathway toward an optimal future for nuclear waste management.

This foundation leads to the introduction of iMAGINE, an innovative and far-reaching concept designed to significantly advance nuclear waste management. The solutions proposed within iMAGINE are aligned with the envisioned ideal future pathway for partitioning and transmutation. Furthermore, we outline the next steps required to establish a comprehensive research, development, and demonstration program. This program aims to serve as the cornerstone for the creation of a national and later even a supranational strategy that advances nuclear waste management and potentially eliminates the need for a long-term deep geological disposal of high-level radioactive waste.

# 1 Introduction

“One of the greatest challenges in the use of nuclear energy is the highly radioactive waste which is generated during power production. It must be dealt with safely and effectively. While technical solutions exist, including deep geological repositories, progress in the disposal of radioactive waste has been influenced, and in many cases delayed, by public perceptions about the safety of the technology. One of the primary reasons for this is the long life of many of the radioisotopes generated from fission, with half-lives on the order of 100,000 to a million years. Problems of perception could be reduced to an essential degree if there were a way to burn or destroy the most toxic long-lived radioactive wastes during the production of energy” [1]. These are the words of Victor Arkhipov, at the time, consultant in the IAEA division of nuclear power and the fuel cycle, published in the IAEA Bulletin number 39 in 1997.

These words demonstrate the relevance of complex, interdisciplinary thinking when trying to deal with solutions for nuclear waste. The challenge is only partly an engineering problem, as it is more a socio-political one. Depending on the socio-economic mindset in specific countries, the core challenge is often defined by the level of public perception of nuclear waste and public acceptance during site selection [2]. The current approaches can be separated between the two extremes, on the one hand Finland [3] and Sweden [4] having completed or at least started construction of final repositories and on the other, Germany [5,6] and the US [7,8] having decided to abandon their chosen sites – the contrast being between a sufficiently safe site already selected for construction and the idea of the ‘safest’ site which has to be determined in a highly complex process. More details on the now restarted site selection process, its complexity, and the associated challenges in Germany have been recently published [9,10]. However, as Victor Arkhipov argues, innovative technologies for novel approaches of improving waste management could be a key factor in influencing the future of how humanity deals with nuclear waste and thus, finally the future of nuclear technologies and their usage. Moreover, such novel technological solution(s), if realized, will address public concerns and could foster higher acceptance of nuclear energy [9-11]. The idea of dealing with nuclear waste in an improved manner through advanced technologies instead of a big geological final disposal is not new. The development of so-called technological solution, partitioning & transmutation (P&T) had been started in the 1990s with the aim to separate and burn nuclear waste and reduce the amount of long-lived radioactive material. However, in the last years, new, much more comprehensive approaches have been developed [12-15] and successively refined [16,17]. The topic of nuclear waste management has not lost its importance in today’s world and has been

critically discussed addressing the UK and international challenges [18]. Additionally, the relevance is demonstrated and the scientific exchange is reflected in a series of high level international meetings like IAEA SNF conference [19] and NEA information exchange meeting on P&T [20], which focus on tackling the nuclear waste challenge.

Looking at the history of nuclear energy, starting with the early concepts and theoretical foundations laid during the initial days of nuclear energy and chemistry, it becomes clear that the need and idea of dealing with nuclear waste in a better manner has existed from the beginning. The development of nuclear reactors and atomic bombs during the Second World War led to a surge in nuclear research. Scientists quickly realized that nuclear fission can not only produce a huge amount of energy, but also produces a wide variety of radioactive isotopes, some with very long half-lives. The first ideas for dealing with nuclear waste were formulated as early as the 1940s, as described by General Groves in 'Now it can be told': "We always thought that it would be possible by intensive research to eliminate much of this radioactive problem in the future. We also hoped to recover the Uranium remaining in the existing solutions and to reduce the bulk of the radioactive waste materials, thus making them easier to handle." [21] However, the primary focus during this period was on the delivery of nuclear weapons and later, on harnessing nuclear energy for civilian applications and the management of the immediate waste products during the time of 'Atoms for Peace' [22].

With the creation of Partitioning & Transmutation (P&T) some proponents of the technology had promised that this technology can ultimately solve the waste problem. Carlo Rubbia said: "It is shown that a cluster of 5 EAs [Energy Amplifiers] is a very effective and realistic solution to the elimination ... of the present and foreseen (till 2029) LWR-Waste stockpiles of Spain, but with major improvements over Geologic Storage, since: (1) only a Low Level Waste (LLW) surface repository of reasonable size is ultimately required ... " [23]. Building on the technology proposed by Carlo Rubbia, just recently, Franz Strohmer, the head of fuel & reprocessing of Transmutex, said transmutation was the "first technology that has been taken seriously by a nuclear waste agency to reduce the amount of nuclear waste". He said "it ... would reduce the time it remains radioactive to 'less than 500 years'" [24].

## **2 History of P&T and the relevant technologies**

In the conceptual development phase in the 1950s-1970s, different reactor types were developed, some of them with the potential of burning nuclear waste in a fast spectrum

such as the Experimental Breeder Reactor (EBR-I) as first power producing reactor [25], which was based on a sodium cooled fast reactor concept. It was followed by EBR-II in USA [26], Rapsodie [27] in France, a sodium-cooled fast neutron loop-type reactor with a thermal output of 40 MW, and the KNK II [28] in Karlsruhe, Germany, a fast sodium-cooled reactor with an electric output of 21 MW. In parallel to the development of fast reactor technologies, other technologies which formed the basis for partitioning ideas were developed. Researchers began to explore chemical processes for separating different radioisotopes from spent nuclear fuel (SNF) for civil applications. The goal was to recycle valuable fissile materials like Plutonium and Uranium. Early methods included solvent extraction processes such as PUREX (Plutonium and Uranium Recovery by EXtraction), which was originally developed during the Manhattan Project and patented late in the 1940s [29] and became a standard in the civil nuclear industry. The industrial application of separation of valuable elements from the spent fuel and their re-introduction into the reactor was demonstrated commercially in Belgium by partially re-fuelling a LWR in the 1960s [30]. However, the following decades were mainly dominated by electric energy production and the optimization of the reactor systems regarding safety and economy, while reprocessing was mainly used to separate fissile material for military use.

The shift of reprocessing to civil uses was supported by the French government and strengthened by the 1973 oil crisis, as well as the French fast reactor programme with first connection of the PHENIX reactor to the French national electricity grid in December 1973 [31]. La Hague site, which currently has nearly half of the world's light water reactor spent nuclear fuel reprocessing capacity, also started operation in 1976 [32]. Almost at the same time, on 7th April 1977, US President Jimmy Carter banned the domestic reprocessing of commercial reactor spent nuclear fuel [33], leading to a big blow on the US programmes and abandoning the ambitions for establishing a closed fuel cycle system in the US. Meanwhile, some small-scale research has been undertaken in P&T [34,35] and advanced methods have been developed to reuse some of the fuel from EBR-II [36] as HALEU (High-Assay Low Enriched Uranium) resource. In contrast, in Europe, the French decisions were followed by the approach to commercial reprocessing in the UK through setting up of the oxide fuel reprocessing plant THORPE in 1994 [32] at the Sellafield site. This site already hosted other non-commercial reprocessing facilities like the MAGNOX reprocessing plant in operation since 1964 [32]. The focus of the commercial reprocessing facilities was on the treatment of thermal UOX (Uranium Oxide, commercial LWR fuel) reactor fuel where the Plutonium is formed through the breeding process and thus appears micro dispersed. During the testing of reprocessing MOX (Mixed Oxide) fuel, problems were discovered due to solubility issues



[37]. Such problems were not observed as the focus of the treatment processes was on UOX to separate Plutonium as a source of fuel for MOX (for LWRs operation), while the reprocessing of MOX fuel was not envisaged as a commercial service. Closed fuel cycle operation in reactors has been demonstrated in France in a collaborative effort between the reprocessing in La Hague, the MOX production in the MELOX plant and the irradiation and power production in PHENIX [38].

However, the vision of Partitioning and Transmutation (P&T) is much larger than just recycling and burning Plutonium. The ultimate vision is solving the final disposal problem for long-lived heat producing waste. Interestingly, the first experiments inserting minor actinide containing fuel into experimental nuclear reactors to burn these isotopes are much older than what is typically seen as the starting of the P&T programmes. "In the 70s, minor actinide (Np, Am) containing mixed oxide fuels were designed and successfully irradiated in fast reactors: KNK II and PHENIX. The composition of the fuel covered both the homogeneous and heterogeneous recycling of minor actinides" [39].

## **2.1 From Pu utilization in fast reactors to closing the fuel cycle and finally to P&T as a strategy to reduce the challenge of nuclear waste**

The first strong push to develop and later demonstrate the technology of partitioning & transmutation (P&T) of transuranic isotopes had been created by two important, relatively large international projects: the OMEGA programme in Japan and the CAPRA/CADRA project in France. The OMEGA programme, which was launched in 1988: "In addition, the Japan's Atomic Energy Commission submitted in October 1988 a report entitled 'Long-Term Program for Research and Development on Nuclide Partitioning and Transmutation (P&T)', from the viewpoints of conversion of High Level Waste (HLW) into useful resources and its disposal efficiency. The program plots a course for technological development up to the year 2000 and is called 'OMEGA' which is the acronym derived from Options for Making Extra Gains from Actinides and fission products" [40,41], was the first major worldwide project related to P&T. Shortly after the announcement of the OMEGA program, the CAPRA/CADRA project was started in France in the beginning of the 1990's: "CAPRA-CADRA was created in response to the 1991 French law which mandated a 15-year research programme to investigate the technical options available for the nuclear fuel cycle in France" [42] with a slightly different aim, investigation of future opportunities to burn excess Plutonium in fast reactors. While the Japanese OMEGA project already focused on the whole system of partitioning & transmutation, the French CAPRA/CADRA project was only dedicated to transmutation,

with the major focus on reuse and incineration of Plutonium in the Superphenix reactor which had been taken out of industrial operation at this time. “The potential of fast reactor systems to burn Plutonium and minor actinides (MAs) (Np, Am, Cm) was studied within the CAPRA/CADRA program (Barré, 1998)<sup>1</sup>. CAPRA mainly deals with managing the Plutonium stockpile and CADRA is related to the burning/transmutation of MAs and long-lived fission products” [43]. This tradition of providing funding for partitioning and transmutation was kept in the follow up step. The next major step in transmutation in Europe was the launch of the Integrated Project EUROTRANS as a part of the 6th EU Framework Programme (FP). Among the prior research and development topics of EURATOM 6th Framework Programme is the management of high-level nuclear wastes. In particular, the development of technical solutions of nuclear waste management is considered important [44]. IP EUROTRANS has been followed by a huge number of smaller projects in FP 7 and now in HORIZON 2020. These focus on specific problems related to partitioning and transmutation, or are integrated into projects with a broader focus, such as the development of fast reactors. In parallel, partitioning was funded through “EUROPART: EUROpean research program for the PARTitioning of minor actinides and some long-lived fission products from high active wastes issuing from the reprocessing of spent nuclear fuels” [45], with the aim to define the processes for the partitioning of minor actinides by investigating hydrometallurgical and pyrometallurgical processes [15]. Similar to EUROTRANS, EUROPART has been followed by several projects on more specific issues on nuclear chemistry and the link to fuel production, e.g. the European Horizon 2020 GENIORS project [46], later followed by PATRICIA [47]. A review of a wide range of different separation processes has been published [48].

Two very specific, mostly policy-oriented projects have been undertaken in Germany following the nuclear phase out decision taken in 2011. The Federal Ministry for Economic Affairs and Energy (BMWi) and the Federal Ministry of Education and Research (BMBF) launched a comprehensive study managed by the National Academy of Science and Engineering (acatech) to create a robust scientific overview for an evidence-based decision on the future of the P&T research under the boundary conditions of the nuclear phase out decision taken by the government. The acatech study consisted of two parts: one concerned with technological issues (“Studie zur Partitionierung und Transmutation (P&T) hochradioaktiver Abfälle” [49]), and the second part concerned with chances and risks for the society (“Gesellschaftliche Implikationen der Partitionierungs- und Transmutationsforschung” [49]). The information collected in the German study on P&T [50]

---

<sup>1</sup> Barré, B., 1998. The Future of CAPRA. 5th Int. CAPRA Seminar, Karlsruhe

has been used to create the basis for the acatech POSITION “Partitioning and Transmutation of Nuclear Waste. Chances and Risks in Research and Application” (“Partitionierung und Transmutation nuklearer Abfälle. Chancen und Risiken in Forschung und Anwendung” [51]). The results of the acatech study, as well as the acatech POSITION have been discussed with representatives of the funding ministries and later presented at both national [52] and international levels [53]. In October 2021, Germany started another policy related project PETRUS (“Partitioning and Efficient Transmutation, Studie mit Fokus auf innovativen Strategien in Russland) [55] with the aim to better understand the changes and opportunities created through the closed fuel cycle programme in Russia, as it was announced at the International Information Exchange Meeting on Actinide and Fission Product Separation and Transmutation (IEM P&T) in Manchester in 2018. In this meeting, Russia announced its commitment to P&T as a future solution for waste management [54]. The PETRUS project (funded by the Federal Ministry for the Environment, Nature Conservation, Nuclear Safety and Consumer Protection) identified the relevant progress in Russia regarding aqueous and pyrochemical reprocessing with downstream minor actinide separation at the Mayak facility, and transmutation in homogeneous or heterogeneous mode in the sodium cooled fast reactor BN-800. For future research, the project identified huge investments into a new reprocessing facility, the Proryv project (construction and commissioning of a nitride fuel production facility and the construction and commissioning of a lead cooled fast reactor), and the BN-1200 project. At the same time, the long-term research will focus on minor actinide burning in Molten Salt Reactors and the fuel production for closed fuel cycle and P&T [55].

The current situation can be summarized in the following way: Research continues to refine partitioning methods and improve the efficiency and safety of transmutation processes. The implementation of P&T on an industrial scale faces significant challenges, including high costs, technical complexities, and regulatory hurdles. In general, interest in research and development (R&D) related to P&T has visibly declined, as reflected in the significant decrease in active international projects and publication activity on P&T topics. The most recent overview publication “Current state of partitioning and transmutation studies for advanced nuclear fuel cycles” [56] identified the reduced publication activity and shows how specialized P&T research has become, maybe losing sight of the general challenge of dealing with nuclear waste. This study demonstrates the ongoing separation of the work into specific, isolated, traditional work areas such as separation, manufacturing and irradiation of targets, and core physics – instead of an integral approach to face the challenge and the demand of cross-disciplinary understanding and holistic optimization. Another overview publication “Trends and Perspectives on Nuclear Waste Management: Recovering, Recycling, and

Reusing” [57] points into the same direction of the classical approach using separated steps: used fuel processing, conditioning, partitioning, transmutation. However, it at least discusses some new approaches for the reuse of some materials and recognizes the opportunities of integrated systems “recently emerging tendency to consider reactor, fuel cycle, and waste as parts of the same integrated system” [57].

## 2.2 The current status

The demonstration of P&T has been in general delivered on the lab scale for single challenges, starting with the demonstration of the possibility of closed fuel cycle operation [37]. This was followed by the demonstration of the opportunity to separate Americium from the waste stream [58] and to produce americium bearing target fuel [59]. The final step included irradiating the manufactured Americium targets in different reactors and delivering the post irradiation examination [60,61]. However, the development of P&T technologies has got stuck and not progressed well into the next step, the integrated demonstration of the systemic interplay of the single steps in a full system. The current demonstration has been based on existing technologies, mostly the use of sodium cooled fast reactors and aqueous reprocessing technologies, while the evaluation of the potential gain has almost exclusively been focussed on the idea of reducing the radiotoxicity of the waste stream.

The characterization of P&T resulting from the EUROPART, EUROTRANS, and the follow-up programmes can be summarized in the following way:

- Mainly application of existing technologies, especially solid fuel and multi-recycling
- Concentration only on Pu and Am, while transmutation of Cm and fission products have been deferred
- Classical separation as a series of dependent stages forming a typical, already seen as a given, arrangement in a closed fuel cycle system rather than an overall systemic integrated nuclear system
  - fuel production – typically MOX fuel and separated minor actinide targets, homogenous and heterogeneous approaches have been theoretically investigated
  - reactor design – typically Sodium and Lead cooled fast reactors and more advanced technologies like accelerator-driven system (ADS) have been partly investigated

- reprocessing – typically based on aqueous reprocessing extending the PUREX process with some downstream separations, using more advanced group separation processes has been partly demonstrated on lab-scale
- conditioning/final disposal – typically based on the existing conditioning systems after aqueous reprocessing, applying vitrification of the ‘soup’. The related final disposal arrangement has been taken over from classical steps after reprocessing
- Lack of coordinated thinking through the disciplines
- Optimization of the single steps rather than the whole integrated systems (lack of systemic thinking)
- Limited thinking along the lines of reducing radiotoxicity with little interaction with the final disposal community

The current status has been discussed in the last IEM on P&T organized by NEA at their headquarters in Paris in October 2023 [61] in the form of panel sessions with the following results. P&T is

- Much more challenging than expected - many challenging process steps need to be developed, demonstrated and coordinated
- Limited in scope - transmutation of fission products does not seem to be promising
- Too expensive – demand for reprocessing facilities, and innovative, very specific reactors with limited potential for wide range operation
- Too complex – very challenging complex processes through different disciplines which would need to be coordinated and optimized
- Very tedious – long cooling times and demand for multi-recycling of material through the reactor
- Not effective enough on the final disposal – Pu and Am are not the limiting elements in the final disposal design and safety studies which are typically dominated by highly soluble fission products like Iodine (I-129) or Selenium (Se-79)

Maybe some additional facts could be added:

- There is no sustainable business model for P&T – it does not seem reasonable that the government should not only pay for the research but also for the implementation and application. However, the separation of energy production and waste management [62] has resulted in this situation

- Novel and ground-breaking scientific investigations have already been done and published, and the scientific high potentials have partially moved on to new, more attractive challenges
- Now, it would be the time for a new systemic and economical implementation strategy, overcoming the named challenges and attracting large scale investments
- The separation of fissile materials leads to a so-called Plutonium economy causing proliferation concerns following the NPT (Treaty on the Non-Proliferation of nuclear weapons) which would reduce the potential application of P&T to very few nations

Three different highlights could be concluded from the arguments given above, regarding the future of partitioning and transmutation.

- The idea of P&T was an avenue of research which has not been successful and should be given up – consequently it is time to focus on delivering the final disposal as envisaged in times before the idea of P&T came up
- Continue as it is, which does not seem to be promising, due to the fading interest of the researchers, the governments, and potential investors
- Take learnings of the past and apply these for the next steps. This requires re-focussing on the general idea of creating a waste management without the demand for a geological disposal facility for high level waste through the application of innovative technologies with a strict focus on making the technology attractive for future real-world application

However, a close look onto points one and two will not comply with sustainability and environmental regulations of today's world. In contrast to this, option three, the most promising one in our view, should be chosen. Will it then necessitate the development of a new vision for P&T? Looking back into the general plan for P&T, there was always the vision that there is no need for a deep geological final disposal. At least this was promised, even if it was never called a vision. However, P&T has meanwhile got massively into critique, since the reduction of the radiotoxicity, the core measure used for the success, has never been proven to be the relevant parameter for not requiring deep geological disposal.

Meanwhile, much more comprehensive visions have been developed and published, for e.g. zero waste nuclear of the iMAGINE project [62], in the wider sense provides a vision for the ideal nuclear energy system for the future. A detailed description of iMAGINE will be delivered in the following in the chapter, 'A potential response, the approach

used in iMAGINE'. It does this while meeting the requirements for an 'IDEAL NFC', as presented by Andrej Shadrin at a side event of the 68<sup>th</sup> IAEA GC in 2024 [63] with the three points:

- Recycling of Uranium and Plutonium without increasing fuel cost
- No deep geological disposal for radioactive waste
- Partitioning and burning of Np, Am, Cm in molten salt reactors, fast reactors, ADSs

Both these works clearly show that P&T should be embedded in the much wider view of the nuclear fuel cycle instead of being seen as a singular action on creating a long-term solution for the nuclear waste problem. Transmutation and a transmutation system, like MYRRHA [65] cannot be seen as a sole solution without the related fuel production and reprocessing, since one of the key problems will be the required multi-recycling. P&T should deliver a business opportunity through not only solving the waste problem but simultaneously delivering vast amounts of energy. However, it should not be forgotten that these are visions; thus it should not be assumed that a solution will be found which will completely eliminate the demand for a deep geological disposal. However, the mission could be to avoid the need for a deep geological repository for high level waste – mainly spent nuclear fuel – aiming to turn the demand to a cooling storage facility for 300 to 1000 years for the heat-producing, highly radioactive residues, or ideally their further use as a heat source. The long-lived fission products could be either stored in a to-be designed much smaller deep geological disposal, or in the case of Germany in Schacht Konrad, the repository for low- and intermediate-level radioactive waste [64].

Based on the critiques outlined above, along with the expanded vision and mission, certain adaptations will be essential for P&T to ensure a successful future. Changes will be necessary to progress toward this goal. It may be beneficial to rename certain elements or to distinguish between different approaches, making it easier to differentiate the P&T of the 1990s — which may not have met all expectations — from future approaches aimed at addressing longstanding critiques.

In our view, it may be wise to avoid using the vision of "no deep geological disposal," as this could be perceived as an overpromise. Instead, adopting a vision such as "*No need for a deep geological repository for high-level waste*" may be more realistic. Another potential option is to rebrand future projects under a title like "*Technologies to reduce the final disposal challenge*," providing a new direction and working title. A potentially more compelling approach would involve creating clearer distinctions to underscore this evolution, such as the following:

- P&T = the traditional Partitioning & Transmutation with the focus on the reduction of radiotoxicity as defined in the 1990s with the core aim of burning the transuranic isotopes [64]
- P&T+ = P&T, but with new downstream processes, following reprocessing and partitioning, for the separation of specific elements (separation of the waste stream along half-lives of specific elements) to reduce the final disposal challenge
- Integrated P&T+ = delivering on the objectives of P&T+ through advanced, integrated approaches to avoid a Plutonium economy to allow the use of the technology even in non-nuclear weapon states

There are several possible approaches to achieving the above mission, two of which are: a) either the Russian approach based on existing technologies, a multi-recycling based two-tier system of solid fuelled fast reactors and an advanced waste burner, and aqueous reprocessing with several follow up stages to better deal with the elements remaining in soup from reprocessing (re-use and storage) or b) the new integrative approach of iMAGINE which encompasses 'Integrated P&T+' as well as closed fuel cycle. The iMAGINE programme has been created with the aim of delivering the most advanced waste management solution [66] which is in strong contrast to other molten salt reactor projects in Europe as well as in the US which mainly aim at energy production. If this new vision or at least the mission can be accomplished, the new partitioning and transmutation represent a promising solution to the challenge of the future nuclear waste management. From their theoretical foundations in the mid-20th century to ongoing research and future demonstration projects, these technologies have finally the potential to transform the nuclear industry by minimizing the environmental and societal impact of nuclear waste and the mining of new resources [10].

### 3 The ideal way into the future

To better realize the vision in the future, it is important to invest in the definition of comprehensive requirements for an ideal future solution. What would an ideal integrated future system look like that would truly fulfil P&T's mission of reducing the challenge of final disposal?

1. Making **fuel** accessible during operation to:
  - 1.1. Avoid multi-recycling, with its tediously long operational times due to the required long cooling times before transport (due to radiation exposure risk) and reprocessing (due to the risk of radiolysis of the solvents)



- 1.2. Avoid separation of fissile material to reduce proliferation risk
  - 1.3. Avoid carry over of fissile material into the potential disposal stream
  - 1.4. Avoid fuel production processes which lead to high radiation doses to workers
2. Creating a **new reactor system** which delivers on the specific challenges
  - 2.1. Delivering sufficient breeding to avoid demand of feeding of fissile material during operation
  - 2.2. Delivering breeding in a homogenous mode, to avoid the demand for the separation of fissile materials and thus reduce the proliferation concerns, as well as to avoid the formation of weapon grade material which is typically formed through short term irradiation of pure fertile material
  - 2.3. Being able to burn all transuranic isotopes, not only Am
  - 2.4. Robust against fission product accumulation to allow separation methods to operate on reasonably high concentrations
  - 2.5. Allowing access to the fuel during operation (as already mentioned in the first line)
3. Developing an advanced '**reprocessing**' system which
  - 3.1. Allows the clean-up of fuel during operation to avoid cooling times and multi-recycling
  - 3.2. Operates on high radiation levels, the so-called hot fuel
  - 3.3. Avoids the separation of fissile material to reduce the proliferation risk (see above)
  - 3.4. Avoids carry-over of fissile material into the waste stream (see above)
  - 3.5. Allows the optimization for the clean-up efficiency to avoid the demand for highly expensive, 99.9 % efficiency solutions
  - 3.6. Allows tailored waste streams catering to the demand of the final disposal design and safety
  - 3.7. The separation of specific elements for the re-use of materials which are in demand, like, medical radioisotopes
  - 3.8. The mentioned points above lead most probably to a salt clean-up system based on reverse reprocessing
4. A **conditioning** system
  - 4.1. Allowing the preparation of material/element-wise streams for re-use
  - 4.2. Allowing the tailored conditioning for specific waste streams
  - 4.3. Tailored along the demands of final disposal design and safety
5. A waste **disposal**
  - 5.1. System which takes advantage of the opportunities arising from the new system through an optimized design and safety approach

- 5.2. Scientific community delivering a critical analysis of the options to use facilities already existing or under construction for the disposal of the left-over waste streams
- 5.3. Scientific community which interacts with the waste management system developers to make the best out of the new opportunities
- 5.4. Applying a substantially reduced final disposal system which is accepted by a potential host community and the wider public

In short, the demand has to be formed based on what is required to avoid the demand for a deep geological disposal for high level waste and delivered through a highly coordinated, collaborative effort involving almost all expert branches in nuclear technologies. In addition, system-level integrated cost optimization will be required to ensure an economically attractive solution. However, for this economic analysis, it is important to keep in mind that a well designed system will have additional potential for cost reduction in the fuel cycle by avoiding/minimizing the need for mining and enrichment. However, some of these above-mentioned demands cannot be fulfilled with the current approaches and technologies. This clearly indicates that new thinking and optimization is required. Perhaps, this is just the indicator why the development of classical P&T has slowed down. To progress, the idea of P&T has to be developed further into a new level.

In case a solution is desired and required to avoid the deep geological disposal facility for highly active waste, the ideal system should even be able to deal with the legacy waste of specific countries, like the already vitrified reprocessing waste in Germany [67]. iMAGINE has the potential to improve the situation for the disposal of these waste streams, too. Thus, this should be at least a national, if not a multi-national, effort run through a well-coordinated and focussed programme.

The first decision towards the direction of the application of a molten salt system has already been taken by Russia some years ago by replacing the tier two system, an ADS in the EUROTRANS Programme, with a molten salt system. The key argument for the decision was to limit the radiation dose to the workers in the solid fuel production of transuranic bearing fuel [54]. Molten salt reactor development is meanwhile driven by more than a dozen companies, e.g. in France, US, and Denmark and others.

## 4 A potential response, the approach used in iMAGINE

iMAGINE aims to develop an integrated fuel cycle system based on a molten salt reactor with self-sustained breeding and salt clean-up through reverse reprocessing [68]. The potential for changing the final disposal challenge of the system is discussed in detail in a specific publication [69].

The use of a molten salt reactor system will reduce the challenge of fuel production (see 1.4 of the above list), as only the dissolution step of a pyro-reprocessing would be required initially and which will be without direct involvement of humans and is meanwhile, standard in reprocessing technologies. This is in strong contrast to the solid fuel production which is still dependent on the involvement of humans. The integrated system with the reactor and the directly co-located salt clean-up based on reverse reprocessing will deliver on:

- (1.1) since the salt fuel will be cleaned during operation;
- (1.2) since the system will be designed to separate fission products instead of fissile material;
- (1.3) since the stream with the fissile material will always be sent back into the reactor. The cleaning efficiency does not need to be on an extreme level, which will significantly reduce the risk of carryover; if more clean-up is required, the throughput can be increased instead of the separation efficiency.

The fast, chlorine-based molten salt reactor is designed to operate in self-sustained, homogeneous breeding using  $\text{NaCl-UCl}_3\text{-UCl}_4$  salt as fuel which allows a very high loading of heavy metal ~56 % to assure sufficient breeding (2.1) as well as breeding in a homogeneous mode (2.2), and access to the fuel salt during operation (2.5) for cleaning, but not to separated fissile material eliminating the risk of misuse. The operational mode of a fast reactor with separation of fission products allows to keep not only Uranium and Plutonium, but also all minor actinides in the core to burn them efficiently (2.3) while the fast reactor is much more robust in its operation against fission product poisoning than a thermal reactor (2.4) and will allow reasonably high fission product concentrations for efficient separation.

The proposed salt clean-up, based on reverse reprocessing, allows immediate access to the salt fuel during operation (3.1) and will thus operate on hot fuel (3.2). The concentration of fission products on separation avoids access to fissile material (3.3), while the

reduced efficiency demand will limit the carryover (3.4) and avoid the problem of seeking 99.9 % efficient processes (3.5). It will deliver elementwise waste streams (3.6) and thus, has the potential to deliver materials for re-use (3.7).

The elementwise separated waste streams will also allow re-use (4.1) as well as specific conditioning, if required (4.2). It will even offer the possibility to tailor various streams for later storage or disposal (4.3), which is in strong contrast to the appearance of the 'soup' in classical aqueous reprocessing. The proposed iMAGINE approach will allow taking maximum advantage of the elementwise sorted fission products and, in turn, avoid a geological disposal facility (GDF) for high-level waste (HLW). This makes the optimized design and safety approach (5.1) obsolete and allows concentration on the efforts to alternative disposal route(s) for medium and low-level waste, like Schacht Konrad in Germany [64], for the leftover non-heat-producing long-lived waste stream (5.2). This already seems to be a promising approach to make the best out of the new opportunities (5.3) since it would allow avoiding the demand for a deep geological disposal for high-level waste (5.4). More details on the waste management options through iMAGINE are given in [70]. Based on the proposed technologies, iMAGINE would deliver on the widest possible objectives of integrated P&T+ making a GDF for HLW obsolete [10].

A full analysis of the proposed concept has been successfully completed [some selected publications: 68-71] and the results need a staged experimental validation now, as stepping stone for progress. There is an urgent necessity to implement specific single effect experiments in fuel production and clean-up chemistry, reactor physics, materials interaction, operational chemistry, and heat transfer to improve the accuracy of simulations, and to demonstrate and establish technologies. In the second stage, an integral experimental demonstration with energy production is required to study the interplay of multi-physics effects. A national and later a supraregional research, development and demonstration (RD&D) programme for the innovative systems must be implemented to progress. Such a RD&D programme would allow these countries, which decide to take these next steps, a leading international scientific and technological dominance. It would showcase the techno-political leadership to deliver a leading net-zero technology with all the related export opportunities for its industry.

## 5 Conclusions

Partitioning and Transmutation technologies are currently at a crossroads – they either require a redirection and refocus, or the approach will be shelved since the major aim as given below:

“We conclude that EA [Energy Amplifier]-driven incineration — when compared to direct Geological Disposal — is environmentally more acceptable and economically more advantageous.”, “(1) only a Low Level Waste (LLW) surface repository of reasonable size is ultimately required;” [23]

has not been fully achieved. Up to now, Partitioning and Transmutation technologies are not able to avoid a final disposal for long-lived, heat producing waste as promised. At the panel discussion at the NEA IEM P&T in Paris [61], the experts agreed that P&T, as it is developed today, is not effective enough on the final disposal.

The demonstration of P&T on lab-scale has been in general successfully delivered: starting with the demonstration of the possibility of closed fuel cycle operation, followed by the opportunity to separate americium from the waste stream, to produce americium bearing target fuel, and finally to irradiate the targets in different reactors and to deliver the post irradiation examination. However, the progress of P&T technologies has got stuck in this phase (lab-scale demonstration) and not progressed well into the next step, the demonstration phase on engineering level. The lab-scale demonstration has been based on existing technologies, mostly using sodium cooled fast reactors and aqueous reprocessing, while the evaluation of the potential gain has almost exclusively been focussed on the idea of reducing the radiotoxicity of the waste stream.

To give P&T a new direction and focus, we have defined the requirements for a P&T system optimized to fulfil the promises of the past. This requires a significant change in the technologies, their application, and optimization. However, if developed well, P&T can deliver on the defined requirements and expectations. This means that waste management presents an opportunity for a paradigm shift — from solutions developed in the 1970s to innovative approaches for handling nuclear waste based on 21st century technologies. In this regard, iMAGINE has been developed as an integrated technological solution. iMAGINE simultaneously contributes as a new source of nuclear energy, while addressing public concerns and complementing new sustainability and environmental regulations.

To put the developments in a wider view, P&T can deliver a solution which avoids putting the burden of nuclear waste on the future generation for several 100,000 years. Such a solution has the potential of creating tremendous economic benefits through better utilization of the waste instead of building a geological disposal facility, putting the investment into a grave without any chance of revenue. In addition, the technology can deliver on climate mitigation by opening a massive energy resource (which was not exploitable up to now) for future generations to ensure a safe and affordable net-zero energy supply. Moreover, it greatly minimizes the risk of proliferation, which has always been seen as an inherent problem in closed fuel cycle solutions and P&T applications. In Addition, the iMAGINE technology will allow significantly better use of Uranium, giving access to a massive energy resource for future generations.

## References

- [1] Viktor Arkhipov Future Nuclear Energy Systems: Generating Electricity, Burning Wastes, IAEA BULLETIN, VOL. 39, NO.2 June 1997, available:  
<https://www.iaea.org/sites/default/files/publications/magazines/bulletin/bull39-2/39204783033.pdf>, accessed 14/01/2025
- [2] Attitudes towards radioactive Waste, Special Eurobarometer 297, available  
[https://www.iaea.org/sites/default/files/ebs\\_297\\_en.pdf](https://www.iaea.org/sites/default/files/ebs_297_en.pdf), accessed 13/11/2024
- [3] Trial Run of Final Disposal started today in Olkiluoto, available:  
<https://www.posiva.fi/en/index/news/pressreleasesstockexchangerelases/2024/trialrunoffinaldisposalstartedtodayinolkiluoto.html>, accessed 13/11/2024
- [4] Final disposal of spent nuclear fuel, available:  
<https://www.government.se/articles/2022/01/final-disposal-of-spent-nuclear-fuel/>, accessed 13/11/2024
- [5] Gorleben shuts after exclusion from repository site search, available:  
<https://www.world-nuclear-news.org/Articles/Gorleben-shuts-after-exclusion-from-repository-sit>, accessed 13/11/2024
- [6] Germany closes Gorleben salt dome, available:  
<https://www.neimagazine.com/news/germany-closes-gorleben-salt-dome-9094029/>, accessed 13/11/2024

- [7] Victor Gilinsky, Why US nuclear waste policy got stalled. And what to do about it, available: <https://thebulletin.org/2024/07/why-us-nuclear-waste-policy-got-stalled-and-what-to-do-about-it/>, accessed 13/11/2024
- [8] Blue Ribbon Commission on America's Nuclear Future: Executive Summary, January 2012, available: [https://www.energy.gov/sites/prod/files/2013/04/f0/brc\\_finalreport\\_jan2012.pdf](https://www.energy.gov/sites/prod/files/2013/04/f0/brc_finalreport_jan2012.pdf), accessed 13/11/2024
- [9] Themann, D., Schwarz, L., Di Nucci, M. R., and Brunnengräber, A. (2021a). Power over, power with und power to bei der Standortsuche für ein Endlager. *Forschungsjournal Soziale Bewegung Plus* 34
- [10] Merk, B., Litskevich, D., Detkina, A., Noori-kalkhoran, O., Jain, L., Derrer-Merk, E., Cartland-Glover, G. (2023). iMAGINE-Visions, Missions, and Steps for Successfully Delivering the Nuclear System of the 21st Century. *ENERGIES*, 16(7). doi:10.3390/en16073120
- [11] Denk, A. (2024). Exclusive public—an analysis of public participation in the site selection procedure for a repository for nuclear waste [Original Research]. *Frontiers in Political Science*, 6. <https://doi.org/10.3389/fpos.2024.1271062>
- [12] Nakamura, M. et al. (1992) Present Status of the Omega Program in Japan. Second International Information Exchange Meeting on Actinide and Fission Product Separation and Transmutation Argonne, USA, 1992
- [13] Plutonium Management in the Medium Term A Review by the OECD/NEA Working Party on the Physics of Plutonium Fuels and Innovative Fuel Cycles (WPPR), Nuclear Science ISBN 92-64-02151-5, OECD 2003,
- [14] Knebel, J. et al. (2004) IP EUROTRANS: A European Research Programme for the Transmutation of High Level Nuclear Waste in an Accelerator Driven System. Actinide and Fission Product Partitioning & Transmutation Eighth Information Exchange Meeting Las Vegas, Nevada, USA 9-11 November 2004
- [15] Madic, C. et al (2006) EUROPART:European Research Programme for Partitioning of Minor Actinides within High Active Wastes Issuing the Reprocessing of Spent Nuclear Fues, 9th IEM on Actinide and Fission Product Partitioning and Transmutation, Nîmes, 25-29 /09/2006
- [16] Merk, B., Rohde, U., Glivici-Cotruta, V., Litskevich, D., & Scholl, S. (2014). On the Use of a Molten Salt Fast Reactor to Apply an Idealized Transmutation Scenario for the Nuclear Phase Out. *PLOS ONE*, 9(4). doi:10.1371/journal.pone.0092776

- [17] Merk, B., Litskevich, D., Whittle, K. R., Bankhead, M., Taylor, R. J., & Mathers, D. (2017). On a Long Term Strategy for the Success of Nuclear Power. *Energies*, 10(7), 867. doi:10.3390/en10070867
- [18] Pemberton, B. Waste not, want not? UK nuclear waste disposal: a stakeholder perspective. 2024;1(4). <https://doi.org/10.20935/AcadEng7405>
- [19] International Conference on the Management of Spent Fuel from Nuclear Power Reactors: Meeting the Moment, available: <https://www.iaea.org/events/sfm24>, accessed 03/07/2024
- [20] Information Exchange Meeting on Actinide and Fission Product Partitioning and Transmutation, available: <https://www.oecd-nea.org/pt/>, accessed 03/07/2024
- [21] Leslie R. Groves, Now It Can Be Told: The Story Of The Manhattan Project, Da Capo Press; Revised ed. edition (22 Mar. 1983)
- [22] Atoms for Peace Speech, <https://www.iaea.org/about/history/atoms-for-peace-speech>, accessed 17/07/2024
- [23] Fast neutron incineration in the energy amplifier as alternative to geologic storage: the case of Spain - CORE Reader) C. Rubbia, S. Buono, Y. Kadi and J.A. Rubio, CERN/LHC/97-01(EET), available: <https://core.ac.uk/reader/25209571>, accessed 13/11/2024
- [24] Jürg Meier, A Geneva startup wants to recycle nuclear waste into new energy, NZZ, available: <https://www.nzz.ch/english/startup-promises-to-recycle-nuclear-waste-into-new-energy-ld.1832198>, accessed 13/11/2024
- [25] EBR-I lights up the history of nuclear energy development, available <https://inl.gov/feature-story/ebri-lights-up-the-history-of-nuclear-energy-development/>, accessed 13/11/2024
- [26] Catherine Westfall, Vision and reality: The EBR-II story, available; <https://www.ne.anl.gov/About/reactors/EBR2-NN-2004-2-2.pdf>, accessed 13/11/2024
- [27] J. Guidez, L. Martin, Review of the Experience with Worldwide Fast Sodium Reactor Operation and Application to Future Reactor Design, available; [https://www-pub.iaea.org/MTCD/publications/PDF/P1360\\_ICRR\\_2007\\_CD/Papers/J.%20Guidez.pdf](https://www-pub.iaea.org/MTCD/publications/PDF/P1360_ICRR_2007_CD/Papers/J.%20Guidez.pdf), accessed 13/11/2024
- [28] Marth, W., The history of the construction and operation of the German KNK II fast breeder power plant, KfK-5456 (November 94)



- [29] Anderson, Herbert H. and Asprey, Larned B. & Asprey, Larned B., "Solvent extraction process for plutonium", US patent 2924506, issued 1960-02-09
- [30] Belgoprocess: History, available: <https://www.belgoprocess.be/history-milestones/?lang=en>, accessed 13/11/2024
- [31] Sauvage, J.-F., PHENIX: 30 years of history: the heart of a reactor, available: sau04.pdf, accessed 13/11/2024
- [32] nuclear fuel cycle: Processing of Used Nuclear Fuel, available: <https://wna.origindigital.co/information-library/nuclear-fuel-cycle/fuel-recycling/processing-of-used-nuclear-fuel>, accessed 13/11/2024
- [33] PRESIDENTIAL DOCUMENTS: JIMMY CARTER, 1977, available: <https://www.nrc.gov/docs/ML1209/ML120960615.pdf>, accessed 13/11/2024
- [34] Lessons Learned from Recent Nuclear Fuel Cycle Scenario Studies T. Taiwo (ANL, US) Fifteenth NEA Information Exchange Meeting on Actinide and Fission Product Partitioning and Transmutation, Manchester, UK, 30 September-3 October 2018
- [35] Justin T. Cooper Development of a TRUEX Digital Twin for Minor Actinide Recycling using Spectral Data Acquisition, 16th Information Exchange Meeting on Actinide and Fission Product Partitioning and Transmutation, Paris 2023
- [36] Robin Roper, Megan Harkema, Piyush Sabharwall, Catherine Riddle, Brandon Chisholm, Brandon Day, Paul Marotta (2022) Molten salt for advanced energy applications: A review, *Annals of Nuclear Energy*, Volume 169, 2022
- [37] Tianchi Li, Fang Liu, Zhou Jia, Fangxiang Luo, Taihong Yan, Weifang Zheng (2024) Dissolution of mixed oxide(MOX) fuel in nitric acid: A review, *Heliyon*, Volume 10, Issue 6
- [38] Merk, B., Stanculescu, A., Chellapandi, P., & Hill, R. (2015). Progress in reliability of fast reactor operation and new trends to increased inherent safety. *Applied Energy*, 147, 104-116. doi:10.1016/j.apenergy.2015.02.023
- [39] Koch, L. (1990) System-immanent Long-lived Radioisotope Transmutation. First International Information Exchange Meeting on Actinide and Fission Product Separation and Transmutation 1990, Mito, Japan, <https://www.oecd-neo.org/pt/docs/iem/mito90/mit-4-01.pdf>, accessed 10.06.2013
- [40] Nakamura, M. et al. (1992) Present Status of the Omega Program in Japan. Second International Information Exchange Meeting on Actinide and Fission Product Separation and Transmutation Argonne, USA, 1992, <https://www.oecd-neo.org/pt/docs/iem/argonne92/arg02.pdf>, accessed 10.06.2013

- [41] Kawarada, S., The OMEGA programme in Japan: A base for international co-operation - An overview of Japan's programme in transmutation and partitioning, IAEA BULLETIN, 3/1992, available:  
<https://www.iaea.org/sites/default/files/publications/magazines/bulletin/bull34-3/34302393537.pdf&ved=2ahUKEwj71LSdwquHAXVHQUEAHVaBB3MQFnoECCAQAQ&usg=AOvVaw2zHDQB5efRQCkyBFwsgl4i>, accessed 17/07/2024
- [42] Plutonium Management in the Medium Term A Review by the OECD/NEA Working Party on the Physics of Plutonium Fuels and Innovative Fuel Cycles (WPPR), Nuclear Science ISBN 92-64-02151-5, OECD 2003, <http://www.oecd-neo.org/science/docs/pubs/nea4451-plutonium.pdf>, accessed 10.06.2013
- [43] Vasile, A. et al. (2001) The Capra – Cadra Programme”, Proc. ICONE 8, 8th conference on Nuclear Engineering, April 2–6 2000, Baltimore, US, Professional Engineering Publishing, Suffolk, UK.
- [44] Knebel, J. et al. (2004) IP EUROTRANS: A European Research Programme for the Transmutation of High Level Nuclear Waste in an Accelerator Driven System. Actinide and Fission Product Partitioning & Transmutation Eighth Information Exchange Meeting Las Vegas, Nevada, USA 9-11 November 2004,  
[http://www.oecd-neo.org/pt/docs/iem/lasvegas04/11\\_Session\\_V/S5\\_01.pdf](http://www.oecd-neo.org/pt/docs/iem/lasvegas04/11_Session_V/S5_01.pdf), , accessed 10.06.2013
- [45] <https://igdtb.eu/activity/europart-european-research-program-for-the-partitioning-of-minor-actinides-and-some-long-lived-fission-products-from-high-active-wastes-issuing-from-the-reprocessing-of-spent-nuclear-fuels/>
- [46] About GENIORS: Turning spent nuclear fuel into a resource, available:  
<https://www.geniors.eu/about-geniors/>, accessed 13/11/2024
- [47] Partitioning And Transmuter Research Initiative in a Collaborative Innovation Action (PATRICIA) | patricia H2020, available: <https://patricia-h2020.eu/en>, accessed 14/01/2025
- [48] P. Baron et al (2019) A review of separation processes proposed for advanced fuel cycles based on technology readiness level assessments, Progress in Nuclear Energy, Volume 117, 2019
- [49] Studie zur Partitionierung und Transmutation (P&T) hochradioaktiver Abfälle available: <http://doku.uba.de>, accessed 10.06.2013

- [50] Renn, Ortwin (Hrsg.): Partitionierung und Transmutation. Forschung – Entwicklung – Gesellschaftliche Implikationen (acatech STUDIE), München: Herbert Utz Verlag 2014  
[http://www.acatech.de/fileadmin/user\\_upload/Baumstruktur\\_nach\\_Website/Acatech/root/de/Projekte/Laufende\\_Projekte/Transmutation/PuT\\_Studie\\_komplett\\_2013-10-22.pdf](http://www.acatech.de/fileadmin/user_upload/Baumstruktur_nach_Website/Acatech/root/de/Projekte/Laufende_Projekte/Transmutation/PuT_Studie_komplett_2013-10-22.pdf), accessed 27.11.2014
- [51] acatech (Ed.): Partitioning and Transmutation of Nuclear Waste. Opportunities and Risks in Research and Application (acatech POSITION PAPER), Munich 2014. <https://en.acatech.de/publication/partitionierung-und-transmutation-nuklearer-abfaelle-chancen-und-risiken-in-forschung-und-anwendung/>, accessed 14/01/2025
- [52] Merk, B., Geist, A., Modolo, G., Knebel, J. (2015) Results and Conclusions from the German P&T Study – A View of the Contributing Helmholtz Research Centers, 46th Annual Meeting on Nuclear Technology, Berlin
- [53] Merk, B., Geist, A., Modolo, G., Knebel, J. (2014) The German P&T study – results and conclusions in the view of the contributing Helmholtz Research Centers, Actinide and Fission Product Partitioning and Transmutation 13th Information Exchange Meeting, 23.-26.09.2014, Seoul, Republic of Korea
- [54] A. Khaperskaya, Khomyakov Yu, Shadrin A, Feinberg O., Conceptual approaches and the main directions of R&D on partitioning and transmutation of minor actinides and long-lived fission products in the Russian Federation State atomic energy corporation “Rosatom”, Manchester, 15th International Exchange Meeting on Partitioning and Transmutation 2 October 2018 Manchester
- [55] Abschlussbericht: „Partitioning and Efficient Transmutation, Studie mit Fokus auf innovativen Strategien in RUSSland (PETRUS)“, Förderkennzeichen 1501639A-B, available: <https://www.grs-fbw.de/Archiv/ArchivSearch/DownloadSingleFile?guid=ad1f829d-93ee-4f74-b3bf-3c7cfe954b45>, accessed 13/11/2024
- [56] Kooyman, T. (2021). Current state of partitioning and transmutation studies for advanced nuclear fuel cycles, Annals of Nuclear Energy, Volume 157,
- [57] Terranova, Maria Letizia, and Odilon A. P. Tavares. (2024). "Trends and Perspectives on Nuclear Waste Management: Recovering, Recycling, and Reusing" Journal of Nuclear Engineering 5, no. 3: 299-317.  
<https://doi.org/10.3390/jne5030020>

- [58] P. Zsabka, A. Wilden, K. Van Hecke, G. Modolo, M. Verwerft, T. Cardinaels (2023) Beyond U/Pu separation: Separation of americium from the highly active PUREX raffinate, *Journal of Nuclear Materials*, Volume 581
- [59] Fanghänel, T., Glatz, JP., Konings, R.J.M., Rondinella, V.V., Somers, J. (2010). Transuranium Elements in the Nuclear Fuel Cycle. In: Cacuci, D.G. (eds) *Handbook of Nuclear Engineering*. Springer, Boston, MA
- [60] E. D'Agata, S. Knol, A.V. Fedorov, A. Fernandez, J. Somers, F. Klaassen (2015) The behaviour under irradiation of molybdenum matrix for inert matrix fuel containing americium oxide (CerMet concept), *Journal of Nuclear Materials*, Volume 465
- [61] 16th Information Exchange Meeting on Actinide and Fission Product Partitioning and Transmutation , available: [https://www.oecd-neo.org/jcms/pl\\_20161/16th-information-exchange-meeting-on-actinide-and-fission-product-partitioning-and-transmutation-16iempt](https://www.oecd-neo.org/jcms/pl_20161/16th-information-exchange-meeting-on-actinide-and-fission-product-partitioning-and-transmutation-16iempt), accessed 13/11/2024
- [62] Merk, B., Litskevich, D., Peakman, A., & Bankhead, M. (2019). The Current Status of Partitioning & Transmutation and How to Develop a Vision for Nuclear Waste Management. *ATW-INTERNATIONAL JOURNAL FOR NUCLEAR POWER*, 64(5), 261-266.
- [63] Innovative Nuclear Energy Systems with Closed Fuel Cycles, Side event at 68th IAEA General Conference, 18 September 2024, Vienna International Centre, Vienna
- [64] M. Salvatores, I. Slessarev & M. Uematsu (1994) A Global Physics Approach to Transmutation of Radioactive Nuclei, *Nuclear Science and Engineering*, 116:1, 1-18, DOI: 10.13182/NSE94-A21476
- [65] Konrad repository, available: <https://www.bge.de/en/konrad/>, accessed 14/01/2025
- [66] MYRRHA - A global one-of-a-kind, available: <https://www.sckcen.be/en/infrastructure/myrrha>, accessed 14/01/2025
- [67] Merk, B., Litskevich, D., Bankhead, M., & Taylor, R. J. (2017). An innovative way of thinking nuclear waste management - Neutron physics of a reactor directly operating on SNF. *PLOS ONE*, 12(7). doi:10.1371/journal.pone.0180703
- [68] Merk, B., Detkina, A., Litskevich, D., Noori-Kalkhoran, O., & Cartland-Glover, G. (2022). A HELIOS-Based Dynamic Salt Clean-Up Study for iMAGINE. *APPLIED SCIENCES-BASEL*, 12(17). doi:10.3390/app12178748

- [69] Merk, B., Detkina, A., Litskevich, D., Drury, M., Noori-kalkhoran, O., Cartland-Glover, G., Petit, L., Rolfo, S., Elliott, J. P., Mount, A. R. (2022). Defining the Challenges-Identifying the Key Poisoning Elements to Be Separated in a Future Integrated Molten Salt Fast Reactor Clean-Up System for iMAGINE. APPLIED SCIENCES-BASEL, 12(9).
- [70] Merk, B., Detkina, A., Litskevich, D., Patel, M., Noori-kalkhoran, O., Cartland-Glover, G., Efremova, O., Bankhead, M., Degueldre, C. (2022). A First Step towards Zero Nuclear Waste-Advanced Strategic Thinking in Light of iMAGINE. ENERGIES, 15(19)
- [71] Merk, B., Detkina, A., Noori-kalkhoran, O., Jain, L., Litskevich, D., & Cartland-Glover, G. (n.d.). New Waste Management Options Created by iMAGINE through Direct Operation on Spent Nuclear Fuel Feed. Energies, 16(21)



# Thermal-hydraulic analysis of spallation target for accelerator-driven systems

*Xu Cheng, Abdalla Batta and Joachim Knebel*

*Karlsruhe Institute of Technology (KIT), Karlsruhe, Germany*

## Abstract

Transmutation with an accelerator-driven system (ADS) was considered as a promising concept for nuclear waste treatment. Since 1990s extensive research activities were carried out at the Research Center Karlsruhe (now Karlsruhe Institute of Technology, Campus North), to develop ADS, including sub-critical reactors and spallation targets with liquid lead or lead-bismuth eutectic (LBE) as spallation materials. Both experimental studies and numerical analysis were carried out to investigate the thermal-hydraulic behavior of various spallation targets. For these purposes the KALLA laboratory was built up and operated since early 2000s under the leadership of Prof. Robert Stieglitz for many years. The numerical analysis was divided into two classes, i.e. system thermal-hydraulics (STH) analysis and 3-dimensional CFD (computational fluid dynamics) simulation. The system thermal-hydraulics code HETRAF was developed to investigate the thermal-hydraulic performance and to support the design of the entire spallation target system. CFD simulations were carried out to investigate the detailed flow and heat transfer behavior around the active part of spallation targets. This paper summarizes the main results of numerical studies on three different spallation targets, i.e. the ISTC-target, the MEGAPIE-target and the XADS target.

**Keywords:** Spallation target, thermal hydraulics, ISTC target, MEGAPIE target, XADS-target

## 1 Introduction

Transmutation of long-lived radionuclides using an accelerator-driven system (ADS) is a promising solution for reducing the long-term radiotoxicity of nuclear wastes [1-3]. As illustrated in Figure 1.1, an ADS consists mainly of three parts: an accelerator for high energetic protons, a spallation target in which neutrons are produced via spallation

reaction and a sub-critical reactor core in which the transmutation of radioactive waste, e.g. minor actinides (MA), takes place. The spallation target connects the accelerator with the sub-critical reactor and is an extremely challenging issue in the deployment of ADS. Dependent on the power level of the proton beam, there exist three different types of spallation targets, as illustrated in Figure 1.2.

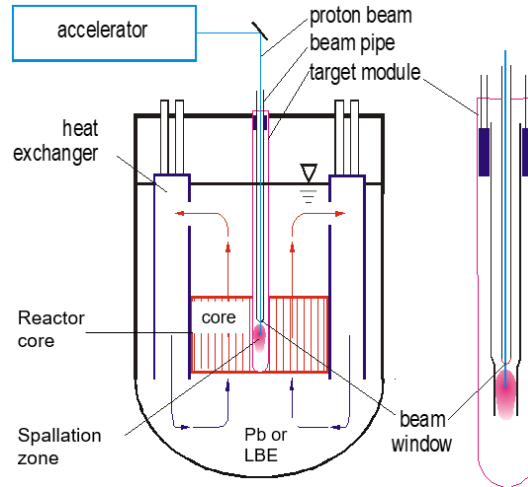


Figure 1.1: Sketch of an ADS<sup>[1]</sup>

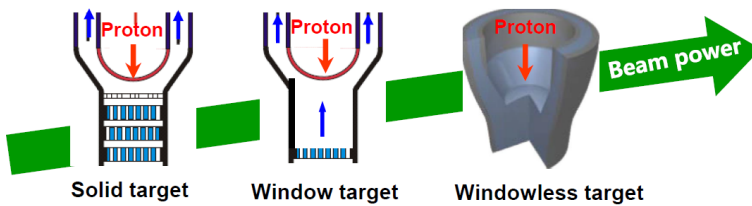


Figure 1.2: Three types of spallation targets

At low proton beam power level, e.g. in order of 100 kW, heavy solid elements such as Uranium are used as spallation material, which is located inside an enclosure made of tungsten. Heat generated in the spallation material is removed by coolant flowing over the tungsten enclosure. The upper power limit for this structure is determined by the heat removal capability of coolants, e.g. in case of sodium cooling, boiling determines the upper limit of heat removal.



As the power level increases, heat from the solid spallation target can't be sufficiently removed. An effective solution is to replace solid spallation material with heavy liquid metal such as lead or lead-bismuth eutectic. In this case heavy liquid metal takes both functions of spallation material and coolant. With proper design, overheating of the coolant can be avoided. However, separation of spallation material from the vacuum tube of the proton beam is required. For this purpose, a structure with a solid window has been considered [4-6]. Generally, reaction of proton beam with the window material produces high heat power density and, subsequently, high heat flux, which leads to high window temperatures and possibly to a damage of the beam window. Studies in the past indicated that spallation targets with beam window might be feasible for the proton beam up to several megawatts.

An ADS with a reactor power of about 1000 MW requires a proton beam power of about 20 MW or even higher [7]. Thus, spallation targets with beam windows are not suitable for this kind of application. A possible solution is to remove the beam window, the so-called windowless targets. In this case the separation is realized by a free surface of coolant flow. Windowless targets are only feasible if the free surface is stable, local coolant temperature is well below the saturation value and the entrained coolant droplets in the beam tube are negligibly small.

Since end of 1990s, KIT Campus North (former Research Center Karlsruhe, FZK) was actively involved in the thermal-hydraulic design and analysis of various spallation targets. In the first stage focus was put on targets with beam window. Table 1 lists three window targets, which had been intensively investigated at FZK.

Table 1.1: Spallation targets

<i>Target</i>	<i>Proton energy [MeV]</i>	<i>Beam power [MW]</i>	<i>Spallation material</i>	<i>Coolant</i>
<i>ISTC</i>	<i>800</i>	<i>1.0</i>	<i>LBE</i>	<i>LBE</i>
<i>MEGAPIE</i>	<i>600</i>	<i>1.0</i>	<i>LBE</i>	<i>LBE</i>
<i>XADS</i>	<i>600</i>	<i>3.6</i>	<i>LBE</i>	<i>LBE</i>

Figures 1.3 to 1.5 show the sketch of the three spallation targets. The ISTC target was designed and investigated in the frame of the ISTC-559 project [4] under the collaboration of research institutions from Europa, Russian and USA. The main objective of the ISTC project is to develop a window target with liquid LBE and concentrated on the active part of the target. Many different options of target design were proposed and

optimised. One of the selected design options, which was suggested for further investigation is illustrated in Figure 1.3.

The MEGAPIE (MEGAwatt Pilot Experiment) project is an European project with the aim to develop and test a 600 kW power LBE cooled spallation target with beam window [5,8]. FZK was contributing to the design of the MEGAPIE target, covering thermal hydraulics, neutronics and material science. Based on enormous numerical simulations, one of the design options, as shown in Figure 1.4, was suggested for further investigation. As seen, in this design option a bypass jet was foreseen to eliminate the flow stagnation zone near the window centre and to enhance the turbulence intensity in the near window region.

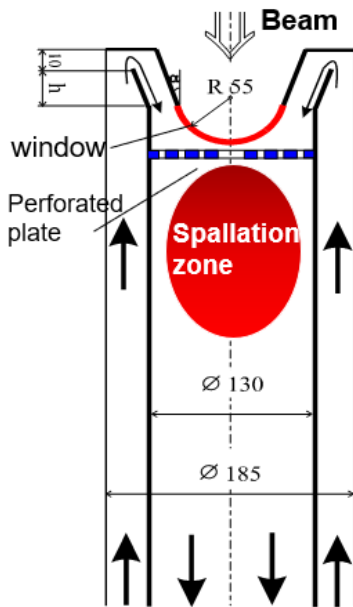


Figure 1.3: ISTC target [11]

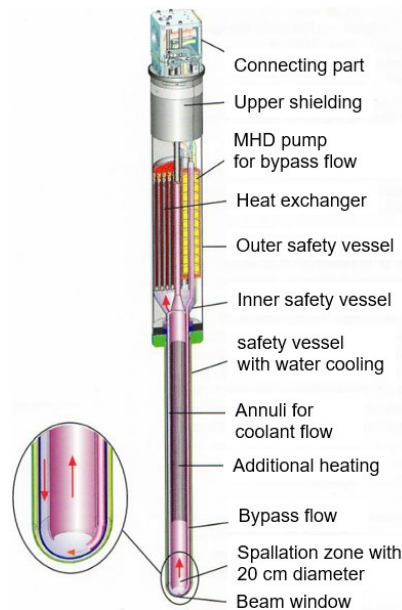


Figure 1.4: MEGAPIE target [1]

One of the key milestones in the European ADS roadmap [9] was the design and construction of the European eXperimental ADS (XADS). One of the reactor core concepts is a LBE cooled reactor with 80 MW thermal power and with a window target [6,10]. The target unit is in the centre of the XADS core and consists of several co-axis cylinders. As shown in Figure 1.5, it is composed of an evacuated central beam tube inside a shell forming the physical boundary to the surrounding core assemblies. The proton beam enters the beam tube at the upper end, penetrates the window at the lower end and impinges on the upward flowing LBE. Heat is removed from the spallation zone in a heat

exchanger at the upper elevation inside the target unit. One of the main features of this compact target module is its capability to remove the spallation heat via purely natural convection.

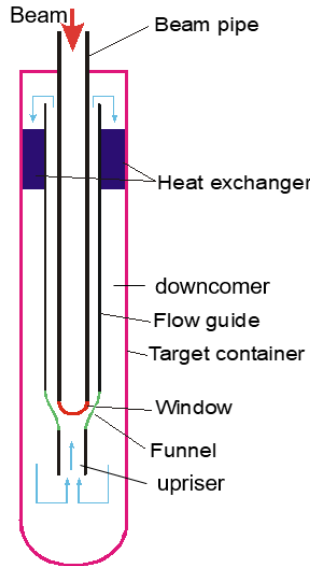


Figure 1.5: XADS target [12]

The thermal-hydraulic investigation at FZK consists of two parts. In the first part, the entire target system, incl. the cooling systems necessary for the operation of the spallation target was taken into consideration. Dynamic behaviour and safety performance of the target system were analysed. This was the case for both MEGAPIE target and the XADS target.

The second task concentrated on the thermal-hydraulic behaviour of the active part of the spallation target. Detailed flow structure and cooling capability of the active part, especially near the window region, was assessed and the geometric configuration of the active part optimized. In addition, experimental investigations were carried out with selected design structures, to confirm the feasibility and to provide experimental data for validation of the numerical codes.

This paper summarizes some research activities and their results for three spallation targets with beam windows, as listed in Table 1.1. In chapter 2, studies on thermal hydraulics of the entire MEGAPIE target systems were presented, whereas chapter 3 focuses on the investigation of flow and heat transfer behavior of the active part of the three spallation targets.

## 2 Thermal hydraulic analysis of the entire MEGAPIE target system

For the numerical analysis of the dynamic behavior of the MEGAPIE target system, the one-dimensional code HETRAF is applied, which was originally developed and validated for studying the dynamic behavior of the cooling system of a super-conducting magnet, which is cooled by super-critical helium [13]. The code can simulate a multi-loop system with thermal coupling between loops. There are modules considering different components, e.g. pump and bypass.

### 2.1 Dynamic behavior of the MEGAPIE heat removal system

The entire heat removal system consists of three loops, i.e. the primary loop, the intermediate loop and the third loop, as schematically indicated in Figure 2.1.

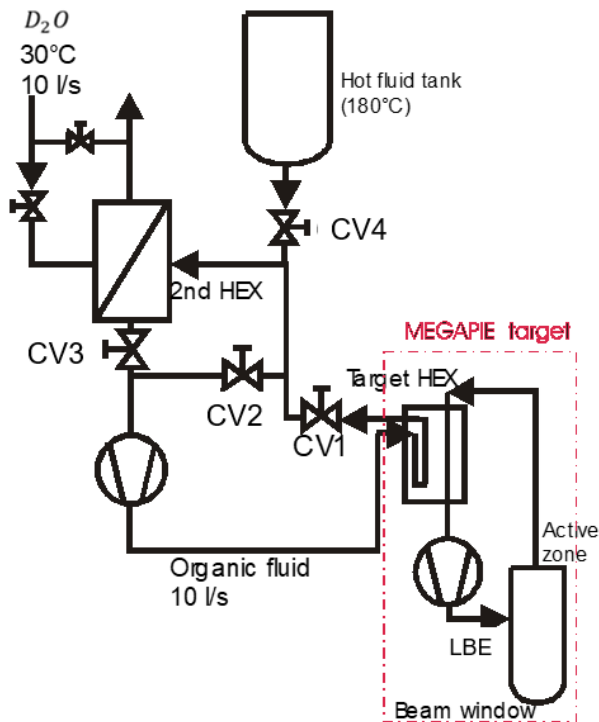


Figure 2.1: Schema of the MEGAPIE heat removal system [14]

In the primary loop, LBE is circulated with two EM-pumps, cools down the beam window and the spallation zone and enters the target heat exchanger, where heat is transferred to the intermediate loop. The nominal flow rate of LBE is 4 l/s. The thermal power released in the spallation target is about 650 kW. The target heat exchanger is in the upper part of the target module and consists of 12 cooling pins. The geometrical and technical data of the primary loop are taken from the project partner [14,15].

In the intermediate loop, the organic fluid (Diphyl) is used to keep the operating pressure in the intermediate loop as low as possible (<10 bar). The nominal flow rate of the organic fluid is about 10 l/s. An expansion accumulator tank with hot fluid is connected to the loop. This provides one option to avoid freezing of LBE in the case of the beam interrupt transient. Another option to avoid the freezing of LBE is the activation (opening) of the control valve CV2, and at the same time the closure of the control valve CV3. The effectiveness of these options needs to be investigated.

The third loop is an existing loop at the SINQ facility. This loop uses heavy water D<sub>2</sub>O as coolant. The nominal flow rate is 10 l/s and the temperature of D<sub>2</sub>O entering the second heat exchanger is 30 °C. Both pre-test and post-test analysis were conducted. The main objective of the pre-test simulation was to understand the performance of the target system and to optimize the cooling system design, if required. The post-test analysis was focused on the comparison with experimental data, to evaluate the feasibility of the numerical model.

## **2.2 Pre-test analysis**

Steady state as well as four transient cases, as shown in Table 2.1, were analyzed and are presented in the present paper. The first two transient cases are related to the loss of the pump head (LoPH) in different loops. In these cases, flow is reduced and the coolant temperature increases.

An excessive temperature of LBE in the primary loop would lead to a damage of the structure material, e.g. the beam window.

An excessive temperature in the intermediate loop may result in a high loop pressure. In case of beam interrupt, the temperature of LBE in the primary loop must be kept above the freezing point, to avoid a blockage of the flow path and, subsequently, a damage of the primary loop.

Table 2.1: Transient cases analyzed

Transient cases	Main phenomena	Safety concerns
Loss of pump head (LoPH) in the primary loop	Reduced flow and increased temperature of LBE	Excessive hot spot in the primary loop
Loss of pump head (LoPH) in the intermediate loop	Reduced heat removal capability of the target HEX	Excessive hot spot in the primary and the intermediate loop
Beam interrupt	Reduced thermal power & coolant temperature	Freezing of LBE in the primary loop

### 2.2.1 Steady state condition

Figure 2.2 shows the temperature distribution of coolant in the primary loop. At the entrance of the target heat exchanger (starting point of the flow path of the primary loop, i.e. flow path length=0), the temperature of LBE is 335 °C. Through the heat exchanger it is cooled down to 245 °C. Due to the heat transfer through the guide tube, LBE in the annular gap is warmed up for about 25 °C. About 100 °C temperature rise is obtained in the spallation zone. The maximum LBE temperature in the spallation zone is about 370 °C.

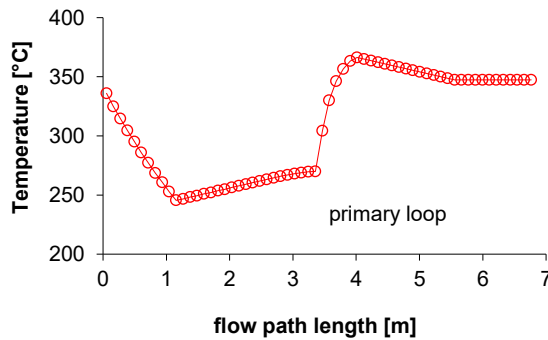


Figure 2.2: Coolant temperature under steady state conditions

### 2.2.2 Loss of the pump head in the primary loop

Figure 2.3a shows the normalized mass flow of LBE in case of the loss of the pump head in the primary loop. The mass flow rate reduces quickly and reaches in about 5s its minimum value, which is about 50 % of the nominal value. After then the mass flow rate increases again due to the enhanced buoyancy effect. Under the steady state natural convection condition the mass flow rate is about 60 % of the nominal value. The LBE temperature in the spallation zone, as shown in Figure 2.3b, increases rapidly and reaches its maximum in about 5s. Due to the increase in mass flow rate, the temperature of LBE in the spallation zone decreases again from 465 °C down to about 440 °C, which is about 70 °C higher than that under the normal operating condition. The short-term coolability of the beam window needs to be analyzed for the case that the main flow pump loses its pump head and the bypass injection pump is still in its full operation.

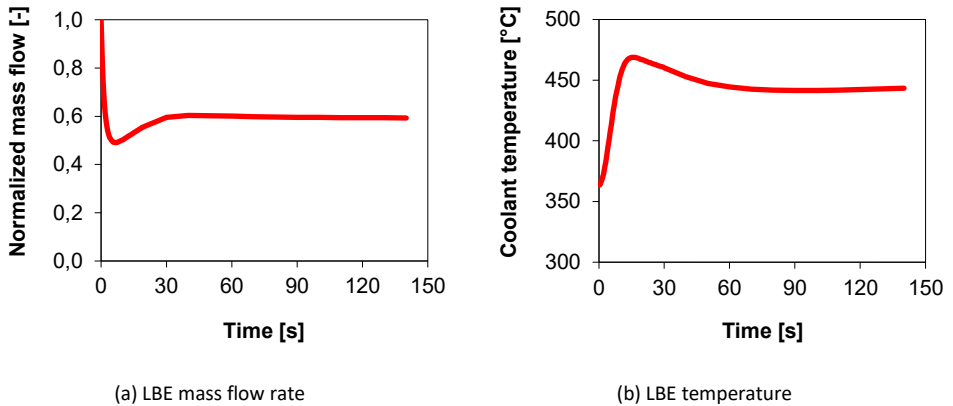


Figure 2.3: LBE mass flow rate and temperature under LoPH in primary loop

### 2.2.3 Loss of pump head in the intermediate loop

Figures 2.4 shows the transient results in case that the pump in the intermediate loop loses its pump head (LoPH). Three curves present the LBE temperature in the spallation zone and the organic fluid temperature at the exit of the heat exchanger, respectively. After the loss of the pump head, the mass flow rate in the intermediate loop reduces rapidly to 1 %. The reduction in the mass flow rate and, subsequently, in the heat removal capability of the heat exchanger, leads to an increase in the LBE temperature in the primary loop. In the first 20 seconds the temperature in the spallation zone is hardly

affected. After then it increases and reaches about 600 °C in 5 minutes. Obviously, safety measures must be activated, to avoid the failure of the beam window. An increase of more than 200 °C in the temperature of the organic fluid at the exit of the heat exchanger is obtained in 5 minutes. A much stronger increase in the temperature of the solid wall facing to the organic fluid is observed. A possible onset of boiling of the organic fluid must be checked. In case that boiling takes place, the pressure in the intermediate loop will increase. Safety measures are, therefore, required to limit the pressure in the intermediate loop.

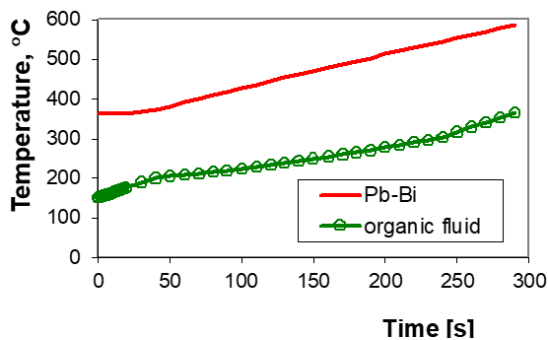


Figure 2.4: Temperature behavior under LoPH in the intermediate loop

#### 2.2.4 Single beam trip

The operation record of the SINQ accelerator at PSI (Paul Sheer Institute) shows that the proton beam can be interrupted frequently [16]. The duration of the beam interrupts varies in a large range, from milliseconds to several minutes. In case of a beam interrupt, heat source is reduced (close) to zero. The LBE temperature in the primary loop decreases. If necessary, safety measures must be activated to keep the lead-bismuth temperature above the freezing point (123 °C), to avoid blockage of the flow path and, subsequently, the damage of the target. Figure 2.5 shows the LBE temperature at the exit of the target heat exchanger, where the LBE temperature has the lowest value in the primary loop. The temperature reaches the freezing point after about 4 minutes. Therefore, safety measures must be activated in case of a beam interrupt with a duration larger than 4 minutes.



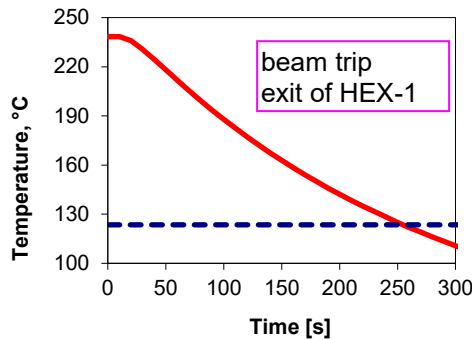


Figure 2.5: Temperature behavior under the single beam interrupt transient

## 2.3 Post-test evaluation

The MEGAPIE target was implemented into the SINQ facility and tested for a period of about 5 months according to the requirements and specifications of the MEGAPIE project team. The post-test data of thermal hydraulic behavior were distributed among the MEGAPIE working group members.

During the MEGAPIE experiments, data is recorded every 5 seconds. For the experimental period of about 5 months, more than 2 million records for more than 200 parameters are made which implies a huge amount of test data.

### 2.3.1 Steady state conditions

As the first step, steady state conditions were assessed. For this purpose, measured data of the beam current are used to determine steady state conditions. A steady state point is then clarified, if the beam current in a predefined time duration, e.g. 3 hours, shows a fluctuation of less than 10 %. In the present analysis one steady state case is selected with the following conditions:

- LBE mass flow rate: 38.2 kg/s
- Oil mass flow rate: 9.78 kg/s
- Beam current: 1250  $\mu$ A
- Inlet temperature of oil: 192.7°C

The values of various parameters at steady state conditions are derived by averaging the corresponding measured data over the time duration.

Figure 2.6 shows the calculated (red line) and the measured (symbols) LBE temperature distribution in the target loop. Here the reference position (position=0) is the elevation of the lower edge of the guide tube. It is seen that the LBE temperature level at the target heat exchanger is well predicted by the HETRAF code. The numerical results indicate an increase in the LBE temperature about 10 °C through the down-comer of the LBE container. This gives a much lower LBE temperature at the lower head of the container (before it is heated up by proton beam) than all the measured temperature values around this region. Inside the guide tube, the measured temperature values are also much higher than the calculated ones. This indicates clearly an under-prediction of the heat transfer through the guide tube, i.e. from the guide tube inside to guide tube outside. An excellent agreement is achieved, if the heat transfer through the guide tube is enhanced by a factor of 5, as indicated in Figure 2.6b. This multiplication factor was thus used in further simulations.

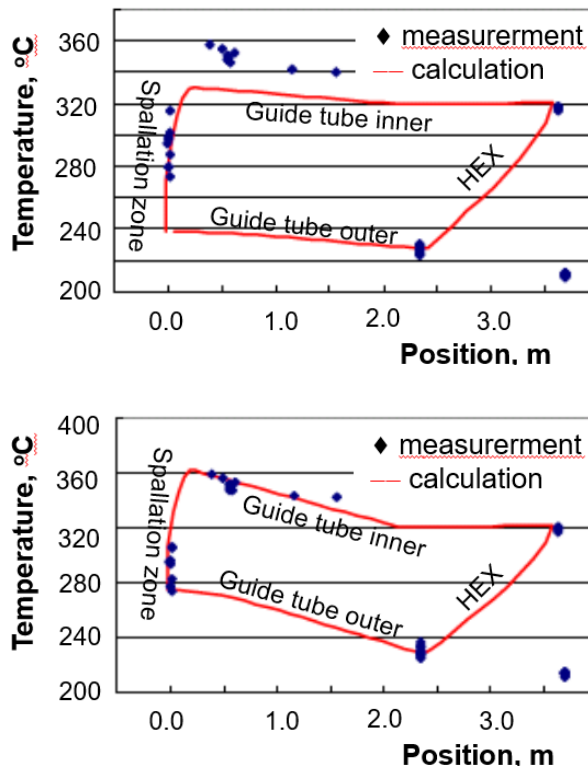


Figure 2.6: Calculated (red line) and Measured (symbols) temperature distribution in the LBE target loop: a) (top) with original heat transfer model and b) (bottom) with multiplication factor 5

### 2.3.2 Beam trip transient

During experiments, the beam trip transient started at the end of the steady state time. The beam should be shut down for certain duration and recover again. That means beam current should reduce to zero and then increases again to original value, as presented in Figure 2.7.

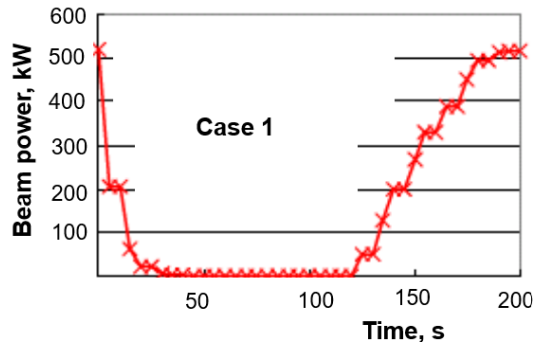


Figure 2.7: Beam power variation during the beam trip transient

Figure 2.8 compares the transient behavior of the calculated LBE temperature with the measured temperature at the inlet of the HEX, at the exit of the HEX and the highest LBE temperature in the riser (referred as peak temperature in this paper), which corresponds to an elevation about 0.5 m above the lower edge of the guide tube.

Generally, a good agreement for both temperatures is obtained between the numerical results and the test data. After the beam trip starts, the LBE peak temperature decreases sharply. The HETRAF code shows a faster decrease in the peak temperature than the measured values.

Related to the LBE temperature at the HEX inlet, the HETRAF code shows a delay of the temperature reduction for a few seconds. This corresponds to the fluid transfer time from the active zone to the HEX. However, the test data indicates a reduction in temperature without delay.

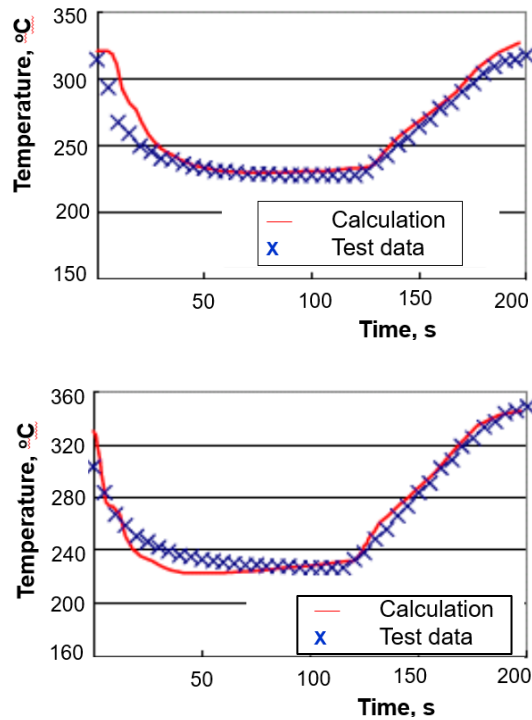


Figure 2.8: Comparison of calculated with measured LBE temperature at HEX inlet (top) and LBE peak temperature (bottom)

### 3 Thermal hydraulic behavior of the active part of targets

This chapter describes the thermal hydraulic analysis of the active part of the three window targets, as listed in Table 1.1. For the ISTC target, numerical (CFD) analysis was carried out in the beginning stage, to identify design options worth further investigations. One of the selected design options is shown in Figure 1.3. Both experimental studies and detailed numerical analysis were then focused on the selected design option.

Similar procedure was taken for the MEGAPIE target. Extensive numerical analysis was carried out by several European institutions to find suitable design options for further studies. Subsequently, experimental confirmation tests for the selected target designs were performed at FZK using water and LBE.

Related to the XADS target, investigations were concentrated on numerical analysis. Because this target was foreseen to be integrated into the XADS reactor and coupled with the accelerator. Numerical analysis was also performed for transient scenarios, which consider the coupled behaviour of the entire target system. In this case, coupled numerical analysis of STH program HETRAF for the entire target system and detailed CFD simulation for the active part was required.

### **3.1 ISTC target**

From the thermal-hydraulic point of view, design of a spallation target requires detailed knowledge about the velocity and temperature distribution, which can only be achieved using CFD codes. The reliability of CFD codes for their application to spallation targets needs to be assessed and validated. For this purpose, experimental investigation was performed to assess the CFD model and as well as to provide additional understanding to the hydraulic behaviour in the active part of the ISTC target.

#### **3.1.1 Experimental studies**

Experimental studies were carried out in the test facility HYTAS (HYdraulic behavior in TARGET Systems) with water as working fluid [17]. The focus of the experimental studies is on the hydraulics (or flow) behaviour in the active part. The similarity of the hydraulic behavior can be established, if identical geometrical structure and the same Reynolds number were provided.

Figure 3.1 shows schematically the HYTAS test facility. The loop is operated under an atmospheric pressure and isothermal conditions with the maximum volumetric flow rate of 100 m<sup>3</sup>/h. It consists mainly of a water storage vessel, a pump, a heat exchanger, a purification device, a buffer tank and the test section. The heat generated by the pump is removed via the heat exchanger, so that the water temperature in the test section is kept constant.

Geometric configuration of the test section is shown in Figure 3.2, similar to the selected design option in Figure 1.3. The flow channel has a square outer surface with a dimension of 150 mm x 150 mm and a circular inner surface with a diameter of 130 mm (Figure 3.2a). The channel wall is made of optical glass and suitable for a high accuracy LDA measurement (as seen Figure 3.1).

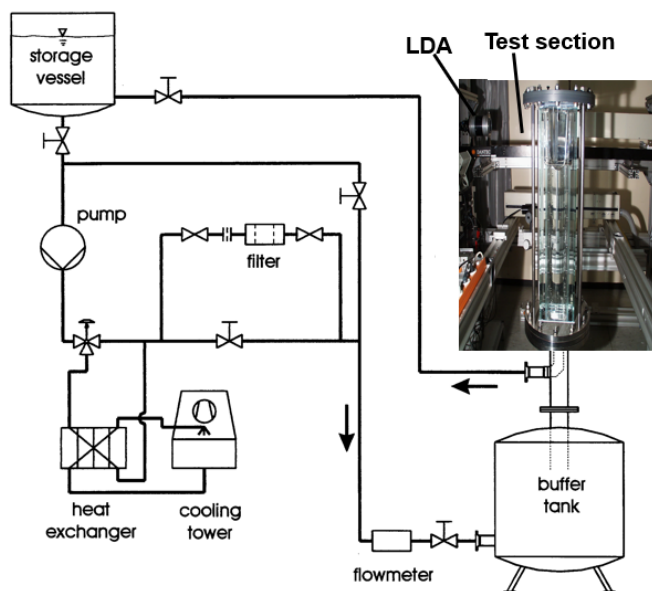


Figure 3.1: HYTAS test facility [17]

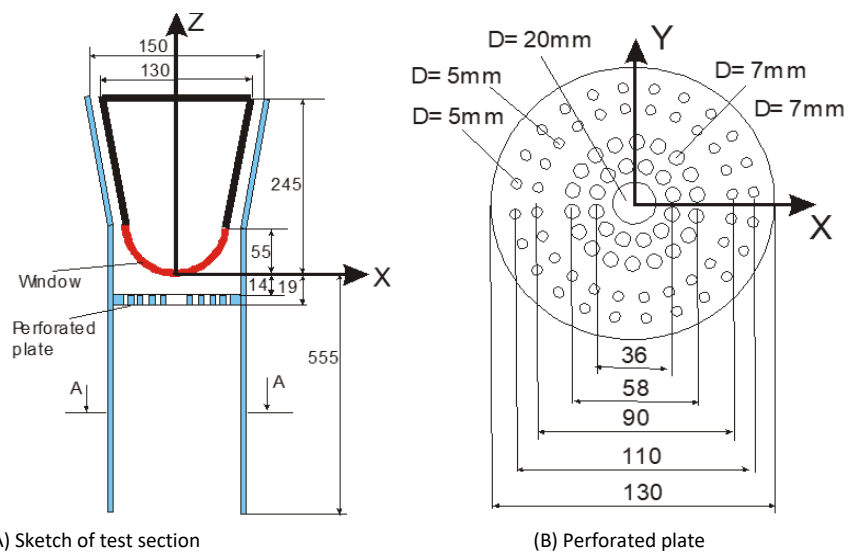


Figure 3.2: Test section, unit in mm [17]

The connection between the loop and the test section is designed in such a way, that the flow in the test section can be bi-directional, i.e. either flowing upwards or downwards through the channel. To eliminate flow stagnation near the window centre and to reduce the flow re-circulation zone, a perforated plate with distributed holes is proposed (Figure 3.2b) and installed close to the window. The plate is located 14 mm below the window surface center. The thickness of the plate is 5 mm.

The flow rate was varied from 5 m<sup>3</sup>/h to 20 m<sup>3</sup>/h. This corresponds to a Reynolds number in the lower part of the flow channel from 6,500 to 27,000, corresponding to the values of liquid LBE flow in the target. The local velocities were measured with 2-D Laser-Doppler Anemometry (LDA).

Experimental measurements were carried out with both downward and upward flow with and without perforated plate, to figure out the effect of the perforated plate on the flow behaviour, especially the formation of flow vortex.

#### (A) Tests without perforated plate

Figure 3.3 shows the flow structure near the beam window for both upward flow (Figure 3.3a) and downward flow (Figure 3.3b) without perforated plate. As seen, for upward flow, smooth flow streamlines with small flow stagnation zone near the window centre were observed, whereas in the downward flow, two large vortices (flow recirculation) occur downstream of the window and in the spallation zone. Flow stagnation zones near the window centre as well as large vortices in the spallation zone should be reduced or eliminated for ADS applications. Thus, perforated plates were introduced.

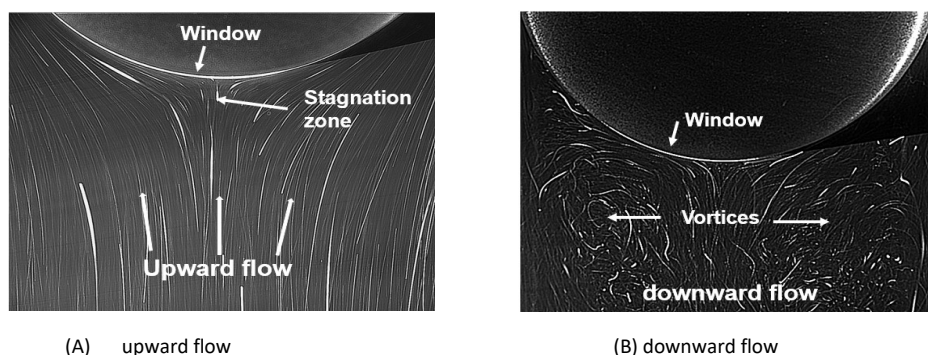


Figure 3.3: Flow pattern around the beam window without perforated plates [17]

## (B) Tests with perforated plate

Figure 3.4 shows results indicating the profile of the axial velocity at different elevations in case of upward flow with the perforated plate.

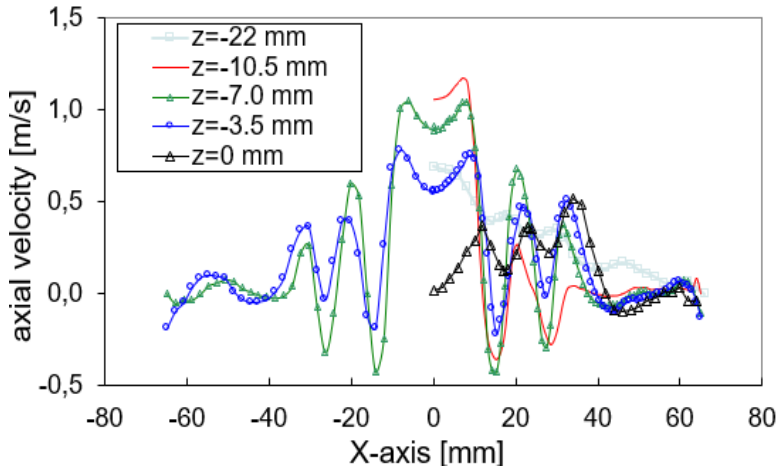


Figure 3.4: Measured velocity profile for upward flow with the perforated plate [17]

At elevations far away from the perforated plate, the velocity profile is similar to that of a developed turbulent flow in a pipe. The velocity profile changes by approaching the perforated plate. The velocity in the channel center increases, while it decreases in the outer region. Very close to the perforated plate ( $z = -22$  mm), a wavy profile is formed with several velocity peaks due to the holes on the perforated plate. Downstream and close to the perforated plate ( $z = -10.5$  mm), a strong wavy profile of the axial velocity is obtained. The maximum velocity in the center is about 1.2 m/s, four times larger than the average value. Between the holes negative axial velocity appears. This indicates the presence of small flow vortices between the holes. The results show a well symmetric distribution of the axial velocity and confirm the high accuracy of the applied LDA measurement technique.

Figure 3.5 shows the profile of the axial velocity of downward flow with the perforated plate. The flow close to the perforated plate is strongly affected by the presence of the perforated plate. Obviously, the perforated plate forces the fluid flowing towards the window region. This causes a slightly upward flow in the region close to the channel wall. Close to the perforated plate, velocity in the central region increases. At the elevation 3.5 mm upstream the perforated plate ( $z = -10.5$  mm), the axial velocity in the



center is as high as 0.8 m/s. At the elevation 3 mm downstream the perforated plate ( $z=-22$  mm), the axial velocity in the center increases to about 1.6 m/s. The velocity profile changes rapidly with the distance from the perforated plate, however, it deviates still far from that of a developed turbulent flow, even at the elevation  $z=-200$  mm, where the velocity in the center is still significantly higher than the average value.

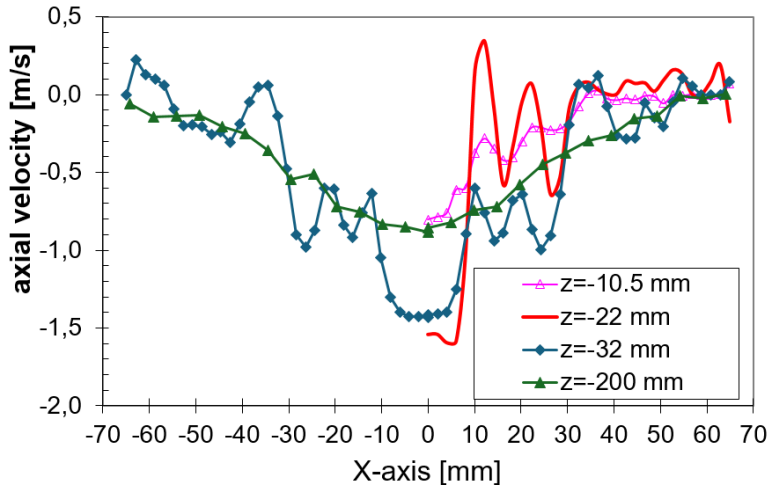


Figure 3.5: Velocity profile of downward flow with the perforated plate [17]

### (C) Comparison with test data without perforated plate

Figure 3.6 compares the numerical results with the test data at two elevations around the window center for upward flow without perforated plate. Upstream the window center ( $z=-10$  mm), a good agreement between the numerical results and the test data is obtained. A large deviation is only observed in the region close to the outer wall surface and at window center elevation ( $z=0$ ). Experiments show a high velocity peak near the outer wall surface, whereas no such peaks are predicted by CFD simulations. This deviation is also observed for downward of the window center elevation ( $z>0$ ).

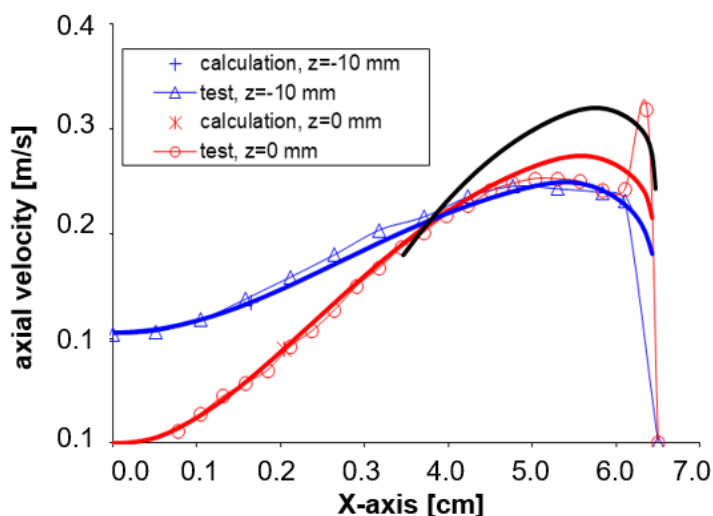


Figure 3.6: Comparison of numerical results with test data for upward flow without perforated plate [17]

#### (D) Comparison with test data with perforated plate

Figure 3.7 compares the numerical results with the experimental data for upward flow with the perforated plate. Results are shown at two elevations close to the perforated plate, i.e. 3 mm upstream the plate ( $z=-22$  mm) and 3.5 mm downstream the plate ( $z=-10.5$  mm). Generally, the numerical results agree well with the experimental data. However, the CFD simulation slightly over-predicts the velocity peak in the central region.

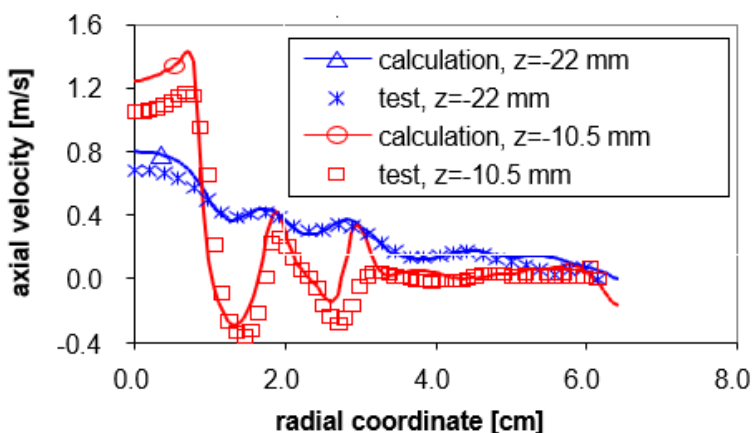


Figure 3.7: Comparison of numerical results with test data for upward flow with the perforated plate [17]

Figure 3.8 compares the calculated axial velocity with the experimental values for downward flow with the perforated plate. Results along two lines are presented, i.e. 3.5 mm upstream ( $z=-10.5$  mm) and 3 mm downstream ( $z=-22$  mm) the plate. The flow behavior downstream the plate is well simulated by the CFD code. Upstream the perforated plate, larger deviation between the test data and the numerical results is obtained. The experiment gives a very low flow velocity in the outer region, and a slightly higher velocity in the central region.

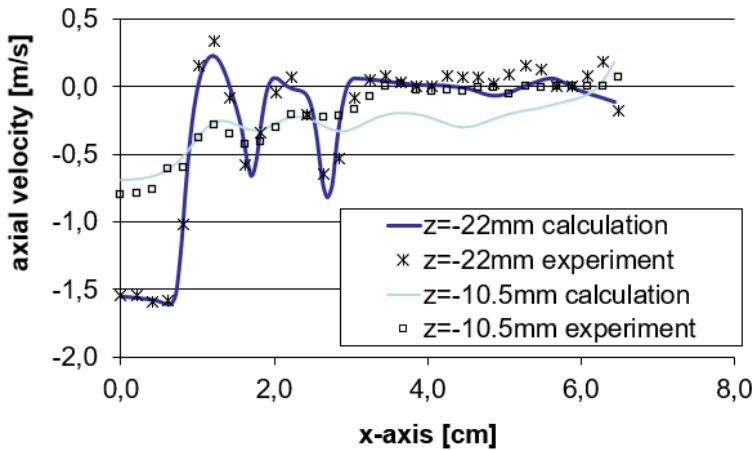


Figure 3.8: Axial velocity of downward flow with the perforated plate [17]

### 3.2 MEGAPIE target

During the design phase, various concepts were taken into consideration. Among of them the concept with injection bypass was intensively investigated and optimized at FZK. The structure of the active part of the MEGAPIE target, which was also tested in KALLA laboratory, is shown in Figure 3.9. The main flow has a fluid temperature lower than that of the bypass flow. The outlet area of the bypass nozzle is  $200 \text{ mm}^2$ . The maximum flow rate through the bypass jet is about  $3 \text{ m}^3/\text{h}$ . The inlet cross-section of the bypass pipe is located far above the target bottom. Before LBE enters the bypass tube, it is heated up and allows a warm-up of the bypass flow of about  $50^\circ\text{C}$ .

For the numerical simulation, the lower part of the target is considered. Further simplifications are made assuming adiabatic boundary conditions to the ambient surroundings. The coordinate system used and the positions of 10 thermocouples on the window surface are also indicated.

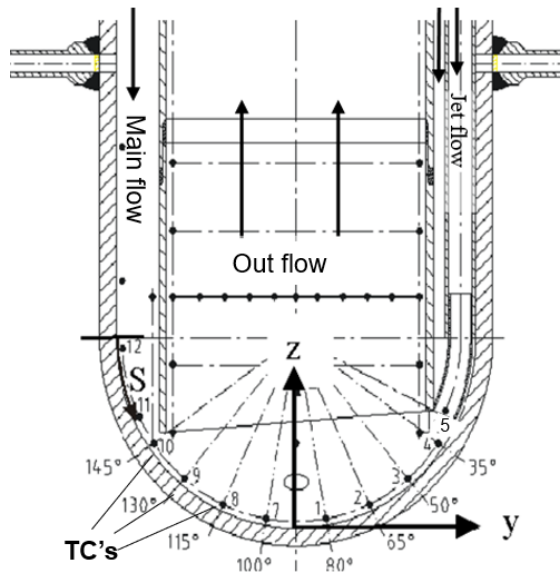


Figure 3.9: Active part of the selected MEGAPIE target design [18]

The origin of the reference coordinate system (x-y-z) is the central point of the window inner surface. One additional coordinate  $S$  is used to account the length along the window inner surface. The origin of this coordinate  $S=0$  corresponds to the angle  $\theta = 0$ . In the following, numerical results are presented for the conditions:

- Total flow rate:  $Q_{total} = 18\text{m}^3/\text{h}$
- Bypass flow rate:  $Q_{jet} = 1.2\text{m}^3/\text{h}$
- Inlet temperature of main flow:  $T_{in} = 573\text{ K}$
- Inlet temperature of bypass flow:  $T_{jet, in} = 623\text{ K}$

Figure 3.10 shows the velocity and temperature contours in the lower part of the target. It is seen that the bypass jet flow, after it exits the bypass nozzle with higher velocity, mixes with the main flow. It generates a flow region with high velocity in the rise tube opposite to the bypass jet, whereas a low velocity region and flow re-circulation occurs in the rise tube close to the bypass jet. Obviously, the bypass jet detaches the window surface, shortly after it exits the nozzle. A lower velocity region is thus observed close to the window. The cold main flow determines the temperature profile over about one-half of the window surface. A temperature peak on the window surface is obtained close to the window center. This indicates a reasonable thermal mixing behavior for the window center region, but also the necessity to optimize the bypass jet design.

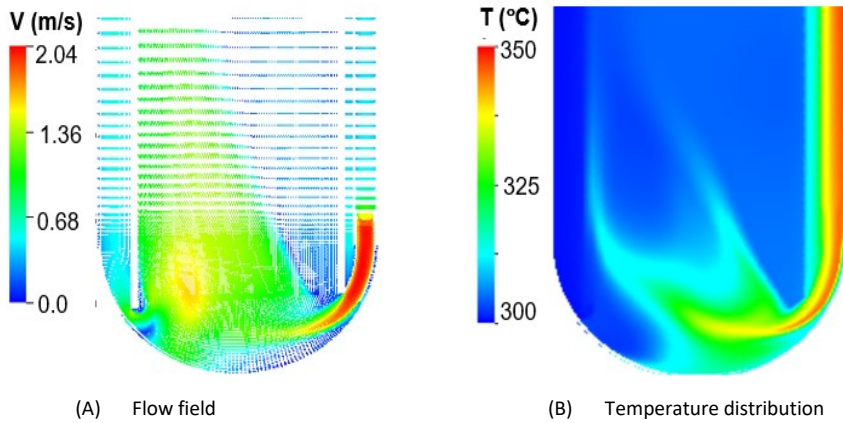


Figure 3.10: Calculated flow fields and temperature distribution in the active part of the MEGAPIE target [18]

In addition to numerical analysis, experimental investigations were carried out in the KALLA laboratory [19]. The experiment simulates the lower part of the MEGAPIE target with the same geometrical structure as that taken for numerical analysis. The bypass flow is electrically heated up with an electrical power up to 72 kW, which allows a warm-up of the bypass flow of about  $\Delta T=120^{\circ}\text{C}$ . During the experiment, LBE temperatures are measured at various positions in the lower part of the test section, incl. those close to the beam window, as indicated in Figure 3.9.

Figure 3.11 compares the temperature distribution predicted with CFD simulation with experimental data. The numerical simulation shows a shift of the temperature peak to the left side. This indicates a larger region affected by the bypass flow. In general, there exists significant deviation between the numerical results and the experimental data.

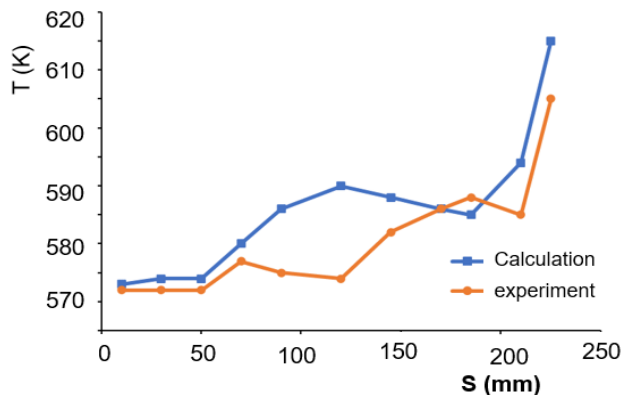


Figure 3.11: Predicted temperature on the window surface with the test data [18]

### 3.3 XADS spallation target

One of the reactor core concepts is a LBE cooled reactor with 80 MW thermal power and with a window target. The target unit, as illustrated in Figure 1.5, is in the centre of the XADS core and consists of several co-axis cylinders. A 600-MeV proton beam enters the beam tube from the top and produces a large heat deposition in LBE as well as in the window. The deposited heat is removed in a heat exchanger at the upper end inside the target unit. A LBE natural circulation flow inside the target unit is driven by buoyancy force. The total height of the target unit is about 8 m. FZK was engaged in the design optimization of this compact target module. Both the system analysis codes (HETRAF) and the CFD code CFX-5 were used. With the system codes, heat removal system and its components were optimized to achieve optimum heat removal behaviour. Global flow conditions were provided for detailed CFD analysis. With CFX-5, the cooling capability of the beam window was assessed and the geometric configuration of the active part of the target was optimized.

Figure 3.12 presents the geometric structure of the active part of the XADS target. During the thermal hydraulic analysis, several geometric parameters were optimized such as the diameter of the funnel and of the guide tube, the funnel structure, especially lower end of the funnel. These parameters affect not only the capability of natural circulation, but also the flow and heat transfer behaviour in the active part of the target.

#### 3.3.1 Steady state conditions

Since the target is cooled by natural circulation, thermal hydraulic conditions of incoming flow to the computational domain must be calculated using the STH Program HETRAF. At first, a calculation was performed for the reference design having a 3-mm thick window ( $\delta = 3\text{ mm}$ ). Figure 3.13 shows the contour of both the velocity and temperature in the lower part of the target. As expected, high and well uniform distribution of velocity inside the funnel (rising channel) is obtained. Approaching the window surface, flow velocity is generally reduced due to flow area extension. Near the window center, a large zone with low velocity appears. Flow separation occurs both in the downcomer beneath the funnel and in the rising channel. The predicted maximum LBE velocity is 1.28 m/s, well below the design limit 2 m/s due to erosion problem. High temperature can be observed in the window center as well as beneath the funnel, where flow separation occurs. The maximum outer surface temperature counts to 473 °C. The maximum temperature of the guide tube is 450 °C, slightly lower than that of the window outer surface.

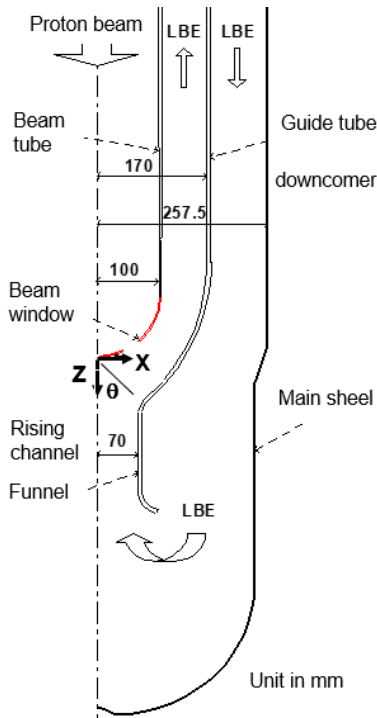


Figure 3.12: Geometric structure of the lower part of the XADS spallation target [20]

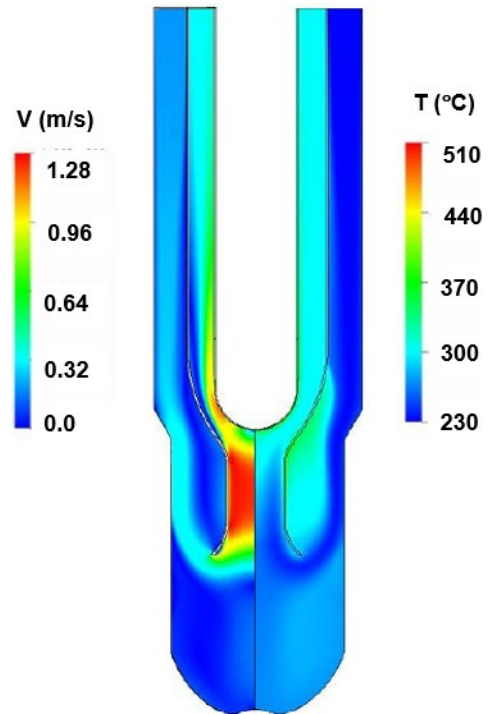


Figure 3.13: Velocity field and temperature distribution of LBE

### 3.3.2 Beam trip transient

The operating experience of existing accelerators showed that beam trips occur very frequently [21]. Beam trips produce thermal cycle and cause additional stress, which would become one of the main issues of structural material failure. In the technical specification of the accelerator for XADS, the frequency of beam trips with a time duration longer than 1 second must be kept below 5 interrupts per year. No special requirements are defined for the beam trips with a beam interrupt duration shorter than 1 second. The present analysis focuses on beam trips with an interrupt duration shorter than 1 second.

Beam trips with four different interrupt durations, i.e. 0.1, 0.3, 0.5, and 1.0 second, were investigated. The results showed that the LBE mass flow rate and the LBE temperature at the inlet of the computational domain, i.e. inlet into the downcomer, are hardly changed during these beam trips with a short interrupt duration. In case of the beam trip with an interrupt duration of 1 s, the change of the LBE mass flow rate is less than 2 % and the change of the LBE temperature at the exit of the heat exchanger is less than 1 K. Therefore, in the CFD calculations the inlet boundary conditions were kept unchanged.

Figure 3.14 presents the predicted temperature at the central point of the window outer surface. During beam interrupt, the beam window undergoes a temperature drop up to 207 °C for the trip period of 1 s, whereas the maximum temperature drop is only 32 °C for the trip period of 0.1 s. The steepest slope is located between 0 and 0.5 s after the beam interrupt, regardless of the investigated interrupt duration. The predicted maximum temperature change rate is as high as 412 °C/s, which occurs at 0.1 s after the beam interrupt.

With regard to the maximum temperature change rate, beam trips with a trip period shorter than 1 s could also be a crucial event affecting the integrity of the window although no attention was paid to these trips in the technical specification of the XADS accelerator. Moreover, it is expected that beam trips with a trip period shorter than 0.1 s zusammen do not have enough time to reach the maximum temperature change rate of 412°C/s. It is thus concluded that related to both the maximum temperature drop and the temperature change rate, beam trips with a trip period shorter than 0.1 s are less critical than those with a trip period longer than 0.1 s.

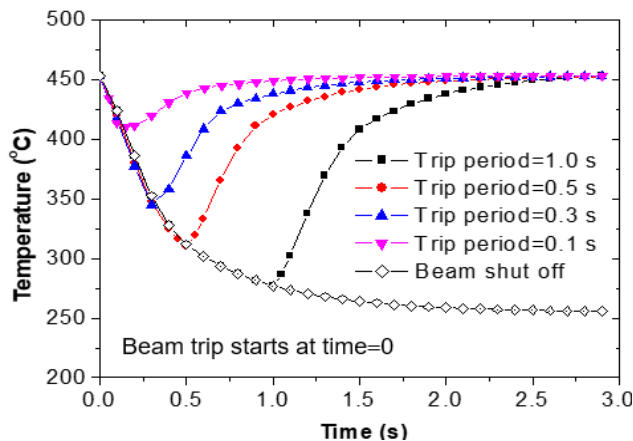


Figure 3.14: Temperature at center of window outer surface under beam trip conditions [20]



## 4 Summary

For many years the Research Center Karlsruhe has carried out extensive research works on thermal hydraulics of spallation targets cooled with liquid Pb or LBE. Both experimental investigations and numerical studies were performed, which include system level as well as 3-dimensional thermal hydraulics behaviour. This paper presents some of the results related to three different spallation targets, i.e. ISTC-target, MEGAPIE-target and XADS-target. The main conclusions achieved as below:

- For system thermal hydraulics analysis, the numerical simulation program HETRAF was developed and well validated based on the post-test data of the MEGAPIE-target.
- For 3-dimensional fluid dynamics simulation, the commercial CFD program CFX5.6 was applied. Comparison with the experimental data obtained with the ISTC-target confirms the high reliability of the selected CFD model for the simulation of velocity field.
- In the ISTC-target without perforated plate, a large flow stagnation zone near the beam window in case of upward flow or larger vortices in the spallation zone in case of downward flow are obtained. Thus, perforated plate is necessary, to enhance and guarantee the cooling capability of the beam window.
- Comparison with the experimental data obtained with the MEGAPIE target in the KALLA laboratory indicates, however, a large deviation of the temperature distribution between the CFD results and the experimental data. Improvement of the selected CFD model is required.
- Several transient scenarios of the MEGAPIE target system were analyzed. It shows that under unprotected loss of pump head in the primary loop, the LBE flow in the primary loop decreases down to about 60 % of the original value and the LBE temperature in the spallation zone increases up to about 450 °C, which would not lead to failure of the beam window. Serious problem would, however, be expected in case of unprotected loss of pump head in the secondary loop. A continuous increase in the LBE temperature in the spallation zone is obtained with an increasing rate of about 1.0 °C/s. Thus, safety measurements are required to avoid failure of the beam window.
- In case of beam trips in the MEGAPIE target, the lowest LBE temperature would approach the freezing value in about 4 minutes. Thus, for long beam trips, safety measurements are required, e.g. reduction or stop of the cooling through the secondary loop.

- In the MEGAPIE-target with bypass jet, the thermal hydraulics performance is very sensitive to geometric design of the bypass jet. Further validation of CFD models is necessary, so that it can be used for systematic design optimization.
- The XADS-target operates under natural circulation mode. The thermal hydraulics behavior is, thus, sensitive to the geometric design of the entire target system. In general, the proposed reference design is feasible related to the heat removal capability. However, there is still large room for further optimization.

## References

- [1] Knebel, J.U., Heusener, G., 2001. Untersuchungen zur Transmutation und zu Beschleuniger getriebenen Systemen (ADS) im Forschungszentrum Karlsruhe, Radioaktivität und Kernenergie, Forschungszentrum Karlsruhe, Mai 2001, ISBN 3-923704-26-7
- [2] DOE, October 1999. A report to congress – a roadmap for developing accelerator transmutation of waste (ATW) technology, DOE/RW-0519.
- [3] OECD/NEA, 2002. Accelerator driven system (ADS) and fast reactors (FR) in advanced nuclear fuel cycles – A comparative study. OECD Nuclear Energy Agency
- [4] Yefimov, E., 1998. The main results of feasibility study of liquid metal targets and the working plan on the project #559, Kick-off meeting on the ISTC project #559, February 1998, Obninsk, Russia
- [5] Bauer, G.S., et al. 2001. MEGAPIE: A 1 MW Pilot Experiment for a Liquid Metal Spallation Target, Journal of Nuclear Materials, 296, 17-33, 2001.
- [6] Coors, D., et al., 2004. Target units for XADS primary system. EURADWASTE '04, Luxembourg, March 29-31, 2004.
- [7] Rubbia, C., et al. 1995. Conceptual design of a fast neutron operated high power energy amplifier, CERN/AT/95-44 (ET), September 1995.
- [8] Fazio et al., 2008. The MEGAPIE-TEST project: Supporting research and lessons learned in first-of-a-kind spallation target technology, Nuclear Engineering and Design 238 (2008) 1471–1495
- [9] European Technical Working Group on ADS, April 2001. A European roadmap for developing accelerator-driven systems (ADS) for nuclear waste incineration.

- [10] Carlucci, B., 2003. The European project PDS-XADS, "Preliminary Design Studies of an eXperimental Accelerator-Driven System". In: Proceedings of the International Workshop on P&T and ADS Development 2003, Mol, Belgium, October 6-8, 2003.
- [11] Cheng, X., Slessarev, I., 2000. Thermal-hydraulic Investigations on Liquid Metal Target Systems, Nuclear Engineering and Design, Vol. 202, pp.297-310, 2000
- [12] Cheng, X., Stieglitz, R., Knebel, J.U., 2004. Heavy Liquid Metal Thermal-Hydraulics in ADS, Jahrestagung Kerntechnik, May 25.-27., 2004, Düsseldorf, paper 218
- [13] Cheng, X., 1994. Numerical analysis of thermally induced transients in forced flow of supercritical helium, Cryogenics, Vol.34 (1994), No.3, 195-201
- [14] Leung, W.H., 2003. RELAP5 Model of the Triple-Loop Heat Removal System, PSI report TM-34-03-11, October 2003
- [15] Sigg, B., 2001. Concept and Engineering-Design Requirements for the MEGAPIE Heat Removal System with Intermediate Organic Coolant, Internal Memorandum, June 11, 2001
- [16] Bauer, G.S., et al., 2000. Description of SINQ and boundary conditions for MEGAPIE. In: 1st MEGAPIE general meeting, CEA, Cadarache, June 14-15, 2000.
- [17] Cheng, X., Batta, B., Tak, N.I., 2006. Investigation on turbulent heat transfer to lead-bismuth eutectic flows in circular tubes for nuclear applications, Nuclear Engineering and Design, vol. 236, no. 4, pp. 385–393, 2006
- [18] Batta, A., Daubner, M., Cheng, X., 2004. Investigation on turbulent mixing process in MEGAPIE target configuration, Jahrestagung Kerntechnik, Berlin, May 25.-27., 2004, Düsseldorf, paper 203
- [19] Stieglitz, R., Daubner, M., Batta, A., Lefhalm, C.H., 2007. Turbulent heat mixing of a heavy liquid metal flow in the MEGAPIE target geometry – The heated jet experiment, Nuclear Engineering and Design 237 (2007), 1765-1785
- [20] Tak, N.I., Neitzel, H.J., Cheng, X., 2005. Computational fluid dynamics analysis of spallation target for experimental accelerator-driven transmutation system, Nuclear Engineering and Design, Vol.235 (2005), pp.761-772
- [21] Pierini, P., 2003. Reliability study of the PDS-XADS accelerator. In: Proceedings of the International Workshop on P&T ADS Development 2003, Mol, Belgium, October 6-8, 2003



# Analysis of the Steam Line Break (SLB) accident for the SMART Small Modular Reactor (SMR)

... with multi-physics/-scale coupled codes

Kanglong Zhang <sup>1</sup> and Victor Hugo Sanchez-Espinoza <sup>1</sup>

<sup>1</sup> Karlsruhe Institute of Technology, Institute for Neutron Physics and Reactor Technology, Karlsruhe, Germany

## Abstract

This paper presents an analysis of a Steam Line Break (SLB) accident scenario for the SMART Small Modular Reactor (SMR), utilizing multi-physics and multi-scale thermal-hydraulic (TH) coupled codes. The study is conducted as part of the EU McSafer project, using the coupled code system TRACE/PARCS/SubChanFlow (SCF), where SCF handles core TH, TRACE manages TH for non-core components, and PARCS is responsible for core neutronics. The coupled code successfully captures the critical accidental sequences during the SLB, including the core power reduction, the mass flow rate decrease, the coolant temperature increase, and the eventual establishment of natural circulation within the reactor vessel. The complex thermal-hydraulic and neutronic phenomena during the transition from forced circulation to natural flow in the core and the primary loop are well described by SCF, TRACE, and PARCS respectively, benefiting from the codes' dynamic interaction. Additionally, using SCF instead of TRACE for core analysis improves the prediction of cross-flow and safety parameters, such as the Departure from Nucleate Boiling Ratio (DNBR). Finally, the results prove that the SMART reactor is able to stay safe during an SLB accident. The results obtained from TRACE/SCF/PARCS are compared with the results obtained from the multi-physics code TRACE/PANTHER. The similar plant and core behaviors predicted by the two coupled codes indicate the reliability of this work.

**Keywords:** Multi-physics, Multi-scale, SMART, Steam Line Break (SLB), TRACE/PARCS/SubChanFlow

# 1 Introduction

Small Modular Reactors (SMRs) adopt a modular design concept throughout their development, construction, and deployment phases (International Atomic Energy Agency, 2021). SMRs incorporate advanced technologies (classified by the International Atomic Energy Agency (IAEA) (International Atomic Energy Agency, 1997)) like compact Reactor Pressure Vessels (RPVs) and passive decay heat removal systems, which enhance overall safety. These innovations make SMRs a promising option for the future of nuclear power, offering carbon-free energy solutions. Currently, several water-cooled SMRs, including SMART (Kamalpour & Khalafi, 2021), NuScale (Sadegh-Noedoost et al., 2020), and CAREM (Tashakor et al., 2017) are under development globally.

In the licensing process frame of water-cooled SMR, safety analysis of transients where non-symmetrical behavior of the core could occur, such as Steam Line Break (SLB), boron dilution, and control rod ejection, is mandatory. This requirement stems from the licensing experience of large Pressurized Water Reactors (PWR). For instance, two-loop large PWR could suffer recriticality and unsymmetrical power increase during under-cooling transients like the SLB accident, as half of the core is affected. The impact decreases with an increasing number of loops, which is typical for water-cooled SMRs. Therefore, it is of great interest to investigate the SLB transient in water-cooled SMR with integrated RPV, where the Steam Generators (SG) are located inside the RPV and additional constructive devices are designed and placed around the core to promote primary coolant mixing, as in the SMART reactor.

Well-qualified codes are essential for performing those analyses. In recent years, advanced simulation codes based on multi-physics and multi-scale Thermal-Hydraulic (TH) coupling approaches have been increasingly applied to better predict the behavior of compact and heterogeneous core designs under transients and multidimensional flow inside the RPV and core of water-cooled SMRs. Tools such as NECP-CLAMPERL (Xu et al., 2022) and TRACE/SCF (Zhang et al., 2021), initially applied to simulate transients of large nuclear power plants, are now extensively used for SMR analysis. Additionally, high-fidelity multi-physics tools involving Monte Carlo codes such as Serpent2/SubChanFlow(SCF) (Ferraro et al., 2020) and Serpent/SCF/Transuranus (García et al., 2021), are being developed and validated for the direct prediction of safety parameters, accounting for local feedback in pin/subchannel level simulations. A comprehensive review of these coupling activities from a multi-scale TH perspective is provided in (Zhang, 2020).

The Karlsruhe Institute of Technology (KIT) has initiated the EU project McSafer (Sanchez-Espinoza et al., 2021) devoted to the experimental and numerical investigations of water-cooled SMR cores and plants, applying advanced multi-physics and multi-scale TH methods in addition to industry-like tools. Within the project, the SLB transient of the SMART reactor is analyzed with different simulation approaches. For example, KIT uses the coupled code TRACE/PARCS/SCF. This paper presents the comparative analysis performed by KIT. Chapter 2 introduces the codes and coupling methodologies used. Chapter 3 provides a detailed description of the SMART reactor and the transient scenario. Chapter 4 discusses the models developed for the SLB analysis. Chapter 5 presents the results obtained from both codes. Finally, Chapter 6 summarizes the main conclusions.

## 2 The coupled codes and coupling methodology

The coupled code includes three codes:

- 1) TRACE - developed by the U.S. Nuclear Regulatory Commission (NRC), a system thermal-hydraulic code for transient analysis in Light Water Reactors (LWR) (Bajorek et al., 2015).
- 2) PARCS - developed by the U.S. NRC, a three-dimensional (3D) reactor core neutronic code that solves both steady-state eigenvalue and time-dependent neutron diffusion and low-order transport equations for Cartesian and hexagonal meshes (Downar et al., 2012).
- 3) SubChanFlow (SCF) – developed at KIT, a sub-channel TH code solves a system of three mixture equations for mass, momentum, and energy with one additional equation to account for the lateral flow (Imke & Sanchez, 2012).

The coupling of TRACE, PARCS, and SCF is implemented based on the ICoCo approach (SALOME Platform, n.d.-b). This integration requires secondary development for each code, involving the following steps:

- 4) Function and source code modularization: modularize functions and source code, such as initialization, steady-state solution, and transient solution.
- 5) Mesh construction: Create meshes for inter-code data translation and post-processing.
- 6) Development of the code-specific ICoCo module: Develop the ICoCo module (interface) for each code, which standardizes the methods for encapsulating the code into C++ classes and transforms the codes's native functions into class methods.

A C++ supervisor manages the interaction among the coupled codes and facilitates inter-code data transfer through the ICoCo interfaces. The foundational structure of this coupling system is illustrated in Figure 2.1.

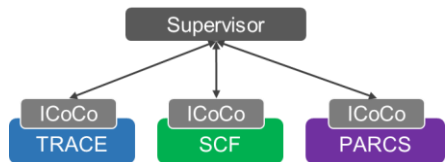


Figure 2.1: Overall structure of the coupling code TRACE/PARCS/SCF.

The coupled code uses the domain-decomposition coupling method. In this setup, SCF describes the core TH, TRACE handles the TH of all the reactor parts except the core, including the RPV with integrated components (such as SGs, pumps, and pressurizer), steam and feedwater lines, and other safety systems. PARCS is responsible for the core neutronics. Figure 2.2 delineates the different domains managed by each code.

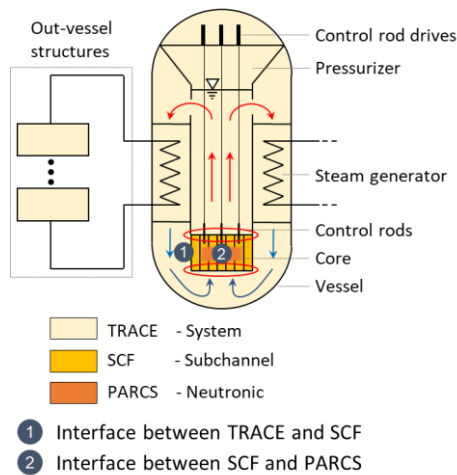


Figure 2.2: The domain allocations of the coupled code TRACE/PARCS/SCF.

Two interfaces exist between the TH codes at the core inlet and outlet. Data transfer between TRACE and SCF is automated by a mesh-to-mesh superposition using the MEDCoupling library (SALOME Platform, n.d.-a), which manages data transfer between different domains stored in distinct meshes. Following a study on accuracy and stability study for multi-scale TH coupling systems (Zhang & Sanchez-Espinoza, 2023), a con-



servative data transfer strategy is adopted. The data transferred at the interfaces include:

- Thermal hydraulic coupling at the core inlet (2D):
  - Pressure (SCF -> TRACE).
  - Mass flow rate (TRACE -> SCF).
  - Heat flow rate (mass flow rate times coolant temperature)(TRACE -> SCF).
- Thermal hydraulic coupling at the core outlet (2D):
  - Pressure (TRACE -> SCF).
  - Mass flow rate (SCF -> TRACE).
  - Heat flow rate (mass flow rate times coolant temperature)(SCF -> TRACE).
- Neutronic coupling for the core (3D):
  - Power (PARCS -> SCF).
  - Fuel temperature (SCF -> PARCS).
  - Coolant temperature (SCF -> PARCS).
  - Coolant density (SCF -> PARCS).

In the supervisor, explicit temporal coupling (operator-splitting) is used for this coupling approach. Additionally, techniques like overrelaxation and stagger-time-step are implemented to enhance the robustness and efficiency of the coupling simulation within the generic multi-physics and multi-scale system.

## **3 The SMART reactor and the Steam Line Break (SLB) Transient**

### **3.1 Short description of SMART**

The System-integrated Modular Advanced Reactor (SMART) stands as a pioneering Small Modular Reactor (SMR) design crafted by the Korea Atomic Energy Research Institute (KAERI) (Chung et al., 2015). With a thermal power output of 330 MW, SMART contributes 100 MW to electricity generation. What sets SMART apart is its ingeniously integrated primary coolant system, housing all crucial components within the RPV. This design optimizes space utilization and enhances operational efficiency. At the heart of SMART's thermal power production lie eight modular-type, once-through helicoidal SG. These generators play a pivotal role in the energy conversion process, producing superheated steam at 30 °C on the secondary side under normal operational conditions. The seamless flow of coolant through the RPV and core is ensured by the operation of four canned pumps strategically placed within the system. Additionally, SMART employs an

in-vessel pressurizer meticulously engineered to maintain system pressure levels consistently throughout various design basis events. This pressurizer stands as a crucial safety feature, safeguarding the integrity of the system against potential overpressure scenarios.

Within the core, SMART features 57 Pressurized Water Reactor (PWR)-like fuel assemblies, meticulously arranged to optimize energy output while ensuring safety and reliability. To guarantee uniform coolant flow distribution at the core inlet, SMART employs a sophisticated Flow-Mixing Header Assembly (FMHA) in conjunction with a flow skirt positioned at the outlet of the SGs. This careful engineering ensures optimal performance and thermal efficiency across the entire reactor core. Figure 3.1 illustrates the general RPV diagram of SMART, providing insight into its compact design, highlighted components, and key structures housed within the vessel.

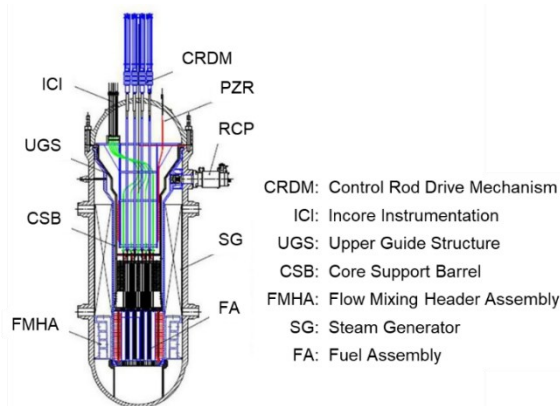


Figure 3.1: RPV diagram of the SMART reactor (Choo et al., 2014).

Beyond its primary components, SMART incorporates an array of secondary side auxiliary circuits and safety systems interconnected with the RPV. Among these, the pressurizer safety valve serves as a critical safety measure, designed to prevent overpressure events within the RPV. Another integral safety system is the Passive Residual Heat Removal System (PRHRS), which assumes a crucial role in ensuring continuous reactor cooling during abnormal shutdown scenarios. Activating the PRHRS directs steam from the secondary side into a large pool, where it undergoes condensation before circulating back to the SG inlet via natural circulation mechanisms. This process effectively dissipates excess heat from the system, maintaining operational stability and safety.

### 3.2 The Steam Line Break (SLB) transient scenario (Etcheto et al., 2023)

Figure 3.2 schematically represents the RPV, SGs, Feedwater Isolation Valves (FWIVs), Steam Isolation Valves (SIVs), and the Passive Residual Heat Removal System (PRHRS), which includes one Emergency Cooldown Tank (ECT), four Heat Exchangers (HXs), one accumulator per HX, connecting pipes, and PRHRS Isolation Valves (IVs). During normal operation, feedwater passes through the FWIVs, enters the RPV, flows through the SGs from bottom to top, exits the RPV, passes through the SIVs, and finally reaches the Main Steam Line (MSL). The models used in this study consider the feedwater as a constant inlet mass flow rate boundary condition, and the turbine as having a fixed outlet pressure.

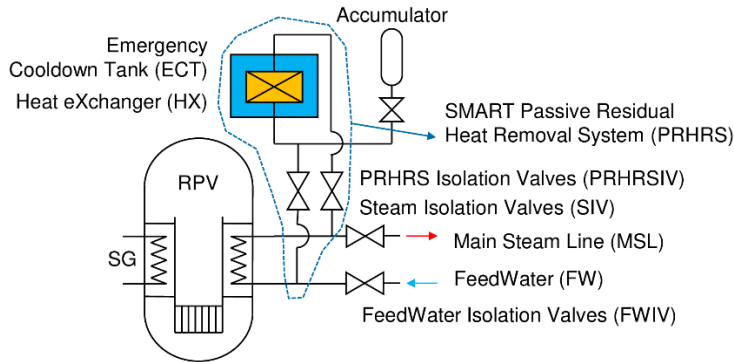


Figure 3.2: Scheme of the SMART main components and systems involved in the SLB accident.

There are eight SGs and four PRHRSs. Each two SGs corresponds to one PRHRS, as shown in Figure 3.3. The steam lines from all eight SGs are connected to a single MSL. In this analysis, the SLB is assumed to occur in the steam line of SG1, with a double-end guillotine break considered. The released water inventory due to this break originates from both SG1 and SG2, as SG2 is connected to SG1 through the PRHRS. During normal operation, the FWIVs and SIVs remain open, while the PRHRSIVs are closed (solid valves are closed, and open valves are empty).

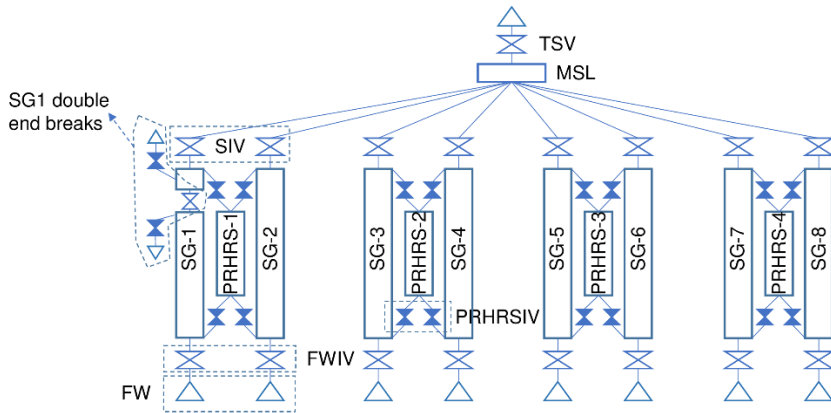


Figure 3.3: The schematical configuration of the steam line break and the configurations of the components.

To model a double-ended break in TRACE, three valves are used, as shown in Figure 3.3. Two solid valves (solid indicates closed) and one empty valve (empty indicates open) are positioned at the site of the Steam Line Break (SLB) to simulate the double-ended break. During SLB, the empty valve closes, and the two solid valves open, allowing feedwater to flow out of the system through these valves. To maximize the consequences of the SLB accident, the loss of offsite power is assumed to occur as soon as the break happens.

The primary safety concern of the analysis is to determine whether there is a significant return to power and recriticality, despite the reactor being shut down, due to the positive reactivity insertion caused by the cooldown of the primary coolant, as is common in large PWRs.

The sequence of events is as follows:

- Initial event: a double-ended break occurs near the SIV of the SG1 steam line, coinciding with a loss of offsite power.
- Rapid secondary pressure reduction occurs due to the break in SG1, and all four main pumps begin coasting down.
- SCRAM is triggered when secondary pressure drops below 2 MPa.
- FWIVs, SIVs, and Turbine Stop Valve (TSV) close within 0.1 seconds after SCRAM.
- PRHRSIVs open, connecting the PRHRS with the steam and feedwater lines within 0.1 seconds.
- The transient duration is 500 seconds.

It is important to note that the break in SG1 also affects SG2, as both are connected to the same PRHRS. In the TRACE model, SG1 and SG2 correspond to the third and fourth sectors of the VESSEL component, respectively.

## **4 Description of the models for the different codes**

This section delineates the models for TRACE, PARCS, SCF, and PANTHER, discussed in section 2.

### **4.1 The TRACE model**

The TRACE SMART consists of a 3D VESSEL component that represents the RPV, Figure 4.1. This model employs cylindrical discretization to incorporate internal structures like the Fine Motion Head Assembly (FMHA) and the Flow Skirt. The SMART Reactor configuration includes 8 SGs within the RPV, arranged equidistantly between the barrel and the RPV's external wall. Consequently, the RPV is divided into 8 azimuthal cells. To precisely capture the complex geometry of the four FMHAs, the model allocates 3 radial cells in the downcomer zone. Two additional radial cells are included to model the space occupied by the barrel and the core. The RPV is segmented into 21 axial cells of different sizes according to the geometrical peculiarities.

In the upper section of the RPV, the pressurizer is modeled as a pressurizer-type pipe that connects to the RPV through eight pipes. This setup is integrated with safety relief valves that have opening and closing pressures of 18.7 MPa and 15.0 MPa, respectively. Located near the pressurizer are four centrifugal canned pumps designed with radial (outward) inlet suction and axial (downward) discharge. These pumps, positioned upstream of the SGs, link to the RPV and heat structures through pipes designed for tube bank cross-flow, facilitating heat transfer to the secondary circuit. The model also includes BREAK and FILL components located at the two interface planes between TRACE and SCF, which are used for data transfer.

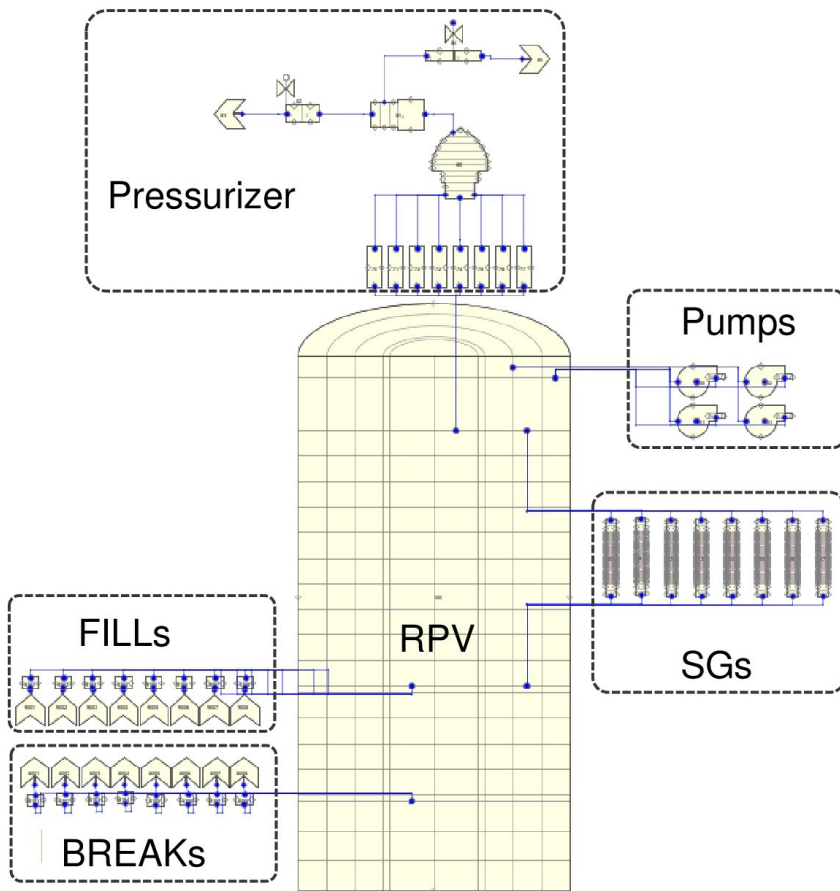


Figure 4.1: The TRACE model of the SMART Reactor Pressure Vessel (RPV).

The secondary side, as shown in Figure 4.2, includes eight helical, once-through SGs. Each SG features its own FeedWater (FW) system, including FeedWater Isolation Valves (FWIVs) and Steam Isolation Valves (SIVs). These valves are designed to respond to various operational scenarios, such as loss of feedwater, loss of offsite power, or low steam line pressure. In the simulation, the FW system is modeled using TRACE's FILL components linked to the FWIVs. Adjacent to these valves are the helical tubes of the SGs, which connect to heat structures that facilitate heat exchange with the primary circuit. The steam generated within these SGs is channeled through the SIVs to the turbine. This pathway includes the Main Steam Line (MSL) and the Turbine Stopping Valve (TSV), with the turbine itself represented by a BREAK component in the model.

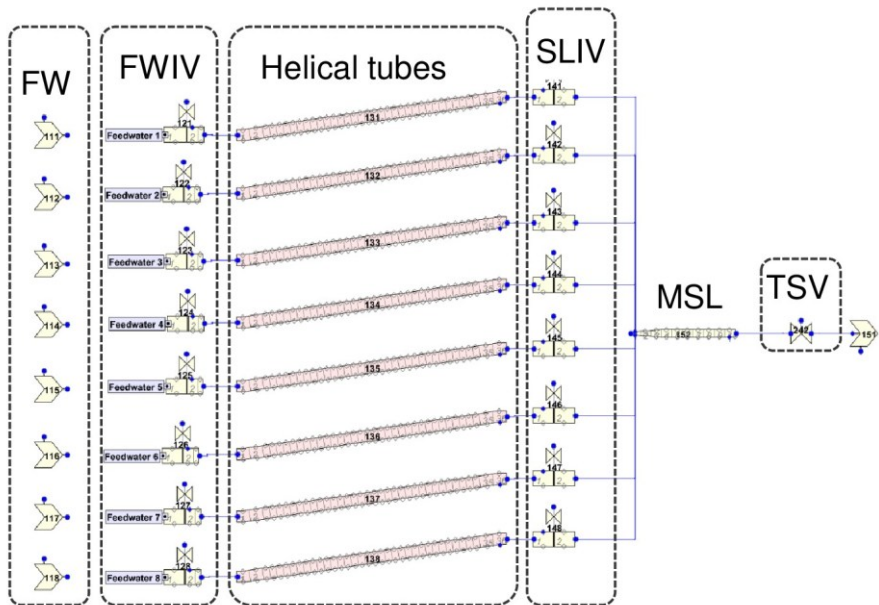


Figure 4.2: The TRACE model of the SMART steam lines on the secondary side (FW - FeedWater, FWIV - FeedWater Isolation Valve, SIV - Steam Isolation Valve, MSL - Main Steam Line, TSV - Turbine Stopping Valve).

The PRHRS is a critical safety feature on the secondary side, designed to passively cool the core by dissipating residual heat during accident scenarios, such as an SLB, as illustrated in Figure 4.3.

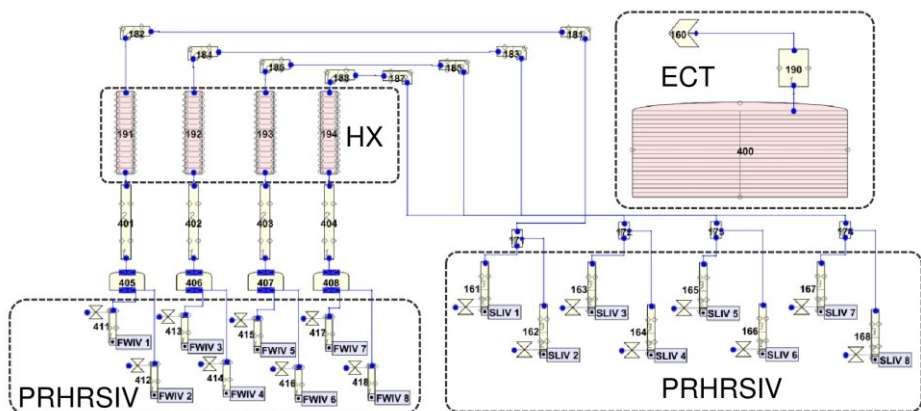


Figure 4.3: The TRACE model of the SMART Passive Residual Heat Removal System (PRHRS) on the secondary side (PRHRSIV-PRHRS Isolation Valve, HX-Heat Exchanger, ECT-Emergency Cooling Tank).

During such events, the closure of the FWIVs and SIVs triggers the steam produced in the SGs to rise towards the Heat exchangers (HXs). Here, the steam condenses and cycles back to the SGs, establishing a natural circulation loop. The condensation heat is transferred from the HXs to the Emergency Cooling Tank (ECT), which is equipped with an atmospheric vent, modeled as a break component to regulate pressure consistently. To safeguard against excessive pressure accumulation, the system includes relief valves calibrated to activate at pressures similar to those of the pressurizer relief valves. This mechanism is crucial for maintaining system integrity and preventing the atmospheric release of vapor, which may contain fission products.

## 4.2 The PARCS and SCF models

The PARCS core model for the SMART reactor, depicted in both top and 3D views in Figure 4.4, provides a brief representation of the core's neutronic dynamics. This discretized model consists of 57 radial nodes, with one node allocated per fuel assembly for the active core. Additionally, 40 nodes are dedicated to the radial reflectors, each matching the dimensions of a fuel assembly. Vertically, the core is segmented into 22 layers, with the top and bottom layers representing the axial reflectors, and the remaining 20 layers designated for the active core region. Each node in the PARCS model corresponds directly to a node in the TRACE model within the Cartesian VESSEL component. The cross-sections were generated using the Monte Carlo neutronics code, Serpent2 (Leppänen et al., 2015).

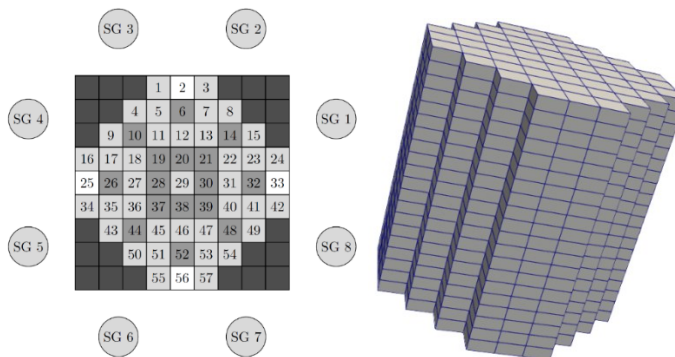


Figure 4.4: Upper view (left) and 3D view (right) of core (SGs included in left figure). Dark gray - the blocked channels, Gray - the FAs with CR are extracted, Light gray - the FAs with CR are inserted, and White - the FAs without CR (left figure).



The axial and radial discretization employed for the SCF input closely mirrors that of PARCS, with 57 cells in an XY plane representing the square fuel assemblies, as depicted in Figure 4.4, and 20 cells in the axial direction. Unlike PARCS, SCF does not consider the reflector. The exchange of variables between these two codes is facilitated by the ICoCo interface, as detailed in section 2.5. In SCF, the fuel rod is radially discretized into 10 zones in the fuel and 2 zones in the cladding. Boundary conditions for the SCF model at the core inlet and outlet are derived from the TRACE model, as explained in section 2.5.

## 5 The discussion of results

The subsequent sections present the results of both the SS and TS results obtained from KIT by the coupled code TRACE/PARCS/SCF. It is to be noted that the results are compared to the TRACTEBEL (TBL) (Etcheto et al., 2023) who also analyzes the same SLB scenario with the coupled code TRACE/PANTHER (PANTHER is the neutronic code) within the framework of the McSafer project.

### 5.1 The steady-state result

Table 5.1 presents a comparative analysis of the primary TH parameters computed by the TRACE code, juxtaposed with results documented in literature. The observed differences are minimal, with most variables exhibiting variances of less than 1.0 %.

Table 5.1: Steady-state results of Steam Line Break (SLB) accident for SMART reactor with TRACE/PARCS/SCF (KIT) and TRACE/PANTHER (TBL)

Parameter	Reference (Alza-ben et al., 2019)	TBL (diff. %)* (Etcheto et al., 2023)	KIT (diff. %)*
Primary pressure (MPa)	15.0	15.0 (0.0)	15.0 (0.0)
Core Power (MW)	330.0	330.0 (0.0)	330.0 (0.0)
Core inlet T (K)	568.85	567.9 (0.2)	563.3 (1.0)
Core outlet T (K)	596.15	596.15 (0.0)	591.0 (1.0)
Total mass flow rate (kg/s)	2090.0	2090.0 (0.0)	2088.3 (0.08)
Core pressure drop (kPa)	Between 5-45	24.3	27.9

\*  $diff \% = (Val - Ref) / Ref * 100$

In the simulations conducted at KIT, the inclusion of the SCF method enables an overall examination of core TH. Figure 5.1 and Figure 5.2 illustrate the three-dimensional temperature distributions of both fuel and coolant within the core region, simulated by SCF. These representations capture the core's state under full power conditions, depicting the hottest regions predominantly at the periphery radially, and at the upper and lower extremes axially.

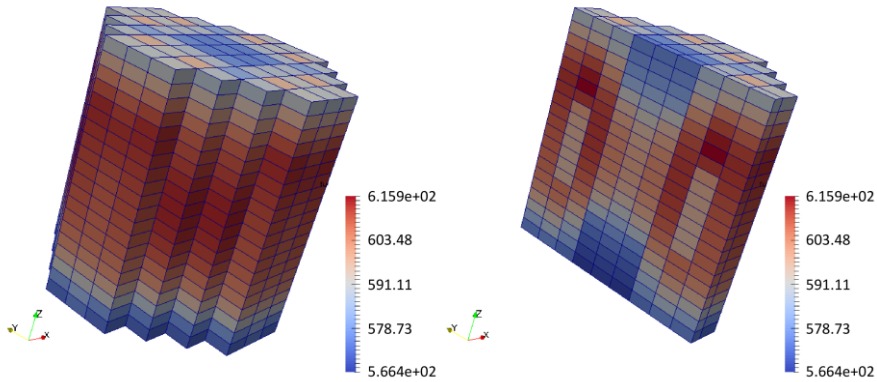


Figure 5.1: The fuel temperature distribution in the core predicted by SubChanFlow (SCF) at the hot full power condition which is the initial condition of the Steam Line Break (SLB) transient.

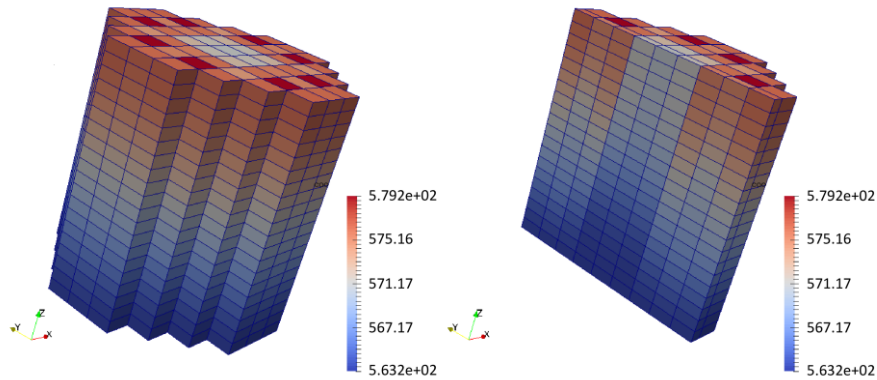


Figure 5.2: The coolant temperature distribution in the core predicted by SubChanFlow (SCF) at the hot full power condition which is the initial condition of the Steam Line Break (SLB) transient.

## 5.2 The transient result

As previously mentioned, the total simulation duration for the transient scenario spans 500 seconds, with the SLB event initiating at 100 seconds. The break occurs at the SG1 tube adjacent to the SIV. Upon occurrence, coolant from SG1 and a portion from the MSL surge through the break initially, causing a sudden pressure drop in SG1. Subsequently, PRHRS-1 connects to SG1 due to this low-pressure indication, resulting in coolant discharge from both PRHRS-1 and SG2. Overall, coolant from SG1, SG2, PRHRS-1, and some from the MSL exits through the double-end break. Figure 5.3 illustrates the cumulative coolant mass lost through the break, as computed by both KIT and TBL.

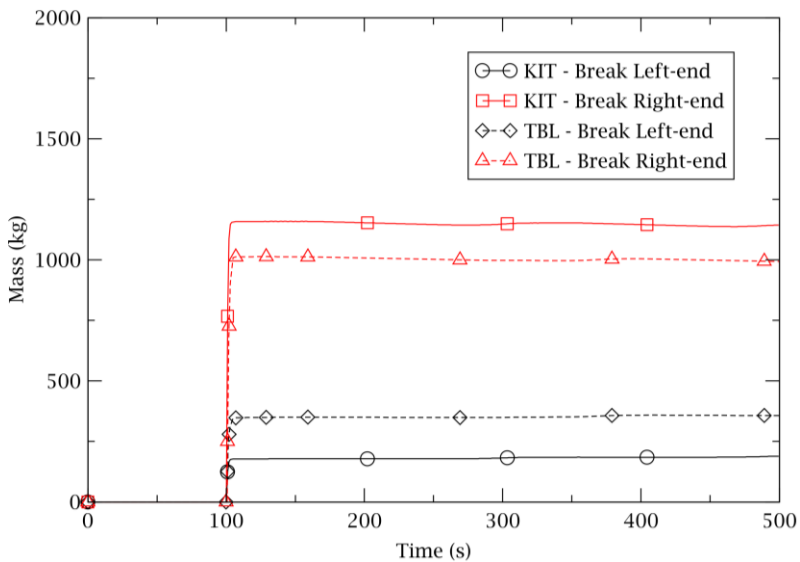


Figure 5.3: The accumulated coolant mass that flows out from the double-end break over time.

The left-end break is situated on the FWIV side, while the right-end break is adjacent to the SIV. The figure indicates that both solutions predict a similar total coolant loss through the breaks, approximately 1350 kg, as expected. Moreover, both solutions foresee more coolant discharge from the right end than the left. This discrepancy stems from the break's proximity to the SIV, facilitating greater coolant discharge from SG2 and PRHRS through the right end. Despite overall agreement, notable differences persist between the two solutions. Specifically, KIT's calculated mass difference between the two break ends exceeds that of TBL (Etcheto et al., 2023). This discrepancy arises from

different modeling approaches: both organizations position the break's right ends directly on the SG1 tube, while, KIT models the left end of the break on PRHRS1, whereas TBL places it on SG2. Given that PRHRS1 is closer to the left end of the KIT break, a higher coolant discharge is anticipated.

Figure 5.4 and Figure 5.5 illustrate the pressure evolution within the SG tubes during the SLB transient, including the results from TRACE/PARCS/SCF by KIT and TRACE/PANTHER by TBL. While minor discrepancies are evident, both solutions exhibit broadly similar trends in pressure behavior. Initially, SG1 and SG2 undergo a rapid pressure drop due to coolant loss through the break, quickly stabilizing near atmospheric pressure (approximately 100,000 Pa) for the remainder of the transient.

The pressure curves in the remaining six SG tubes follow a similar pattern, initially spiking due to the isolation of feedwater, which leads to an accumulation of heat, and subsequently decreases as the PRHRSs begin to mitigate the heat buildup in these units. This pressure decrease reflects the effective heat removal facilitated by the PRHRS connections.

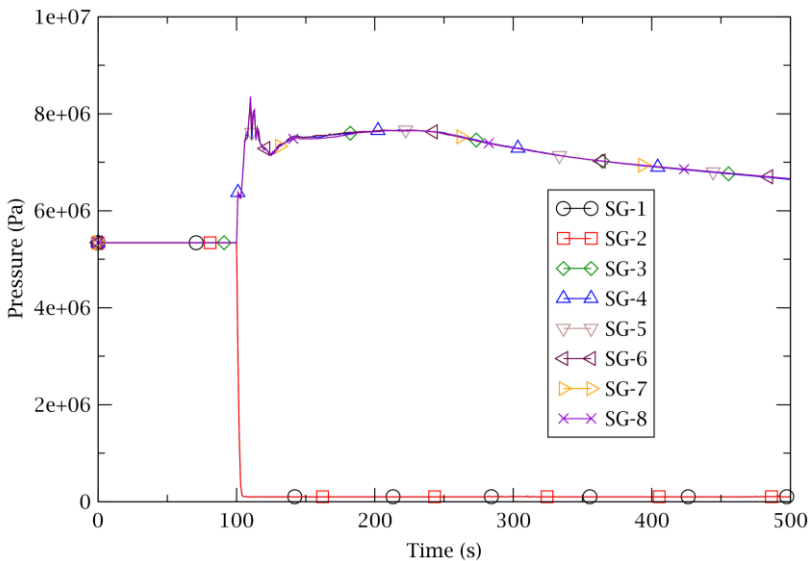


Figure 5.4: The pressure in the Steam Generator (SG) tubes of TRACE/PARCS/SCF over time during the Steam Line Break (SLB) transient for the SMART reactor.

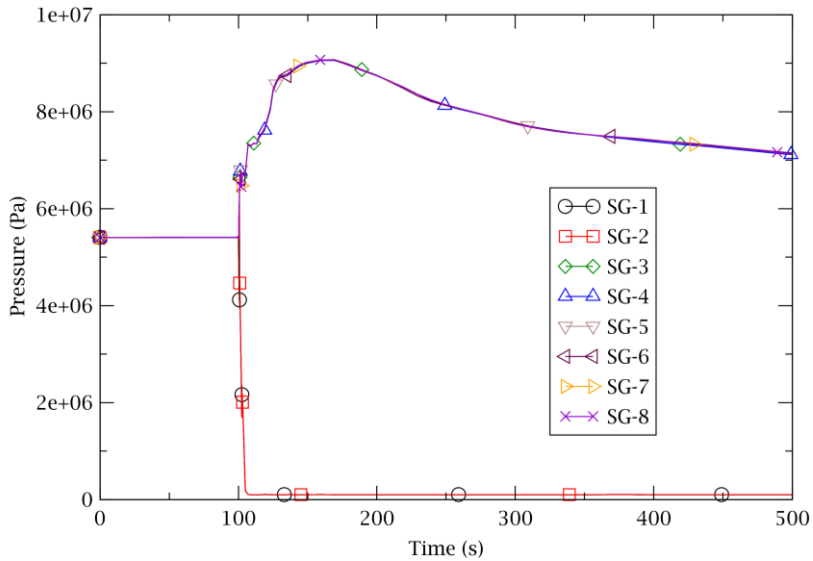


Figure 5.5: The pressure in the Steam Generator (SG) tubes of TRACE/PANTHER over time during the Steam Line Break (SLB) transient for the SMART reactor.

The efficacy of the PRHRS in removing heat can also be assessed by examining the development of the inner wall temperature at the outlet of the SG tubes, as depicted in Figure 5.6 and Figure 5.7.

Despite some disparities attributable to differing modeling approaches and codes (mainly for the empty SG1 and SG2 which depend on the temperature of the primary coolant), both solutions exhibit consistent global trends. Specifically, for SG1 and SG2, the inner wall temperatures initially decrease sharply due to intense vaporization through the break, followed by an increase resulting from the loss of heat sink (due to the emptying of SG1, 2, and PRHRS1), and subsequent oscillations without significant temperature increase, owing to interactions with other loops.

Conversely, the other six SGs demonstrate similar temperature profiles, characterized by an initial sharp decrease upon connection to PRHRS2-4 (where the coolant is cooler), subsequent increases following feedwater isolation, and eventual slight decreases to quasi-stable values facilitated by heat removal via the PRHRSs.

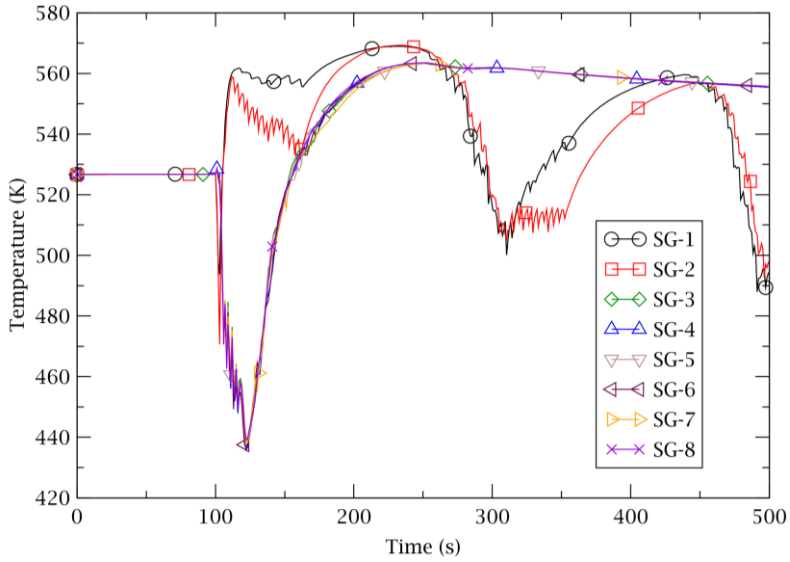


Figure 5.6: The inner wall temperature at the Steam Generator (SG) tubes' outlet of TRACE/PARCS/SCF over time during the Steam Line Break (SLB) transient for the SMART reactor.

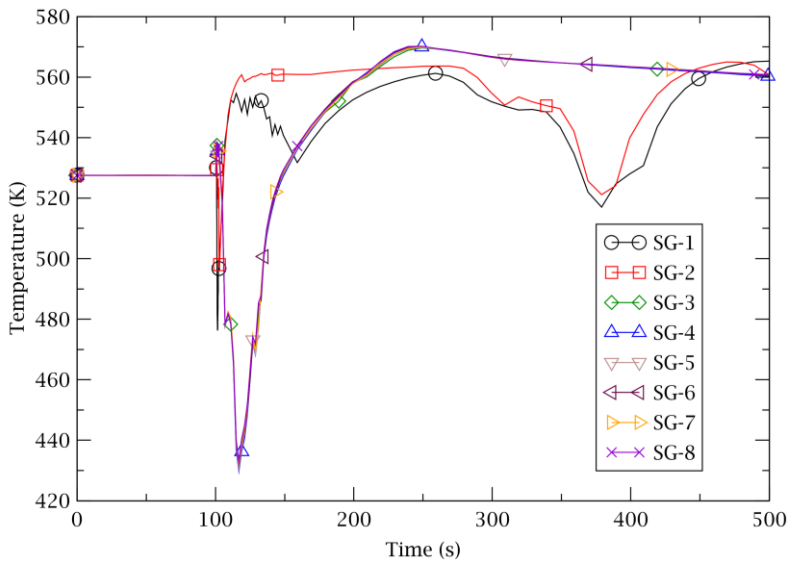


Figure 5.7: The inner wall temperature at the Steam Generator (SG) tubes' outlet of TRACE/PANTHER over time during the Steam Line Break (SLB) transient for the SMART reactor.

The temporal evolutions of the pressure and inner wall temperature within the SG tubes serve as explicit evidence of the PRHRS efficacy in heat removal capability during the SLB transient, further affirming the persistence of mass flow within the SG tubes and PRHRSs.

Figure 5.8 and Figure 5.9 illustrate the mass flow rate through the SG tubes during the SLB transient, as predicted by TRACE/PARCS/SCF and TRACE/PANTHER, demonstrating good agreement between the two. Initially, the mass flow rates in SG1 and SG2 undergo a sharp increase followed by a rapid decrease to zero.

Conversely, the mass flow rates in the remaining six SGs exhibit slight oscillations before gradually converging to approximately 5 kg/s. Given the absence of external pump acceleration, these observed flow patterns signify natural circulations, thereby validating the passive safety features inherent in the SMART reactor, epitomized by the PRHRS.

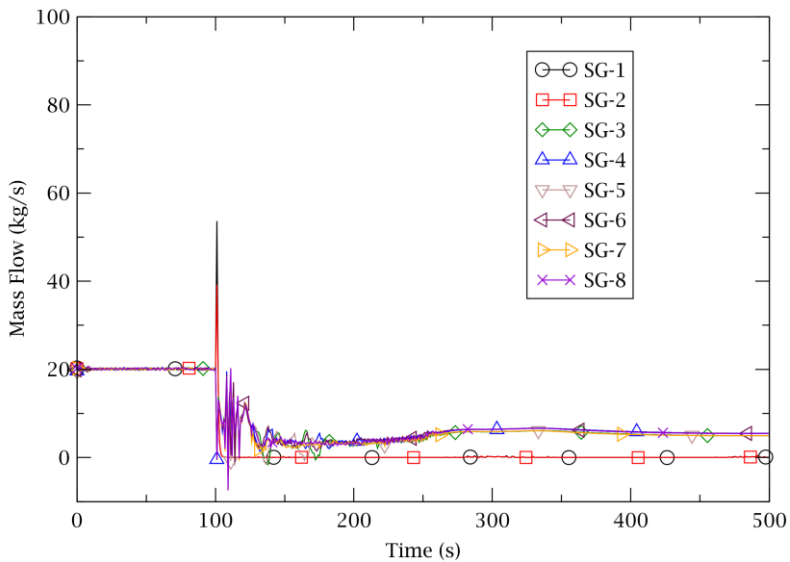


Figure 5.8: The mass flow rate through the Steam Generator (SG) tubes of TRACE/PARCS/SCF over time during the Steam Line Break (SLB) transient for the SMART reactor.

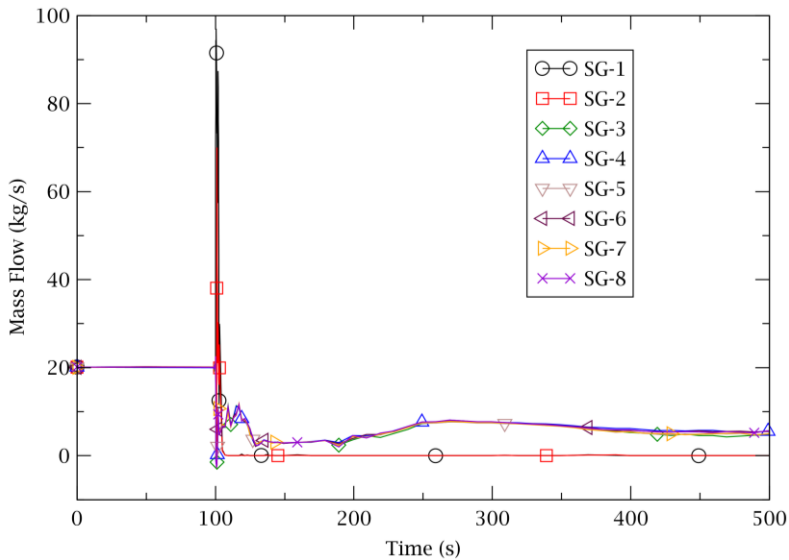


Figure 5.9: The mass flow rate through the Steam Generator (SG) tubes of TRACE/PANTHER over time during the Steam Line Break (SLB) transient for the SMART reactor.

It is important to acknowledge that the “safe state” at the end of the transient is not only due to the effectiveness of the PRHRs but also to the interplay of other systems, which can either positively or negatively impact the reactor control. In this context, key systems include the SCRAM and the shutdown of the four main pumps. Upon initiation of the SLB, the low-pressure trip from SG1 triggers the SCRAM, resulting in a rapid decrease in power. Concurrently, the four main pumps begin to coast down, simulating a loss of offsite power supply and intensifying the significance of the SLB transient. Figure 5.10 and Figure 5.11 illustrate the total evolution of the power and pump speed throughout the transient respectively. It is evident that once the SCRAM is triggered, the core power rapidly decreases to approximately 8 % of nominal power in less than 1 second, gradually decreasing thereafter while maintaining a small residual power until the end of the transient. Meanwhile, the main pumps undergo a complete shutdown in approximately 13 seconds, stopping to provide the driving force for coolant flow. As discussed earlier, the TH parameters on the secondary side indicate that this residual heat can be adequately removed, which further indicates the establishment of natural flow within the primary circuit or the RPV, facilitating the continuous removal of core heat to the SGs.



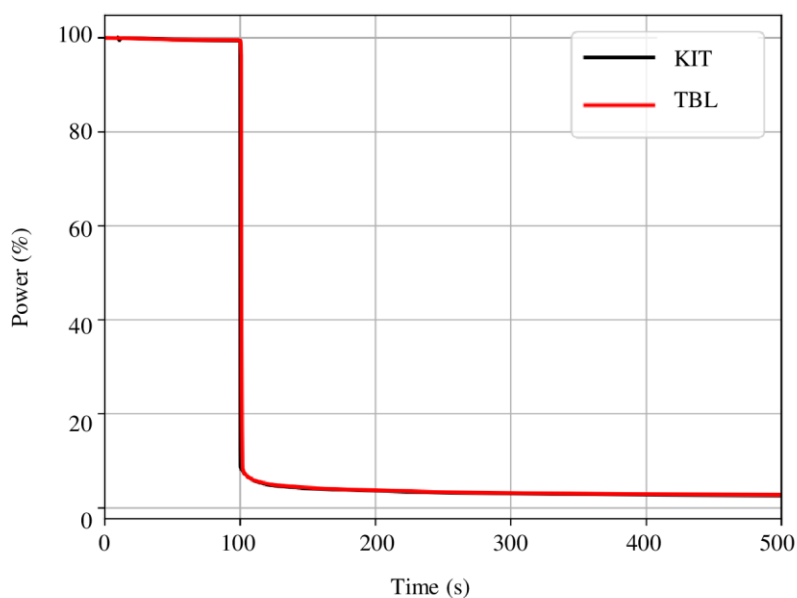


Figure 5.10: The power evolution over time during the Steam Line Break (SLB) transient for the SMART reactor.

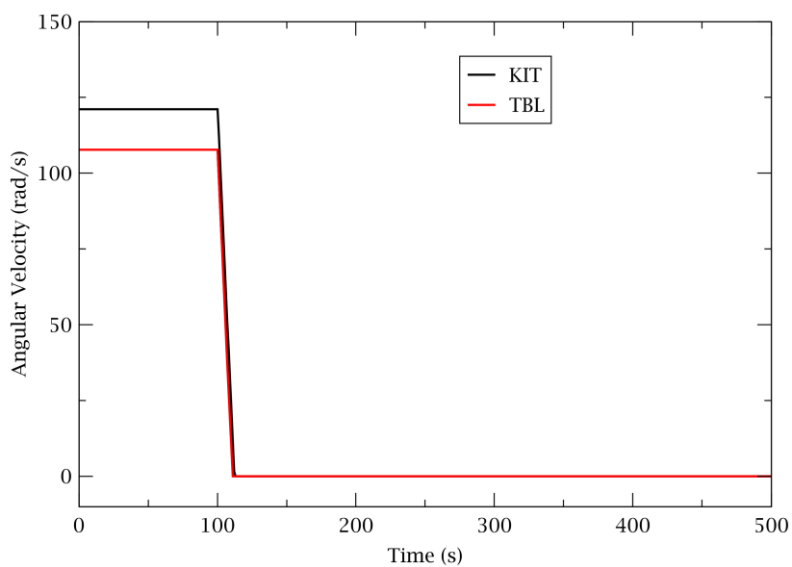


Figure 5.11: The pump speed over time during the Steam Line Break (SLB) transient for the SMART reactor.

Figure 5.12 and Figure 5.13 illustrate the mass flow rates through the SGs on the primary side predicted by the TRACE/PARCS/SCF and TRACE/PANTHER, where the two computations agree well globally.

Following the initiation of the pump coast-down, the mass flow rates in all 8 SGs initially drop sharply, mirroring the decreasing angular velocity of the pump impellers, to a low level of less than 50 kg/s. Subsequently, these rates slightly recover and stabilize until the end of the transient. With the pumps fully shut down, the observed mass flow rates through the SGs are indicative of the establishment of natural circulation on the primary side.

The curves clearly show that mass flow persists only in SG3-8, maintaining a rate of about 25 kg/s, whereas SG1 and SG2 exhibit almost no coolant flow, consistent with the tube dry-out in these two SGs as previously noted in Figure 5.8 and Figure 5.9.

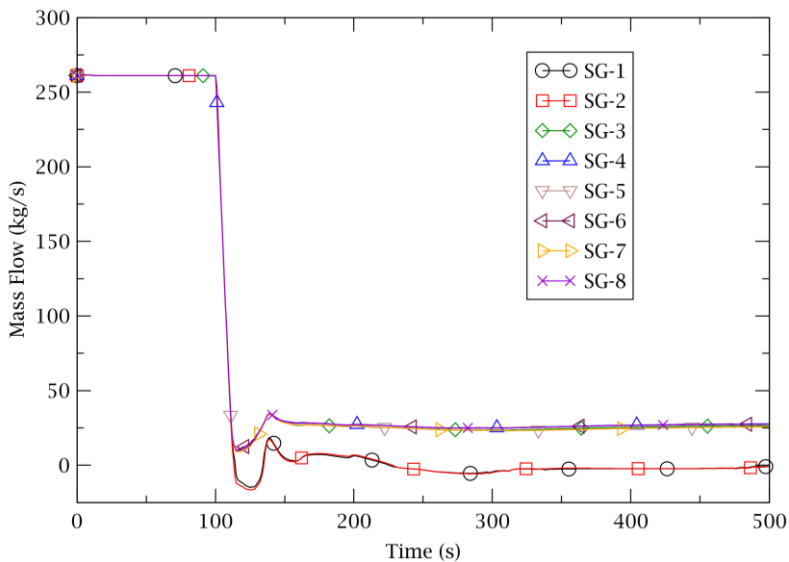


Figure 5.12: The mass flow rate through the Steam Generator (SG) at the primary side of TRACE/PARCS/SCF over time during the Steam Line Break (SLB) transient for the SMART reactor.

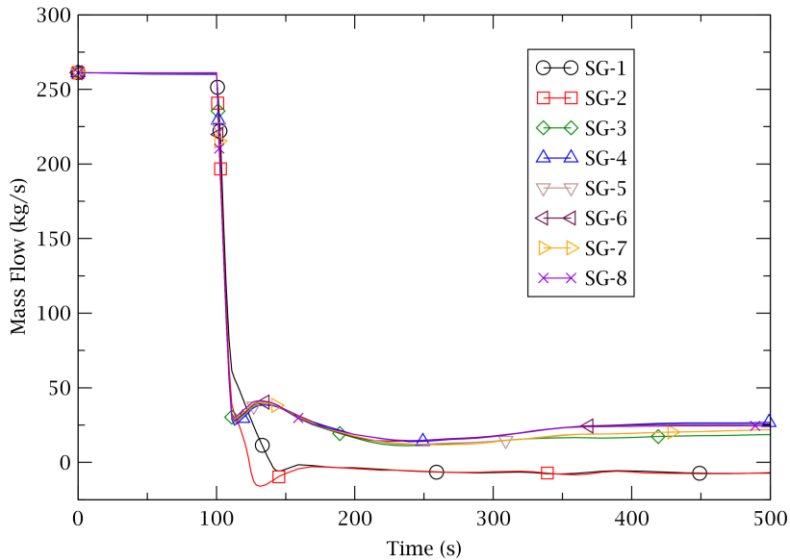


Figure 5.13: The mass flow rate through the Steam Generator (SG) at the primary side of TRACE/PANTHER over time during the Steam Line Break (SLB) transient for the SMART reactor.

The figures reveal that the mass flow rate distribution in the upper part of the RPV before entering the downcomer is azimuthally unsymmetrical. However, an even core inlet flow is crucial for reactor control and safety. To enhance the coolant mixing in the downcomer and lower plenum, the SMART reactor incorporates several components, including the Flow Mixing Header Assembly (FMHA) which is depicted in Figure 3.1.

Figure 5.14 and Figure 5.15 display the mass flow rate at the core inlet predicted by the two codes, with legends representing the eight TRACE azimuthal sectors corresponding to the SGs—though not the SGs themselves. The curves for the eight sectors at the core inlets show nearly identical trends, indicating a uniform inlet mass flow rate to the core. This demonstrates effective coolant redistribution through the downcomer and lower plenum, an effect successfully captured by both TRACE/PARCS/SCF and TRACE/PANTHER. However, the TRACE/PARCS/SCF solution tends to approach zero and oscillate slightly before transitioning to natural flow. This behavior is also reflected in Figure 5.12 and Figure 5.13, which is likely due to the coupling in TRACE/SCF that splits one closed TH domain into two open TH domains. The impact of this multi-scale TH coupling on the TH simulation warrants further investigation.

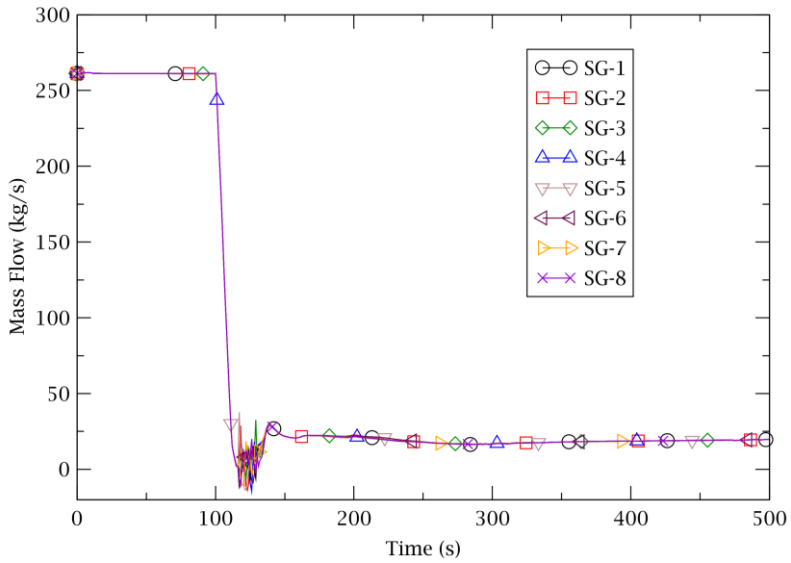


Figure 5.14: The core mass flow rate of TRACE/PARCS/SCF over time during the Steam Line Break (SLB) transient for the SMART reactor.

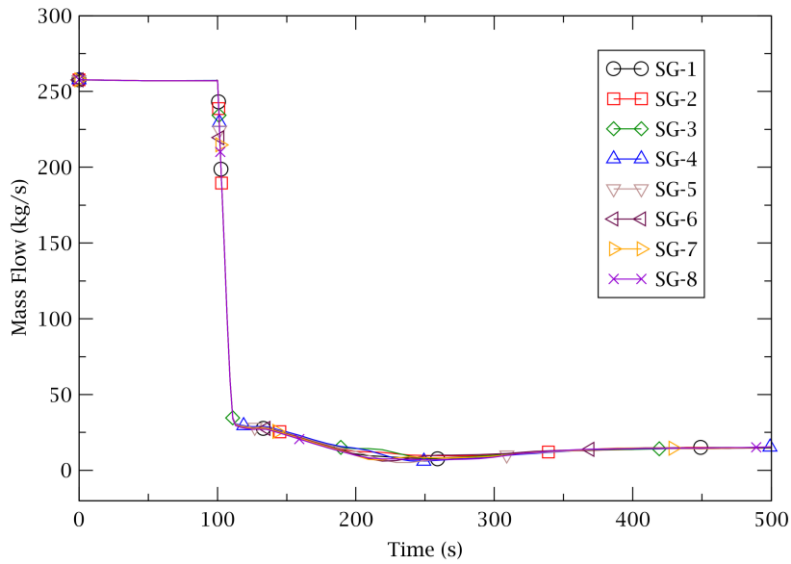


Figure 5.15: The core mass flow rate of TRACE/PANTHER over time during the Steam Line Break (SLB) transient for the SMART reactor.

The primary focus of those aforementioned analyses is to validate the decay heat removal capability and to ensure the core's cooling efficacy, for which, the direct parameters to be examined are the coolant temperatures at the core inlet and outlet.

Figure 5.16 displays those parameters from both the KIT and TBL simulations. There, we can observe two main differences between the two solutions: a) the initial coolant temperature before the transient of TBL is higher than that of KIT, attributed to the lower coolant mass flow rate in the steady state predicted by TBL, as evidenced by reduced pump rotation speed in Figure 5.11; b) KIT produces peaks in the inlet and outlet coolant temperatures during the transient, which is because of the quasi-stagnation of the core inlet flow before the transition to natural circulation.

Both simulations demonstrate an overall decline in coolant temperatures, affirming the safety of the core and reactor throughout the SLB event. This observation aligns with the pressure evolution depicted in Figure 5.17, reinforcing the initial conclusion.

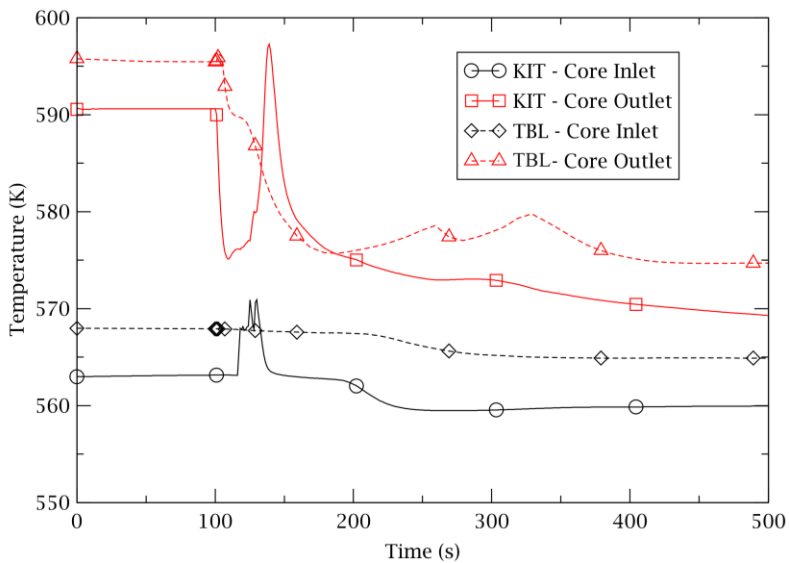


Figure 5.16: The coolant averaged temperature at the core inlet and outlet of TRACE/PARCS/SCF and TRACE/PANTHER over time during the Steam Line Break (SLB) transient for the SMART reactor.

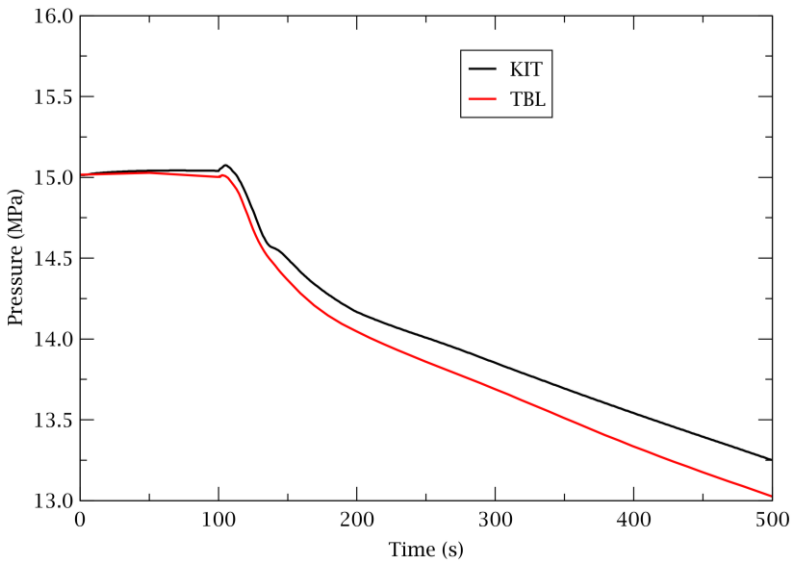


Figure 5.17: The pressure at the pressurizer bottom of TRACE/PARCS/SCF and TRACE/PANTHER over time during the Steam Line Break (SLB) transient for the SMART reactor.

Thanks to the integration of SCF, the simulation conducted by KIT offers the possibility to delve into the detailed TH conditions within the core. Corresponding to Figure 5.1 and Figure 5.2, Figure 5.18 and Figure 5.19 depict the 3D distributions of the fuel and coolant temperatures at the end of the SLB transient.

By employing the same color bar scale, it becomes evident that the fuel temperature illustrated in Figure 5.18 is lower than that depicted in Figure 5.1, devoid of any notable hot points. Similarly, the coolant showcased in Figure 5.19 appears cooler compared to that presented in Figure 5.2.

These findings substantiate the safe condition of both the core and the reactor at the end of the SLB accident, affirming the efficacy of the SMART reactor's passive decay heat removal capabilities.

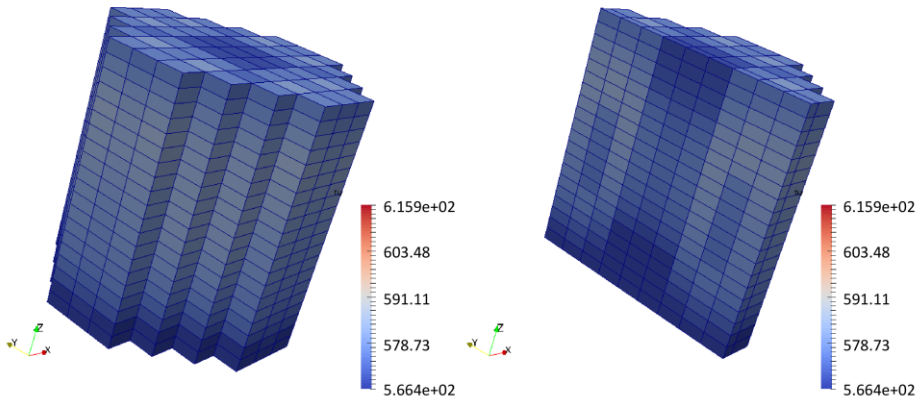


Figure 5.18: The fuel temperature distribution in the core predicted by SubChanFlow (SCF) at the end of the Steam Line Break (SLB) transient.

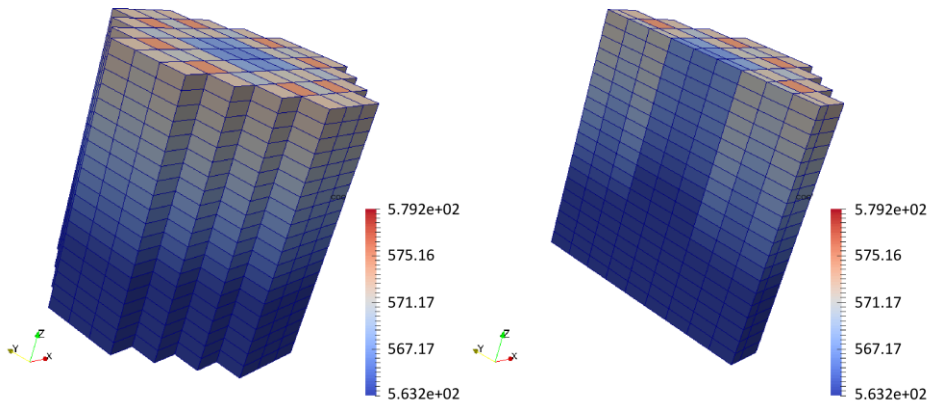


Figure 5.19: The coolant temperature distribution in the core predicted by SubChanFlow (SCF) at the end of the Steam Line Break (SLB) transient.

## 6 Conclusions

The paper presents a safety analysis of the Steam Line Break (SLB) accident for the SMART Small Modular Reactor (SMR), employing the multi-physics multi-scale coupled codes TRACE/PARCS/SCF developed at the Karlsruhe Institute of Technology (KIT). The coupled code successfully captures the key process during the SLB accident, including the triggering of the SCRAM, the power reduction, the loss of offsite power triggering,

and subsequent core mass flow rate reduction due to the main pump coasting down, and the rise in primary coolant temperature due to residual core heat, among others, which gives a more realistic understanding of the SLB accident development.

Another highlight of this analysis is the good prediction of the entire transition sequence from forced convection to the eventual establishment of natural circulation on both the primary and secondary sides, including the thermal-hydraulic and neutronic aspects benefiting from the multi-physics-scale capability of the coupled code.

Furthermore, the detailed 3D distribution of fuel and coolant temperatures at the end of the SLB transient, predicted by SCF, validates the SMART reactor's safe operational status. Overall, the results obtained effectively validate the efficacy of the SMART reactor's passive safety features.

## Acknowledgment

The authors acknowledge the financial support of the NUSAFE program of the Karlsruhe Institute of Technology (KIT) and the European Union's Horizon 2020 research and innovation program under grant agreement No 945063.

## References

- Alzaben, Y., Sanchez-Espinoza, V. H., & Stieglitz, R. (2019). Analysis of a steam line break accident of a generic SMART-plant with a boron-free core using the coupled code TRACE/PARCS. *Nuclear Engineering and Design*, 350, 33–42. <https://doi.org/10.1016/j.nucengdes.2019.05.002>
- Bajorek, S. M., Bernard, M., Gingrich, C., Hoxie, C. L., Ireland, A., Kelly, J., Mahaffy, J., Murray, C., Spore, J., Staudenmeier, J., Thurgood, M., Tien, K., & Whitman, J. (2015). Development, Validation and Assessment of the TRACE Thermal-Hydraulics System Code. 16th International Topical Meeting on Nuclear Reactor Thermal Hydraulics (NURETH-16), 8265–8278.
- Choo, K. N., Cho, M. S., Yang, S. W., & Park, S. J. (2014). Contribution of Hanaro irradiation technologies to national nuclear R&D. *Nuclear Engineering and Technology*, 46(4), 501–512. <https://doi.org/10.5516/NET.07.2014.006>



- Chung, Y.-J., Kim, H.-R., Chun, J.-H., Kim, S.-H., & Bae, K.-H. (2015). Strength assessment of SMART design against anticipated transient without scram. *Progress in Nuclear Energy*, 85, 617–623. <https://doi.org/10.1016/j.pnucene.2015.08.005>
- Downar, T., Xu, Y., & Seker, V. (2012). Theory Manual for the PARCS Kinetics Core Simulator Module.
- Etcheto, J., Zhang, K. & Palmans, N. (2023). Multiscale system/subchannel codes safety analyses of SMART reactor system and intercomparing between codes.
- Ferraro, D., García, M., Valtavirta, V., Imke, U., Tuominen, R., Leppänen, J., & Sanchez-Espinoza, V. (2020). Serpent/SUBCHANFLOW pin-by-pin coupled transient calculations for the SPERT-IIIIE hot full power tests. *Annals of Nuclear Energy*, 142, 107387. <https://doi.org/10.1016/j.anucene.2020.107387>
- García, M., Vočka, R., Tuominen, R., Gommlich, A., Leppänen, J., Valtavirta, V., Imke, U., Ferraro, D., Van Uffelen, P., Milisdörfer, L., & Sanchez-Espinoza, V. (2021). Validation of Serpent-SUBCHANFLOW-TRANSURANUS pin-by-pin Burnup Calculations using Experimental Data from the Temelín II VVER-1000 Reactor. *Nuclear Engineering and Technology*, 53(10), 3133–3150. <https://doi.org/10.1016/j.net.2021.04.023>
- Imke, U., & Sanchez, V. H. (2012). Validation of the Subchannel Code SUBCHANFLOW Using the NUPEC PWR Tests (PSBT). *Science and Technology of Nuclear Installations*, 2012, 1–12. <https://doi.org/10.1155/2012/465059>
- International Atomic Energy Agency. (1997). Status of Advanced Light Water Cooled Reactor Designs 1996, IAEA-TECDOC-968. [http://www-pub.iaea.org/MTCD/Publications/PDF/te\\_968\\_prn.pdf](http://www-pub.iaea.org/MTCD/Publications/PDF/te_968_prn.pdf)
- International Atomic Energy Agency. (2021). Technology Roadmap for Small Modular Reactor Deployment, IAEA Nuclear Energy Series No. NR-T-1.18. [https://www-pub.iaea.org/MTCD/Publications/PDF/PUB1944\\_web.pdf](https://www-pub.iaea.org/MTCD/Publications/PDF/PUB1944_web.pdf)
- Kamalpour, S., & Khalafi, H. (2021). SMART Reactor Core Design Optimization based on FCM Fuel. *Nuclear Engineering and Design*, 372. <https://doi.org/10.1016/j.nucengdes.2020.110970>
- Leppänen, J., Pusa, M., Viitanen, T., Valtavirta, V., & Kaltiaisenaho, T. (2015). The Serpent Monte Carlo code: Status, development and applications in 2013. *Annals of Nuclear Energy*, 82, 142–150. <https://doi.org/10.1016/j.anucene.2014.08.024>
- Sadegh-Noedoost, A., Faghihi, F., Fakhraei, A., & Amin-Mozafari, M. (2020). Investigations of the Fresh-Core Cycle-Length and the Average Fuel Depletion Analysis of

- the NuScale Core. *Annals of Nuclear Energy*, 136.  
<https://doi.org/10.1016/j.anucene.2019.106995>
- SALOME Platform. (n.d.-a). MEDCoupling developer's guide. Retrieved March 21, 2022, from <http://docs.salome-platform.org/latest/dev/MEDCoupling/developer/index.html>
- SALOME Platform. (n.d.-b). MEDCoupling Developers' Guide: The ICoCo API. Retrieved March 21, 2024, from <https://docs.salome-platform.org/latest/dev/MEDCoupling/developer/icoco.html>
- Sanchez-Espinoza, V. H., Gabriel, S., Suikkanen, H., Telkkä, J., Valtavirta, V., Bencik, M., Kliem, S., Queral, C., Farda, A., Abéguilé, F., Smith, P., Van Uffelen, P., Ammirabile, L., Seidl, M., Schneidesch, C., Grishchenko, D., & Lestani, H. (2021). The H2020 McSafer Project: Main Goals, Technical Work Program, and Status. *Energies*, 14(19). <https://doi.org/10.3390/en14196348>
- Tashakor, S., Zarifi, E., & Naminazari, M. (2017). Neutronic Simulation of CAREM-25 Small Modular Reactor. *Progress in Nuclear Energy*, 99, 185–195.  
<https://doi.org/10.1016/j.pnucene.2017.05.016>
- Xu, X., Liu, Z., Wu, H., & Cao, L. (2022). Neutronics/Thermal-hydraulics/Fuel-performance Coupling for Light Water Reactors and its Application to Accident Tolerant Fuel. *Annals of Nuclear Energy*, 166, 108809.  
<https://doi.org/10.1016/j.anucene.2021.108809>
- Zhang, K. (2020). The Multiscale Thermal-hydraulic Simulation for Nuclear Reactors: A Classification of the Coupling Approaches and a Review of the Coupled Codes. *International Journal of Energy Research*, 44(5), 3295–3315.  
<https://doi.org/10.1002/er.5111>
- Zhang, K., Campos Muñoz, A. & Sanchez-Espinoza, V. H. (2021). Development and Verification of the Coupled Thermal-Hydraulic Code – TRACE/SCF based on the ICoCo In-terface and the SALOME Platform. *Annals of Nuclear Energy*, 155, 108169. <https://doi.org/10.1016/j.anucene.2021.108169>
- Zhang, K., & Sanchez-Espinoza, V.H. (2023). Multi-Scale Coupling of TRACE and SubChan-Flow (SCF) in the SALOME Platform Using the Domain Decomposition (DD) Method and a Conservative Data Transfer Approach. 20th International Topical Meeting on Nuclear Reactor Thermal Hydraulics (NURETH-20), 1066–1075.  
<https://doi.org/10.13182/NURETH20-40266>



In this volume, colleagues and friends of Prof. Dr.-Ing. Robert Stieglitz, who died suddenly and unexpectedly on December 6, 2023, pay tribute to his life and his extraordinary achievements as an internationally recognised scientist. Prof. Stieglitz's profound view on fusion research, nuclear technology and renewable energy was appreciated worldwide. The contributions in this volume cover all these areas while reflecting his inspirational influence on the authors.

